The Pennsylvania State University

The Graduate School

Department of Aerospace Engineering

STRUCTURAL DAMAGE DETECTION VIA NONLINEAR SYSTEM IDENTIFICATION AND STRUCTURAL INTENSITY METHODS

A Dissertation in

Aerospace Engineering

by

Fabio Semperlotti

© 2009 Fabio Semperlotti

Submitted in Partial Fulfillments
of the Requirements
for the Degree of

Doctor of Philosophy

August 2009

The dissertation of Fabio Semperlotti was reviewed and approved* by the following:

Edward C. Smith
Professor of Aerospace Engineering
Dissertation Co-Advisor
Co-Chair of Committee

Kon-Well Wang
William E. Diefenderfer Chaired Professor in Mechanical Engineering
Dissertation Co-Advisor
Co-Chair of Committe

Stephen C. Conlon
Assistant Professor of Aerospace Engineering
Dissertation Co-Advisor

George A. Lesieutre
Professor of Aerospace Engineering
Head of the Department of Aerospace Engineering

Martin W. Trethewey
Professor of Mechanical Engineering

*Signatures are on file at the Graduate School

ABSTRACT

During the past decade, the development of Structural Health Monitoring (SHM) systems has attracted considerable interest from several engineering fields. The possibility of monitoring the status (often referred to as "health") of a structure under operational conditions could result in a drastic change in the current maintenance approach. The introduction of SHM systems would allow transitioning the maintenance strategy from a *scheduled* (i.e. Time Based) basis to a *Condition Based* approach. The development of SHM systems relies on availability of reliable techniques to extract the characteristic features of damage from experimental measurements. The research presented in this dissertation consists of an investigation of two new SHM methodologies.

The first technique is based on the use of the Higher order Harmonic Response Signal (HHRS) typical of cracked structures. A theoretical formulation which exploits the nonlinear harmonics in cracked rods is presented. The HHRS provides an effective way to localize nonlinear fatigue cracks without requiring a baseline signal or a finite element model of the healthy structure. The HHRS method is first evaluated through a series of numerical simulations. The HHRS method is then validated through laboratory experiments specifically designed to induce and measure the nonlinear harmonic response in a one-dimensional cracked rod. Experimental results proved that this technique can achieve high accuracy (error lower than 1%). Useful guidelines for the selection of a proper sensory system for HHRS measurements are provided. Finally, the HHRS technique is extended to a two-dimensional plate structure. The characteristic dispersive nature of the dynamic response of plates increases the complexity in the post-

processing phase. A new feature extraction approach, particularly suitable for dispersive system, is presented. Numerical results proved the theoretical approach and provided guidelines for the selection of an appropriate sensory system for data acquisition.

The second technique presented in this work is based on the use of Structural Intensity (SI) as a damage detection tool. Although SI has been used in the past for structural vibrations and noise control systems, applications to damage detection are still very limited. A numerical study exploring the relationship between several structural (loss factors, damage size) and experimental (frequency resolution, sensor size and placements) parameters and the SI field is presented. The changes in SI at discrete structural locations are used as the damage metric. In order to improve performance and adaptability of the SI based system over a wide spectrum of structures, the concept of Active Energy Sink (AES) is introduced. A feedback control system is used to realize the absorption device. The AES design is presented, and validated through experimental testing. An increase in the closed loop loss factors up to $\eta=29\%$ was measured for the low frequency modes. Finally, the concept of Nonlinear Structural Surface Intensity (NSSI) is presented. The SI-based SHM was initially developed by relying on the availability of a baseline for the healthy structure. In order to develop a baseline-free technique, the HHRS is integrated into the SI concept. This approach results in a single technique which benefits from the localization capabilities from the HHRS approach and of the sizing capabilities proper of the SI approach.

TABLE OF CONTENTS

LIST OF FIGURES

LIST OF TABLES

ACKNOWLEDGEMENTS

Many people contributed to the successful completion of this research. I would like to thank my thesis advisors Dr. Stephen Conlon, Dr. Edward Smith and Dr. Kon-Well Wang which provided a very valuable scientific and motivational support throughout the whole course of this research. Thank to their continous dedication in finding research financial support I could work as a Research Assistant for the whole duration of my doctoral studies. I would also like to thank my Ph.D. Committee Members Dr. George Lesieutre and Dr. Martin Trethewey for their valuable technical comments and suggestions.

I gratefully acknowledge financial support for this research from the Center for Rotorcraft Innovation (CRI) under contract number W911W6-05-2-0003, and the Aviation Applied Technology Directorate (AATD) of the U. S. Army Research Development and Engineering Command under contract number W911W6-08-C-0036. The views and conclusions contained in this document are those of the author and should not be interpreted as representing the official policies, either expressed or implied, of the Aviation Applied Technology Directorate or the U.S. Government.

I would also like to thank Mark Catalano, Kirk Heller and Richard Auhl for their continuous support on computers and laboratory setups. I thank the whole staff of the Aerospace Dept. for their continuous help in managing and meeting all the required deadlines related to administrative issues.

CHAPTER 1

Introduction

Aerospace structures operate in an extremely severe environment where the combination of different factors such as external and internal dynamic loads, atmospheric agents and ballistic impacts can induce several types of structural damage. This condition, if not properly monitored, could result in a potentially disastrous mechanical failure.

For this reason interest in detecting structural damage, at the earliest possible stage, has always been a major issue in the structural health monitoring community. The introduction of a sensitive and efficient damage detection system able to monitor the health of an in-service structure would result in either a considerable improvement in the performance and safety of a mechanical system and/or in a drastic decrease of its maintenance cost.

The maintenance operations for a civil aircraft are generally scheduled based on life expectations of major parts and/or subcomponents, obtained either through analytical simulations or experimental data based on the specific fatigue behavior. Although fatigue cracks initiation and propagation are sufficiently well known in metallic materials, the estimated life of a mechanical component is always evaluated applying high safety factors in order to take into account phenomena not included in the fatigue analytical model such as material imperfections, average mechanical properties, analytical or Finite Element (FE) models inaccuracy, uncertainties on the applied external load etc. This aspect becomes even more critical when considering composite materials where the fatigue and crack propagation laws are much less accurate.

In a few cases the analytical data can be matched and refined through the statistical analysis of defects encountered by a specific component during its service life. Of course, this approach assumes that the component has already accumulated a sufficient number of service hours to allow for the development of a meaningful and representative statistical database. This data must be measured in a wide range of working conditions in order to include all the possible load cases experienced by the structure during its operating life. It clearly appears that this approach cannot be generally implemented for new structural components where flight data are still not available.

The described maintenance approach results in:

- ✓ A heavy maintenance schedule essentially based on analytical predictions and not on the effective detection of a damaged component.
- ✓ The replacement of mechanical components that might still have residual life.
- ✓ Increased maintenance costs (purchase of new components, aircraft on ground etc.).

The introduction of an effective and reliable in-flight damage detection system could foster the transition towards a new maintenance approach which would no longer be based on pre-scheduled maintenance operations and components replacement but on an assessment of the real conditions of the structure. This new approach is generally referred to as *Condition Based Maintenance* (CBM).

1.1 Health and Usage Monitoring Systems

Structural Health Monitoring (SHM) is a fairly new engineering field oriented to the development of damage detection systems able to facilitate the transition from scheduled maintenance to condition based maintenance.

In the aerospace field, systems implementing a structural health monitoring approach are generally called Health and Usage Monitoring Systems (HUMS). This acronym highlights the two main objectives of a HUMS system:

- ✓ monitoring the “Health” or structural integrity.
- ✓ monitoring the “Usage” level.

Currently, the structural integrity of aerospace systems is guaranteed by a combination of numerical predictions, NDE inspections on new manufactured components and a tight maintenance schedule. There is no subsequent capability to identify unpredicted damage occurring during the operating conditions and in between scheduled maintenance operations. In particular, damage such as ballistic impacts, structural overloads and atmospheric agents cannot be predicted and accounted for in a scheduled maintenance approach and might result in the failure of primary structures.

The first goal of a HUMS system is targeted at identifying and monitoring the evolution of this kind of flaws that might reduce the structural integrity.

Nonetheless, it must be considered that aerospace structures are among the mechanical systems experiencing the most severe dynamic loads deriving from the operating environment. The structural designing and life predictions are performed based on flight envelopes. These data integrate all the admissible flight conditions for a specific aircraft. However, even if two identical aircraft are flown inside the flight envelope and for the same number of flight hours, they will experience different loads. This situation results from a combination of factors such as different environmental conditions, different mission profiles and different handling. The consequence is a different "usage" of the mechanical system which cannot be captured by only monitoring the total number of flight hours and by satisfying the limitations imposed by the flight envelope.

The implementation of HUMS onboard of aerospace systems is intended to provide a continuous monitoring capability in terms of structural integrity and usage conditions.

1.2 Damage and Damage State Classification

One of the main goals of HUMS is monitoring the initiation and propagation of structural damage. Nevertheless, providing a clear definition of damage is not such an easy task. The definition of damage strongly depends on the "*scale*" used to inspect the mechanical component (Figure 1.1). At macro-scale level damage can be defined as a fatigue crack on the leading edge of a rotor blade (Figure 1.1c) or as a hole produced by a ballistic impact (Figure 1.1d). On the contrary, at micro-scales every material system is intrinsically damaged. At microscopic level materials exhibit voids (Figure 1.1b) and dislocations (Figure 1.1a) that are the origin of structural faults. Even if the scale of interest was more accurately chosen on the base of the specific system to be analyzed, the question of how to define damage would still persist.

The definition of damage, given by Farrar [1], provides a better way to address this problem. Damage is "any change introduced into a system that adversely affects its current or future performance".

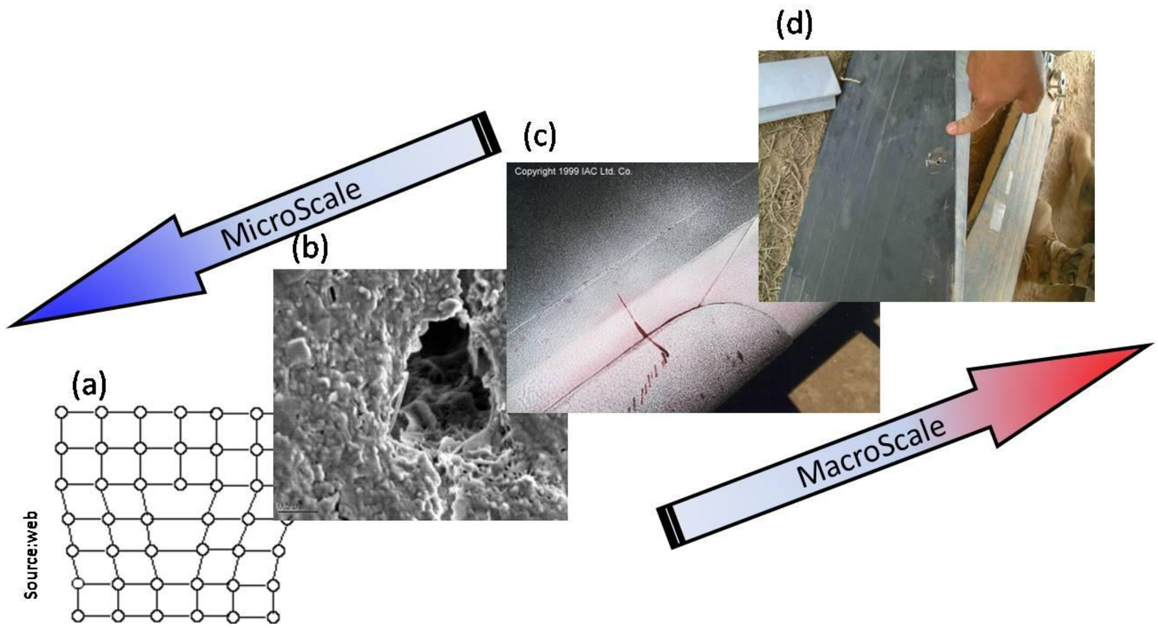

Figure 1.1. Schematic showing the impact of the length scale on the definition of the structural damage.(a) dislocation and (b) void into the material, (c) fatigue crack on the leading edge of a rotor blade, (d) ballistic impact on a rotor blade.

According to this definition, the damage is no longer evaluated in terms of its presence but, instead, in terms of visible effects on the system functionalities. Although being more appropriate for defining damage from a HUMS point of view, this definition still leaves some uncertainties. To clearly define the damage state, the minimum size upon which the structural performance is considered degraded must be identified. In general, every mechanical system has different requirements and therefore the definition of damage is really application dependent.

The second important issue that must be addressed when developing damage detection systems is defining the set of information that must be collected to clearly identify the damage state. In 1993, Ritter [2] proposed a damage state classification that was widely accepted by the HUMS community. According to this classification, the status of a mechanical system can be clearly assessed once the following set of information is determined:

Level 1) Determination of the presence of the damage.

Level 2a) Determination of the geometric location of the damage.

Level 2b) Determination of the nature of the damage.

Level 3) Determination of the severity (extent) of the damage.

Level 4) Prediction of the remaining service life.

By answering these fundamental questions we can clearly identify if damage exists (Level 1), where it is located (Level 2a), what kind of damage is affecting the structure (Level 2b) and what are its characteristic dimensions (Level 3). Level 1 through 3 identify what is generally called “diagnostic” phase.

Level 4 is generally not included in the capabilities of a HUMS system because it deals with the fatigue analysis and fracture mechanics fields. It is generally listed in the damage state classification because it represents the next logical step to completely assess the status and the remaining service life of a mechanical system. Level 4 is more commonly referred to as "prognostic" phase.

1.3 Literature Review on Structural Health Monitoring Techniques

During the past decade, several Structural Health Monitoring techniques exploiting different areas of physics, data post processing and transducers development were proposed by the research community. SHM has been proven to be a very interdisciplinary field where the detection sensitivity and accuracy can be achieved only by a combined use of advanced techniques coming from different engineering areas. Techniques able to interrogate and sense the structure in a very controlled fashion as well as post-processing approaches able to extract small features from numerically or experimentally measured data are just an example of key areas in SHM.

The proposed literature review describes relevant research in the area of Health and Usage Monitoring Systems applied to aerospace, mechanical and civil structures. In particular, the literature pertaining the detection and the location of the damage will be analyzed and one of the possible classifications of these methodologies will be presented. To this regard, it must be stressed that there exist many possible ways to classify the damage detection methods depending on the main parameters retained as guidelines. In this review the different methods will be first classified depending on their ability to sense the damage on a "global" or "local" scale. Then, each of these two classes will be further classified depending on the detection approach effectively used to monitor the health of the structure.

HUMS systems rely on information collected through different techniques belonging to various engineering areas. In particular, during the last years a great interest was given to signal post-processing procedures. These techniques have been seen as a powerful way to extract useful information about the damage even when the acquired signal from the damaged structure is very close to the baseline signal (healthy structure). A review of these methods will be presented in the following sections.

1.1.1 Global Damage Detection Techniques

The global non-destructive damage detection techniques rely on the analysis of measurable changes in the global behavior of the structure in order to verify the existence, the location and the extent of the damage. The undergoing assumption is that the presence of a defect modifies the mass, stiffness and/or damping matrices, resulting in a modification of the global structural dynamic behavior of the system.

In this class of technique, the structure is inspected as a whole [3] through the observation and the analysis of global structural parameters like basic modal properties [4] (as, for instance, frequencies and mode shapes), strain distribution, changes in structural matrices (model updates), etc.

1.1.2 "Vibration-Based" Damage Detection Techniques

One of the most important and widely studied categories belonging to the global damage detection methods is the so called "Vibration-based" damage detection technique.

This methodology relies on the analysis of changes in the measured dynamic properties estimated through a comparison with a Finite Element model or with a set of baseline experimental data of the healthy structure. This approach has received considerable attention over the past 30 years and it has attracted new interest over the past decade. The increase in this activity is due to the technological improvements in cost-effective computing memory and speed, sensors and adaptation of finite element methods [4].

Many different approaches have been proposed in the past to observe the state of a mechanical structure through the analysis of its dynamic behavior. However, all of these methods underlie the same overall idea: when the damage occurs it produces a change in the modal parameters and, consequently, in the dynamic behavior of the structure. The discrepancy between the modal properties of the healthy structure and those of the damaged structure can be analyzed in order to provide information about the existence, the location and the extent of the damage.

Although this class of methods has been widely studied using different approaches (shift in structural frequencies, changes in modal shapes, changes in Frequency Response Functions etc.) some serious issues have still to be solved in order to make it a valuable method for an in-flight damage detection system.

Vibration based methods, in fact, can have limited sensitivity to small size defects due to the global character of the modal parameters, but for some applications can provide a useful metric. Moreover, these methods require high accuracy vibration measurements in order to achieve reliable results. Nevertheless, even increasing the number of acquisition data points, for instance, we can only affect the accuracy of the data but we cannot get any supplemental information about the damage. This is, once again, due to the global character of the frequency based approach.

Here below the reader can find a description of the most common frequency-based damage detection methods, studied in the past, by the SHM community.

1.1.2.1 Frequency Shift

One of the first methods that were investigated in the framework of the frequency based damage detection technique relies on the shift produced by the damage in structural natural frequencies. Many authors showed as variations of the structural parameters (stiffness, damping and mass) produced by an incipient damage can be detected and analyzed through the shifts produced in the structural response frequencies.

It should be noted that the frequency shift method has significant practical limitations, although many improvements have been done achieved in the past years in order to solve these difficulties. In particular, the frequency shift method generally has a low sensitivity that requires either very precise measurements or large levels of damage. Additionally, this method provides information for Level 1 of detection but it has a very low content of information to accomplish Level 2 and 3 [5-7]. Frequency shift for a multi-damaged structure typically yields an under determinate problem where the quantity of information provided by the frequency shift is not enough to uniquely determine all the damaged-induced structural parameter variations.

An exhaustive overview of the frequency shift based methods studied in the past can be found in [5-7].

1.1.2.1.1 Sensitivity Enhancing Feedback Control Through Eigenstructure Assignment

Different techniques have been proposed to overcome the lack of sensitivity intrinsic to the frequency shift based methods. The greatest part of these approaches were based on the definition of proper damage indices capable to extract and compare the frequency shift of different structural modes. These approaches, however, can be interpreted as a sort of data post-processing that, along with the signal post-processing techniques we will analyze later on, allows a more accurate analysis of the measurement data through a higher sensitivity to small changes in the output. These techniques do not increase the content of information in the output data, and consequently do not increase the intrinsic sensitivity of the method.

Jiang et al. [8] proposed an improved frequency shift based technique, including a sensitivity enhancing feedback control, through eigenstructure assignment. Using multiple control inputs/actuators the closed-loop eigenvalues and eigenvectors can be assigned by means of a Singular Value Decomposition (SVD) based eigenstructure assignment. Jiang formulated an algorithm to optimally assign the eigenvalues and eigenvectors that yield enhanced closed-loop natural frequency sensitivity which, finally, leads to improved damage detection performance.

Also, this method allows overcoming the problem related to the solution of an under-determinate system of equations typical of the frequency-shift approach.

1.1.2.2 Mode Shape Changes

Changes in mode shapes have been regarded in the past as a possible indicator for structural damage. According to Doebling [4], West [9] proposed for the first time the possible use of mode shape information for the location of structural damage without relying on the use of a finite element model. The Modal Assurance Criterion (MAC) is used to determine the level of correlation between mode shapes obtained from tests conducted on the same structure in damaged and undamaged configuration. The mode shapes are partitioned using various schemes and the change in MAC across the different partitioning techniques is used to localize the structural damage.

The MAC is defined by Allemang and Brown [10] as:

$$MAC\left(\{\Phi_{\mathrm{X}}\}_i, \{\Phi_{\mathrm{A}}\}_j\right) = \frac{\left|\{\Phi_{\mathrm{X}}\}_i^T \{\Phi_{\mathrm{A}}\}_j\right|^2}{\left(\{\Phi_{\mathrm{X}}\}_i^T \{\Phi_{\mathrm{X}}\}_j\right)\left(\{\Phi_{\mathrm{A}}\}_j^T \{\Phi_{\mathrm{A}}\}_j\right)} \tag{1.1}$$

where Φ_i indicates the eigenvector associate with the *i-th* mode while the X and A subscripts refer to experimental and analytical vibration modes, respectively.

This method, however, has been shown to be relatively insensitive to damage. Fox [11] shows that single-number measures of mode shape changes such as the MAC are relatively insensitive to damage in a beam with a saw cut. The “Node line MAC” (i.e. the MAC based on measurement points close to a node point for a particular mode) was found to be a more sensitive indicator of changes in the mode shape caused by damage. Graphical comparison of relative changes in mode shapes was proved to be the best way of detecting the damage location when only resonant frequencies and mode shapes were examined. Moreover, the MAC does not provide explicit information about the location of the damage, i.e. where the mode shapes show discrepancies.

Many other formulations of the MAC have been proposed in the literature in order to overcome this last problem. Lieven and Ewins [12] proposed the co-ordinate MAC (COMAC) in order to retain information about the coordinates where two sets of mode shapes do not agree.

Kim et al. [13] proposed the combined use of the COMAC and the PMAC (Partial MAC which correlates part of modal vectors) concepts, referred to as the Total MAC, which allows for the isolation of the structural areas where damage occurred.

1.1.2.3 Mode Shape Curvature/Strain Mode Shape Changes

An alternative to using mode shapes, in order to obtain spatial information about sources of vibration changes, is to use mode shape derivatives such as curvature.

Pandey et al. [14] demonstrate that absolute changes in mode shape curvature can be a good indicator of damage for the beam structure they consider. They used a central finite differencing scheme in order to evaluate the mode shape curvature (υ''_{ij}) produced by a prescribed mode Φ_r at a certain location j, as described by the following relation:

$$\upsilon''_{ij} = \frac{\phi_{(j+1)r} - 2\phi_{jr} + \phi_{(j-1)r}}{h^2} \tag{1.2}$$

where ϕ_{jr} is the modal displacement for mode shape r at the coordinate j and h is the distance between the measurements coordinates.

Since a local reduction in stiffness is associated with a local increase in the curvature (υ'') this parameter can provide information to detect, locate and quantify the damage. Stubbs et al. [15-16] presented a method based on the decrease in modal strain energy between two structural DOFs (for the linear-elastic Bernoulli-Euler beam), as defined by the curvature of the measured mode shapes. In a more recent research, Stubbs et al. [17] examined the feasibility of localizing damage using this technique without baseline modal parameters. Baseline modal parameters of the healthy structure, in fact, are estimated through a finite element model of the healthy structure.

1.1.2.4 Dynamically Measured Flexibility

Another parameter that can be used to provide information about the health of a system is the dynamically measured flexibility matrix which is used in order to estimate changes in the static behavior of the structure. The dynamic flexibility matrix is a transfer function defined as the inverse of the static stiffness matrix, consequently the flexibility matrix relates the applied static force and the resulting structural displacement. Each column of the flexibility matrix represents the displacement of the structure resulting from a unit force applied at the corresponding DOF. The measured flexibility matrix can be estimated from the mass-normalized measured mode shapes and frequencies. This method normally uses an approximate flexibility matrix based on the first few structural modes. The result is, obviously, an approximation because only by considering all the mode shapes and frequencies we can get the complete static flexibility matrix. However this produces a large amount of data to be processed consequently increasing the calculation time and the space needed to store the data.

Typically, the damage is estimated by comparing the flexibility matrices synthesized by the modes of the damaged and the undamaged structure, respectively.

Several methods [4] have been investigated in the past in order to exploit the information about the damage included in the flexibility matrix. Some of them are the comparison of flexibility changes [18,19], the unity check [20,21], the stiffness error matrix method [22,23] and the measured stiffness matrix [24,25].

From a general point of view, the measured flexibility matrix is more sensitive to changes in the lower frequency modes of the structure because of its dependence on the inverse of the square of the modal frequencies. On the contrary, the stiffness matrix is more sensitive to higher order modes.

1.4 Structural Model Updating Technique

Another class of damage detection methods is the so called “Structural Model Updating” technique. This method can be used in conjunction with a large number of damage detection techniques even if , in the past, it was often applied together with the frequency-based methodology. For this reason and in the frame of this review, this class of methods has been considered as making part of the frequency-based methods.

The model updating method relies on the modification of structural model matrices (mass, stiffness and damping) in order to reproduce as close as possible the experimental static or dynamic response of a structure.

This method aim is to identify the updated matrices, which consists in perturbed matrices with respect to the nominal undamaged model, by solving a constrained optimization problem based on the structural equations of motion, the nominal model and the experimental data. The comparison of the updated matrices with the nominal ones provides an indication of the existence, the location and the extent of the damage.

Several approaches have been proposed in the past to solve this optimization such as methods based on the objective functions and constraints [26], optimal matrix update [27], sensitivity based update methods problem [4], eigenstructure assignment [28-30] and hybrid matrix update [31,32]. It must be observed that, independently of the method used to solve for the perturbation matrices, all of these methods need an n-DOF finite element model of the undamaged structure to characterize the damage.

Level 1, 2, and 3 damage identification is achieved if the degrees of freedom associated with the perturbations and the values of each of the perturbations are identified.

1.5 Local damage detection techniques

As opposed to the global damage detection methods listed above, the local damage detection techniques allow for monitoring a limited part of the structure providing ideally a higher resolution. One of the general drawbacks of these techniques is that, because they can sense small structural features, they require a higher number of sensors and/or actuators in order to guarantee coverage of the whole system. These techniques also require specialized sensors and large bandwidth data acquisition systems.

The advantage of this kind of methods is a higher resolution and sensitivity to smaller damage than what can be detected through global damage detection techniques.

It must be noted that the greatest part of these techniques were originally used for on-ground Non Destructive Tests (NDT). As already highlighted, these techniques generally provide a better sensitivity and resolution to the damage but also require bulky equipments operated by qualified technicians.

During the recent years, many authors have investigated the possibility of transferring the technology applied in nondestructive evaluation to structural health monitoring applications. A review of the most popular local damage detection techniques is now presented.

1.1.3 Electro-Mechanical Impedance method

The application of the electro-mechanical impedance (EMI) method for Structural Health Monitoring applications was first proposed by Liang *et al.* [33]. This method uses high frequency structural excitations (typically higher than 30 KHz), produced through surface bonded PZT patches, to monitor changes in the structural impedance.

Liang showed that the overall electro-mechanical admittance Y of the mechanical system, i.e. the inverse of the electro-mechanical impedance Z, is a function combining the mechanical impedance of the PZT patch ($Z_{a,eff}$) and that of the host structure ($Z_{s,eff}$):

$$Y = \frac{1}{Z} = \frac{I}{V} = j\omega \frac{l^2}{h}\left[\varepsilon_{33}^{T} - \frac{2d_{31}^{2}\overline{Y^{E}}}{(1-\upsilon)} + \frac{2d_{31}^{2}\overline{Y^{E}}Z_{a,eff}}{(1-\upsilon)(Z_{s,eff}+Z_{a,eff})}\left(\frac{tankl}{kl}\right)\right] \tag{1.3}$$

where ω is the resonance frequency, k is the wavenumber, l and h are the half length and thickness of the rectangular PZT patch, ε_{33}^{T} and d_{31} are the permittivity at constant stress and the piezoelectric strain coefficient, υ and $\overline{Y^{E}}$ are the Poisson ratio and the complex Young modulus of elasticity of the PZT patch.

By comparing the admittance signature of the system, taken at a certain time during its operating life, with a baseline admittance signature (reflecting the behavior of the healthy structure, often referred as the pristine state) we can identify possible variations in the structural dynamics induced by the defect.

Bhalla et al. [34-36] investigated practical issues in the implementation of the impedance method providing a procedure to extract the structural impedance of the host structure by the global admittance signature and to relate these variations to those of structural parameters. They introduced also the concept of “active” admittance signature where the part coming from the PZT is filtered out.

Parametric studies have also been proposed in order to determine the influence on the different parameters on the sensitivity and the accuracy of impedance measurements. Stokes and Clouds [37] assessed that to ensure high sensitivity to incipient damage the electrical impedance should be measured in a high frequency range (30-400 KHz) because the wavelength of the excitation must be shorter than the characteristic length of the damage.

Esteban et al. [38] developed a parametric study to define the sensing region of an impedance sensor. They found that, in general, the sensing region of these sensors is closely related to the material properties of the host structure, geometry, frequency range being used and properties of PZT material. The sensing radius has been estimated between 0.4m in composite structures and 2m in simple metal beams. Moreover, at frequencies higher that 500KHz the sensing region becomes very small and the PZT bonding layer’s behavior considerably affects the measurement.

Raju [39] performed an extensive experimental study on the effects of actuator excitation level, test wire length, multiplexing (using a single wire for accessing multiple sensors) and boundary condition changes. He concluded that variations of these parameters do not significantly affect the impedance signature.

Castanien and Liang [40] introduced the transfer-impedance using non-co-located sensors in order to obtain more global information about the conditions of the structure and to reduce the number of sensors needed to inspect the whole system.

Other references on the EMI method can be found in [41] and [42].

1.1.4 Lamb Waves

An approach that has received a considerable attention during recent years is based on the use of Lamb [43] waves to detect structural damage. Lamb waves are ultrasonic waves of plain strain that occur in a free plate where traction forces must vanish at the upper and lower surfaces [44]. This method has been attracting the interest of many researchers due to its capability to provide more information about the damage existence and severity than other methods previously explored. Although this method looks promising for damage identification, the analysis of the reflected waves in complex structures and the identification of the propagation characteristics in composites materials are still complicated phenomena that need to be further investigated. Saravanos et al. [45] presented a damage detection technique targeted to the detection of delaminations in composite materials by using using Lamb waves generated through embedded piezoelectric sensors.

More recent studies performed [46 - 48] concentrated on the generation of directional Lamb waves through the use of specifically designed transducers. Kessler et al. [49] applied Lamb waves to detect damage in composite structures providing an experimental procedure capable of determining the Time of Flight (TOF) of a wave pulse between an actuator and a sensor. They also proposed a sensitivity study investigating the different parameters (such as actuators and sensors geometry, actuation signal properties and specimen properties) affecting the sensitivity to the damage like.

1.1.5 Acoustic emissions

The Acoustic Emission (AE) method uses the elastic waves generated by crack initiation, moving dislocations and disbands, to detect eventual faults into the structure. When damage occurs in a structure the rapid local redistribution of the stresses around the damaged area creates elastic waves that propagate into the host structure in all directions [50]. These waves can be collected by an array of sensors and analyzed in order to derive information about the damaged area.

Despite a good sensitivity to damage this method cannot be used to realize a continuous monitoring of the structure because it requires a stress redistribution (i.e. a change in the equilibrium state of the defect) to generate the acoustic emission. Moreover, the multiple waves generated by the same source (and following each one a different path to the sensor), make the interpretation of the signal quiet complicated [51]. Even the ambient noise has to be accurately filtered out before analyzing the signal [52].

1.1.6 Impact-Echo Testing

Another method belonging to the local damage detection technique is the Impact-Echo (IE) testing. This method requires a stress pulse applied to the structure by an impact source. The resulting stress waves propagate into the structure and are reflected by eventual defects (cracks, disbonds etc.). The reflected waves are, then, collected by a network of sensors and the damage location is extracted by analyzing the "echo" (i.e. the reflected wave) produced by the defect. The echo provides information based on the time of flight of the wave from the impact point to the sensor location.

The IE method, however, requires an external source to generate the pulse and, consequently, does not represent a proper methodology for an on-line autonomous fault detection system. Moreover, this method has been proved not to be very effective for small size damage due to the relatively low frequencies involved [53].

1.6 Post-processing techniques

Considerable improvements to the sensitivity and accuracy of the damage detection techniques came, during the last decade, from the application of advanced signal post-processing techniques.

Post-processing techniques are not intended to increase the intrinsic sensitivity to the damage, which will still be determined by the selected damage detection method, as previously stated. The goal of these techniques is to isolate and extract features relevant to the damage from the measured structural response either at global or local level.

When dealing with incipient damage, in fact, the differences between the healthy and the damaged signals are generally very small and a direct comparison between the absolute values of these measurements could not be sensitive enough to reflect the actual changes in the structural properties. This is particularly important when using global techniques where the effect of a structural damage on the overall response could be extremely small and localized. In addition to that, every experimental measurement is unavoidably contaminated with noise, or other extraneous effects, which results in masking eventual (small) changes in the measured structural response.

For these reasons, post-processing techniques have become more and more important to accurately filter out the noise component from the measured signal and to effectively detect and amplify small changes in the output signal.

1.1.7 Damage index

One of the first approaches used to extract information from the measurement data is the so called “Damage Index” (DI). The main idea is to derive a metric that can directly compare the response of the healthy and damaged structure and provide a scalar output that can be used as index to identify and possibly quantify the damage.

Many different damage indices have been proposed in the past especially in the frame of the frequency-shift based methods. Many of them are based on structural frequency measurements implying different weighting or normalization techniques. Others are based on the Modal Assurance Criterion (MAC) and its modified versions. The main disadvantage related to the use of these indices is their inability to track changes in nonlinear and non-stationary signals.

An exhaustive survey of damage indexes can be found in Montalvão et al. [6].

1.1.8 Fast Fourier Transform and Wavelet Transform

One of the most popular techniques for signal post-processing is the Fourier transform which breaks down a signal into constituent sinusoids of different frequencies. Another way to think of Fourier analysis is as a mathematical technique to transform our view of the signal from time-based to frequency-based. Unfortunately, after the transformation of the signal to the frequency domain, time information is lost. This means that, when looking at a Fourier transform of a signal, it is impossible to tell when a particular event took place.

If the signal properties do not change much over time this drawback is not very important. However, typical signals encountered in damage detection contain numerous non-stationary or transient characteristics. Fourier analysis is not suited to detect them.

The first logical step to improve the Fourier analysis has been the introduction of the Short Time Fourier Transform (STFT) or Fast Fourier Transform (FFT). This is a so called “windowing” technique because we can analyze a small section of the signal at a time, breaking the entire time interval into smaller sub-intervals.

The STFT represents a sort of compromise between the time and frequency based views of a signal, providing information about when and at what frequencies a signal event occurs. However, we can only obtain this information with limited precision which is related to the particular size chosen for the window. Moreover, the size chosen for the window has to be the same for all the subintervals, this means that if the signal has transients or non-stationary contents we can analyze them with limited resolution.

The Wavelet transform (WT) represents the evolution of the FFT. The WT is a windowing technique where we can adopt variable-sized windows. Wavelet analysis allows the use of long time intervals to get more resolution at low-frequencies, and shorter intervals at high-frequencies. This property guarantees very high resolution all over the frequency range. The WT has been widely applied, during the past years, by the SHM community to post-process experimental data [54].

Yan and Yam [55] used the WT to decompose the spectral energy of the structural dynamic response of a composite plate with embedded piezoelectric sensors/transducers. The proposed method successfully succeeds in identifying a crack matrix affecting the 0.06% of the total area.

Amaravadi et al. [56] proposed a technique that combines the curvature mode shape with the wavelet maps. The mode shapes are double differentiated using the central difference approximation to obtain the curvature mode shapes. Then a wavelet map is constructed for the curvature mode shapes. It is shown that this method can be used to determine the location of the damage.

Another interesting application has been proposed by Kitada [57] who applied WT to determine stiffness and damping coefficients in structures with severe material nonlinearities without any preliminary assumption about nonlinear characteristics of the structure. The identification of structural parameters for linear, bilinear and Ramberg-Osgood stress-strain rules is successfully addressed.

1.1.9 Neural Networks

Neural Networks (NN) are biologically inspired artificial intelligence representations that mimic the functionality of nervous systems. As in nature, the network structure and functionalities are determined by the connections between elements. These systems can be also “trained” to perform a particular function by adjusting the values of the connections (weights) between elements. NN are currently applied in many different fields to solve identification or classification problems, to develop control system, for pattern recognition, optimization problems etc.

The application of Neural Networks to the damage detection systems has been considerably increased during the last years due to their capability to deal with several types of damage, at different locations, within the same structure.

Hatem et al. [58] applied NN to damage detection in CFRP composites. Four types of damages were considered (circular holes, delaminations, surface cracks and through cracks). Damage was then identified by a generalized regression network.

Yam et al. [59] used, instead, the energy spectrum of the wavelet transform of the dynamic response to reduce the number of inputs of a NN used to detect cracks in honeycomb sandwich plates.

1.7 Damage Detection Systems on Helicopters

The literature review presented in the previous paragraphs gave an overview of some of the most popular techniques investigated in the past years for possible application in SHM systems. Nevertheless, these techniques still belong to research environments and their application to real mechanical systems in operating conditions requires further analysis and experimental validation. For these reasons, the maintenance approach of current helicopter structures is still heavily based on a scheduled maintenance approach. However, during the past years some basic health and usage monitoring systems have been integrated on aircraft in order to keep track of unexpected rotor behavior during the prescribed service life. The greatest part of these methods, however, is still rudimental and the provided data require the presence of the pilot or of the ground personnel to be interpreted.

One of the simplest onboard usage monitoring systems is Flight Time Monitoring. This system accurately records operating time, flight regimes and events such as take-offs and landings, flights, rotor starts, external load cycles and time with rotors running. These data will be successively analyzed in order to refine the expected safe-life time for the critical components, taking into account the specific flight conditions experienced by a certain rotor. Therefore they do not provide an instantaneous feedback to the pilot concerning the status of the rotorcraft system.

Another usage monitoring system is based on the measurement of oil temperature, oil pressure or shaft torque level. The time and the level of the exceedence and flight parameters (such as altitude, airspeed and outside air temperature) are recorded and stored in a flight computer for post flight evaluations. Differential Pressure Indicators (DPS) are becoming very popular for monitoring the debris level in fluid lines which could provide indications of gearbox malfunctioning [60].

During the last few years, HUMS systems on rotorcraft platforms have evolved essentially towards vibration measurement based systems. Acceleration levels are collected at many different critical locations and stored along with other relevant information (such as time stamps, flight parameters etc.) in the flight data computer. These systems are generally known as Digital Source Collectors (DCS) [61]. Possible application of real time data transfer are also being considered in order to reduce the amount of data to be stored in the flight computer and to allow a more rapid and efficient analysis of the flight measurements.

Another popular, and maybe the most advanced HUMS system currently onboard helicopters, is the Automatic Rotor Track and Balance (ARTB) system. The original goal of this system was to reduce structural vibrations due to vertical and lateral unbalances related to unequal lift and mass distribution in the rotor system.

Successively, its use was extended in order to provide an insight on possible rotor faults. This system, in fact, balances the inertial and aerodynamic loads acting on the blade, adjusting the position of a dedicated mass along the blade itself. This system needs an optical sensor to measure the relative position of each blade, accelerometers to measure the harmonics on the fuselage and an onboard processor to reduce data.

The transformation between vibration measurements and blade position may be thought of as a sensitivity matrix relating three adjustments (pitch link extension, blade weight, and trim tab position) to a change in rotor performance. This system, however, can identify only damages affecting the global behavior of the blade and can provide very little information about the nature of the damage itself.

A detailed literature review concerning HUMS applications for helicopter can be found in [62].

1.8 Problem Statement and Research Objectives

This research focuses on the development of Structural Health Monitoring (SHM) technologies with specific applications to rotorcraft primary structures. Rotorcraft represent good examples of mechanical systems where the transition from *scheduled maintenance* to a *condition based maintenance* approach is expected to provide considerable improvements from several perspectives. The decrease in the maintenance cost and the increase in safety and reliability are among the most interesting examples.

The main goal of the current research is not proving the need of health monitoring systems for rotorcraft applications, which is already well documented in the literature

[63,64], but instead investigating possible techniques for the implementation of HUMS systems on helicopter structures.

The literature review highlighted how, despite several SHM techniques being investigated in the past decade, only limited methods proved to be viable approaches to address the damage state classification. Nevertheless, many of these techniques rely on the use of a baseline signal and/or a finite element model of the healthy structure (in the case of model update techniques). The application of these techniques to monitor a mechanical system in operating conditions results in several important limitations.

The use of a baseline signal can be very problematic when trying to achieve a high level of accuracy and repeatability. Baselines are extremely dependent on the specific environmental and loading conditions upon which they are estimated. This dependence makes them very sensitive to the smallest variations. The sensitivity problem is even more accentuated when the damage assessment is performed with the system in operating conditions. In this last case, multiple databases corresponding to the different operational regimes should be previously acquired and stored. Nonetheless, creating a comprehensive reference database including the dependence from environmental conditions and their correlation with the loading parameters was proven to be extremely challenging [65].

In a similar fashion, the model updating techniques experiences limitations in their practical implementation. This class of methods requires the development of an accurate Finite Element (FE) model of the healthy structure that is normally a very challenging task to accomplish when dealing with complex mechanical systems. The development of an accurate FE model is even more challenging when modeling the structural response in a high frequency range. The simulated structural response is very sensitive to the local mechanical properties and the modeling approach. The model updating methods are also very time consuming and require considerable computational resources. These techniques generally do not lend themselves for the implementation of an onboard damage detection technique. These considerations suggest that the identification algorithm should possibly be based only on the evaluation of experimental measurements without relying either on baseline signals or on finite element models of the test structure.

The overall objective of this research is performing a feasibility study of two novel damage detection techniques for applications in Health and Usage Monitoring Systems of helicopter structures. The results presented in this study are mainly intended to develop and establish the capabilities of these techniques as damage detection tools. Although general guidelines for key parameters will be provided, no attempt was made to optimize the system performance.

In particular, this research will focus on studying two damage detection strategies for possible future application on helicopter primary structures such as:

1. Rotor blades.
2. Airframe structures.

Following the indications provided by the literature review and taking into account the limitations associated with the use of either a baseline signal or a FE model of the host structure, a selection of possible technical requirements to develop an improved damage detection technique were made.

Specific requirements are:

- ✓ Addressing Level 1 and Level 2a of the damage state classification.
- ✓ Not relying on a baseline of the healthy structure.
- ✓ Not relying on a FE model of the host structure.
- ✓ Reduced number of sensors.

Two possible concepts were selected as suitable candidates for structural health monitoring applications. These techniques are based on:

1. Higher order Harmonic Response Signals (HHRS).
2. Structural Intensity.

The first approach exploits the Higher order Harmonics proper of the nonlinear dynamic response of a cracked structure. A novel technique, denominated Higher Order Harmonic Response Signals (HHRS), based on the analysis of the information carried by the nonlinear dynamic response of the damage structure, is presented. This technique was conceived to perform damage detection and localization in slender structures for possible applications on rotor blades.

Specific objectives for this task are to:

1. Evaluate the feasibility of a damage detection technique which performs damage identification only relying on measured data. The system must be able to identify the damage without relying either on a baseline database or on a FE model of the healthy structure.
2. Develop an active interrogation technique able to exploit the information carried by the Higher order Harmonic response signal characteristic of

cracked structures. Although the phenomenon of the higher order harmonic generation in cracked structures has been theoretically and experimentally studied in the past years, the use of this concept for damage localization has never been investigated before.

3. Develop the analytical formulation supporting the application of the HHRS technique in slender isotropic structures. This task includes the development of the numerical model for both the damage detection algorithm and the data post processing technique.
4. Develop a finite element model based procedure to simulate the response of a cracked structure and to numerically validate the HHRS technique.
5. Design and conduct a laboratory experiment able to validate the HHRS technique. This task includes the selection of a proper sensory system capable of generating and sensing higher order harmonics.
6. Extend the HHRS formulation to plate structures. The HHRS technique is initially formulated for isotropic rods which behave as non-dispersive one-dimensional waveguides. The dynamic response of plate structures is dispersive in nature and the effect of the boundary conditions is much more severe. The development of a post processing technique able to account for these effects is required to apply the HHRS to plates.

The second approach investigated in this research is based on the Structural Intensity (SI), or Power Flow, concept. This approach is intended for possible applications on more complex mechanical system such as helicopter transmission frames.

The SI was used, in the past, as a tool to control noise and vibration in a mechanical system. Although the SI is a more mature concept with respect to the HHRS, there are a few applications of this methodology for damage detection purposes. The objective of the second part of this research is formulating a Structural Intensity based damage detection technique.

Despite the overall requirements set at the beginning of this research, the SI approach is first investigated by using a baseline signal of the healthy structure. Due to the lack of literature on this technique, this preliminary investigation is intended to build the necessary knowledge about the physical relations between the structural damage and the changes produced in the SI field.

Specific objectives for this task are to:

1. Perform a parametric study to identify the effects of functional parameters (structural, numerical and experimental) on the SI field. This step is also intended to provide general guidelines for the selection of key parameters when performing numerical simulations and experimental measurements.
2. Define a metric able to extract from the SI measurements features relevant to the damage. Features extraction is one of the key steps in damage detection. It allows extracting information about the damage starting from the raw measurements of the physical quantity the selected technique relies on. In the present case the SI is the physical quantity exploited for damage detection.

3. Develop an SI based linear damage detection technique for the localization of linear behaving defect such as open fatigue cracks and ballistic impacts. In particular, the possibility of exploiting the previously defined metric for damage localization is evaluated.
4. Develop and experimentally validate an Active Energy Sink (AES) concept. The SI requires an energy sink to create a clear energy flow through the system. The possibility of creating an energy sink through an active control device will be investigated.
5. Evaluate the feasibility of a Nonlinear Surface Structural Intensity approach. This technique is intended to combine in a single approach the benefits of the HHRS and SI based methods. This approach should yield a technique able to detect, locate and size nonlinear defects such as fatigue cracks.

1.9 Organization of the Thesis

This thesis is divided in eight chapters. Chapter 1 provides a general introduction to the Structural Health Monitoring objectives and applications as well as a comprehensive literature review of the main damage detection strategies investigated in the past. The chapter concludes with a description of the problem statement and of the objectives for the current research.

Chapters 2 to Chapter 4 describe the Higher order Harmonic Response Signals (HHRS) which is the first of the two techniques addressed in this research. In particular, Chapter 2 starts with a general description of the main properties of vibrating cracked structures and how this can be exploited for fatigue crack localization. Then, the analytical foundation and the numerical formulation are addressed providing the necessary analytical tools to perform the damage identification. Chapter 2 provides the HHRS formulation for isotropic non dispersive one-dimensional systems. The chapter concludes presenting the results from a numerical investigation aiming to validate the HHRS approach.

In Chapter 3, a specific experiment is designed to provide experimental evidence of the HHRS technique proposed in the previous chapter. Guidelines for the transducers selection, sensors placement and the experimental setup for higher order harmonic measurements are also provided. The experimental results for two different damaged specimens will be presented in order to prove the applicability of the damage localization technique to one-dimensional structures.

Chapter 4 extends the HHRS technique to isotropic bi-dimensional plate structures. The physical principle of the damage localization based on the higher order harmonics, typical of fatigue cracks, is transferred to plate structures. A specific data post-processing technique, that is more suitable for features extractions in dispersive 2D structures, is presented and used to perform a numerical feasibility study on this technique.

Chapters 5 to Chapter 7 deal with the formulation and experimental investigation of a Structural Intensity (SI) based damage detection technique. In particular, Chapter 5 presents the theoretical background on the SI as well as a comprehensive parametric study. This study is intended to highlight the role of key parameters when using the SI as damage detection tool. A possible metric for damage detection based on SI measurements is proposed and applied for damage localization in a linear domain.

Chapter 6 introduces the concept of Active Energy Sink (AES). The AES is investigated as a possible approach to enhance the SI based technique following the findings in Chapter 5. A preliminary design of the AES is proposed along with experimental results.

Chapter 7 formulates the concept of Nonlinear Structural Surface Intensity (NSSI). The main physical principle supporting the NSSI is first introduced. Then, the description of a numerical technique to calculate and simulate the NSSI in cracked plates is presented.

Chapter 8 presents the main findings and conclusions obtained in this research. It also summarizes the main contributions and the suggested path forward to further develop the presented techniques.

CHAPTER 2

Higher Order Harmonic Response Signal Technique

The first technique investigated in this work as a potential candidate for damage detection application in helicopter rotor blades and airframe structures is based on the use of nonlinear dynamics concepts. In particular, the characteristic nonlinear response of a cracked structure was exploited to identify and locate a specific kind of structural damage. According to the system requirements previously discussed (Chapter 1), the damage identification was performed without requiring either a baseline signature or a finite element model of the healthy structure.

The first part of this chapter will present the analytical background and the theoretical formulation supporting the new damage detection algorithm. The technique is demonstrated both through a wave propagation approach and through the Harmonic Balance (HB) method (which is a specific technique to solve for the dynamic frequency response of nonlinear structures). Once the damage detection algorithm is formulated, a specific finite element modeling approach for the simulation of transient response of cracked structures is presented. This modeling approach is based on the use of commercial finite element software in order to easily allow the future extension to more complex mechanical assemblies.

In the second part of this chapter the finite element model is used to generate a numerical database representing the dynamic response of the test structure under different damage conditions. These results are used to numerically validate the proposed technique and to provide general guidelines to perform an experimental investigation (Chapter 3).

2.1 Dynamics of Cracked Structures

The dynamics of cracked structures has attracted a considerable interest during the past decade. The capability of modeling and predicting the dynamic response of damaged structures by taking into account the local behavior proper of the defect has been regarded as a powerful and effective way to enhance sensitivity and accuracy of both the Non-Destructive Evaluation (NDE) and the Structural Health Monitoring (SHM) techniques. When a crack is in a closed configuration, in fact, ultrasonic waves are less sensitive to the damage. In closed configuration the crack has a higher coefficient of transmissibility therefore the reflected wave (which is the parameter generally exploited by ultrasound based techniques to perform the detection) becomes weaker and the distinctive signature of the damage less evident. The use of nonlinear harmonics generated by the dynamic excitation of closed fatigue cracks was recently exploited by other researchers to increase the sensitivity to incipient cracks and is often referred to as Contact Acoustic Nonlinearity (CAN) [66].

Although a complete description of the properties of a nonlinear system is beyond the scope of this work, a short review of some of the main features involved in the nonlinear dynamic response of a cracked structure is needed for understanding the proposed technique. The main concepts will be summarized hereafter while the reader is directed to specific publications [67-69] for an in depth description of the fundamental concepts of nonlinear system dynamics.

In the past few years, researchers have pointed out the peculiar behavior characteristic of a cracked structure when excited by an external dynamic load [70-73]. As an example, when a structure is excited by a single tone external excitation (as a sinusoidal wave) the frequency spectrum of its nonlinear structural response is no longer dominated only by the frequency of the excitation signal. Higher order harmonics, whose frequencies have a prescribed relation with the driving frequency, appear in the spectrum as result of the nonlinearity [67,68].

This concept can be further clarified with an example. Consider the linear frequency response of an isotropic rod excited by a sinusoidal external longitudinal excitation as in Figure 2.1. Assuming that the structural response is monitored in terms of the displacement history at one end, the correspondent frequency content can be easily extracted by performing a Fourier transform of the signal. The frequency spectrum, shown in Figure 2.1, exhibits a sharp peak at the frequency of the external excitation which is the dominant frequency. The effect of leakage is also visible in the spectrum due to the choice of the windowing and sampling parameters. The presence of, however, does not reduce the generality of this example which is presented only for illustration purposes.

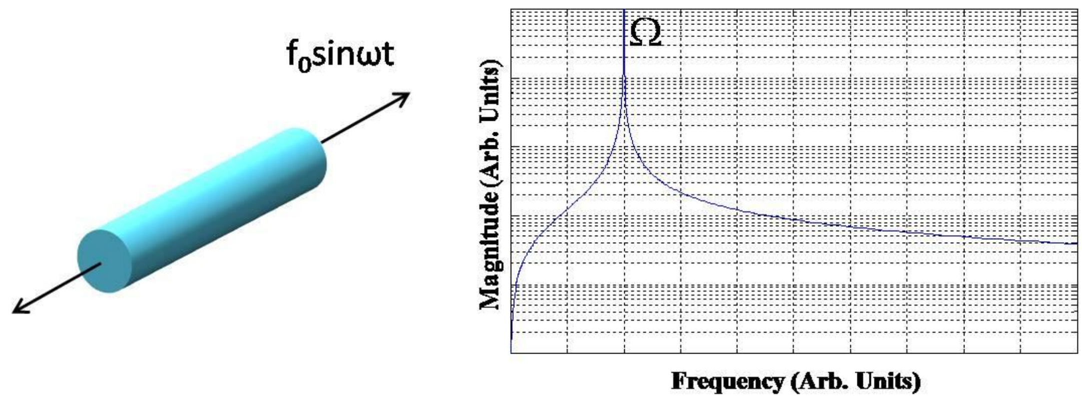

Figure 2.1. (left) Schematic of a rod excited by a longitudinal periodic load; (right) Fourier transform of the output displacement.

If the same approach is followed to analyze the response of a cracked rod, where the crack is modeled as a breathing crack (§2.2.2), a frequency content rich in higher order harmonics can be expected (Figure 2.2).

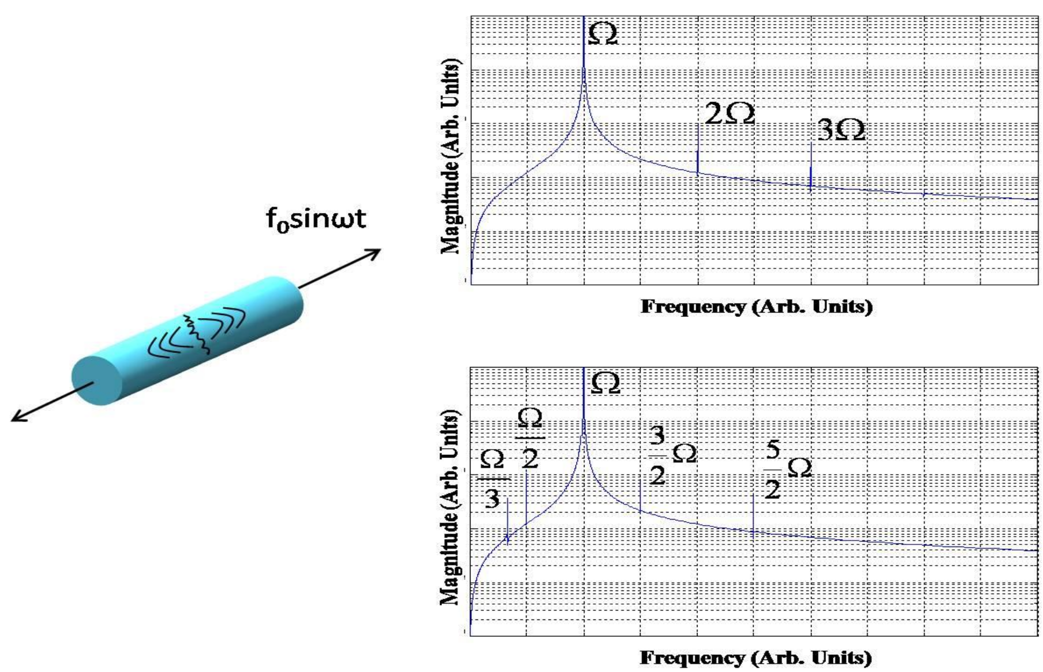

Figure 2.2 (left) Schematic of a cracked rod excited by a longitudinal periodic load; (top-right) driving frequency Ω and superharmonic components; (bottom-right) driving frequency Ω and subharmonics.

Due to the nonlinear nature of the dynamic system the vibrational energy injected into the structure at a very specific frequency leaks into adjacent frequency bands. These phenomenon generates new harmonics that can be integer multiple or fractional multiple of the driving frequency and are commonly denominated super-harmonics and sub-harmonics, respectively.

In this chapter a specific technique able to identify the damage location by exploiting the information carried by the higher order harmonics generated at the crack interface will be presented.

2.2 Theoretical Approach

To illustrate the proposed approach without losing generality, a rectangular isotropic beam with free-free boundary conditions is used as a test structure. A single fatigue crack type defect is assumed to be developed by the structure as a consequence of a High Cycle Fatigue (HCF) environment. Under this assumption the structure can be considered linear in terms of mechanical properties, except for a very small area close to crack tips where the material undergoes plastic deformations. At its earliest stage, the crack can reasonably be considered in a closed configuration that is the two sides of the crack stay in contact at the initial instant.

As already demonstrated by other researchers, a fatigue crack at its earliest stage exhibits a peculiar behavior when excited by a dynamic load. The excitation forces the crack to open and close (commonly referred to as "breathing"). The resulting clapping of the crack edges produces a series of impacts which generate elastic wave fronts propagating into the structure. As stated previously, the frequency content associated with these wave fronts is rich in higher order harmonic components which become the distinctive feature of the crack.

In the following paragraphs, a specific analytical approach able to identify the location of a breathing crack by exploiting the specific information carried by the higher order harmonics generated at the crack interface will be presented. Although the damage detection technique will be initially validated using a finite element model of a cracked structure, the proposed technique does not rely on either a FE model or a baseline database of the healthy structure in order to perform the damage assessment.

2.2.1 Localization of an Unknown Wave Source

The damage localization technique presented in this research is synthesized based on the algorithm presented by Doyle [74-75] to determine the location of an unknown dispersive pulse in an isotropic beam. The algorithm was originally formulated to determine the spatial location of an external impact using strain measurements.

For the purpose of damage localization, an algorithm to determine the spatial location of an unknown wave source generating a continuous non-dispersive longitudinal wave in an isotropic rod was first derived.

Given the rod in Figure 2.3**,** subjected to an external longitudinal dynamic load and assuming the origin of the longitudinal axis coincident with the point of excitation, the equation of motion can be written as:

$$EA\frac{d^2u}{dx^2} + \omega^2\rho Au = 0 \tag{2.1}$$

where *E* the Young modulus, *A* the cross sectional area of the rod, ω is the resonance frequency, ρ the material density and *u(x)* the longitudinal displacement field.

While the boundary condition is:

$$EA\frac{\partial u(x,t)}{\partial x} = F(t) \qquad \text{at } x=0 \tag{2.2}$$

where *F(t)* is the external longitudinal excitation applied on the rod.

The boundary condition can be rewritten in spectral form for the generic frequency component of order *n* in the following way:

$$EA\frac{du_n(x)}{dx} = F_n \tag{2.3}$$

where u_n and F_n represent the spectral component of the displacement field and of the external force.

Considering the well established general solution of the homogenous wave equation in spectral form:

$$u(x,t) = \sum Be^{-i(kx-\omega t)} + \sum Ce^{i(kx+\omega t)} \tag{2.4}$$

where *B* and *C* are constant of integrations, *k* is the wave number and *i* is the imaginary unit.

Substituting (2.4) in (2.2) the solution for the forward moving wave can be written as:

$$u(x,t) = -\frac{1}{2EA}\sum_n \frac{\hat{F}_n}{ik_n} e^{-i(k_n x-\omega_n t)} \tag{2.5}$$

where $u(x,t)$ represents the displacement field in the rod at the time t at location x.

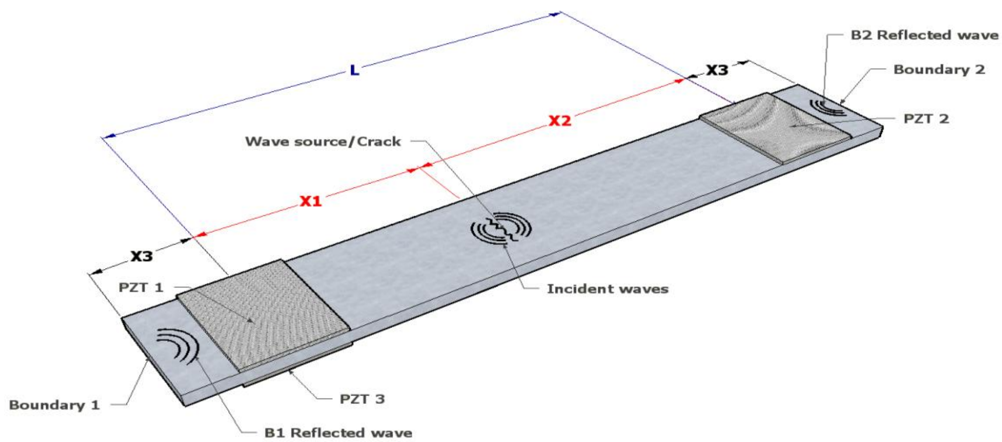

Figure 2.3. Schematic of a rod with a wave source in an unknown location.

To emphasize the relation between the phase terms, Equation (2.5) can be written as:

$$D_n e^{i\varphi_n} = D_{0n} e^{i\varphi_{0n}} e^{-ik_n x} \tag{2.6}$$

where D_n and D_{0n} are constant coefficients describing the amplitude while φ_n, φ_{on} and $k_n x$ represent the estimated phase at the location x, the initial unknown phase of the excitation and the change in phase due to the propagating wave, respectively.

The relation between the estimated phase and the location x of the applied force can be calculated from Eqn. (2.6) and is equal to:

$$\varphi_n = \varphi_{0n} - k_n x \tag{2.7}$$

Inverting Eqn. (2.7) with respect to x gives the basic relation to find the location of the wave source:

$$x = \frac{1}{k_n}(\phi_{0n} - \phi_n) \tag{2.8}$$

Equation (2.8) provides the distance x between the origin of the reference system (previously assumed coincident with the source location) and the point where the phase φ_n is measured. This equation has two unknowns, x and φ_{0n}, therefore cannot be directly solved for the location of the source. To overcome this problem two measurement points can be used, one on each side of the source (Figure 2.3). Writing Eqn. (2.8) for the two different points and knowing the absolute distance between the sensors we get the following set of equations:

$$x_1 = \frac{1}{k_n}(\varphi_{0n} - \varphi_{1n})$$

$$x_2 = \frac{1}{k_n}(\varphi_{0n} - \varphi_{2n}) \qquad (2.9)$$

$$x_1 + x_2 = L$$

Finally, eliminating the initial phase φ_{0n} we get:

$$\begin{aligned} x_1 &= \frac{1}{2}L - \frac{1}{2k_n}(\varphi_{1n} - \varphi_{2n}) = \frac{1}{2}L - \frac{\Delta\varphi_n}{2k_n} \\ x_2 &= \frac{1}{2}L + \frac{1}{2k_n}(\varphi_{1n} - \varphi_{2n}) = \frac{1}{2}L + \frac{\Delta\varphi_n}{2k_n} \end{aligned} \qquad (2.10)$$

Before solving Eqn. (2.10), the measured phases φ_{1n} and φ_{2n} must be unwrapped. In this way the ambiguity at $\pm\pi$, produced by the arctangent function when calculating the phase, can be easily overcome.

In Eqn. (2.10), the source location is calculated estimating the difference in the path length travelled by the waves towards point 1 and 2 where the structural response is collected. Both magnitude and sign of the $\Delta\varphi_n$ are equally important for an accurate localization of the source.

Eqn. (2.10) is derived considering only the wave generated at the point source. This set of equations would give, theoretically, the exact estimate of the source location if we considered an unbounded structure where the propagating signal hits the sensors only once. In a finite structure, however, boundaries produce reflected waves that propagate back towards the sensors giving additional phase contributions. In a linear behaving structure this problem has been overcome acquiring only the first passage of the initial signal [74-75] and appending the long term theoretical solution for the beam dynamic response. This procedure provides a good estimate of the spectral content while removing the effects of the reflected waves.

In this work, however, we investigate a different approach where:

a. The spectral content is estimated from the acquired steady state response including, therefore, boundary and crack reflections. The reason for considering the steady state is due to the fact that the initial transient response does not include necessarily the super-harmonic components.

b. The host structure is weakly nonlinear: therefore there is not a closed form solution which could be used to append the long term response to the measured data.

2.2.2 Breathing Crack as a Source of Excitation

When a cracked structure is subjected to an external periodic dynamic excitation the external load produces tensile and compressive stresses on the two edges of the crack leading to a continuous (eventually periodic) opening and closing of the crack, usually referred as “breathing”. The series of impacts produced by the clapping of the two edges, when subjected to compressive stresses, creates new wave fronts whose frequencies are integer multiples or fractional multiples of the driving frequency associated with the external dynamic load. This behavior suggests that the breathing crack can be considered as a source of excitation whose frequency spectrum contains the driving frequency plus its super-harmonic and/or sub-harmonic components. Under this assumption, the crack behaves as a wave source similarly to what is illustrated in §2.2.1. The phase information associated with the higher order harmonic components can therefore be processed in a similar fashion to what is illustrated by Eqn. (2.10). This will result in locating the position of the super-harmonics source that, ultimately, is the spatial location of the crack.

In cracked structures the dynamic response is nonlinear due to the presence of the breathing crack. The crack is, in fact, associated with a localized discontinuity in the stiffness value. When the crack is open, due to a tensile stress state, the local stiffness drops to a value $K_{op.}$ When the crack is closed, due to a compressive stress state, the local stiffness is restored to the value $K > K_{op}$ associated with the healthy structure. When the system is excited by an external dynamic excitation, which alternates compressive and tensile stress states on the crack, the continuous opening/closing behavior of the crack induces a periodic change in the local stiffness (between the limit value K and K_{op}) which determines the nonlinear character of the overall dynamic response.

The presence of a breathing crack makes the system weakly nonlinear [76-77]. A weak nonlinear system is generally defined as a system where the dynamic response converges to an almost periodic steady state solution despite the nonlinearity. In order to extend the algorithm described in §2.2.1 to the present structure we need to derive the phase based relation, equivalent to Eqn. (2.10), valid for the steady state response of a weakly nonlinear system.

In this study, the external dynamic load is assumed to be a single frequency periodic excitation applied in the longitudinal direction so that the dynamic response of the structure can be described according to the wave propagation in a rod. The other assumptions made in this paragraph are summarized hereafter:

a. The clapping of the crack, produced by the external dynamic excitation, takes the place of the wave source (i.e. external impact) considered in §2.2.1.
b. The crack can be considered as a weak nonlinearity and the steady state solution is almost periodic.
c. The dynamic response of the structure under the external axial load can be described according to the wave propagation theory in rods.

2.2.3 Harmonic Balance Solution of a Weakly Nonlinear Rod

The first step involved in the extension of Eqn. (2.10) to determine the crack location is evaluating the phase relation at the steady state between the wave source/crack location and another point in the structure.

According to Musil [78], the dynamic response of a structure including a breathing crack can be calculated using a finite element model (Figure 2.4) where the breathing crack is modeled through a piecewise linear spring. The system can be described by the following dynamic equation:

$$M\ddot{u}(t) + C\dot{u}(t) + Ku(t) + f_c(t) = F(t) \tag{2.11}$$

where M, C and K represent the mass, damping and stiffness matrices, $f_C(t)$ is the restoring force produced by the spring with piecewise linear stiffness and $F(t)$ is the external applied dynamic load.

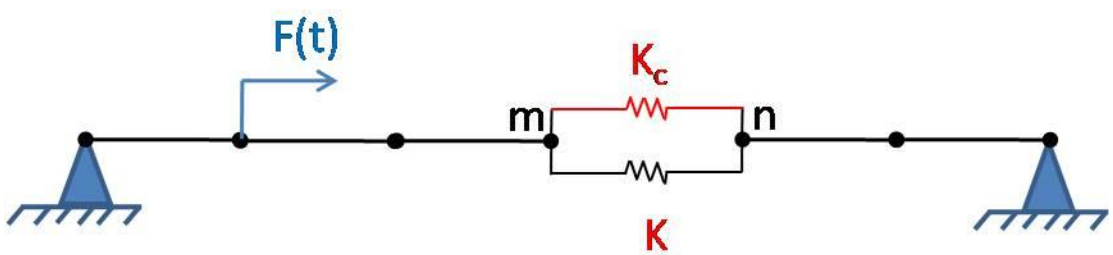

Figure 2.4. Schematic of the finite element model of a rod including a bilinear spring.

The piecewise linear spring allows taking into account the opening/closing behavior of the crack which, as explained before, is associated with a change in the local stiffness. In this study, the longitudinal response of the structure will be analyzed therefore only an axial spring will be considered.

The effect of the spring can be expressed in the following way:

$$f_c(t) = K_C[u_n(t) - u_m(t)]d_C = K_C u_C(t) d_C = K_C u_C(t) H[u_C(t)] d_C \tag{2.12}$$

where $u_C(t) = [u_n(t) - u_m(t)]$ represents the relative axial displacements of the two end points of the nonlinear spring (i.e. the two edges of the crack) having a stiffness K_C. $H[u_C(t)]$ is the Heaviside step function used to localize the stiffness change, whereas f_C=0 represents the unchanged stiffness condition (crack closed) and $f_C = K_C u_C(t) d_c$ represents the stiffness decrease due to the crack opening. The vector $d_C=[0,\ldots,1,\ldots,1,\ldots,0]^T$ characterizes the location of the crack.

In order to calculate the steady state response of this nonlinear system the Harmonic Balance (HB) approach can be applied to the system of equations (2.11) and (2.12). The dynamic excitation can be expressed in Fourier series as follow:

$$F(t) = \sum_k F_k e^{i(k\omega t + \varphi_k)} \qquad \text{for k=0,1,2,3,....} \tag{2.13}$$

where F_k, $k\omega$ and φ_k represent the amplitude, frequency and phase of the k-th harmonic of the excitation load, respectively.

Following the same approach we can expand the displacement field in Fourier series:

$$u(t) = \sum_k u_k e^{i(k\omega t + \psi_k)} \qquad \text{for k=0,1,2,3,....} \tag{2.14}$$

The restoring force f_c can be approximated through the Fourier series [76] as:

$$f_c(t) = \sum_{k=0}^{\infty} f_{ck} \left[cos(k\omega t) + \delta_k\right] \qquad \text{for k=0,1,2,3,....} \tag{2.15}$$

where f_{ck} is the amplitude of the k-th harmonic of the restoring force and δ_k is an initial phase.

Substituting the expressions (2.13), (2.14) and (2.15) in (2.11) we obtain the solution of the equation of motion for the *k-th* harmonic:

$$e^{i\Psi_k}u_k - G_k(ik\omega)e^{i\varphi_k}F_k = -f_{Ck}e^{i\delta_k}G_k(ik\omega)d_c \qquad \text{for k=0,1,2,3} \qquad (2.16)$$

where $G_k(ik\omega)$ represents the transfer function of the mechanical system for the *k-th* harmonics. Eqn. (2.16) could be solved for u_k that, once substituted back into Eqn. (2.14), will yield the resulting displacement field of the rod. In this application, however, we are interested in using this equation to extract the phase relation that holds at the steady state between the input force, the output displacement and the restoring force of the spring.

Observing that the transfer function in the right hand term of Eqn. (2.16) can be written as:

$$\begin{aligned} G_k(ik\omega)d_c &= G_k(ik\omega)d_m - G_k(ik\omega)d_n = \{g_m(ik\omega)\}_k - \{g_n(ik\omega)\}_k \\ &= \{g_c(ik\omega)\}_k \end{aligned} \qquad (2.17)$$

where the $\{g_c(ik\omega)\}_k$ represents the transfer function between the two end points of the bilinear spring for the generic harmonic of order k. Rewriting $\{g_c(ik\omega)\}_k$ in exponential form and substituting in Eqn. (2.16) we obtain:

$$e^{i\Psi_k}u_k - G_k(ik\omega)e^{i\varphi_k}F_k = -f_{Ck}e^{i\delta_k}e^{i\Gamma_k}g_{ck}(k\omega) \qquad \text{for k=0,1,2,3} \qquad (2.18)$$

where the term $f_{ck}e^{i\delta k}$ represents the *k-th* harmonic of the restoring force produced by the axial spring, while $e^{i\Gamma k}g_{Tk}(k\omega)$ also depends on the spatial location of the spring.

Equation (2.18) represents the steady state equilibrium equation for a weakly nonlinear system at the generic harmonic of order k. From equation (2.18), the phase relation between the displacement, the applied external force and the crack restoring force can be extracted. The applied external force is chosen to be a periodic function at a specific frequency ω. Therefore, F_k in Eq. (2.13) is different from zero only for $k=1$ which corresponds to a periodic signal of frequency ω. Under this assumption, the phase relation at the super-harmonic frequencies (i.e. for k=2,3,4…..) is given by:

$$\Psi_k = \delta_k + \Gamma_k \tag{2.19}$$

where Ψ_k is the phase associated with the nodal displacement, δ_k is the initial unknown phase of the spring restoring force and Γ_k is a phase associated with the transfer function through the spring. As previously observed, the phase term Γ_k is related to the spatial location of the crack and therefore is a function of the longitudinal coordinate x. Given the assumption that the structure under analysis has a linear behavior, except for the area located around the crack, the phase Γ_k can be written as:

$$\Gamma_k(x) = -k_n x \tag{2.20}$$

according to the longitudinal wave propagation theory in a linear structure.

Under these assumptions, Eqn. (2.19) is equivalent to Eqn. (2.7). This result allows extending the range of applicability of Eqn. (2.7) to the steady state solution of a weakly nonlinear rod. As a remark, note that all the phases are calculated with respect to the external excitation.

2.2.4 Optimal Sensor Placement

The sensors placement plays a major role in the performance of the proposed localization algorithm. Although Eqn. (2.19) states that the phase measurement can be performed at any point on the structure, particular attention must be given to the location of the measurement points.

The changes in the phase associated with the travelling wave and occurring at each one of the sensor locations, after each reflection, are listed Table 2.1. According to Figure 2.1, the sensors are assumed to be symmetrically located with respect to the geometric boundaries. Under this assumption, the absolute value of the phase difference $\Delta\varphi$ is always constant, while at the even order reflections the $\Delta\varphi$ changes sign. Note that, for simplicity, the initial phase φ_{0n} (equivalent to the term δ_k in Eqn. (2.20)) is omitted because this constant term cancels out when calculating the phase difference $\Delta\varphi$.

Even if the phase difference occurring at the even order reflections changes sign, the corresponding amplitude is always lower than the *(m-1)* odd order reflections (because they travelled a larger distance), where *m* represents the even order reflections. Consequently, even if the overall amplitude will be affected the resulting phase difference $\Delta\varphi$ will keep the same sign determined by the incident waves.

On the contrary, if the sensors are not symmetrically located with respect to the boundaries the phase difference associated with the odd order harmonics also changes in absolute value. Even if the wave resulting from the superposition of the odd order reflected waves will have small amplitude (when considering a sufficient number of reflections), the associated phase difference can still produce a shift on the measured $\Delta\varphi$ that can considerably affect the performance of the detection algorithm.

Table 2.1. Change in phase after the boundary reflections; m = 2,4,6,… indicates the even order reflections.

	Sensor 1	**Sensor 2**	**Phase Difference $\Delta\varphi=\varphi_2-\varphi_1$**
Incident Wave	$k_n x_1$	$k_n x_2$	$k_n (x_2-x_1)$
1st Reflected Wave	$k_n x_1 + 2k_n x_3$	$k_n x_2 + 2k_n x_3$	$k_n (x_2-x_1)$
2nd Reflected Wave	$2k_n x_2 + 4k_n x_3 + k_n x_1$	$2k_n x_1 + 4k_n x_3 + k_n x_2$	$-k_n (x_2-x_1)$
***(m-1)-th* Reflections**	$(m-1)k_n x_1 + 2(m-1)k_n x_3 + (m-2) k_n x_2$	$(m-1)k_n x_2 + 2(m-1)k_n x_3 + (m-2) k_n x_1$	$k_n (x_2-x_1)$
***m-th* Reflections**	$mk_n x_2 + 2mk_n x_3 + (m-1)k_n x_1$	$mk_n x_1 + 2mk_n x_3 + (m-1)k_n x_2$	$-k_n (x_2-x_1)$

These simple considerations show that in order to minimize the effect of the reflected waves the sensors must be placed in a symmetric configuration with respect to the boundaries, as shown in Figure 2.1. In this way, the phase contributions associated with the reflected waves cancels with each other generating a “phase balancing” mechanism. Similar considerations apply also to the phase balancing of the waves reflected from the crack interface and from the far ends of the sensors, respectively.

For the crack interface, it is assumed that their contributions to the overall phase is negligible because the crack area A_c is small compared with the cross sectional area A of the rod $(A_c/A<10\%)$. Also the reflections taking place at the far ends of the sensors can be neglected. Reflected waves from the sensors are symmetric with respect to the boundaries (therefore rules at Table 2.1 apply similarly as shown for the case of boundary reflections) and their amplitude is negligible due to the small interface area between sensor and structure.

2.2.5 Structural Finite Element Model

The algorithm described by Eqn. (2.19) is tested using a three dimensional finite element model of a bar including a single breathing crack. The test structure is a rectangular shaped bar in Aluminum 6061-T6511. The geometrical and mechanical properties are listed in Table2.2.

Table2.2. Bar geometrical and mechanical properties.

Length (m)	**Width** (m)	**Thickness** (m)	**Young Modulus** (GPa)	**Density** ρ (Kg/m^3)	**Poisson's ratio** υ
0.2	*0.008*	*0.0026*	*68.94*	*2700*	*0.33*

The finite element model, shown in Figure 2.5a, was built through the commercial FE software PATRAN using Hexahedral 8 noded linear solid elements.

A nonlinear gap element was used to reproduce the behavior of a "breathing" crack. The gap element acts in principle as a bilinear spring. It has zero stiffness when the end nodes have a positive relative displacement (i.e. when the crack is subjected to a tensile load) or with a theoretical infinite stiffness when undergoing a negative relative displacement (i.e. when the crack is subjected to a compressive load).

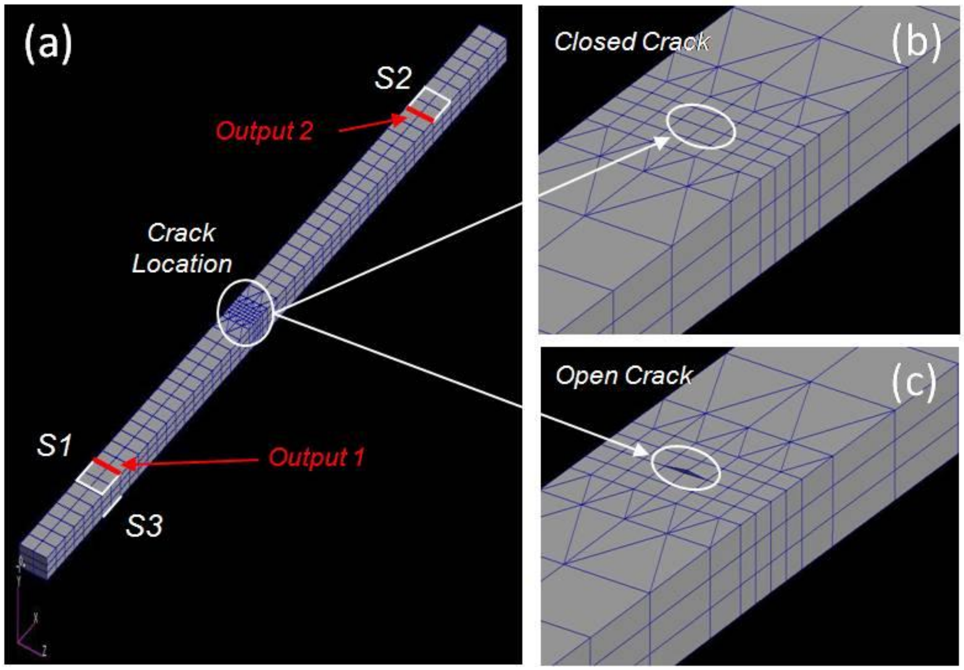

Figure 2.5. a) FE model of the isotropic beam including a breathing crack; the external dynamic excitation forces the crack to (b) close or (c) open periodically.

The gap element allows the two sides of the crack:

a. To close, maintaining the contact and avoiding any material overlapping, when they are subjected to a compressive load (Figure 2.5b).
b. To freely open when they are subjected to a tensile load (Figure 2.5c).

The external dynamic excitation needed to interrogate the system is assumed to be produced by piezoelectric patches bonded onto the host structure and located at 0.04m from the bar ends. These transducers, however, are not physically modeled (this is a reasonable assumption considering that their mass is negligible with respect to the mass of the host structure) although the excitation produced by these actuators is taken into account through a frequency dependent dynamic load acting along the boundary of the patch itself. This load is intended to simulate the high frequency dynamic excitation produced by the piezoelectric actuator when driven with a sinusoidal voltage at a prescribed frequency.

Three PZT transducers are used to interrogate and to sense the dynamic response of the structure. In particular, the actuators labeled as S1 and S3, depicted in Figure 2.5a, are used to excite the structure simulating an axial dynamic load. S1 and S2, instead, are used to collect the dynamic response of the rod.

Based on this modeling approach, different crack configurations will be analyzed.

2.2.6 Nonlinear Time Response Analysis

The previously described FE model was used to simulate the time response of the damaged structure excited by a continuous sinusoidal load. Further information about the selection of the driving frequency will be provided later on in this chapter.

The FE model was solved for the nonlinear time response through the commercial finite element solver MSC-NASTRAN, using a Newmark step by step integration algorithm. A 0.5 μsec time step, corresponding to a Nyquist frequency of 1 MHz, has been used and the integration was carried out up to 80 msec. Also, a material loss factor of 2% was applied. At each time step the structural response is collected in terms of velocity at the edge of the sensors S1 and S2, depicted in Figure 2.5a as Output 1 and 2.

The spectral content of the response is determined by the steady state part of the solution processing it through the Discrete Fourier Transform (DFT). An example of the time response, collected from the S1, along with its spectral content is shown in Figure 2.6 both for the healthy and the damaged configuration.

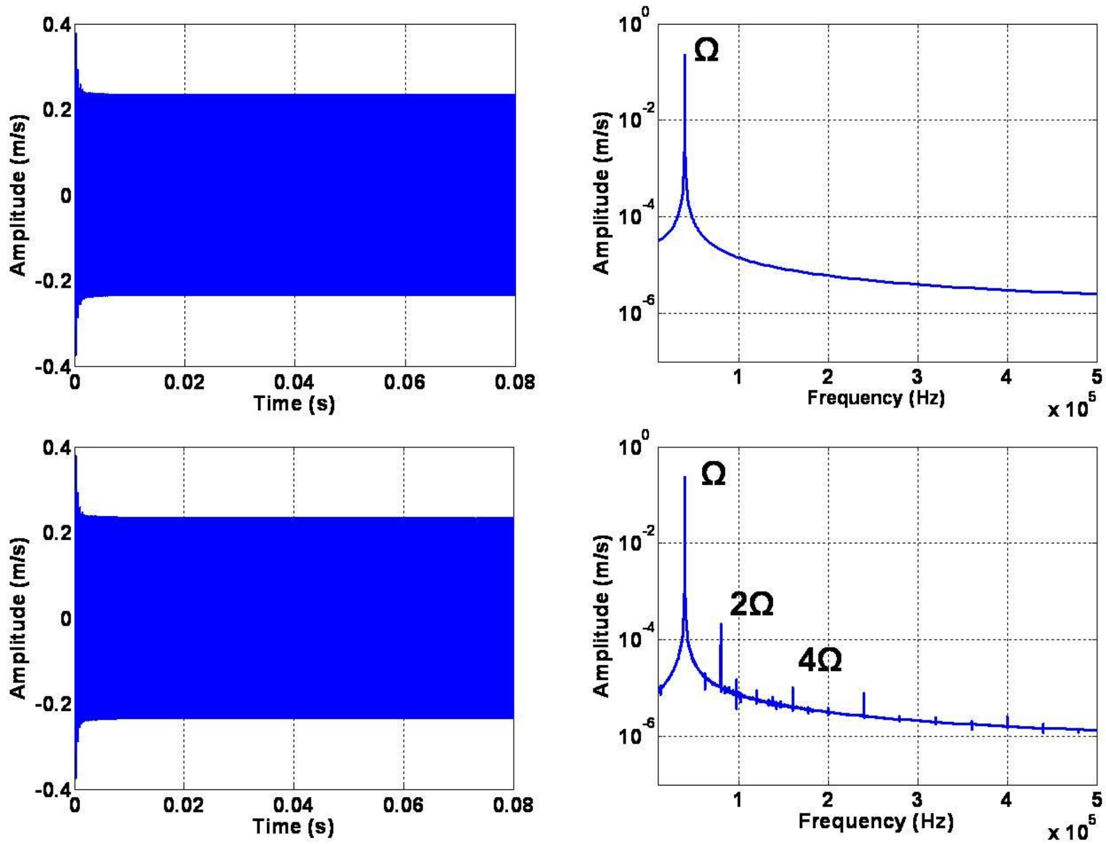

Figure 2.6. Time response and spectral content at sensor 1: (top) healthy structure; (bottom) damaged structure.

A direct comparison of Figure 2.6(b) and Figure 2.6(d) reveals that the presence of the crack is associated with the appearance of super-harmonic components at frequencies that are even integer multiple of the forcing frequency. This is a phenomenon typical of a breathing crack as reported also by other authors [79-81].

2.2.7 Selection of the Driving and Super-Harmonic Frequencies

The selection of the driving frequency of the external load, used to interrogate the structure, is a key parameter in determining the performance of the detection algorithm.

A detailed analysis of the optimal driving frequency is beyond the scope of this work., This paragraph, however, will provide some general guidelines that should be followed in order to get a good estimate of the crack location.

According to the general theory of nonlinear dynamic systems [67,82], in order to maximize the amplitude of the response of the super-harmonic components the driving frequency Ω should be close to $\Omega = \omega_n/m$, where m is an integer number and ω_n is the *n-th* resonance frequency. This simple rule would suggest selecting a driving frequency whose correspondent super-harmonic is as close as possible to a structural resonance.

The proposed damage detection algorithm implies some limitations on the driving frequencies. In the original version of this algorithm, proposed by Doyle in Ref. [75] every frequency guarantees the identification of the location of the impact point. At the natural frequencies, however, the discontinuity in the phase produces considerable oscillation in the estimated phase and consequently in the estimated location. Frequencies corresponding to structural modes therefore should be kept, as much as possible, out of the set of data used to estimate the location.

This limitation still holds for the proposed damage detection algorithm which is based on an analogous use of the phase information. The choice of the driving frequency, therefore, derives from a tradeoff between getting a high amplitude super-harmonic response and a super-harmonic frequency that does not overlap with a structural mode.

Another key observation concerns the frequency components that must be retained in the database used as input for Eqn. (2.19). In the present approach, the location of the crack is carried via the super-harmonic components. For this reason, the location of the crack will be correctly estimated only at frequencies corresponding to a super-harmonic or, in general, to a higher order harmonic.

The driving frequency must be discarded because it corresponds to a signal generated at the actuator location and not at the crack interface. This was also confirmed by the numerical simulations that estimated the crack location coincident with the actuator location when using the phase associated with the driving frequency.

The set of exploitable data for the damage identification is now greatly reduced. In the original version of this algorithm, in fact, every frequency could be effectively processed. This problem will be addressed in the next paragraph where three possible data post-processing techniques are developed and compared.

2.3 Data Post-processing Procedures

The post-processing of the raw data collected on the test structure has already been proven to be a major issue in Structural Health Monitoring. The changes produced by the damage on the output parameters are typically very small when interested in detecting the damage at its earliest possible stage. These changes are often masked either by experimental noise or simply by the overall structural response of the system (which is dominant with respect to the damage signature). This means that, even if the damage detection algorithm is sensitive to the defect, extracting the damage signature from the raw data might still be a challenging task. This issue can lead to an inaccurate characterization or to a completely erroneous estimate of the damage.

Another cause of error, which is directly related to the nature of the HHRS algorithm, is associated with the effect of the wave fronts reflected on the geometric boundaries. As illustrated in §2.2.4, the reflected waves give an additional phase contribution that, if not taken into account, can considerably corrupt the accuracy of the estimated location. A possible way to limit the effects of the reflected waves has already been discussed and is based on a proper placement of the sensors. It must be noted that because the detection algorithm relies on the phase difference at two different locations it is intrinsically robust against additional constant phase terms that cancel out when evaluating Eqn. (2.10). Nevertheless, errors in the evaluation of the relative phase difference $\Delta\varphi$ can significantly affect the estimated damage location. A specific data post-processing procedure therefore is needed to extract the phase information with sufficient accuracy.

Three different data post-processing techniques were developed and compared. Their performances were evaluated in terms of accuracy of the phase estimate and of the robustness against the effect of undesired reflections.

In particular, the presented post-processing techniques are based on:

- ✓ *Discrete Fourier Transform (DFT).*
- ✓ *Transfer Function (TF).*
- ✓ *Hilbert Transform (HT).*

The first two approaches (DFT and TF) have been historically used to evaluate the spectral content and the cross correlation between two time signals. It will be demonstrated, in the following paragraphs, how these techniques do not provide enough accuracy and data points to be effectively used in conjunction with the HHRS algorithm.

The Hilbert Transform, instead, provides an extended data set for each selected frequency due to its capability to retain the time information. This concept will be further clarified in §2.3.3.

2.3.1 Discrete Fourier Transform Based Approach

The first data post-processing approach, investigated in this work, relies on the use of the Discrete Fourier Transform (DFT). This technique is used to evaluate the phase content associated with the signal collected at each sensor. A block diagram illustrating the sequence of operations needed to estimate the crack location is showed in Figure 2.7.

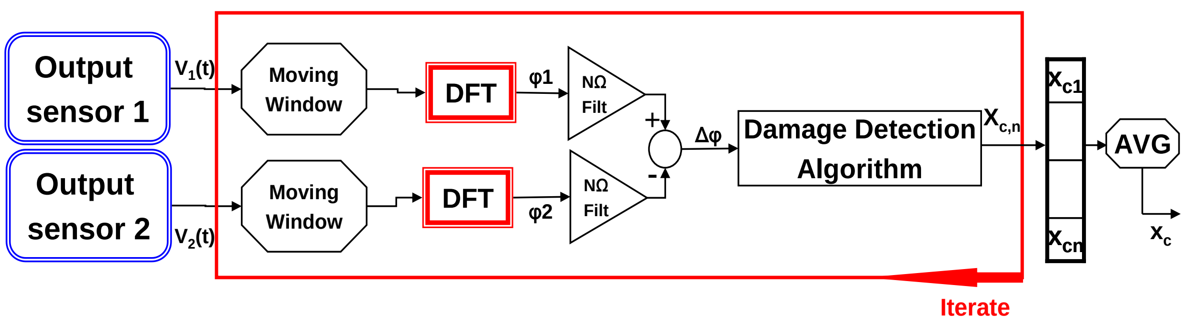

Figure 2.7. Block diagram illustrating the data flow in a Discrete Fourier Transform based approach.

The output collected at the two sensors, labeled as Output 1 and 2, are first processed through a moving window then fed into the DFT block in order to estimate the phase associated to each frequency component. Successively, the phase associated with the super-harmonics is extracted from the spectrum and the $\Delta\varphi$ is estimated. The relative phase difference $\Delta\varphi$ is used as input to the damage detection algorithm in order to estimate the crack location $x_{c,n}$ (where $x_{c,n}$ is the estimated crack location associated with the *n-th* windowed signal). Finally, the result is stored in an array and the procedure is iterated over *n* windowed signals. Once the *n-th* iteration is completed and the array of the estimated locations is completely filled in, the $x_{c,n}$ are linearly averaged to provide the final estimate of the crack location x_c.

The mechanism of the moving window (conceptually similar to a moving average) is illustrated in Figure 2.8. The overall time response is windowed with a Boxcar window of constant length L_w and the first calculation is performed.

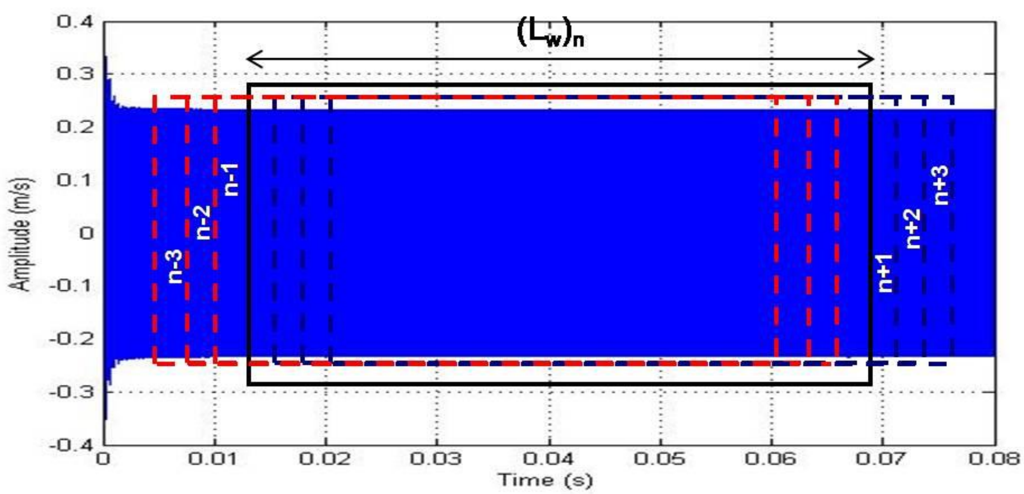

Figure 2.8. Schematic of the moving window procedure.

Then the window is moved *(n-1)/2* times forward and backward, respectively, by a quantity equal to Δt (assumed equal to ΔT in these calculations). The parameter *n* represents the total number of time steps used to solve for the time response. Each window $(L_w)_n$ provides an estimate of the crack location $x_{c,n}$. One of the main goals of the moving window is to minimize the effect of the reflections therefore L_w is chosen to be an even integer multiple of the time of flight *ToF* of the wave. The *ToF* is defined as the time needed for the wave to travel a distance equal to the length *L* of the rod. In this way, taking $L_w=2 \cdot n \cdot ToF$ each reflected wave strikes n-times both the sensors and comes back to the starting point. This procedure allows containing the impact of the reflected wave over the estimated phase difference $\Delta\varphi$ because these contributions cancel out almost completely.

Also, at each iteration the window is moved (forward or backward) of a step equal to the integration time step used for the nonlinear time response (ΔT=0.5 μsec) while the total number of windows is chosen to be equal to an even integer multiple of the ToF. This procedure is intended to limit the effects of the waves close to the edges of the window that most likely are not balanced in a single iteration.

Once the entire set of estimated locations $x_{c,n}$ is populated by using this moving window approach, the array of values is linearly averaged to produce the final estimate of the crack location x_c.

2.3.2 Transfer Function based Approach

The Transfer Function (TF) approach is the second concept investigated in this study as a possible data post-processing technique. The block diagram illustrating the data flow is shown in Figure 2.9.

The TF approach is conceptually similar to the DFT based approach. The relative phase difference $\Delta\varphi$ is estimated calculating the transfer function between the signals collected at the sensors locations. The phase associated with the transfer function results in the phase difference between the two signals which is the desired $\Delta\varphi$.

The block labeled G_{12}, in Figure 2.9, evaluates the transfer function according to the following relation:

$$G_{12} = \frac{P_{12}(f)}{P_{11}(f)} \tag{2.21}$$

where $P_{12}(f)$ is the cross power spectral density between the two measured signals while $P_{11}(f)$ is the auto spectral density of the signal collected at sensor 1.

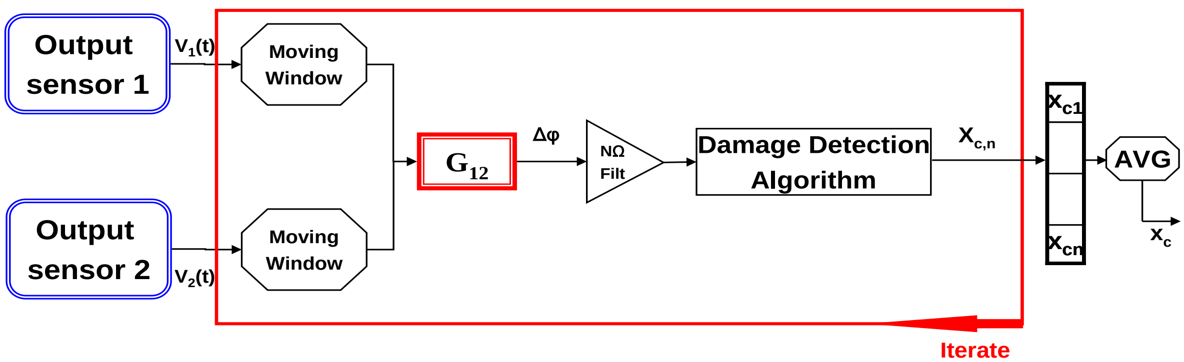

Figure 2.9. Block diagram illustrating the data flow in a Transfer Function based approach.

The same considerations concerning the moving window and the averaging procedure apply to the TF based approach similarly to what discussed in §2.3.1. The TF technique provides n estimates of the crack location which are finally averaged to yield the final estimate x_c.

2.3.3 Hilbert Transform Based Approach

The Hilbert Transform (HT) is the third technique investigated in this work. The Hilbert transform $\tilde{y}(t)$ of a real valued signal $y(t)$ can be described through the definition of the analytic signal *z(t)* [83]. An analytic signal can be defined as a real valued signal where the negative frequency components were previously discarded. In analytical terms it is generally defined as:

$$z(t) = y(t) + j\tilde{y}(t) \tag{2.22}$$

or in polar coordinates:

$$z(t) = A(t)je^{j\theta(t)} \tag{2.23}$$

where *A(t)* is the envelope signal and *θ(t)* is the instantaneous phase of *y(t)*. A third quantity of interest is the instantaneous frequency which is defined as:

$$f(t) = \frac{1}{2\pi}\frac{d\theta(t)}{dt} \tag{2.24}$$

From Eqn. (2.22) follows that the Hilbert transform can be defined as:

$$\tilde{y}(t) = H[z(t)] = Im[z(t)] \tag{2.25}$$

which calculates the imaginary part of the analytic signal *z(t)*.

One of the most interesting features of the HT comes from its ability to retain the time information. When the time signal is processed through the DFT or the TF approach the time information is completely discarded. In these two approaches each frequency component is identified by a single pair of values (amplitude and phase or, equivalently, real and imaginary part). These are typical quantities used to describe the steady state response of linear systems where the resonance frequencies and the amplitude of the response are constant quantities. In nonlinear systems, however, instantaneous amplitude and frequency might oscillate in time around an average value. This information can be retained by using the Hilbert transform because, as shown in Eqns. (2.23) and (2.24), the amplitude $A(t)$, the phase $\theta(t)$ and the frequency $f(t)$ are time dependent.

The HT was used to extract the phase information in a similar fashion to what was previously done with the other techniques. The data flow for the HT based data post-processing is shown in Figure 2.10.

The output collected at the two sensors locations are first processed through a series of zero phase shift band-pass digital filters centered at the super-harmonic frequencies in order to separate the component of the time response due to a specific harmonic. Zero phase shift filters were used to avoid any possible shift in phase due to the filter itself.

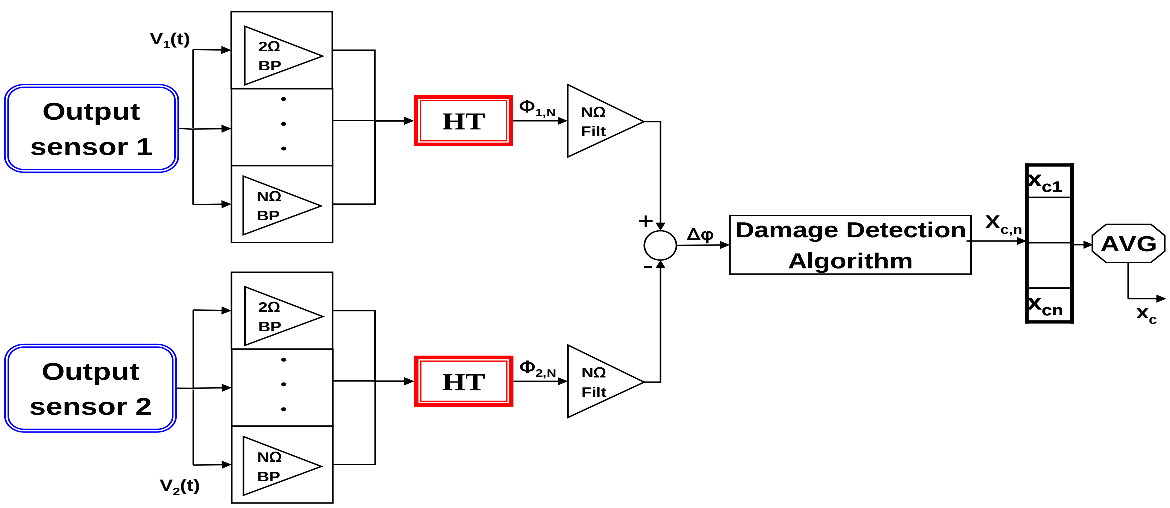

Figure 2.10. Block diagram illustrating the data flow for the Hilbert Transform based approach.

Then, each signal is separately processed through the Hilbert transform in order to get the instantaneous phase $\varphi_{1,n}(t)$ and $\varphi_{2,n}(t)$ associated with the harmonic of order n. Successively, the phase difference $\Delta\varphi_n$ is calculated and fed into the damage detection algorithm block that will produce an estimate of the crack location $x_{c,n}$ based on each super-harmonic component. Finally, the array of the estimated location is linearly averaged to provide the final estimate of the crack location x_c.

2.4 Numerical Results

Numerical simulations were carried out to estimate the performance of the HHRS algorithm along with the data post-processing approaches. The time response of the damaged structure was generated using the FE model discussed in §2.2.5. The crack location was estimated using the three different post-processing procedures previously described.

In particular, five different crack configurations were considered and compared. Each configuration corresponds to a specific breathing crack (2mm x 0.86 mm) in a different location along the longitudinal axis, as showed in Figure 2.11.

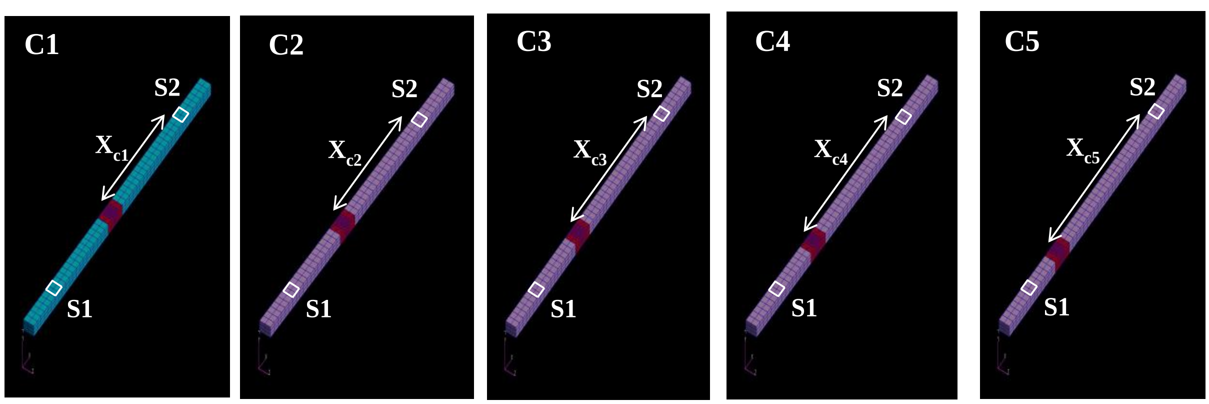

Figure 2.11. Schematic of the five crack configurations.

Starting from the configuration C1 up to the configuration C5, the crack is shifted progressively farther from the sensor S2.

The external excitation used to interrogate the structure is a sinusoidal axial load with a frequency equal to 40kHz and a zero to peak amplitude equal to 100N. The interrogation signal was chosen according to the guidelines previously presented. In particular, the frequency of the interrogation signal was carefully selected to not generate nonlinear harmonics overlapping any resonance frequency. The amplitude was chosen to be in the allowable range (0-200N) of the deliverable force for Micro Fiber Composites transducers, which will be used in the experimental validation of the HHRS technique.

Many other combinations of frequency and amplitude could be used, of course, to interrogate the structure. From a general point of view, the HHRS technique will take advantage of the data collected from multiple interrogation signals. By averaging the estimated crack location due to multiple interrogation signals we could reduce the effect of random errors and improve the overall accuracy.

However, the present choice of the interrogation parameters does not create any loss of generality to the numerical results proposed hereafter.

2.4.1 DFT based data post-processing

The time response produced by the FE model for the different five configurations were post-processed through the DFT based data post processing approach. A comparison between the real and the estimated location of the crack is shown in Table 2.3.

It can be noted that while the configurations C1 and C2 are fairly well predicted (error < 4%), the accuracy of the estimate starts deteriorating from C3 to C5 (error > 50%). For the configuration C5, we observe a wrong estimate of the $sgn(\Delta\varphi)$, where sgn is the sign function. This results in an erroneous prediction of the crack location. From Eqn. (2.10) the crack location is estimated summing or subtracting the phase dependent term from the coordinate of the midpoint of the rod, located at $L/2$. The *sgn(Δφ)*will define if the damage is located on the right hand side or on the left hand side of the rod. To provide a good estimate of the damage location both the magnitude and sign of *Δφ* should be correctly estimated. In particular, a wrong estimate of the *sgn(Δφ)* will result in locating the damage in the wrong portion of the rod.

The inconsistent prediction capability of the algorithm, both in terms of *sgn(Δφ)*and overall accuracy, is even more accentuated when changing the windowing parameters used for the moving window approach. One of the best achievable results calculated using DFT on the first three superharmonics (*2f*, *4f*, *6f*) is shown in Table 2.3.

Table 2.3. Comparison between real and estimated locations calculated (from sensor S2) using the DFT approach and the first three superharmonics.

Crack Configuration	***Real Location*** (mm)	***Estimated Location*** (mm)	***Error*** (%)	***Δφ Real Sign***	***Δφ Estimated Sign***
C1	60	59.53	0.8	+	+
C2	68	70.63	3.8	+	+
C3	76	53.89	-29.1	+	+
C4	84	55.14	-34.4	+	+
C5	92	46.58	50.6	+	-

Different causes have been identified to explain this phenomenon. The DFT approach extracts the phase difference Δφ processing the signal coming from the two sensors as de-correlated signals. This approach might result in an amplification of eventual bias and numerical errors leading to an erroneous estimate of the relative phase difference.

This phenomenon becomes even more important considering that the estimated location depends on the choice of the windowing parameters and from the frequency spectrum resolution. The windowing parameters cannot be matched for both the signals in order to minimize the leakage effect. This produces considerable fluctuations in the predicted values depending on the initial choice of the window.

The DFT approach is also very sensitive to the choice of frequency resolution. We could not achieve a frequency resolution lower than 20Hz because of computational limitations related to the solution of the nonlinear FE model in the time domain.

A simple exercise based on the use of analytically generated sine waves with a known phase difference can easily show the resolution issue. In the frequency range of interest (40-240kHz), the DFT achieve a good accuracy for the phase estimate when using a frequency resolution of 1Hz or lower. The frequency resolution issue can most likely be overcome when acquiring experimental data because the frequency step can be easily reduced to 1Hz or lower. For numerically generated data this is still a major problem preventing the use of this algorithm for prediction purposes.

Finally, it was found that the ratio between the amplitude of the response at the driving frequency S_D versus the amplitude of the response at super-harmonic frequency S_{SH} played an important role in the accuracy of the results. This parameter was indicated as $\beta = S_D/S_{SH}$. The β ratio is a parameter conceptually similar to the *Signal to Noise* (*S/N*) ratio generally used in linear systems analysis. The parameter β can be seen as an indicator of the level of nonlinear response induced by a specific interrogation signal. A high level of nonlinear response is indicated by a low value of the β ratio. The averaged β ratios (i.e. the average between the β ratios at sensor S1 and S2) for each superharmonic are shown in Figure 2.12. The quality of the signal decreases while increasing the order of the harmonic because the amplitude of the nonlinear response decreases (non monotonically) with the order of the superharmonics.

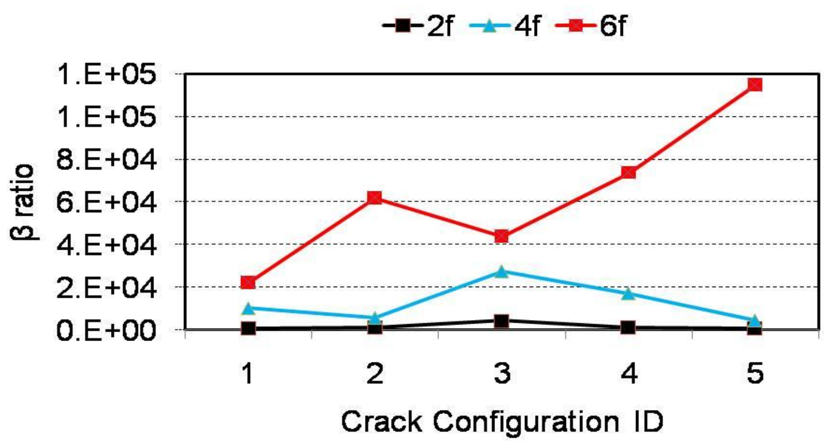

Figure 2.12. Averaged β ratios for the five crack configurations. The value of the β ratios for the first three superharmonics are plotted versus the different crack configurations.

The HHRS technique exploits the information carried by the higher order harmonics therefore it is expected that the most meaningful and accurate information is associated with the harmonic components having the lowest β ratios. This observation seems consistent with the results proposed in Table 2.3 where the errors as well as the β ratios increase from C1 to C5.

In conclusion, the accuracy of the HHRS technique strongly depends on both the frequency resolution and the quality of the nonlinear response signals (β ratios).

2.4.2 TF based data post-processing

The TF based approach was used to post-process the structural response in order to overcome the issues encountered with the DFT based methodology. A summary of the estimated crack locations produced by this approach and using the first three superharmonics (*2f*, *4f*, *6f*) is shown in Table 2.4**.**

Table 2.4 Comparison between real and estimated locations calculated (from sensor S2) using the TF approach and the first three superharmonics.

Crack Configuration	***Real Location*** (mm)	***Estimated Location*** (mm)	***Error*** (%)	***Δφ Real Sign***	***Δφ Estimated Sign***
C1	60	74.43	24.0	+	+
C2	68	70.93	4.3	+	+
C3	76	60.04	-21.0	+	+
C4	84	83.33	-0.8	+	+
C5	92	96.68	5.1	+	+

A good agreement between the actual and the estimated location is obtained for the configurations C2, C4 and C5 with a maximum percentage error of 5.1% corresponding to the configuration C5. Although, configurations C1 and C3 show a higher error (greater than 20%) with respect to the other configurations, a good improvement is obtained through the TF based approach in terms of the *sgn(Δφ)* estimate. The term *sgn(Δφ)* is always well predicted resulting, therefore, in the correct estimate of the crack in the right portion of the beam. The improved consistency of the results is due to the fact that now the relative phase $\Delta\varphi$ is calculated extracting the phase associated to the transfer function between the two signals. This approach is more robust to bias error and provides a higher accuracy (compared with the DFT) even in presence of higher β ratios.

Some of the problems discovered in the DFT approach still persist. The accuracy is still sensitive to the choice of the windowing parameters. In particular, oscillations in the values of the predicted damage location depend on the selected window length and location. Also in this approach, the overall accuracy is limited by the maximum achievable frequency resolution in the numerical frequency response analysis.

2.4.3 HT based data post-processing

As described in §2.3.3, the third data post-processing approach proposed in this work is based on the Hilbert transform. Table 2.5 shows the estimated crack locations obtained through this approach and using the first three superharmonics (*2f*, *4f*, *6f*).

The algorithm shows a fairly good prediction capability. Good estimates are obtained for C1 to C4 while C5 is associated with a larger error. The trend of these results seems to follow, once again, the trend of the β ratios shown in Figure 2.12. The higher β_{6f} values associated with the configuration C4 and C5 tend to decrease the accuracy of the estimate. The crack prediction obtained using only the first two harmonics (*2f* and *4f*) are listed in Table 2.6. The overall errors increases for C1 to C3 showing that the *6f* harmonics had a positive contribution to the location estimate. The accuracy on C4 improves while C5 is almost unchanged.

Table 2.5. Comparison between real and estimated locations calculated (from sensor S2) using the HT approach and the first three superharmonics.

Crack Configuration	***Real Location*** (mm)	***Estimated Location*** (mm)	***Error*** (%)	***Δφ Real Sign***	***Δφ Estimated Sign***
C1	60	58.15	3.08	+	+
C2	68	71.55	-5.22	+	+
C3	76	73.68	3.05	+	+
C4	84	73.87	12.06	+	+
C5	92	70.05	23.86	+	+

Table 2.6. Comparison between real and estimated locations calculated (from sensor S2) through the HT approach and the first two superharmonics.

Crack Configuration	***Real Location*** (mm)	***Estimated Location*** (mm)	***Error*** (%)	***Δφ Real Sign***	***Δφ Estimated Sign***
C1	60	56.12	6.47	+	+
C2	68	72.72	-6.94	+	+
C3	76	70.21	7.62	+	+
C4	84	77.43	7.82	+	+
C5	92	69.7	24.24	+	+

This trend seems to strengthen the role of the β ratios in the HHRS data processing. Further observations on the β ratios will be included in Chapter 3. The limited frequency resolution used in the simulations does not make the numerical results an ideal benchmark for in depth analysis on the parameter β.

Nevertheless, the most interesting outcome of these results is not the overall accuracy but the observed consistency of the results versus the choice of the windowing parameters. In fact, the major advantage produced by this approach (if compared with the TF and the DFT) is that the accuracy of the results is not sensitive to the windowing parameters. Errors lower than 0.01% were calculated due to the use of different windows.

Regardless of the choice for the initial window the results are always very consistent and the term $sgn(\Delta\varphi)$ is always correctly estimated. As a minor remark, the HT approach has proven to be computationally much faster (up to 10 times) than the previous approaches.

The improved consistency of the results is due to the capability of the Hilbert transform to provide the history of the instantaneous phase versus time for each specific super-harmonic. This characteristic results in two major advantages:

1. the phase oscillation due to the effects either of the reflected waves or of the nonlinear behavior of the system can be accurately monitored over time.
2. the average value of the phase can be better estimated due to the extended database of phase values associated with each specific frequency.

An example of the relative phase difference for the *2f* superharmonic calculated through the HT approach is shown in Figure 2.13. While both the DFT and the TF approach provide only one value for the estimated phase difference at a prescribed frequency, the Hilbert transform gives the trend of this value over time. If t_f and t_0 are the initial and final time instant and ΔT is the time step, the HT will provide a total number of samples equal to $N=(t_f-t_0)/\Delta T$.

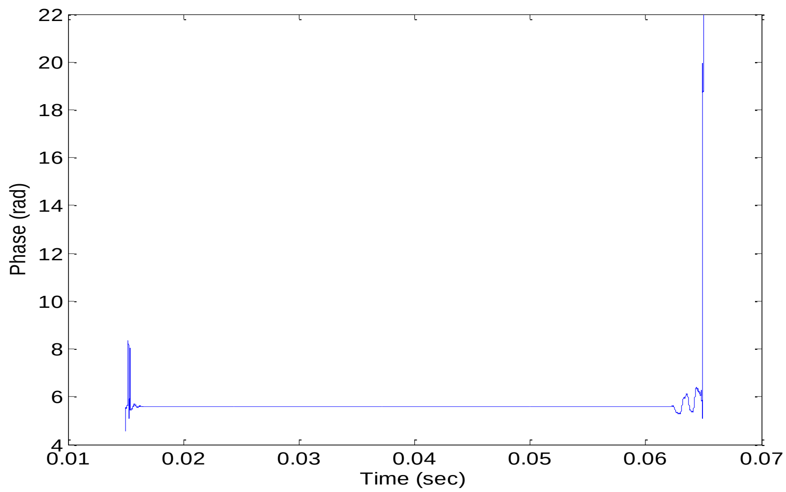

Figure 2.13. Phase difference calculated through the Hilbert transform for the 2Ω super-harmonic. The HT allows tracking the value of the phase difference over time and provides and extended number of samples for the Δφ estimate.

By using the HT approach, even a simple linear average is able to reduce the effect of the reflected waves and of the phase oscillations due to the nonlinearities allowing a good estimate of the $\Delta\varphi$.

Finally, it is expected that the accuracy of this approach can be improved extending the set of data by performing multiple interrogation at different driving frequencies and exploiting the information associated to a larger set of super-harmonics.

2.5 Summary

This chapter presented a novel concept for damage localization in slender isotropic structures. The technique, denominated Higher order Harmonic Response

Signal (HHRS), exploited the characteristic nonlinear dynamic response of a cracked structure. The nonlinear higher order harmonics, generated by a “breathing” crack (i.e. a fatigue crack at its early stage) under the effect of an external interrogation signal, was related to the location of the crack. The analytical formulation of the HHRS technique was illustrated by using both wave propagation theory and a Harmonic Balance (HB) approach.

A numerical technique for the simulation of the dynamic response of cracked structures was also presented. This technique was able to simulate the nonlinear behavior of the crack as well as the generation of higher order harmonics. The response data were processed through a Hilbert Transform based post-processing technique. Numerical results demonstrated that the HT technique enhances the feature extraction capabilities of the HHRS.

Finally, a numerical parametric study to different crack locations was presented. Results validated the proposed technique, demonstrated its localization capabilities and provided useful indications on some key parameters. In particular, the β ratio was presented as a suitable parameter to discriminate between the different nonlinear harmonic components and to improve the accuracy of the HHRS technique. The HHRS technique allowed determining the crack location with a baseline-free and FE model-free approach. This technique, however, still relied on an estimate of the phase velocities to evaluate the wave number at different frequencies. The HHRS in its present formulation is, therefore, still a model based technique.

CHAPTER 3

Higher Order Harmonic Response Signal:

Experimental Validation

This chapter is intended to provide experimental evidence to support the validation process of the Higher order Harmonic Response Signals (HHRS) based damage detection technique presented in Chapter 2.

A specific test setup will be presented in order to implement and validate the HHRS technique. The design procedure for the test bed and the fabrication approach for the damaged specimens will be described first.

Experimental results were acquired on three test specimens, one healthy and two damaged. The specimens consisted in aluminum beams with a single breathing crack in a different location. The selection of sensors, actuators and the data acquisition system will also be presented.

The experimental testing of the HHRS technique presented some interesting challenges from a practical point of view. The first step consisted in identifying a procedure allowing the fabrication of test specimens including a real "breathing crack" type defect. This procedure must be able to initiate and propagate a breathing crack in a controlled fashion without altering the geometric and material properties of the test specimen. As described in Chapter 2, the HHRS technique was numerically tested under specific assumptions, which included the linearity of the material properties. The fabrication approach should be able to guarantee the initiation and propagation of the fatigue crack without generating extended plastically deformed areas in the rest of the specimen. The second step consisted in designing an experimental setup able to reproduce the conditions under which the HHRS algorithm was numerically tested (free-free boundaries, longitudinal excitation, etc.) and to actuate the structure in the prescribed high frequency range. These two steps will be described in the following paragraphs.

3.1 Specimen Manufacturing

The test structure used for the numerical simulations was an aluminum bar with a rectangular cross sectional area and with a single breathing crack. In order to fabricate a specimen according to these requirements, a specific procedure was applied starting from a bare aluminum bar whose geometric and mechanical properties are listed in Table 3.1.

Table 3.1. Experimental test specimen: Beam geometrical and mechanical properties.

Length (m)	**Width** (m)	**Thickness** (m)	**Material**	**Young Modulus** E (GPa)	**Density** ρ (Kg/m^3)	**Poisson's ratio** υ
0.45	0.032	0.0032	Aluminum 6061 T651	68.94	2700	0.33

The bar was initially notched with a circular hole (*1mm Dia*) at the location were the breathing crack had to be initiated. A High Cycle Fatigue (HCF) loading was then applied using a Material Test System (MTS) 810 machine. The test was performed applying an axial load with a stress ratio $R = \frac{\sigma_{min}}{\sigma_{max}} = 0$ ensuring that the specimen was always subjected to tensile stress. The maximum applied load was selected in order to produce a tensile stress into the specimen of 150 MPa that is well below that yield stress of the material. The load cycles were applied at a 15Hz frequency and the test was carried on for 140,233 cycles.

The HCF test was selected in order to initiate a breathing crack without producing global plastic deformation in the specimen, with the only exception of a small region close to the initiation points of the crack.

Following this procedure, two damaged specimens were fabricated. Table 3.2 summarizes the crack size and location with respect to the sensors.

Table 3.2. Real crack size and location in the damaged test specimens.

Specimen #	**Distance from S1 (cm)**	**Distance from S2 (cm)**	**Approx. Crack Length (cm)**	**Crack Thickness**
Specimen A1	17.3	17.3	1.2	Through Crack
Specimen A2	22.8	12.0	1.2	Through Crack

The MTS test equipment and the test specimen used for the experiment are shown in Figure 3.1. An optical microscope image of the breathing crack induced induced by the HCF loading is also shown in Figure 3.1(c).

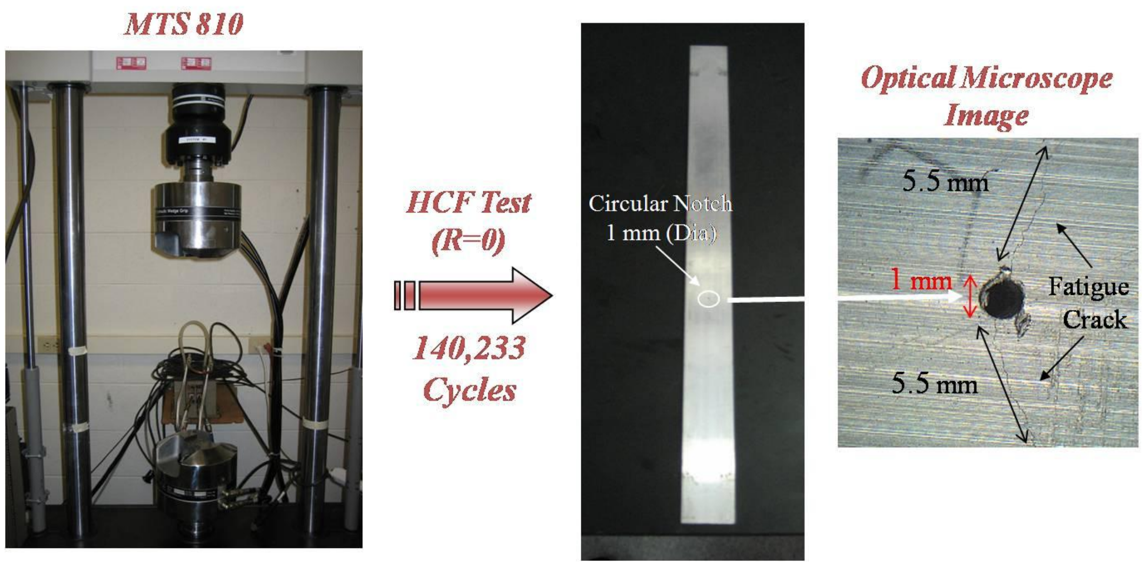

Figure 3.1. Sequence of operations performed to initiate to damage the test specimen; (left) Material Test System 810 equipment, (center) Aluminum beam with 1mm circular hole, (right) optical microscope image of the breathing crack.

3.2 Experimental Setup: Sensors, Actuators and DAQ

Once the damaged specimen was fabricated it was equipped with sensors and actuators needed for the implementation of the damage detection technique. A schematic of the experimental setup used for the data acquisition phase is illustrated in Figure 3.2. Two piezoelectric ceramic patches, labeled 3 and 4 in Figure 3.2, were used to generate the interrogation signal needed to interrogate the test specimen.

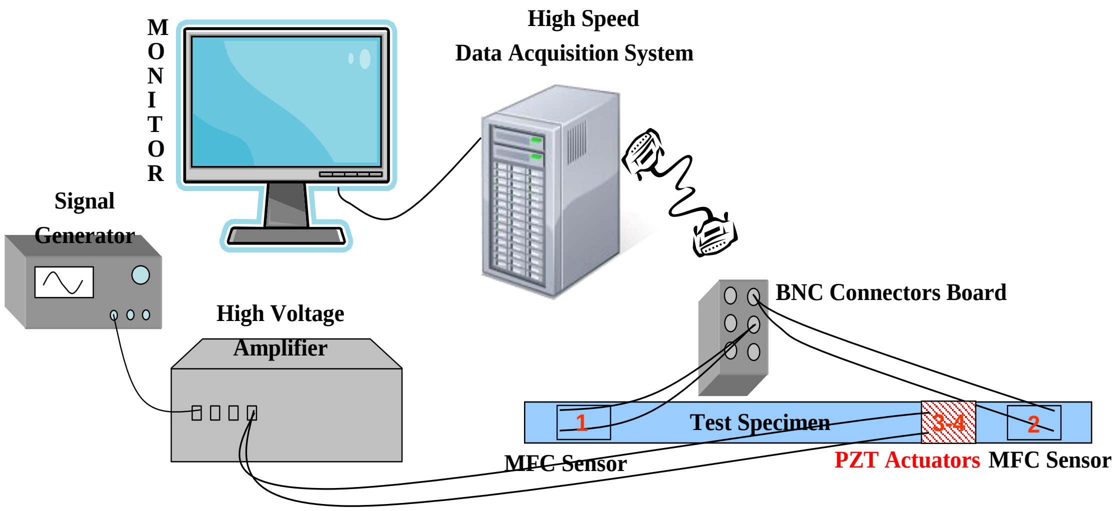

Figure 3.2. Schematic of the setup used for the experimental validation of the HHRS algorithm.

The patches had a d_{31} type polarization and were located symmetrically with respect to the beam neutral axis. The PZT transducers were mounted through silver conductive epoxy so that the common ground was connected directly to the metallic beam. The mechanical and electrical properties of the piezoceramic transducers used in the experiments are listed in Table 3.3. This configuration allowed the generation of quasi-longitudinal waves therefore fulfilling the hypotheses set for the HHRS algorithm.

Table 3.3. Mechanical and electrical properties of the PZT transducers.

Material	Dimensions (cm)			Young Modulus E (GPa)	Poisson ratio υ	C_x (pF)	Tanδ	d_{31} (m/V x 10^{-12})
	Length	Width	Thick					
PZT-502	3.81	1.9	0.254	71.	0.31	3135	<0.4%	-175

The structural response was measured at two different locations by means of two *Macro Fiber Composites®* (MFC) sensors type *2814 P2* (Figure 3.3), labeled 1 and 2 in Figure 3.2. MFC sensors were selected for their high sensitivity and because they could easily be electrically insulated by the rest of the setup. The stripes of piezoceramic material (yellow bars in the schematic of Figure 3.3) constituting the MFC transducers are encapsulated in a kapton envelop. When the MFC is bonded on the test structure, the kapton envelop electrically insulates the pzt material from the structure.

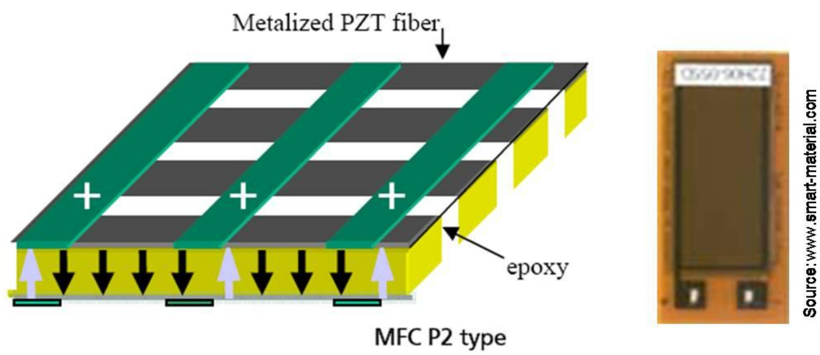

Figure 3.3. (left) Schematic and (right) picture of a Macro Fiber Composite (MFC) transducer.

As a general remark, it should be noted that in an initial configuration of the test setup MFC sensors were used both as sensors and actuators. Their low weight and flexibility were very appealing characteristics to instrument the test structure without perturbing its structural response. During an initial testing phase the MFC transducers that were used as actuators to produce the high frequency excitation experienced consistent heating eventually resulting in the burn out of the epoxy resin and, therefore, in short circuiting pzt stripes (Figure 3.4).

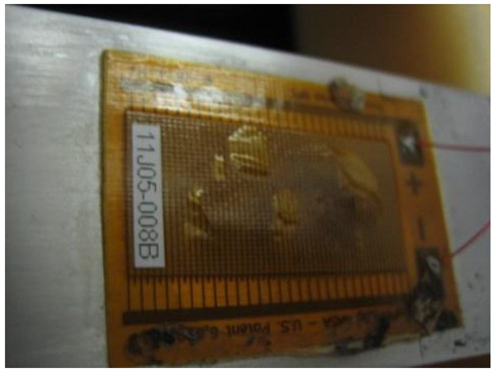

Figure 3.4. MFC with extended burned areas after being driven with high frequency and high voltage excitation.

It was found from the experimental testing that MFCs could withstand driving voltages up to $350V_{0\text{-}p}$ at 40kHz. Above these settings the MFC started overheating. The MFC 2814 P2 are designed to have a broad driving voltage range (V_{max}=1500V, V_{min}=-500V) and deliver the maximum force of about 180N at the maximum voltage. Driving this transducer with a maximum voltage of $350V_{0\text{-}p}$ significantly limited the amplitude of the interrogation signal.

This preliminary testing phase highlighted that the MFC transducers could not deliver the necessary excitation load at the right frequency needed to trigger the nonlinear response of the cracked structure. Therefore, MFC were replaced with standard PZT actuators.

The free-free boundary conditions that were considered in the numerical simulations were approximated laying the beam ends on a two pieces of foam. The resulting instrumented test specimen is shown in Figure 3.5.

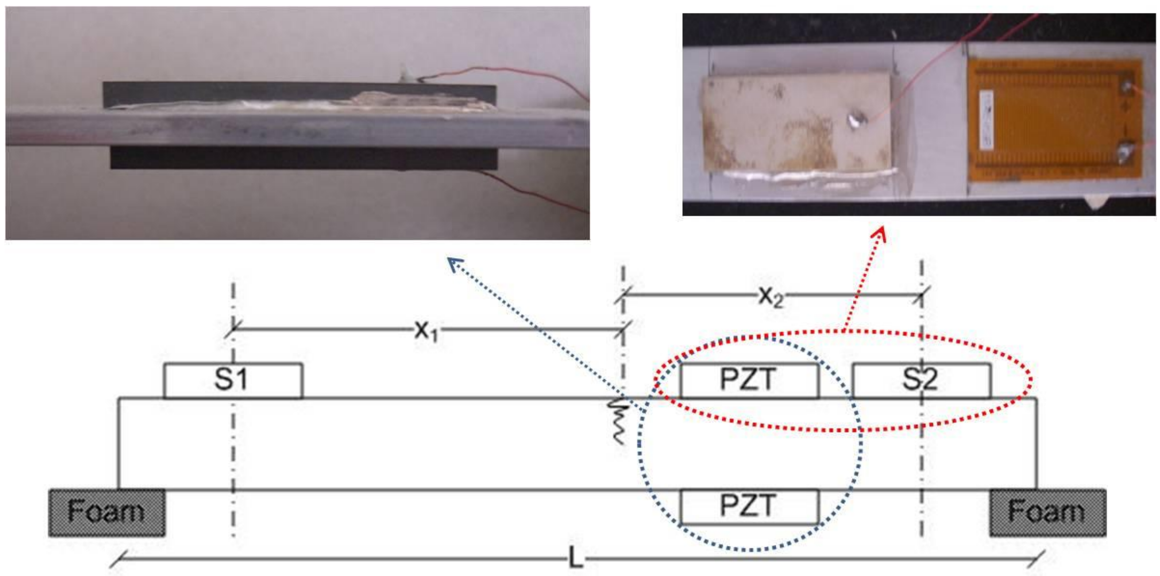

Figure 3.5. (Bottom) Schematic of the instrumented test specimen, (top-left) picture of the PZT actuators, (top-right) picture of the PZT and MFC transducers.

A Sony AFG3000 function generator was used to produce the voltage signal that drives the PZT actuators. This signal was first amplified through a high voltage TREK 350-MS commercial amplifier and then fed into the piezoelectric patches. The response signal collected by the MFC sensors was acquired through a Personal Computer equipped with a National Instruments PCI-6115 high speed (10Ms/sec) data acquisition board. A Labview® code integrating the HHRS algorithm was specifically developed to acquire and process the data.

3.3 HHRS Experimental Results

Each test was conducted driving the PZT actuators with a sinusoidal signal at a specific frequency. Data were acquired using a sampling frequency f_s=1MHz and collecting 1Msample at each measurement. These parameters were selected to ensure a frequency resolution Δf=1Hz. The numerical analysis pointed out that the frequency resolution strongly impacts the accuracy of the phase measurements and, ultimately, of the estimated crack location. The frequency resolution of 1Hz was indicated, in Chapter 2, as an appropriate value for the convergence of the phase value in this frequency range.

The structural response was collected from the two MFC sensors and processed through the HHRS algorithm in order to provide an estimate of the crack location. The estimated location was then compared with the real location to perform an assessment of the HHRS performance.

A set of measurements was initially acquired on the healthy specimen in order to provide a reference baseline. Although the baseline signal is not used by the HHRS algorithm in the damage detection process, it will serve as reference to assess the generation of the higher order harmonic components in the damaged specimens. The presence of the breathing crack, in fact, should generate peaks in the frequency spectrum of the damaged specimen which are not visible in the healthy one.

The response spectrum of two different damaged specimens were measured and compared with the healthy specimen in order to prove the generation of the higher order harmonics due to the system nonlinearity.

3.3.1 Healthy Specimen and Harmonic Distortion

The healthy specimen was initially tested driving the PZT actuators with a sinusoidal input tuned at different frequencies in a range between 20 and 40 kHz. The main reason for performing this frequency sweep was to identify specific excitation frequencies able to trigger the nonlinear harmonic response. As a remark, the upper frequency limit chosen for these tests is dictated by the limited bandwidth of the voltage amplifier used in this application and not by specific requirements of the HHRS algorithm.

The frequency content of the structural response was extracted by Fourier Transforming the time history of the signal acquired at the two sensors. The results for a sinusoidal input at a frequency f_e = 32.15 kHz applied on the healthy specimen are shown Figure 3.6. Note that data are not time averaged which explains the presence of a consistent noise floor.

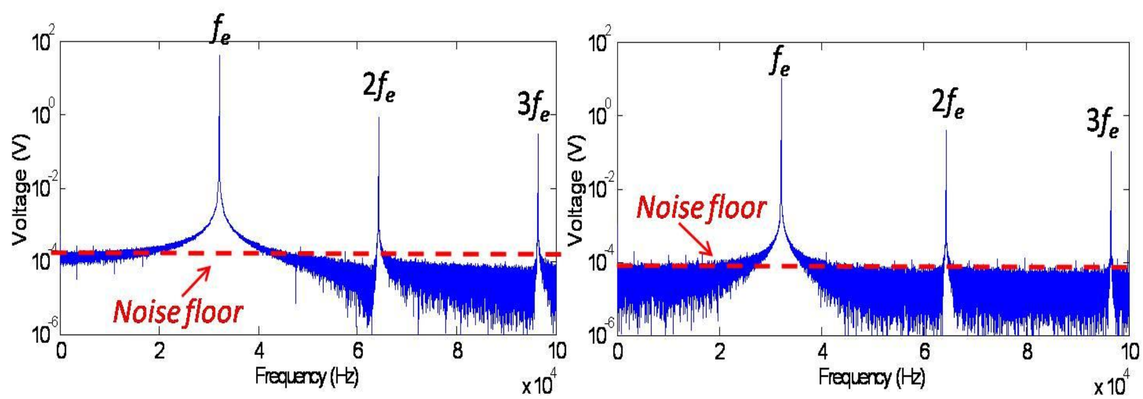

Figure 3.6. Frequency content of the structural response acquired at sensor 1 (left) and sensor 2 (right) on the healthy specimen.

These preliminary results pointed out some of the difficulties that can be experienced experimentally implementing the HHRS algorithm. By analyzing the spectral content we can identify a sharp peak at the frequency of the external excitation as well as two other peaks centered at the first two superharmonic components (i.e. $2f_e$ = 64.3 kHz and $3f_e$ = 96.45 kHz). Nevertheless, this response is generated by a healthy specimen and therefore these peaks are clearly not related to the presence of a crack.

The reason for the appearance of higher order harmonics in the dynamic response of the healthy specimen was later identified as the Harmonic Distortion (HD) effect characteristic of all the electronic devices in the experimental chain. When the digital input signal is converted into an analog output from the signal generator, the sine wave is slightly distorted therefore giving rise to superharmonics components in the frequency spectrum. This phenomenon is even more accentuated when the output from the signal generator is fed into the high voltage amplifier and piezoelectric transducers that add further distortion.

A simple check on the output signals both from the signal generator and the voltage amplifier revealed that the amount of the harmonic distortion was within the specifications for the hardware (Table 3.4) used in these experiments.

Table 3.4. Harmonic Distortion specifications for the selected hardware.

Material	**Harmonic Distortion (dB)**	**Total Harmonic Distortion (%)**
Signal Generator Sony AFG 3000	<60	<0.2
Voltage Amplifier TREK 350MS	N/A	<1

This phenomenon prevents the use of superharmonic components to experimentally investigate the validity of the HHRS approach. The spurious superharmonics produced by the HD overlap with the nonlinear response of the crack deteriorating the signal quality.

In other terms, the superharmonics produced by the HD act similar to background noise significantly reducing the Signal to Noise (S/N) ratio at superharmonic frequencies.

Possible techniques able to clean up the driving signal could be explored. In particular, the output signal from the amplifier could be fed into a bandpass filter centered on the driving frequency in order to remove the harmonics produced by the HD. This will require a high voltage analog filter that is not readily available. The filter could add a phase distortion that should be accounted for in order to prevent a loss of accuracy in the damage localization. Another possible technique implies the use of the so called “Signal Tailoring” where the sinusoidal input signal produced by the signal generator is altered in order to counterbalance the effect of the harmonic distortion. In this way, an almost pure sinusoidal output can be obtained through the use of a non-sinusoidal input. While these techniques could have the potential to solve the problem caused by the HD, they were not explored in this work.

3.3.2 Use of SubHarmonic Response Signals

To solve the problem produced by the HD associated to the electronic equipments a different approach was explored in this research. The new approach is based on the use of the subharmonic and ultrasubharmonic (i.e. subharmonic of higher order) components in order to extract the phase information needed for the HHRS algorithm.

As stated previously, the HHRS algorithm is based on the use of the phase information carried by the higher order harmonics (i.e. superharmonics, subharmonics and ultrasubharmonics) that are generated at the crack interface. In terms of the damage detection algorithm there is no conceptual difference between using either the superharmonic or subharmonic components. They are both generated at the crack interface and therefore carry the same kind of information about the damage. Since the subharmonic and ultrasubharmonic components are not generated by electrical harmonic distortion, they are more reliable indicators of the defect than the superharmonic components.

The physical mechanism behind the generation of subharmonics was investigated by other authors [84-86] and considerable improvements have been accomplished over the past years. Approximated analytical solutions to study the generation of these harmonics were formulated [87-89]. Nevertheless, the nonlinear behavior dominating the structural response of cracked structures is extremely complex and not yet fully understood.

An attempt to demonstrate the generation of subharmonics and ultrasubharmonics in cracked structures was based on the analysis of the delicate balance between the interatomic and the inertia forces between the edges of the crack (Figure 3.7) subjected to an external dynamic excitation [90,91]. When the crack plane A is vibrated at the frequency of the external excitation ω which is lower than the resonance frequency $\omega_B = \sqrt{\frac{k}{m}}$ of the crack plane *B*, the crack plane *B* follows the plane A. If $\omega >> \omega_B$, the plane *B* cannot follow the motion of *A* due to the inertia forces. The resulting period of vibration T_B of the plane *B* will be higher than the period T_A associates to the plane A. The period T_B will determine the period at which impacts occur. The impact of the two edges will occur, therefore, at a frequency that is lower than the driving frequency. This phenomenon induces the crack breathing at a frequency that is a fractional multiple of the driving frequency ω, i.e. at subharmonic frequency. Although a few mathematical models able to capture the subharmonic response were proposed in the past [92,93], the physical phenomenon is still not completely understood.

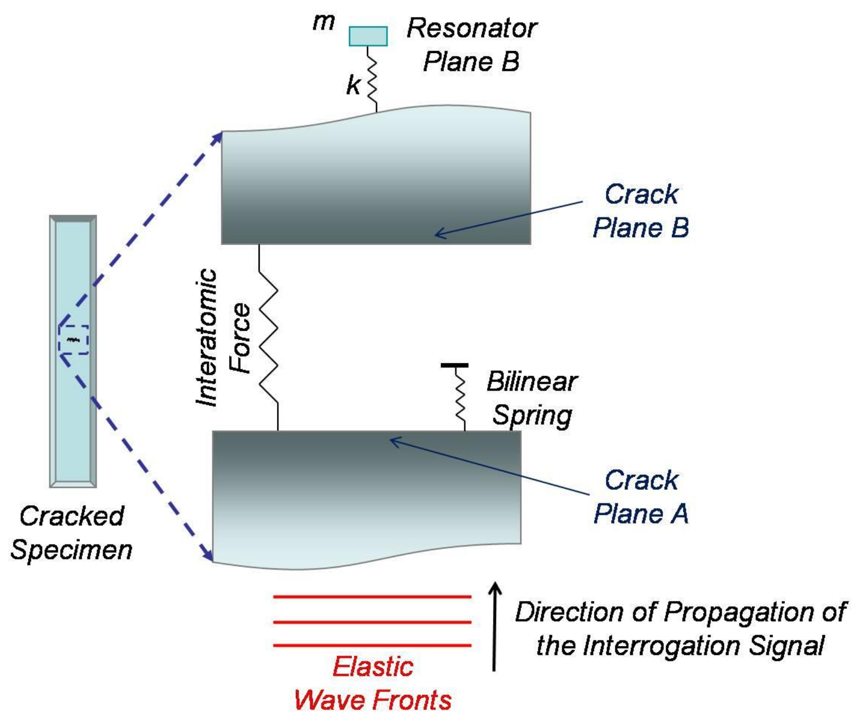

Figure 3.7. Schematic of the interaction

The subharmonic components present a few main differences with respect to the superharmonics. First, the subharmonics are characterized by a threshold behavior which results in the generation of the response at subharmonic level only above a specific amplitude of the external excitation. This phenomenon is related to the adhesion and inertia forces between the two edges of the crack. The driving excitation must have a frequency $\omega >> \omega_B$ which will make dominant the contribution of the inertia forces. At the same time, the amplitude of the driving force must be high enough to overcome the adhesion force at the crack interface.

This is an important aspect to keep in mind, in order to trigger the experimental subharmonic response in a cracked structure, because the optimal response is given by a proper combination of amplitude and frequency of the interrogation signal. Also, once the threshold is exceeded a further increase in the amplitude of the driving signal produces first an increase in the amplitude of the subharmonic response and then induces an avalanche like behavior (i.e. successive period doublings) driving the system to a chaotic response [94].

Besides providing an effecting way to overcome the problem of the harmonic distortion, the subharmonic components have a higher signal to noise ratio [95-97] which is an important parameter determining the accuracy of the estimated damage location through the HHRS algorithm.

3.4 Damaged Specimen – A1

The damaged specimens were tested exploiting the structural response at subharmonic frequencies. The main goal of this experimental phase is to prove the concept of damage localization through the HHRS algorithm by exploiting the subharmonic response. In these experiments, the optimal driving frequencies to trigger specific subharmonic response were experimentally identified. Different excitation frequencies were tested and the signal generating the larger nonlinear response was selected. Further studies will be required to define a deterministic approach for the selection of the properties of the interrogation signal able to trigger a subharmonic response.

For the specimen A1 an external load at a frequency $f_e = \frac{\Omega_e}{2\pi}$ = 32.15 kHz was found to be a proper excitation to trigger the response at the subharmonic frequency of order 2 (i.e. $f_{1/2} = \frac{f_e}{2} = 16.075kHz$) along with its first two ultra-subharmonics components $f_{3/2} = \frac{3f_e}{2} = 48.225kHz$ and $f_{5/2} = \frac{5f_e}{2} = 80.375kHz$. The frequency content of the measured signal is shown in Figure 3.8.

The data acquired from the two MFC sensors were fed into the HHRS damage detection algorithm in order to provide an estimate of the crack location. Ten sets of data were acquired under the same experimental conditions. Multiple sets were acquired in order to improve the accuracy and to assess the repeatability of the measured data.

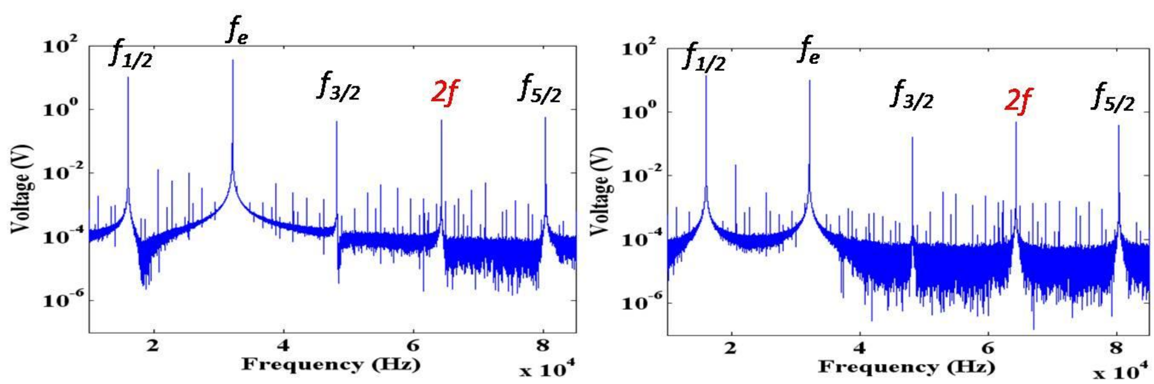

Figure 3.8. Frequency spectrum for the damaged specimen A1 with an external excitation at f_e=32.15 kHz. Response at sensor S1 (left) and sensor S2 (right).

The results for the estimated crack location calculated with respect to the sensor S1 are shown in Figure 3.9. The crack location was estimated using, respectively, the first, the first two and the first three subharmonics/ultrasubharmonic of order *2*. This means that the plot labeled as 1H was calculated using only data provided by the main subharmonic $f_{1/2}$. In the same way, the plot 2H was obtained using $f_{1/2}$ and $f_{3/2}$ while the plot 3H included the data from $f_{1/2}$, $f_{3/2}$ and $f_{5/2}$. The red solid line represents the real location of the crack, the markers give the estimated location of the damage for each set of data while the dotted lines represent the confidence bounds at $\pm 2\sigma$. Due to the small value of the β ratio associated with the first subharmonic component (i.e. a large structural response at subharmonic level), the subharmonic $f_{1/2}$ is able to provide a good estimate of the crack location without needing additional information from the other harmonics. Results in Figure 3.9 clearly show the improvement in the overall accuracy gained when retaining a higher number of harmonics. These plots also confirm the repeatability of the measurements and the capability of the HHRS algorithm to provide an estimate of the damage location within the 95% confidence bounds. This approach assumed a Gaussian distribution of the measured data. A different insight into the experimental results is provided by Table 3.5 which summarizes the averaged estimated location versus the real damage location as well as the standard deviation and the overall error.

Table 3.5. Summary of the estimated crack locations for the specimen A1.

	Real Location from S1 (m)	***Estimated Location*** (m)	***Standard Deviation*** (m)	***Error*** (%)
1H	0.173	0.16325	0.00378	-5.63
2H	0.173	0.17783	0.01425	2.79
3H	0.173	0.17358	0.00997	0.33

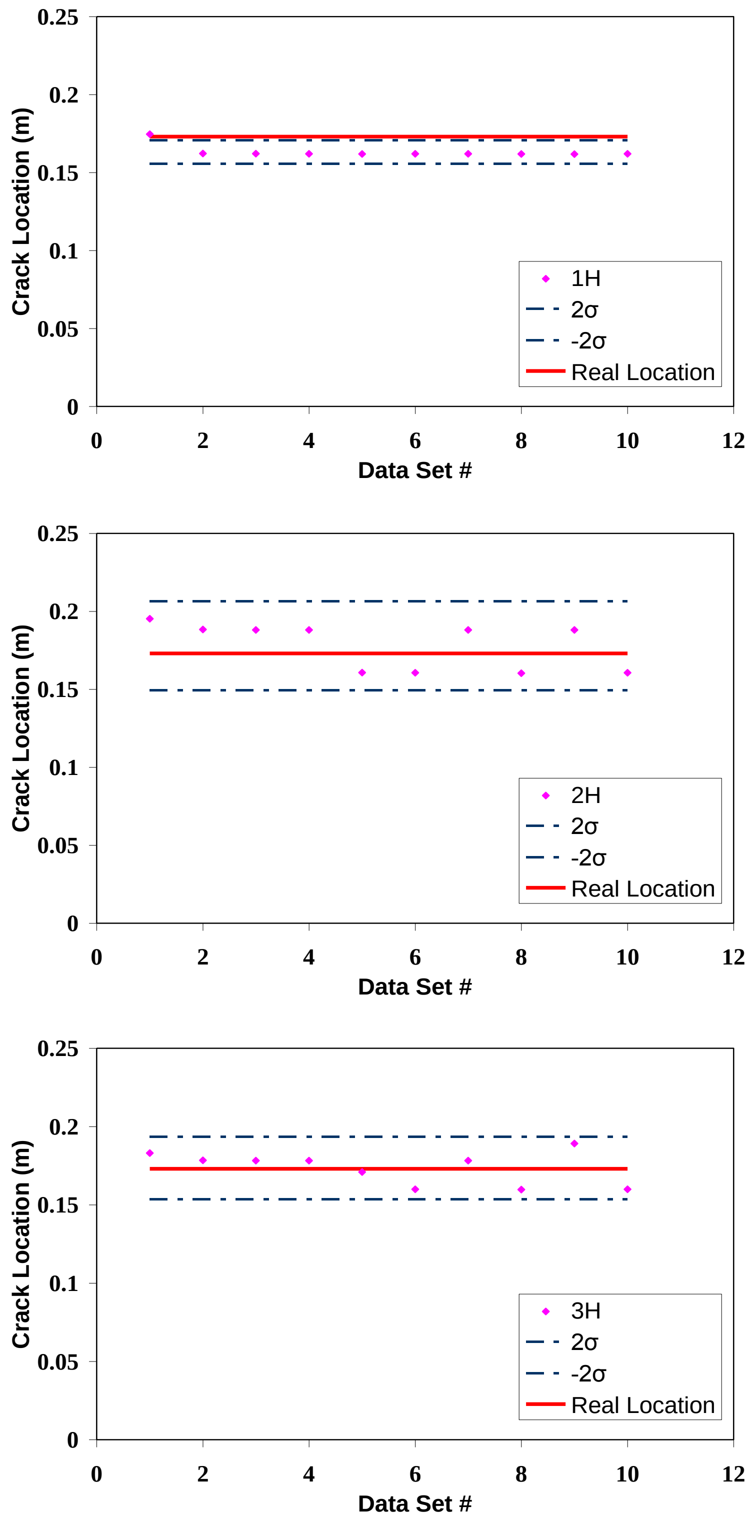

Figure 3.9. Experimental results for the specimen A1. Estimated crack location and confidence bounds at ±2σ using one (1H), two (2H) and three subharmonics (3H), respectively.

In this analysis, the estimated location calculated based on each single set of data and for each harmonic was obtained through a linear average. The low β ratio (Table 3.6) associated with the retained subharmonics made each harmonic a very good candidate to estimate the crack location. It clearly appears how the estimated damage location converges to the real location while increasing the number of retained harmonics. Although this behavior could be expected based on the theoretical formulation of the HHRS algorithm, it does not provide a general rule to determine the number of harmonics to be retained in the calculation. In other words, considering a larger number of higher order harmonics does not necessarily yield more accurate results.

Table 3.6. β ratios for the specimen A1.

	$\beta_{1/2}$	$\beta_{3/2}$	$\beta_{5/2}$
S1	3.58	85.5	65.14
S2	0.71	60.04	25.7
Avg	2.14	72.77	45.42

The capability of providing meaningful information about the damage is strictly related to the quality of the data which mainly depends on the frequency resolution and the β ratio.

More sophisticated techniques to combine low quality data (i.e. with higher β ratio) could be investigated in order to further improve the accuracy of the algorithm. A possible approach will be presented in the following paragraph.

3.5 Damaged Specimen – A2

Following the same approach outlined in the previous paragraphs, a second damaged specimen was tested. The details of the crack type and location are given in Table 3.2.

According to the procedure established in the previous paragraphs, the subharmonic response (Figure 3.10) corresponding to a driving frequency $f_e = \frac{\Omega_e}{2\pi} = 27.210kHz$ and identified by the subharmonic $f_{1/2} = \frac{f_e}{2} = 13.605kHz$ and by the two ultrasubharmonics $f_{3/2} = \frac{3f_e}{2} = 40.815kHz$ and $f_{5/2} = \frac{5f_e}{2} = 68.025kHz$ were used to locate the damage in the specimen A2.

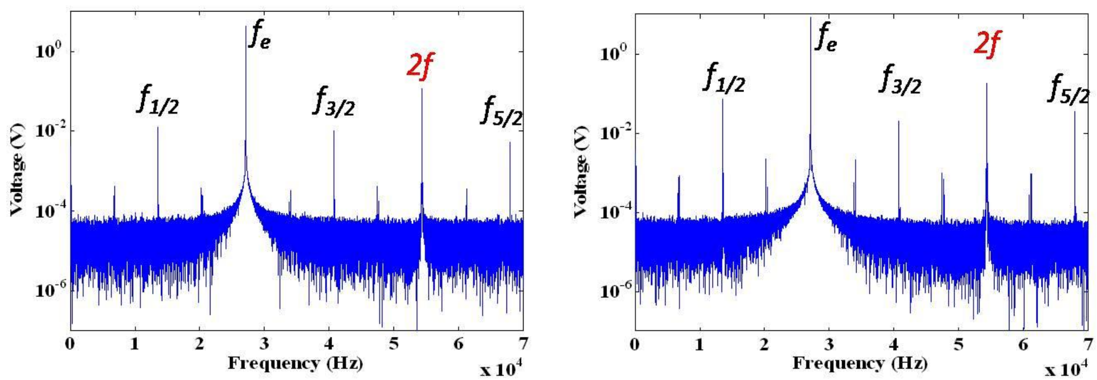

Figure 3.10. Frequency spectrum for the damaged specimen A2 with an external excitation at f_e=27.21 kHz. Response at sensor S1 (left) and sensor S2 (right).

As previously done, ten different sets of data were acquired. Their distribution as well as the estimated location is summarized in Figure 3.11 and Table 3.7, respectively.

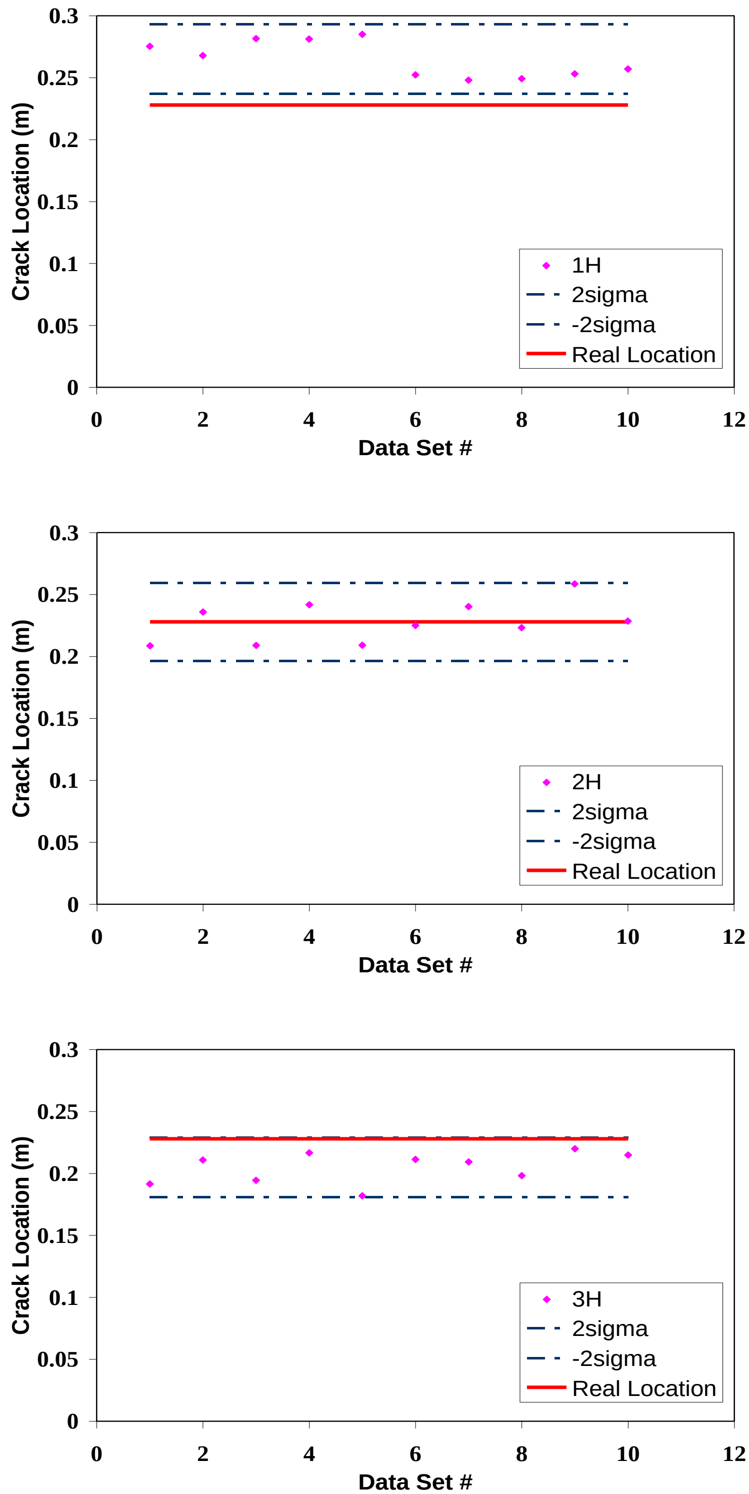

Figure 3.11. Experimental results for the specimen A2. Estimated crack location and confidence bounds at ±2σ using one (1H), two (2H) and three subharmonics (3H), respectively.

The collected data are all contained in a region at ±2σ from the average value which ultimately assures a 95% confidence in the measurements. The subharmonic $f_{1/2}$ has a much higher β ratio than the correspondent value exhibited by the specimen S1 therefore the accuracy of the estimated location is expected to be lower.

As clearly shown in Table 3.7, the first subharmonic provides an estimate of the damage location with a 16% error. The error rapidly converges to zero when including the second harmonic and the real location is again inside the confidence bounds of ±2σ. Including the third subharmonic the error increases again to approximately 10%.

Table 3.7. Summary of the estimated crack locations for the specimen A2.

	Real Location from S1 (m)	***Estimated Location*** (m)	***Standard Deviation*** (m)	***Error*** (%)
1H	0.228	0.2650	0.01399	16.22
2H	0.228	0.2280	0.01570	0.009
3H	0.228	0.2049	0.01193	-10.12
3H Weighted Avg	0.228	0.2287	-	0.3

By comparison with the results presented for the specimen A1, note that specimen A2 needs a larger number of harmonics to converge to the real location. This behavior can be explained recalling the conclusions previously drawn about the influence of the β ratio on the overall accuracy. For the specimen A2, all the subharmonics have a β ratio (Table 3.8) that is much larger than what observed in specimen A1. The quality of the subharmonic response for this specimen is therefore expected to be lower.

Table 3.8. β ratios for the specimen A2.

	$\beta_{1/2}$	$\beta_{3/2}$	$\beta_{5/2}$
S1	340	411	784
S2	270	4023	786
Avg	305	2217	785

This condition results in two main observations. First, a larger number of harmonics must be used to converge to the real solution. Second, not all the harmonics carry the same amount of information about the damage location. By linearly averaging the information extracted from the subharmonics, the contributions from the nonlinear harmonics are not discriminated based on the signal quality. In presence of high β ratios, a better approach would be using a weighted average to combine the information from the different signals.

The overall goal of this work is providing the experimental evidence supporting the HHRS algorithm instead of focusing on the overall accuracy of the technique. Nevertheless, an example is provided to illustrate the possible use of the β ratios in managing low quality data.

In a weighted average approach, the β ratios could be used to calculate the weighting factors of the different terms according to the following relation:

$$\overline{x_c} = \frac{\frac{1}{\beta_{1/2}} x_{\frac{f}{2}} + \frac{1}{\beta_{3/2}} x_{\frac{3f}{2}} + \frac{1}{\beta_{5/2}} x_{\frac{5f}{2}}}{\frac{1}{\beta_{1/2}} + \frac{1}{\beta_{3/2}} + \frac{1}{\beta_{5/2}}} \tag{3.1}$$

where $\overline{x_c}$ is the weighted average of the estimated location. The terms $x_{f/2}$, $x_{3f/2}$ and $x_{5f/2}$ indicates the linear average of the crack locations estimated for the ten data sets from each subharmonic. The terms $\beta_{f/2}$, $\beta_{3f/2}$ and $\beta_{5f/2}$ are the β ratios.

The application of this approach to the specimen A2 results in an estimated location of 0.2287m with an error of 0.3%, as shown in Table 3.7. This approach provides a good improvement on the overall accuracy and reduces the impact of low quality subharmonic signals making the selection of the response signal less critical.

As a concluding remark, it is interesting to note some experimental observations from the measurements on the two specimens. The nonlinear response of the specimen A2 at subharmonic frequencies could be triggered more easily than in the specimen A1. In the specimen A2, the actuators were closer to the damage therefore driving the crack with a higher force (given the same applied input voltage).

Tuning the frequency and amplitude of the interrogation signal to trigger a stable subharmonic response resulted more difficult than in the specimen A1. At certain frequencies the response showed the effects of self-modulation occasionally leading to chaotic behavior. The self-modulation is a precursor of the chaotic behavior in nonlinear systems [86,94]. Once the subharmonic response is triggered by the external excitation, increasing the amplitude of the driving force generally produces an increase in the amplitude of the subharmonic response. The subharmonic response follows this trend up to a maximum excitation force upon which the subharmonic response becomes unstable and the overall response chaotic. This instability is generally preceded by the generation of a large number of subharmonics of increasing order (i.e. $f_{1/2}$, $f_{1/4}$, $f_{1/8}$ etc.) and side frequencies (generally referred to as Ultra Frequency Pair or Combinational Tones). This phenomenon is often referred to as a period doubling cascade. The higher order subharmonics, generally associated with large amplitude, have a dual effect. They create a visible modulation of the time response and eventually drive the system to develop a chaotic response.

The development of the subharmonic response upon increase of the input voltage for a sinusoidal input at a frequency f=27.210 kHz is shown in Figure 3.12a. For an input voltage to the PZTs of $V=200V_{0\text{-}p}$ the system exhibits stable subharmonic response. A further increase in the amplitude ($V= 300V_{0\text{-}p}$) results in an increase of the amplitude of the subharmonics and ultrasubharmonics.

Once the maximum force threshold is reached (limit identified by the 350 $V_{0\text{-}p}$ for this specimen), additional subharmonics of higher order (due to the period doubling cascade phenomenon) as well as a great number of combinational tones appear in the spectra (Figure 3.12b) which results in a self-modulated envelope of the response in the time domain (Figure 3.13). A further increase in the input voltage induces the transition to a fully chaotic dynamic response. This response, however, has not been recorded in order to avoid any damage to the tests specimen due to the high instability associated with this dynamic response.

The development of subharmonic components upon different driving conditions is consistent with what observed by other researchers [85, 98] using ultrasonic non destructive evaluation techniques for the inspection of cracked structures.

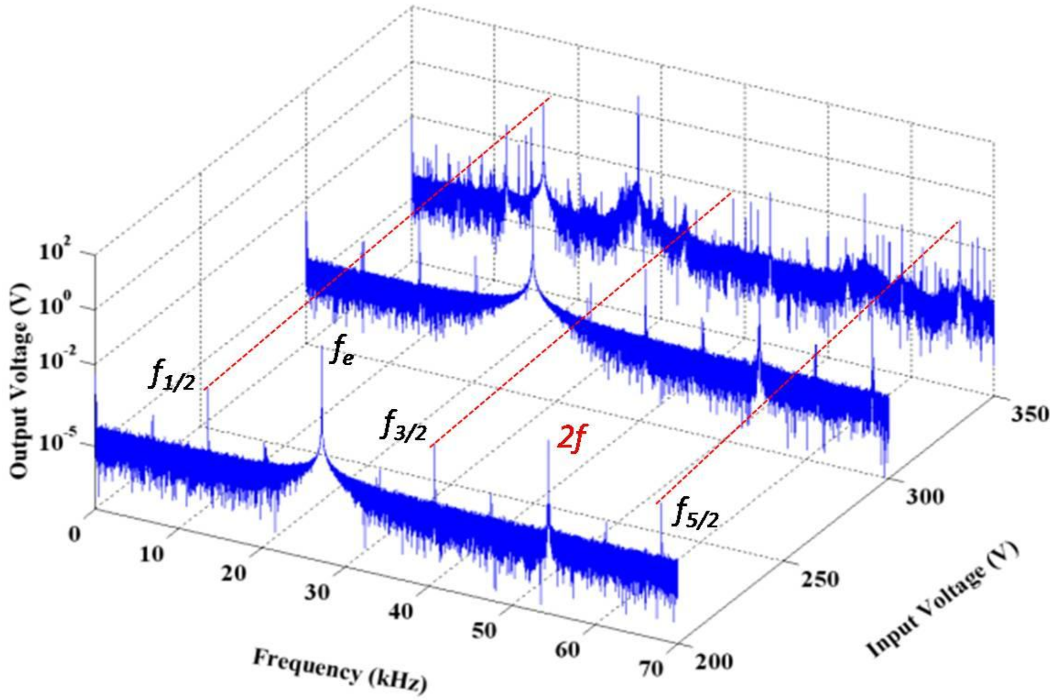

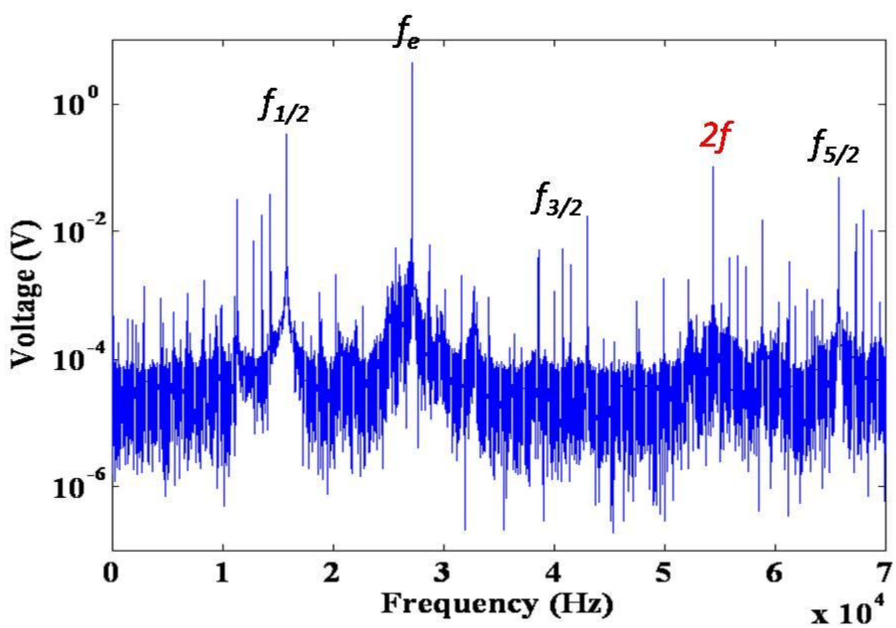

Figure 3.12. Effect of the driving voltage on the subharmonic spectra collected at S1 for the specimen A2. (a) shows a low voltage subharmonic ($200V_{0\text{-}p}$), a stable subharmonic at high voltage ($300V_{0\text{-}p}$) and self-modulation effects ($350V_{0\text{-}p}$). (bottom) detailed view of the response spectrum at $350V_{0\text{-}p}$.

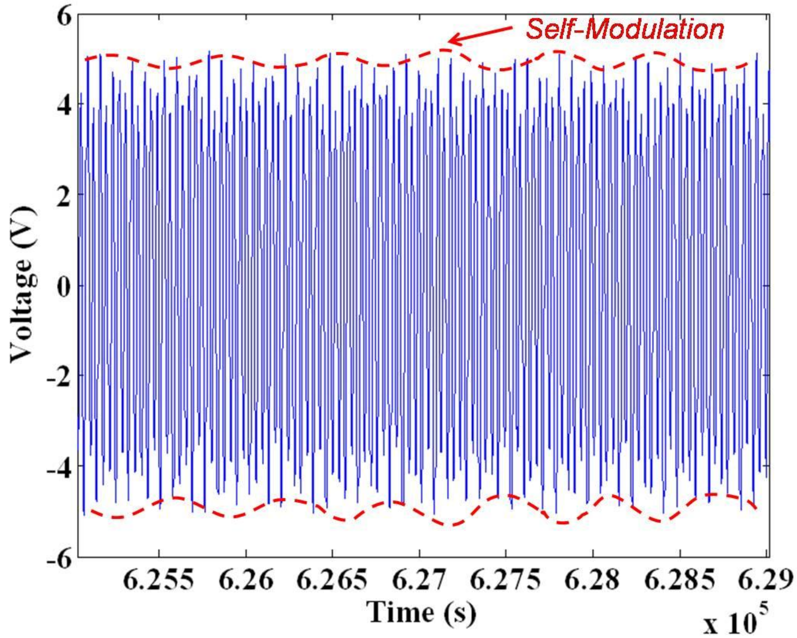

Figure 3.13. Time history at $300V_{0\text{-}p}$ showing the effect of the self modulation.

3.6 Summary

This chapter presented the experimental validation of the Higher order Harmonic Response Signal (HHRS) technique presented in Chapter 2. The approach to fabricate the damaged test specimens and the design of an experimental test bed able to induce and measure nonlinear harmonics was illustrated. Two damaged specimens were tested and compared to the response of the healthy structure to demonstrate the generation of the higher order harmonics due to the system nonlinearity.

The results from dynamic measurements on the healthy specimen suggested that the most suitable nonlinear harmonics to be used for damage detection were the subharmonics. These nonlinear harmonic components were only generated at the crack interface and, therefore, were more reliable indicators of the crack presence.

By using the subharmonic response of the damaged specimens, the localization capabilities of the HHRS technique were illustrated. High localization accuracy could be obtained on both specimens. The experimental results also showed that the measurements were repeatable and that the crack location can be predicted with a 95% confidence.

The use of the β ratio was finally validated by applying it to the experimental results. This parameter provided a criterion to select the nonlinear harmonics to be post-processed through the HHRS algorithm. It also allowed increasing the localization accuracy when dealing with lower quality (low nonlinear harmonic response and noisy data) response.

CHAPTER 4

Higher order Harmonic Response Signals technique: Application to Plate Structures

In the previous chapters the theoretical and experimental aspects related to the formulation of the higher order harmonic response signals (HHRS) were presented. The experimental results showed good agreement with what was anticipated by the numerical simulations and provided a solid evidence of the validity of the proposed technique. The HHRS approach, however, was formulated relying on some simplified assumptions that restrict the applicability of this technique to slender isotropic structures excited by longitudinal non-dispersive waves. This chapter will investigate the possible application of this technique to plate-like structures.

The first part of this chapter will develop the theoretical approach used to extend the HHRS to detection of cracks in plate structures. Then, the proposed approach will be tested through numerical simulations of a metallic plate with a breathing crack in order to assess the validity and the accuracy of the proposed damage detection technique.

4.1 HHRS: Beam vs Plate Structures

The HHRS technique presented in Chapter 2 relied on the phase information associated with the higher order harmonics carried by the elastic waves generated at the crack interface. The effect of reflected waves from the boundary conditions may have a detrimental effect on the accuracy of the estimated damage location. Proper sensor placement, as well as a specific data post-processing, was presented in order to limit the effect of reflected waves on the phase estimate. This approach was tailored to one-dimensional rod structures. One-dimensional structures behave as natural wave guides where the *travelling path* of the wave is always the same while only the *direction* is inverted after the reflection on the boundaries.

In a plate structure, elastic waves reflected on geometric boundaries create complex patterns that make the interpretation of the phase information more complicated. This chapter will concentrate on the development of a different approach which is more suitable for the application of the HHRS to 2D structures.

The damage localization technique presented hereafter still relies on the use of nonlinear structural dynamic concepts characteristic of a cracked structure. Although this technique uses the same physical principle, the way the data are processed and interpreted in order to spatially localize the defect is different from what was previously presented for slender structures. In the current approach the *principal angle* of the strain wave propagating from the crack interface at higher order harmonic frequencies will provide the key information to localize the crack.

Following the same approach of Chapter 2, a possible technique for the localization of wave sources in plate structures will first be presented. Then, this technique will be specialized to the case of breathing crack in order to exploit the information characteristic of a cracked structure.

4.2 Wave Source Localization in Plate Structures

The technique for damage localization in plate structure was synthesized merging the HHRS approach with a well known technique for the evaluation of the direction of propagation of elastic waves. This technique was presented and experimentally tested in the past by several researchers. Interesting applications used rosettes of piezoelectric sensors [99], Bragg fiber optic strain sensors [100,101] and Macro Fiber Composite transducers [102] to sense and extract the different strain components from the measured strain wave. In [102] the location of an external impact on anisotropic flat or curved plate structures was determined by using Macro Fiber Composite sensors in 120° configured rosettes. The main concept this technique relies on is the determination of the principal angle associated with the strain wave generated at the impact point. For the sake of completeness, this technique is briefly summarized hereafter in order to provide the reader with the necessary information to understand the HHRS technique in plates.

First assume that a flat plate experiences an impact occurring at an unknown location (Figure 4.1) and generates strain flexural waves (A_0 wave type) that propagate into the structure. When the wave fronts reach the location S1 and S2 where the strain sensors are located, the principal strain direction can be extracted by using an approach based on strain gauges in rosette configurations [99-102].

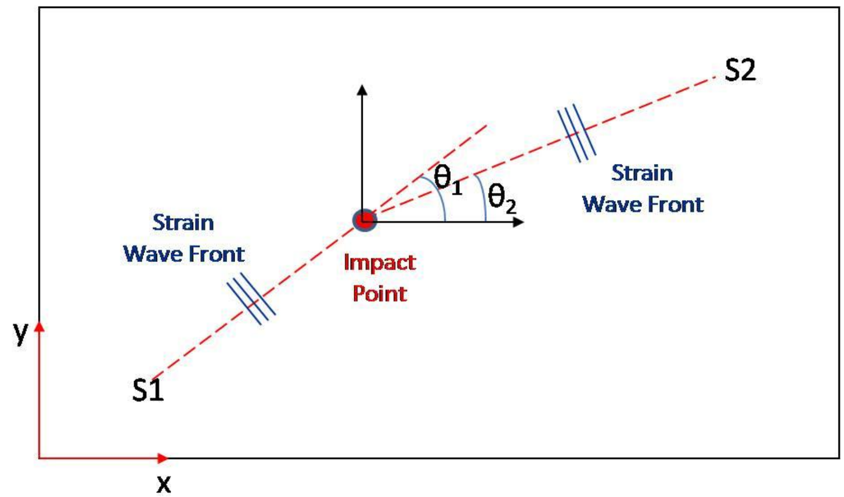

Figure 4.1. Schematic showing the localization technique of an unknown wave source in plate structures.

In the present study strain sensors in a rectangular configuration (0°/45°/90°), instead of a 120° as in Ref. [102], were used. This configuration is consistent with the hardware that will be used for the implementation of the Nonlinear Structural Surface Intensity presented in Chapter 8.

The principal direction of the wave can be determined by using the following relations:

$$\begin{aligned} \varepsilon_{x^*} &= \varepsilon_1 \\ \varepsilon_{y^*} &= \varepsilon_3 \\ \gamma_{x^*y^*} &= 2\varepsilon_2 - \varepsilon_1 - \varepsilon_3 \end{aligned} \tag{4.1}$$

where ε_1, ε_2 and ε_3 are the axial strains in the three strain gauges, ε_{x^*}, ε_{x^*} and $\gamma_{x^*y^*}$ are the normal and shear strains in the rosette reference system.

The principal angle can be calculated as:

$$\theta = tan^{-1} \frac{\gamma_{x^*y^*}}{\varepsilon_{x^*} - \varepsilon_{y^*}} \tag{4.2}$$

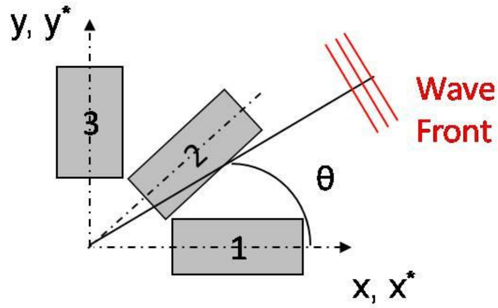

Figure 4.2. Strain sensor in 0°/45°/90° rosette configuration for the determination of the principal strain angle.

If the local reference system (x^*y^*) is aligned with the global reference system (xy), Eqns. (4.1) and (4.2) provide the principal components and principal angle of the strain wave in global coordinates.

The discontinuity at ±90° typical of the inverse tangent function can be solved by using a four-quadrant inverse tangent algorithm or, equivalently, the sign of the numerator and denominator of Eqn. (4.2).

When Eqns. (4.1) and (4.2) are applied to process the signals at sensor S1 and S2 the corresponding principal angles, θ_1 and θ_2, can be used to obtain the spatial origin of the wave source by triangulation. By defining the intersection between the straight line passing through the rosette centroid and having an angle equal to the principal angle, the wave source location is uniquely identified. This result can be achieved using the following simple set of equations [102]:

$$y_s = (x_s - x_1)tan\theta_1 + y_1$$
$$y_s = (x_s - x_2)tan\theta_2 + y_2 \quad (4.3)$$

where (x_s,y_s), (x_1,y_1) and (x_2,y_2) represent the coordinates in the global reference system of the source location and of the centroid of the two rosettes, respectively.

From Eqns. (4.3) the location of the wave source can be simply obtained by solving for x_s and y_s. When the two rosettes are aligned with the location of the wave source (i.e. θ_1=θ_2) the two lines do not intersect. This situation corresponds to a singular point of this algorithm and the source location cannot be calculated. This situation can be overcome by using more than two rosettes. In this way, a pair of rosettes for which Eqn. (4.3) is not singular always exists.

This technique is able to perform the source localization without requiring any information about the structure. As opposed to the HHRS in rods which needs an estimate of the phase velocity, this approach only relies on the evaluation of the principal angles (by calculation or measurements). This feature makes the presented approach suitable for damage detection in anisotropic structures where the phase velocity is also dependent on the direction of propagation.

4.3 Localization of a Breathing Crack in Plate Structures

The localization technique for elastic wave source (§4.2) can be extended to apply the higher order harmonic response signal to perform damage localization in plate structures.

Consider an aluminum plate with a breathing crack in an unknown location (Figure 4.3). When the structure is driven with an external in-plane excitation the alternating tensile and compressive stress state at the crack interface will force the crack to open and close. This periodic motion produces a series of impacts that generates elastic waves propagating into the structure. This is the same physical principle illustrated in Chapter 2 for the dynamic response of a cracked rod.

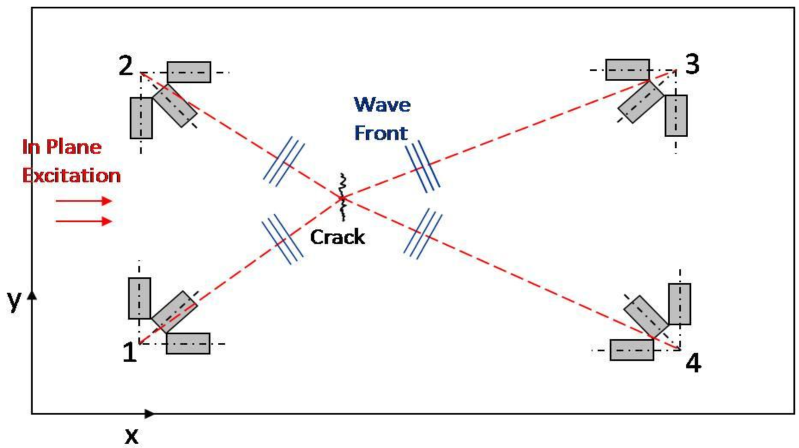

Figure 4.3. Schematic of a cracked plate with rosette of strain gauges for HHRS implementation.

Depending on the characteristic of the periodic interrogation signal (i.e. amplitude and frequency) either superharmonic and/or subharmonic signals can be generated at the crack interface. The localization technique, previously described, can be applied to the higher order harmonic components of the strain wave which are generated by the crack. The identified location will coincide with the spatial origin of the wave fronts at sub and super harmonic frequencies and, therefore, with the crack location.

According to this physical principle and based on Eqns. (4.1), (4.2) and (4.3), the formulation for extracting the principal angle at higher order harmonic frequency is:

$$(\varepsilon_{x^*})_k = (\varepsilon_1)_k$$
$$(\varepsilon_{y^*})_k = (\varepsilon_3)_k \qquad (4.4)$$
$$\left(\gamma_{x^*y^*}\right)_k = (2\varepsilon_2)_k - (\varepsilon_1)_k - (\varepsilon_3)_k$$

where the subscript k indicates the strain components corresponding to the *k-th* higher order harmonic.

In a similar way, the principal angle can be estimated from each higher order harmonic components as:

$$(\theta)_k = tan^{-1} \frac{(\gamma_{x^*y^*})_k}{(\varepsilon_{x^*})_k - \left(\varepsilon_{y^*}\right)_k} \qquad (4.5)$$

where θ_k is the principal angle associated with the *k-th* higher order harmonic.

Finally, Eqns. (4.4) and (4.5) can be used to evaluate the principal angle of the strain wave at nonlinear harmonic frequencies at two different locations. By triangulating between these two sensors the crack location can be found as:

$$(y_s)_k = ((x_s)_k - x_1)tan(\theta_1)_k + y_1$$
$$(y_s)_k = ((x_s)_k - x_2)tan(\theta_2)_k + y_2 \qquad (4.6)$$

where x_s and y_s are the Cartesian coordinates of the estimated crack location identified based on the harmonic of order k.

Eqn. (4.6) allows for the calculation of an estimated crack location from each higher order harmonic components generated by the crack. A very simple approach to combine this information is taking a linear average as follow:

$$x_s = \frac{1}{m}\sum_k x_k$$
$$y_s = \frac{1}{m}\sum_k y_k \tag{4.7}$$

where k indicates the order and m the total number of the higher order harmonics retained in the analysis. As pointed out in Chapter 2, a more effective approach for combining the information from the different harmonics is using a weighted average. The weight coefficients are then estimated by the β ratios (defined in Chapter 2 and 3).

To validate the proposed damage localization technique a numerical analysis is carried out by means of a finite element model of a damaged structure in order to generate the necessary input data for the localization algorithm.

4.4 Nonlinear Finite Element Model

The test structure used for the numerical evaluation of the proposed algorithm is constituted by an aluminum plate (*0.43×0.28×0.0015m*) with free-free boundary conditions and a single breathing crack (through the thickness with a total length of 0.02m).

The finite element model (Figure 4.4) is developed accordingly to the same procedure described in Chapter 2 for the nonlinear analysis on beam structures. The model is built with 3D hexahedral 8 noded linear elements (*0.009×0.009×0.00075m*). The breathing crack was modeled through nonlinear gap elements that allowed reproducing the opening/closing behavior of the crack. The strain gauges were simulated using 4 noded plate elements attached on the top of the plate. This allowed simulating a more realistic experimental condition where the strain sensors are effectively mounted on the top of the surface and, therefore, measure the surface strain.

The excitation is applied in the form of a time varying force on the top surface and in the in-plane direction. The excitation force has an amplitude *A=100N* at a frequency f_e*=20kHz*. At this stage, the frequency of the excitation is arbitrarily chosen. The model is solved for the nonlinear transient response up to the steady state using a time step *Δt=0.5μsec* (equivalent to a sampling frequency of *2MHz*) and for a total number of samples allowing a frequency resolution *Δf=50Hz*.

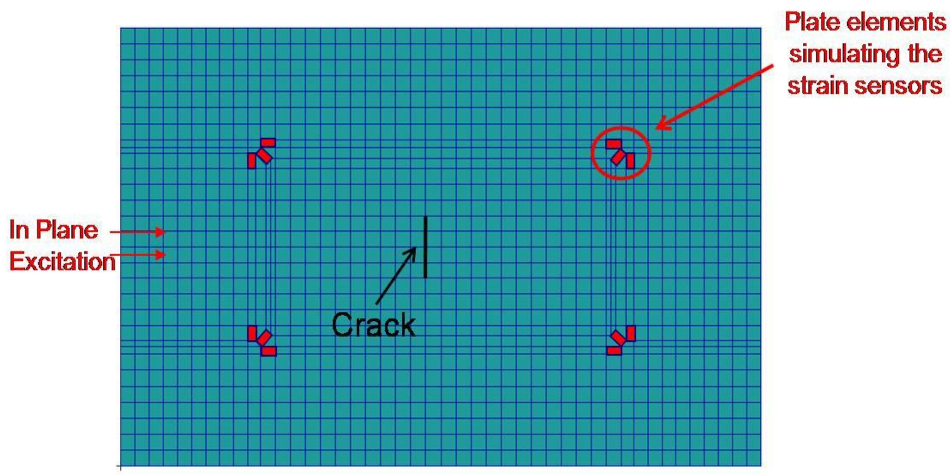

Figure 4.4. Finite element model of the plate structure showing the location of the rosette strain sensors and external dynamic excitation.

The nonlinear transient simulations require an intense computational effort. The frequency resolution and mesh size used in this study result from a trade-off between accuracy on one hand, and maximum time and calculation resources on the other. In finite element modeling, a widely accepted rule to assure the mesh convergence consists in choosing the element length comparable with quarter wavelength of the elastic propagating waves. Nevertheless, element size equal to half a wavelength can still be considered acceptable. In this last case, the model is still able to correctly capture the main structural response but yields a lower numerical accuracy. In the frequency range of interest (*10-80kHz*), the wavelengths associated with the first *Anti-symmetric* mode (*A0*) for the test structure are summarized in Figure 4.5. As a reminder, the mode *A0* is associated with bending waves, at different frequencies, having the same first order anti-symmetric displacement distribution through the thickness. For the current FE model, the wavelength is about twice (i.e. *2cm*) the finite element length at the $2f_e$ superharmonic frequency and decreases to about *1.3cm* at a frequency equal to $4f_e$.

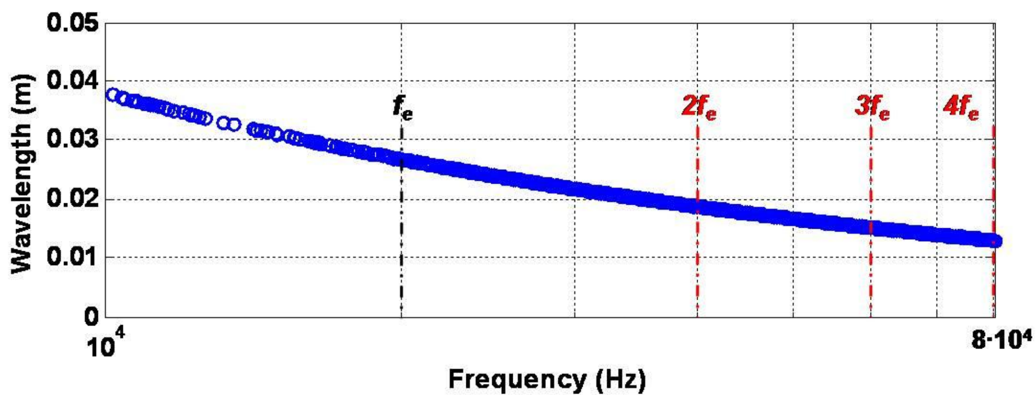

Figure 4.5. Characteristic wavelengths of the A0 mode for the considered plate structure.

A limited numerical accuracy can be expected from this mesh especially at the superharmonic $4f_e$. Nevertheless, the model is still able to capture the physics of the nonlinear system.

The numerical results proposed in this chapter are intended to support a feasibility study to extend the HHRS concept to plate structure. These results will not be used to assess the overall accuracy of the technique. The current FE model can therefore be considered acceptable for the current analysis.

4.5 Data Post-Processing

The dynamic response of the test structure is collected in terms of time history of the different strain components $\varepsilon_{ij}(t)$ at each one of the strain sensors. In particular, the term $\varepsilon_{ij}(t)$ represents the longitudinal strain measured by the *j-th* sensor belonging to the *i-th* rosette. The data processing approach is schematically summarized in Figure 4.6 to facilitate the understanding of the different operations involved in the HHRS damage localization.

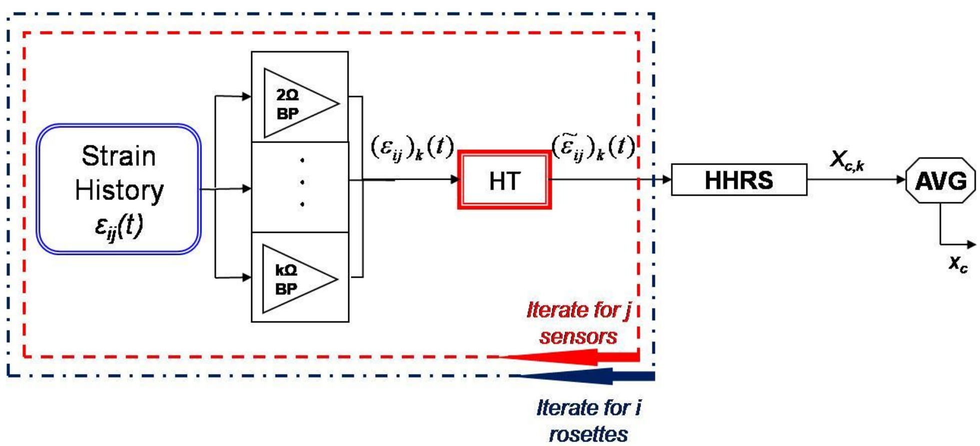

Figure 4.6. Schematic of the HT based data post processing technique for plate structures. The calculated strain components are bandpass filtered to extract the superharmonic components. The filtered signal is Hilbert transformed to get the amplitude envelope that is fed into the HHRS algorithm which yields the crack location.

Before processing the strain through Eqns. (4.4) and (4.5) to extract the principal angles, the strain time histories are processed through a Hilbert Transform (HT) in a similar fashion to what was done for a beam structure, in Chapter 2.

The signal is first processed through a series of digital bandpass (BP) filters centered around the superharmonic frequencies in order to isolate the different frequency components $\left(\varepsilon_{ij}\right)_k(t)$. Then, the filtered signals are processed through the Hilbert Transform to get $\left(\widetilde{\varepsilon_{ij}}\right)_k(t)$ that represents the amplitude envelopes versus time of the strain components at the harmonic of order *k*. Once the Hilbert transform of the filtered signals is calculated (for each strain component and superharmonic frequency) the time dependent signals are averaged over time to get the mean value of the strain amplitude $\langle\left(\widetilde{\varepsilon_{ij}}\right)_k(t)\rangle_t$. Finally, the mean strain values from each sensor and for each harmonic $\langle\left(\widetilde{\varepsilon_{ij}}\right)_k(t)\rangle_t$ are fed into Eqns. (4.4) and (4.5) that yield the prediction of the principal angle. These last two operations are performed in the block HHRS in Figure 4.6. At this stage, the crack location can be estimated using a pair of principal angle estimates for each superharmonic. This means that each superharmonic is, in principle, able to provide an estimate of the crack location.

Of course, the same considerations drawn in Chapter 2 about the β ratio and the quality of the response at higher order harmonic level apply to this technique as well. Therefore, not all the higher order harmonics will provide the same accuracy. Moreover, both the selection of the higher order harmonics and the averaging technique play again a dominant role in determining the overall performance of this approach.

4.6 Numerical Results

Numerical simulations were conducted in order to validate the HHRS technique for damage localization in plate structures. Seven different crack configurations and four rectangular rosettes of sensors were considered, as illustrated in Figure 4.7. Each configuration corresponds to a through the thickness breathing crack with a length $l_c = 0.02m$ in different locations. The structural response was collected at the four rosettes locations. The damage position was triangulated using the following pairs of rosettes *r1-r2*, *r2-r3*, *r3-r4*, *r4-r1*. The first three subharmonics ($2f_e$, $3f_e$, $4f_e$) were retained for damage localization.

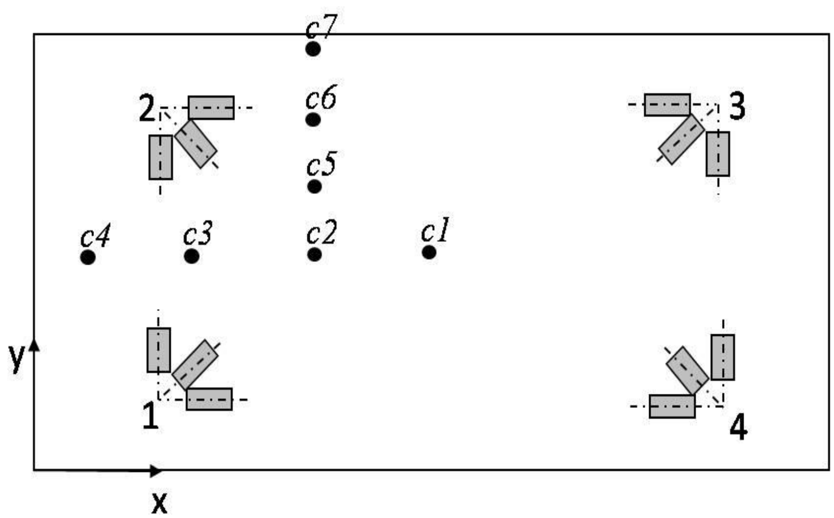

Figure 4.7. Schematic of the crack configurations used to validate the HHRS technique. Four rectangular rosettes of strain gauges are used to provide redundant data.

The comparison between the estimated versus the real locations yielded by the HHRS technique is summarized in Figure 4.8 and Table 4.1. At the prescribed excitation, the localization algorithm provides good predictions for the crack *c1* to *c4*. In these configurations, the damage is located on the mid-line at $y=0.1397m$. Errors on the estimate of the *y* coordinates are almost null while error lowers than *4.2cm* is associated with the *x* coordinates.

The estimate shows lower accuracy when considering the crack configurations *c5* to *c7*. Although *c6* is predicted with good accuracy, *c5* and *c7* show a consistent error on one of the two coordinates. Two possible reasons were identified to explain this increase in the absolute error.

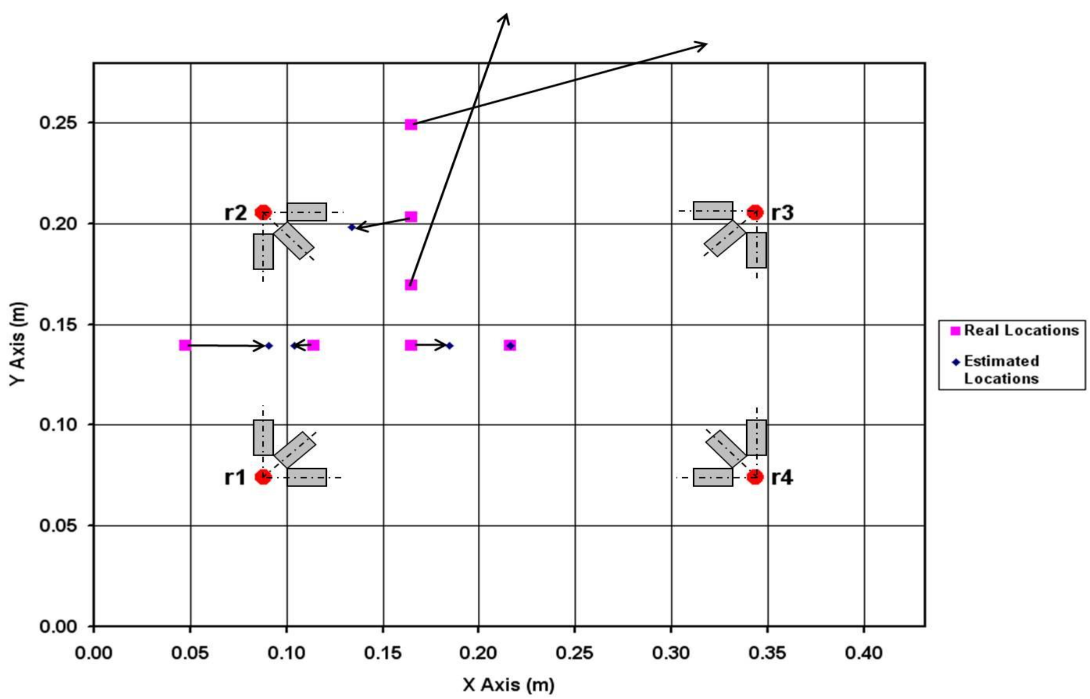

Figure 4.8. Summary of the estimated crack locations for the different damage configurations. The arrows provide the association between real and estimated locations.

The first reason is related to the limited resolution of the structural mesh. This aspect was already introduced in §4.4 and is confirmed by the numerical results. Note that configurations *c1* to *c4* are on the symmetry line of the plate at *y=const* and are also symmetric with respect to the rosettes pairs selected for the triangulation. In this case, the error on the estimate of the *y* coordinate will be equal in magnitude and opposite in sign for the pair r1-r2, r3-r4 and r2-r3, r4-r1. When combining the information from the different rosettes, the errors on the estimate of the *y* coordinate will be automatically averaged out. This explains why the *y* coordinate is accurately estimated for *c1* to *c4* while the *x* coordinates and the configurations *c5* to *c7* are associated with larger errors.

Table 4.1. Estimated crack locations and absolute errors associated to the different coordinates.

	Real Location (m)		**Estimated Location** (m)		**Absolute Error** (m)	
	X_R	Y_R	X_E	Y_E	ΔX	ΔY
c1	0.2159	0.1397	0.2159	0.1397	0.0	0.0
c2	0.1651	0.1397	0.1846	0.1397	0.019	0.0
c3	0.1143	0.1397	0.1038	0.1397	-0.011	0.0
c4	0.0476	0.1397	0.0904	0.1397	0.043	0.0
c5	0.1651	0.1696	0.2070	0.3951	0.042	0.225
c6	0.1651	0.2031	0.1335	0.1985	-0.032	-0.005
c7	0.1651	0.2488	0.3394	0.3387	0.174	0.090

A second important source of error is related to the accuracy of the principal angle estimate. Strain sensors in rosettes configurations are prone to different sources of error [103]. An important parameter is the misalignment of the principal strain axis with the axis of strain measurements. If an estimate of the principal axes direction was known "a priori" the strain gauges could be oriented accordingly to yield the maximum accuracy. Nevertheless, strain gauges in rosettes configurations are generally used to determine principal axes. In this case, their orientation cannot be set "a priori" to maximize the accuracy.

The importance of the misalignment error varies with the specific rosette configuration. Two of the most popular configurations, the rectangular and the delta, are shown in Figure 4.9.

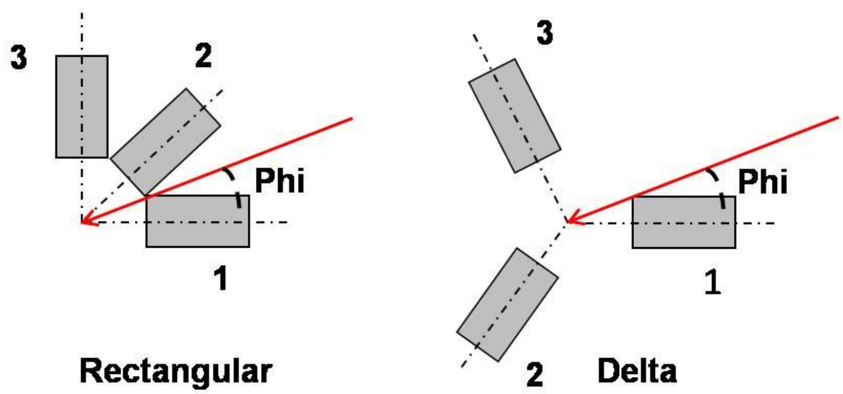

Figure 4.9. Sensors layout for rectangular and delta strain gauge rosette configurations.

The angle *Phi* (Figure 4.9) indicates the orientation of the principal axes with respect to the strain measurement axes. If the actual value of the angle (associated with a simulated strain wave) is plotted versus the measured angle for a $0°$-$90°$ range, the performance of the two configurations can be compared in terms of misalignment error. The results of this test are shown in Figure 4.10. The rectangular rosette has a good accuracy in a range $20°$-$70°$ but generates an error $\varepsilon_{0,90}=11.5°$ when the principal axis is parallel either to sensor 1 or 3. The delta configuration, instead, has $\varepsilon_{0,90}=0°$ and a maximum error of $\varepsilon_{max}=4.4°$ in the intermediate range. It results that the delta configuration would be probably the most appropriate configuration for the HHRS application.

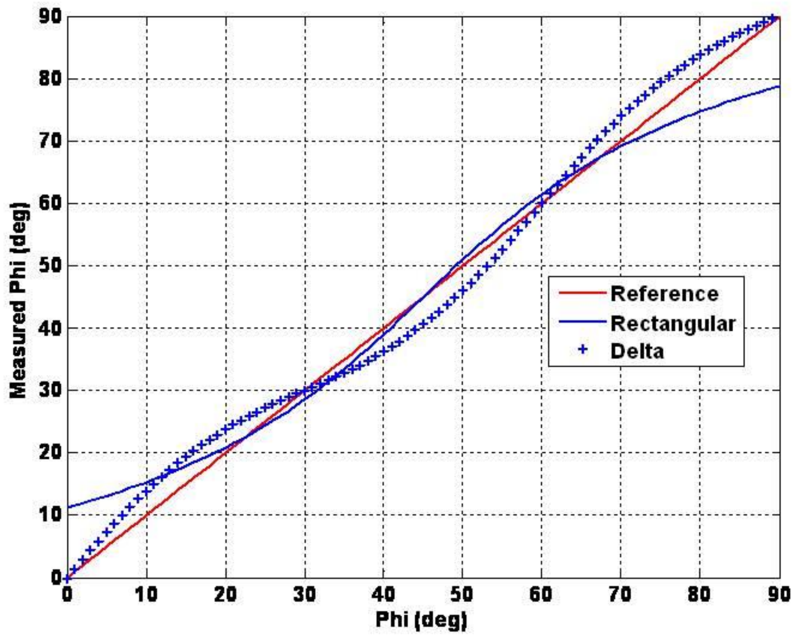

Figure 4.10. Misalignment error between the principal axes and the strain measurement axes.

The effect of the misalignment error on the estimated crack location can be shown with a simple example. Consider the case illustrated in Figure 4.11 where the damage is in configuration *c6* and only the rectangular rosette pair r1-r2 and r2-r3 are used for the triangulation. Two different results are compared.

The first result is based on the assumption of an ideal condition where the strain measurements were free of error. In this case the only error affecting the estimate of location *c6* will be the misalignment error. Under this condition, damage *c6* is at 59° with r1 and at 0.7° with r2 and r3. Once the strain measurements are processed to get the principal angle, the result will be affected by the misalignment error. According to Figure

4.10, r1 will be affected by a 1.5° error while r2 and r3 will read about 11° error. If the damage location is triangulated using the resulting angle from r1-r2 (Figure 4.11, *r12 plus err*) and r2-r3 (Figure 4.11, *r23 plus err*) the resulting estimated location (Figure 4.11, *average*) will have a *2cm* absolute error on both the coordinates. This example shows that, even with ideal measurements, the error introduced by the rectangular rosette is not negligible.

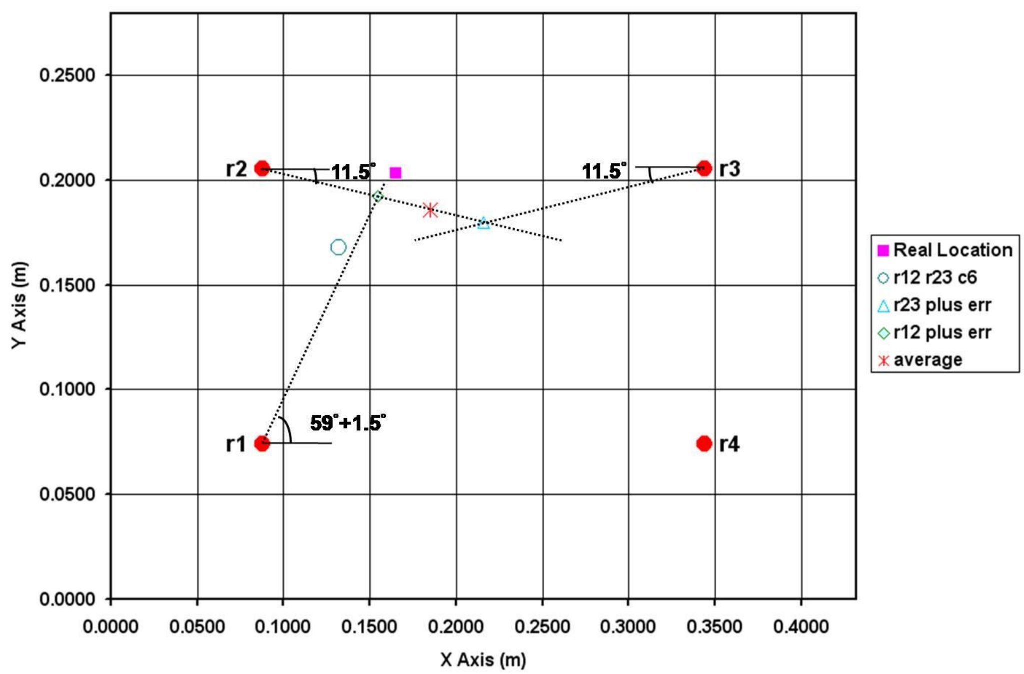

Figure 4.11. Effect of the misalignment error on the estimated crack location.

The second result shown in Figure 4.11 is the *c6* location (Figure 4.11, *r12 r23 c6*) estimated by using HHRS numerical data from *r1-r2* and *r2-r3*. This result has about *4cm* error on both coordinates. Comparing the two results it can be seen how the misalignment error, for this specific case, is about 50% of the absolute error on the HHRS estimate.

In conclusion, the numerical results show the validity of the HHRS approach for the detection of nonlinear fatigue crack in plate structures. Five out of seven configurations were correctly identified with a maximum absolute error of *4cm*. Due to the described numerical approximations and limitations these results are not suitable to assess the overall accuracy of this technique. Nevertheless, previous considerations provide useful guidelines for improving the numerical results and obtaining meaningful data for estimating accuracy and sensitivity.

4.7 Summary

This chapter presented a feasibility study on the HHRS damage localization technique applied to plate structures. The same physical principle, presented in Chapter 2, associated with the nonlinear response of fatigue cracks was exploited for damage detection purposes. A different data post processing technique, more suitable for feature extraction in bi-dimensional dispersive systems, was illustrated. This technique relies on principal strain angle measurements collected at higher order harmonic frequencies. The elastic strain wave generated at the crack interface was collected at discrete locations through strain gauges in rosette configurations. The principal angle was extracted and the damage location was determined by triangulation between two or more rosettes. The HHRS technique was validated through numerical simulations performed by means of a nonlinear FE model of a cracked plate. Results confirmed the detection capability of the HHRS technique and its capability to localize the fatigue crack by using a baseline-free and completely model-free approach. The technique presented in this chapter allowed eliminating the dependence on the phase velocity estimate which was needed, instead, in the HHRS formulation for slender structures.

Useful guidelines for the selection of an appropriate strain gauge rosette configuration to reduce the misalignment error were also provided.

CHAPTER 5

Structural Intensity and Power flow for Structural Damage Detection

As stated in Chapter 1, two different damage detection techniques were investigated in this work. The second technique presented in this research is based on the application of the Structural Intensity (SI) concept as a possible tool for damage detection in complex structures.

The concept of Structural Intensity (SI), which is power flow per unit area, has been extensively used in the past to determine the dominant paths of energy flow associated with the propagation of elastic waves in a mechanical system [104,105]. Structural Intensity was initially exploited as an effective parameter to design structural noise and vibration control systems for mechanical and aerospace structures.

The use of SI for structural damage detection applications is a relatively new concept. Since SI is a vector quantity (defined by magnitude and phase), it provides potential advantages over other frequency based damage detection techniques which generally exploit only changes in vibration magnitude. Previous work performed at the Pennsylvania State University Applied Research Laboratory (PSU/ARL) suggests that

Structural Intensity might be used as an effective tool for damage detection applications [105-107]. In this research the SI concept will be applied to formulate a possible damage detection technique for application on rotorcraft airframes.

In order to provide the reader with the necessary theoretical foundation for understanding the proposed technique, a short review of the main analytical relations and numerical models already existing in the literature will be presented. Then, the results from a parametric study will highlight the effects of key parameters on the SI field. This study is intended to build the necessary background to understand the relation between damage and SI distribution.

The results from a vibration test conducted on a UH-60 transmission frame will also be illustrated and used to refine the damping levels used in the SI simulations. A possible metric for feature extraction will be presented. The concept of Total Transmitted Power will be introduced as a mean to correlate the damage characteristics to the changes produced in the SI field.

This chapter will conclude by presenting a damage localization technique applicable to linear type of defects (open cracks, ballistic impacts). The presented technique exploits the metric previously introduced to identify the damage location in plate structures.

5.1 SI Theoretical Background

Structural intensity (SI) is a vector field, described by magnitude and phase, which indicates the path and the amplitude of the mechanical energy flowing through a vibrating structural component. The location where the mechanical energy enters the structure is generally called the *Energy Source*. The location where the energy is extracted from the system is called the *Energy Sink*. Multiple energy sources and sinks might coexist in the same structure. Aerodynamic loads, propulsion system, rotor and gearboxes, and auxiliary power units are some examples of external and internal sources of excitation. In a similar fashion, vibration isolation systems, structural joints, and structure-fluid coupling are examples of energy dissipation mechanisms.

In order to illustrate the characteristics of the proposed damage detection technique, only one pair of energy source and sink will be used in this study in order to produce a well defined energy flow through the structure. This assumption allows for a more intuitive analysis of the numerical and experimental results without inducing any loss of generality.

From a general point of view, the structural power is defined as the active part associated with the vibration energy. In analytical terms, the power is represented by the time averaged product of a force with the in-phase component of the velocity in the direction of the force. Considering the harmonic response solution for a structure excited by an external periodic force, the power at a prescribed point can be calculated in the following way:

$$P = \frac{1}{2} Real[Fv^*] \tag{5.1}$$

where F is the applied force and v^* is the complex conjugate of the velocity both taken at a prescribed point in the structure. Eqn. (4.1) is equivalent to considering the dot product between the force F and the velocity v.

The structural intensity is defined as the power per unit area A or, equivalently, the stress σ multiplied by the complex conjugate of the velocity. In analytical terms:

$$I = \frac{P}{A} = \frac{1}{2} Real\left[\frac{F}{A} v^*\right] = \frac{1}{2} Real[\sigma v^*] \tag{5.2}$$

The calculation of the structural intensity field in thin plates has been the subject of different studies over the past years [108-110]. The total intensity in a thin vibrating plate (Figure 5.1) is due to the combined action of shear, bending, and twisting waves and can be expressed in their orthogonal components as:

$$I_x = \frac{\langle Q_x \dot{w} \rangle_t + \langle M_x \dot{\theta}_y \rangle_t - \langle M_{xy} \dot{\theta}_x \rangle_t}{h} = I_x^s + I_x^b + I_x^t$$

$$I_y = \frac{\langle Q_y \dot{w} \rangle_t - \langle M_y \dot{\theta}_x \rangle_t + \langle M_{xy} \dot{\theta}_y \rangle_t}{h} = I_y^s + I_y^b + I_y^t \tag{5.3}$$

where the superscripts s, b and t represent the shear, bending and twisting components, the subscript t indicates a time averaged quantity and h is the thickness of the plate.

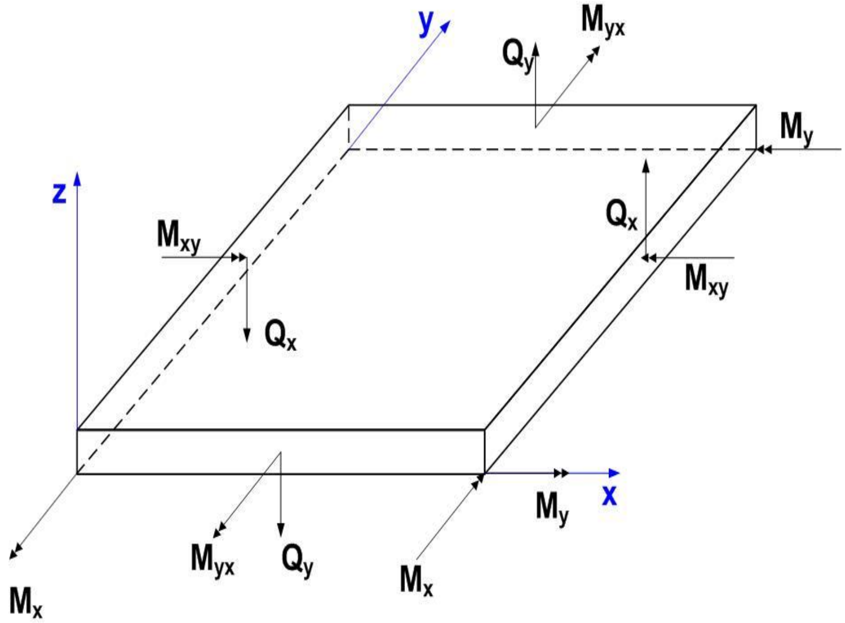

Figure 5.1. Plate differential element showing the sign convention for forces and moments.

The moments (M_x, M_y and M_{xy}) and shear forces (Q_x and Q_y) for thin plates can be expressed in terms of spatial derivatives as follow:

$$M_x = D\left(\frac{\partial^2 w}{\partial x^2} + \upsilon \frac{\partial^2 w}{\partial y^2}\right) \qquad M_y = D\left(\frac{\partial^2 w}{\partial y^2} + \upsilon \frac{\partial^2 w}{\partial x^2}\right)$$

$$M_{xy} = M_{yx} = D(1-\upsilon)\frac{\partial^2 w}{\partial x \partial y} \tag{5.4}$$

$$Q_x = D\frac{\partial}{\partial x}(\nabla^2 \mathrm{w}) \qquad Q_y = D\frac{\partial}{\partial y}(\nabla^2 \mathrm{w})$$

where w is the out-of-plane displacement, D is the flexural rigidity, υ is the Poisson's ratio and ∇^2 is the Laplacian.

The rotational velocities $\dot{\theta}$ are calculated as follow:

$$\dot{\theta}_y = \frac{\partial \dot{w}}{\partial x} \qquad\qquad \dot{\theta}_x = \frac{\partial \dot{w}}{\partial y} \tag{5.5}$$

where $\dot{w}$ indicates the time derivative of the out of plane displacement.

By combining Eqs. (5.3) and (5.4) an expression for the structural intensity in terms of spatial derivatives can be obtained.

Once the SI components are calculated for the two coordinate directions the total structural intensity is simply given by:

$$I = I_x \hat{\imath} + I_y \hat{\jmath} \tag{5.6}$$

Remembering that the structural intensity is a power per unit area, it is measured in W/m^2.

5.2 SI Features Identification for Damage Detection Technique

Structural Intensity was used for several years as a tool for the design of vibration and noise control systems. Only in recent years have researchers investigated its potential as damage detection technique. The initial investigations concentrated on beam structures [111] and power system gearboxes [106] by using a purely data-driven approach. In these preliminary studies, a structural intensity baseline signature, acquired on the healthy structure, was compared with the SI signature of the damaged structure in order to perform the health assessment. Although the SI based SHM system belongs to the "frequency-based" methodologies, it presents some new interesting features with respect to the standard techniques in this category. The SI is a vector field which is described by magnitude and phase (or, equivalently, amplitude and direction). When compared with standard frequency-based techniques that generally compares only changes in magnitude, the SI provides a better insight into the damage effects. An experimental analysis providing a structural damage assessment in terms of SI amplitude and phase changes is described in [112].

One of the goals of this research is to develop a theoretically driven approach for extracting features relevant to the damage from experimentally acquired data. For this reason, the emphasis in this chapter will be on developing a new metric to evaluate the effect of the damage.

5.2.1 Power Flow through Control Surfaces

When the power flow is estimated through numerical simulations or experimentally evaluated by means of a finite differencing scheme, the power distribution can be evaluated over the whole structure providing what are referred to as *SI maps*.

When considering real structures in operating conditions, the number of measurement points available for the SI estimate is very limited. The structural intensity can be calculated only at a discrete number of points which does not allow for the reconstruction of a detailed intensity field throughout the entire structure. In order to assess the structural integrity, a damage detection strategy must be derived in order to relate the changes in the power flow at the measurement points with the characteristics of the damage. The approach proposed in this work is based on measuring the power flow through prescribed Control Surfaces (CS) and relating these changes to the presence (Level 1), location (Level 2a) and extent (Level 3) of the defect.

A control surface is defined as an arbitrary opened or closed surface, delimited by a prescribed number of sensors (generally strain sensors), whose equivalent area is used to integrate the SI in order to get the total mechanical power flowing through it.

In a plate structure, where the stress distribution is assumed to be constant through the thickness, the SI can be easily integrated over the control surface by knowing the stress/strain and velocity distribution on the surface of the plate.

Figure 5.2 shows a possible definition for the control surfaces in a plate structure where two surfaces, labeled Contour 1 and 2, have been defined around the energy source and sink.

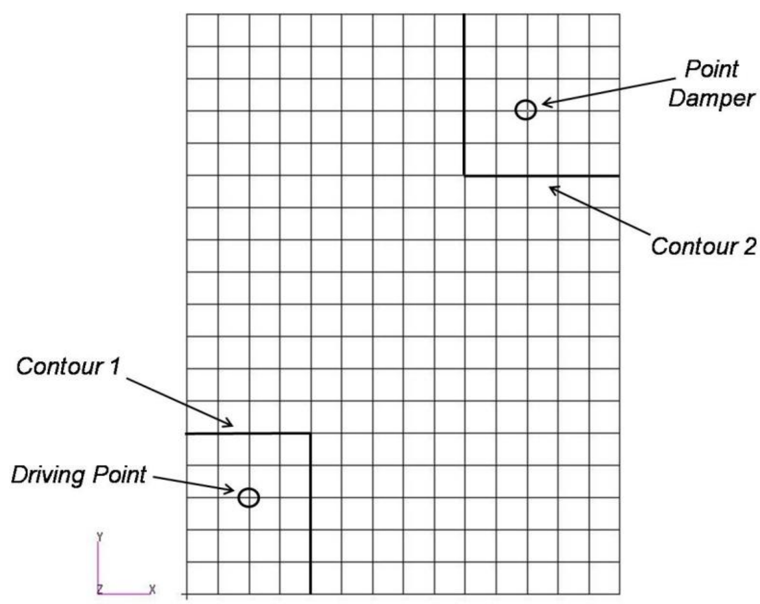

Figure 5.2. Definition of control surfaces for power flow calculations.

For damage identification purposes, we generally define the control surfaces around the energy source and sink. For the sake of simplicity, the control surface around the energy source will be indicated, from now on, as control surface 1 (CS1) while the surface around the energy sink will be labeled as control surface 2 (CS2). Given this configuration, we define the Total Transmitted Power (TTP) as the fraction of power measured at the control surface 2 relative to a given input power at the control surface 1, i.e.:

$$TTP(\omega) = \frac{P_{CS2}(\omega)}{P_{CS1}(\omega)} \tag{5.7}$$

where P_{CS1} and P_{CS2} indicate the power integrated over the control surface CS1 and CS2, respectively.

From a physical point of view, the TTP represents the efficiency of the energy transfer mechanism between two structural points. Although the control surfaces can be defined anywhere in the structure, it is advisable to locate them around the energy source and sink. As will be subsequently clarified, the SI based damage detection technique exploits the changes in the transmitted power to detect the presence and the location of incipient damage in the test structure. To maximize the sensitivity of the technique to a structural damage, the control surfaces must be chosen in order to optimize the TTP measurements.

5.2.2 Finite Element Model based SI calculation

A preliminary assessment of the damage detection capabilities of the SI based SHM was based on numerical simulations of SI maps in both healthy and damaged structures. The procedure used in this work to simulate the SI field in a mechanical system was based on tools available at the PSU-Applied Research Laboratory (ARL) and were specifically developed for SI applications.

The procedure relies on the use of a Finite Element (FE) model of the test structure. The model is solved for its frequency response characteristics allowing for the calculation of the stress and velocity fields needed for the SI estimate. This set of data is then fed into McPow [113] (i.e. M*echanical* Pow*er*) which is a specific in-house code for Structural Intensity calculation. In this work, the commercial software MSC-NASTRAN was used to perform the finite element analysis. The block diagram shown in Figure 5.3 summarizes the data flow for the FE based calculation of the SI.

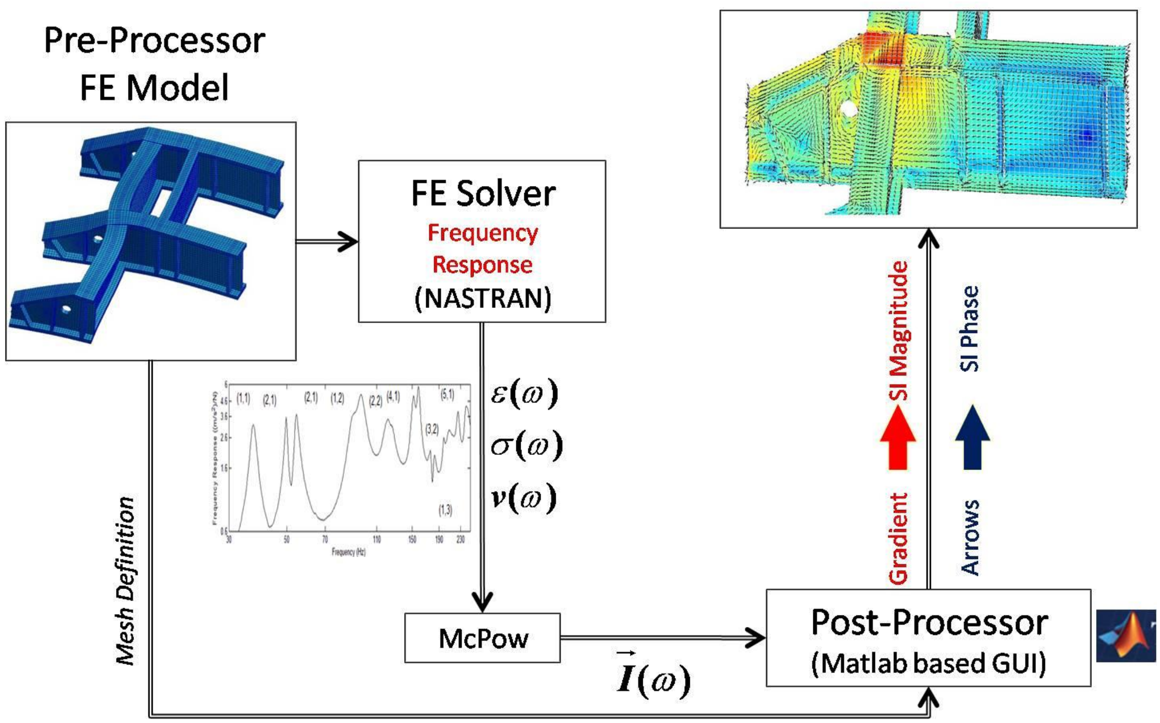

Figure 5.3. Schematic of the FE based SI calculation. The combination of commercial FE solver with McPow allows solving for the SI maps on “virtually” any kind of structure.

5.2.2.1Test Structure and FE Model

The test structure retained for the numerical and experimental investigations was a rectangular 6061-T651 aluminum plate (35”×23”×0.1”).

A 2D finite element model using linear 4-noded shell elements was developed, as shown in Figure 5.2. The mesh grid size was 0.04×0.04 cm which yielded 18×14 elements. This mesh size represented the reference solution for the following analyses and was chosen to exactly meet the experimental grid size that was used for the SI experimental measurements (Appendix A).

The plate model was constrained through pinned boundary conditions which were found to provide a reasonable approximation of the experimental boundary conditions. The energy sink was simulated through one viscous damper element (CDAMP2) acting in the out-of-plane direction. The external excitation was provided through an out-of-plane sinusoidal force.

Unless otherwise specified, the linear frequency response of the plate model was calculated using a frequency sweep from 100Hz to 1kHz. An example of the SI map associated to the fundamental mode (1:1) is shown in Figure 5.4. The colors describe the amplitude of the SI on a dB scale. The unit arrows describe the flow direction.

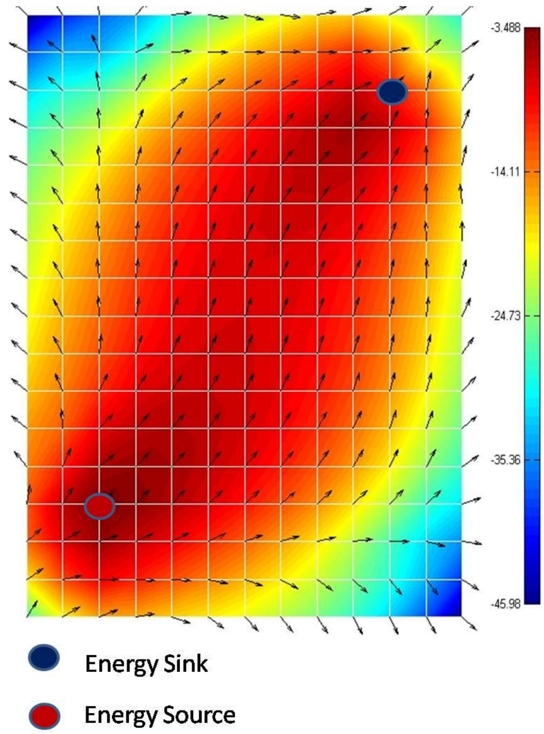

Figure 5.4. Example of SI map for the fundamental mode (1:1) obtained through the FE based approach.

5.2.3 Role of the Energy Source and Sink Location

In order to establish a clear energy path into a vibrating structure, an energy source and sink pair must be present. The energy injected into the system will flow from the energy source to the energy sink following a path influenced by two main parameters:

1. Relative location of the energy source/sink pair.
2. Mode shape excited by the external dynamic load.

The effect of the mode shape will be analyzed in the next paragraph. If there is no energy sink defined in the structure, the injected energy will reverberate in the system following a random path. On the contrary, when a dominant energy sink is present the vibrational energy flows towards the energy sink following a very clear path. The effect of the energy source/sink pair location on the power flow is shown in Figure 5.5.

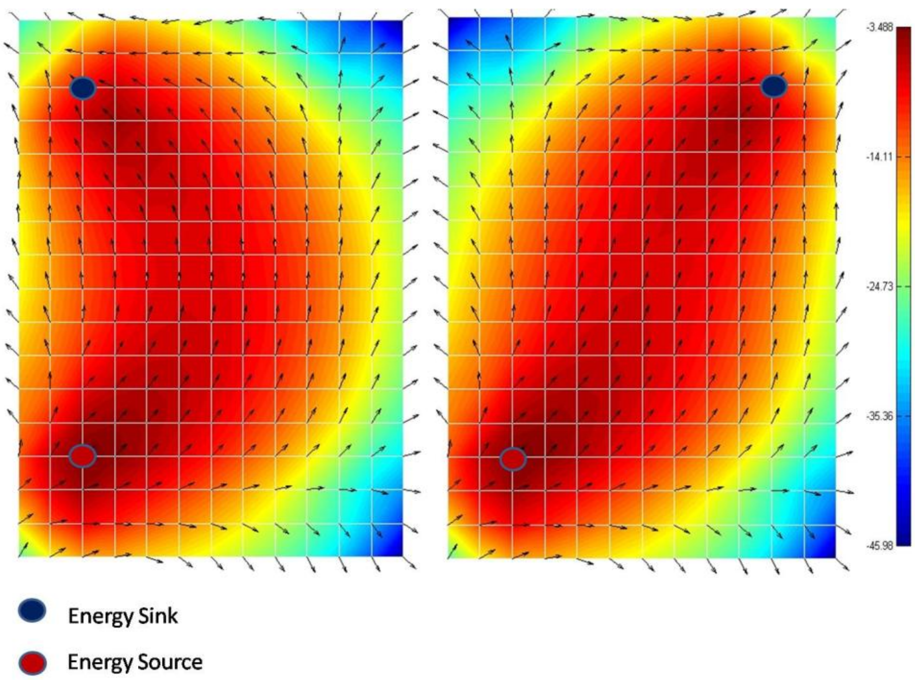

Figure 5.5. Effect of the energy sink location on the SI path. The relative location of the energy source/sink pair contributes to shape the energy path.

The two SI maps are calculated using the same numerical parameters (input power, energy source location, excitation frequency, etc.) with the only exception being the energy sink location. It is clearly visible how the energy source/sink location plays a major role in shaping the power flow.

5.2.4 Role of the Resonance Frequencies

The second parameter which strongly affects the SI distribution in a vibrating structure is the resonance frequency or, equivalently, the mode shape excited by the external dynamic load.

From the analytical expression of the mechanical power, it appears that the component of the velocity in phase with the force at a prescribed grid point has a strong contribution to the power amplitude. It can be expected that the energy flow is shaped to follow the peak of the mode shapes which are associated with the highest velocity components.

Figure 5.6 shows the effect of the frequency on the SI distribution for two different mode shapes. Note that the SI path follows the peaks of the mode shapes and is considerably reduced around the main nodal lines.

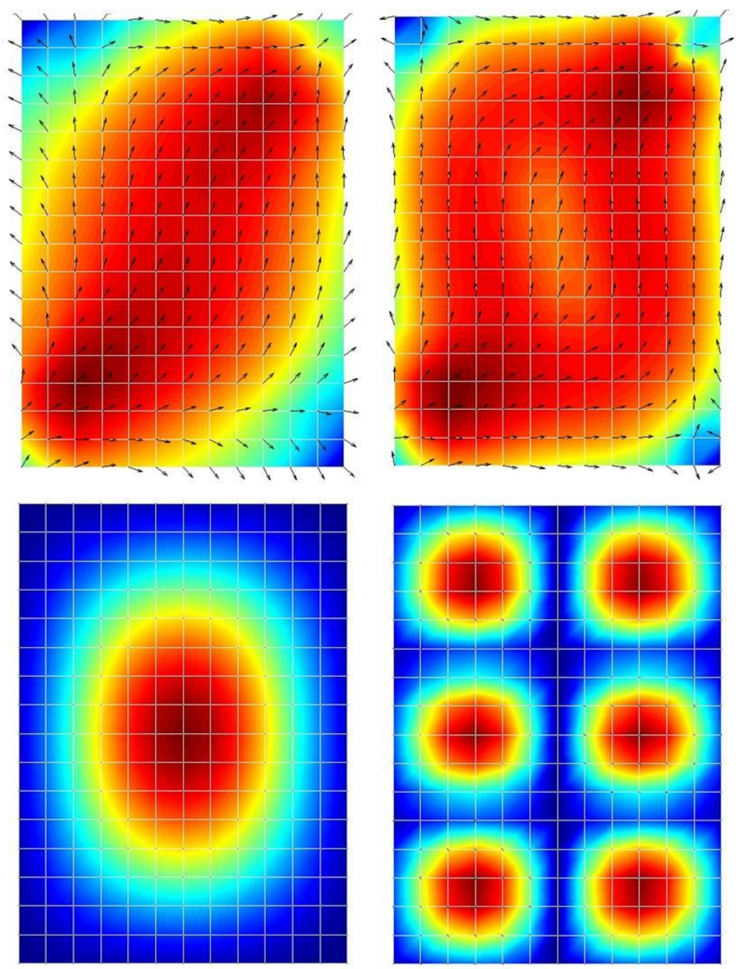

Figure 5.6. Effect of the resonance frequency on the SI path; (top) SI maps, (bottom) associated mode shapes.

This is a typical trend for power flow generated by bending waves. In this case, the maximum power is localized in areas with high mobility, i.e. far from nodal lines. It could be shown that the trend for power generated by shear waves follows, instead, an opposite trend.

5.3 UH-60 Transmission Frame Vibration Test

In §5.4.1 it will be shown in detail how the damping levels characteristic of the test structure affect the identification of the energy path and the sharpness of its gradient. A good resolution of either the energy path or the gradient can be obtained through proper tuning of the energy sink, even in the presence of high material loss factors. It must be kept in mind, however, that lower total transmitted power corresponds to higher dissipation levels.

A clear assessment of the damping effects as well as the expected damping levels on a representative airframe structure is crucial to further develop the SI based SHM for rotorcraft structure applications.

In an effort to derive possible ranges of interest for the different SI functional parameters with reference to a specific application on a helicopter transmission frame, a sensitivity study was performed using experimental loss factors representative of the helicopter frame.

The experimental loss factors were acquired conducting a static vibration test on a UH-60 transmission frame. The schematic of the test structure is shown in Figure 5.7. The transmission frame is that part of the helicopter airframe which supports the propulsion system constituted by the gearbox, the engine and the rotor assembly. The propulsion system is connected to the transmission frame through four attachment points. The vibrational energy, produced by the engine during the operating condition, flows through these attachment points into the transmission frame creating areas with high stress concentration at the Frame Station (FS) joints. This severe loading condition results in a propensity to develop fatigue cracks in proximity of the transmission joint.

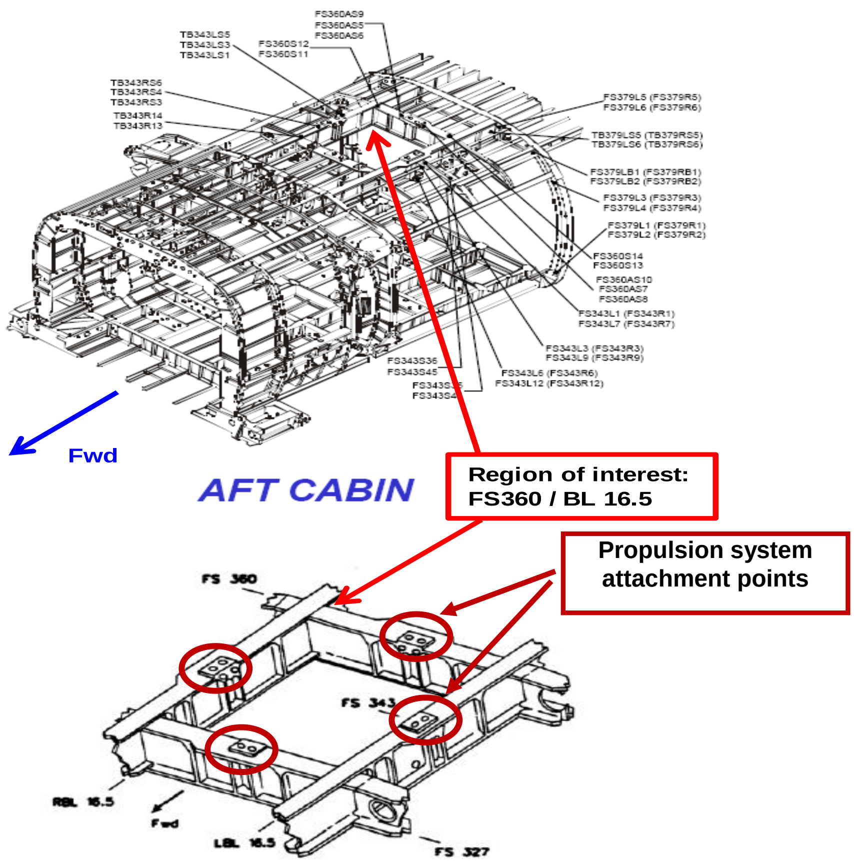

Figure 5.7. Schematic of the UH-60 transmission frame; (Upper) fuselage section showing the transmission frame location, (lower) detailed view of the transmission frame joints and propulsion system attachments.

5.3.1 UH-60 Experimental Loss Factors

The main results obtained from the experimental modal testing of the UH-60 transmission frame during a ground (static) modal test are briefly summarized. The xy in-plane response as well as the z vertical response were evaluated through a roaming hammer test. Four reference accelerometers and fourteen total excitation points were used for the xy (in-plane) direction. Five reference accelerometers (indicated by the number between brackets) and a total of fifteen hit points were used for the z (out-of-plane) direction. An example of the accelerometer layout for the measurements in the z direction is shown in Figure 5.8.

Using the reciprocity concept, the response in correspondence to the hit points was extracted. The low frequency modal loss factors were calculated using a rational fraction polynomial approach implemented in an in-house code.

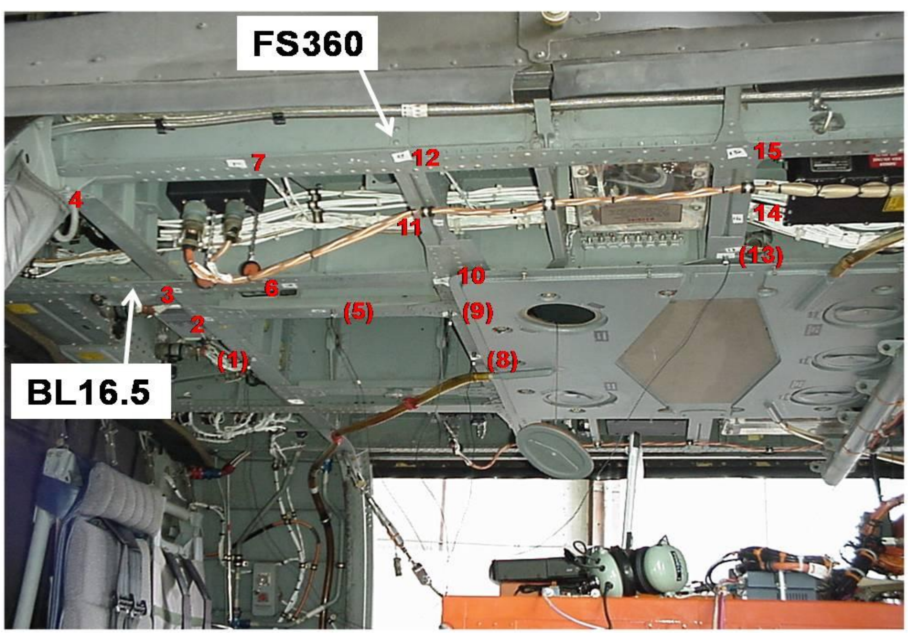

Figure 5.8. Accelerometers layout for the vibration measurement in the vertical direction.

The high frequency band averaged loss factors were also calculated based on the *Decay Rate* (*DR*) approach according to the following relation:

$$\eta_{decay} = \frac{DR}{27.3\, f_0} \tag{5.8}$$

where *DR* is the band decay rate in dB/sec and f_0 is the one third octave band center frequency. The acceleration response, obtained as an average over five decay envelopes (Figure 5.9), where used to estimate the decay rate based loss factors.

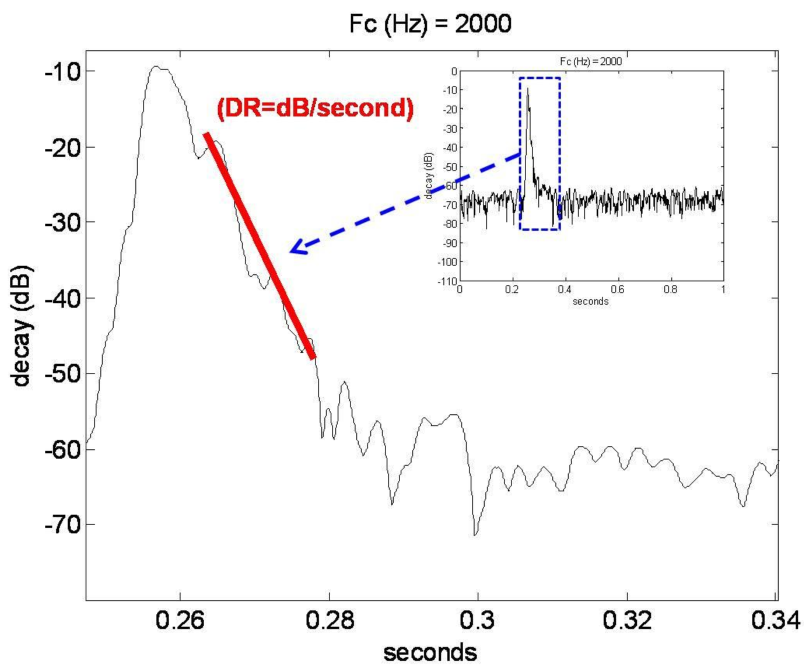

Figure 5.9. Example of decay time envelope used to estimate the decay rate and the associated damping loss factors.

The experimentally identified loss factors estimated in a bandwidth from 0-10kHz are summarized in Figure 5.10. It can be observed that in the low frequency range (100-1000Hz) the measured loss factors range between 0.01 and 0.075. This key information will be used later on in the sensitivity study.

The mobility was also calculated from the measured frequency response function between the driving force F and the acceleration A according to the following relation:

$$Mobility = \left(\frac{1}{2\pi f}\right)\left(\frac{A(f)}{F(f)}\right) \tag{5.9}$$

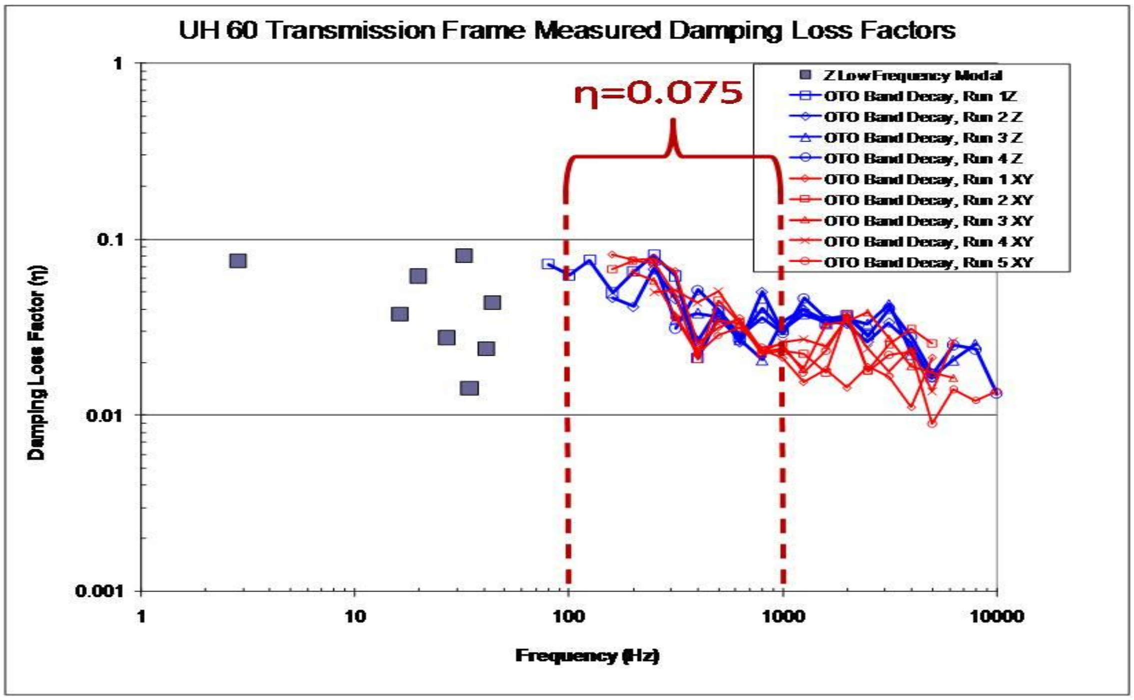

Figure 5.10. UH-60 transmission frame experimental damping loss factors. The loss factors in the frequency band 100-1000Hz range between η=0.01÷0.075.

The impact force was applied, in the vertical direction, at locations 3 and 11 while the response accelerations were collected at locations (1,5,8,9,13). The experimental results are summarized in Figure 5.11 along with the correspondent mode shapes that are visualized using a 2D visualization mesh. The vertical dotted lines indicate the occurrence of the main rotor rotational frequencies and harmonics.

Many resonance peaks of the transmission frame are visible in the mobility plot at low frequency. It is interesting to notice that most of these peaks are associated with a vertical displacement concentrated in the areas either inboard or outboard from the region of interest. These displacements will produce bending stresses at the transmission joints that might be among the possible causes for the initiation and propagation of fatigue cracks. Further details on the UH-60 vibration test can be found in [114].

5.4 Sensitivity Study

The first step in developing a SI based damage detection technique was improving the understanding of the mechanism relating the changes in the power flow to the characteristics of the damage.

For this reason, a clear assessment of the effects of numerical and experimental parameters used to evaluate the SI maps must be performed. This operation was carried out through a numerical sensitivity study where the SI distribution was calculated using the procedure described in §5.2.2. The Total Transmitted Power was used as a possible parameter to monitor changes in the structural response due to the presence of the damage.

Based on general observations related to the physical mechanism controlling the SI distribution, the following classes of parameters were investigated:

1. Structural parameters
2. Numerical/Experimental parameters

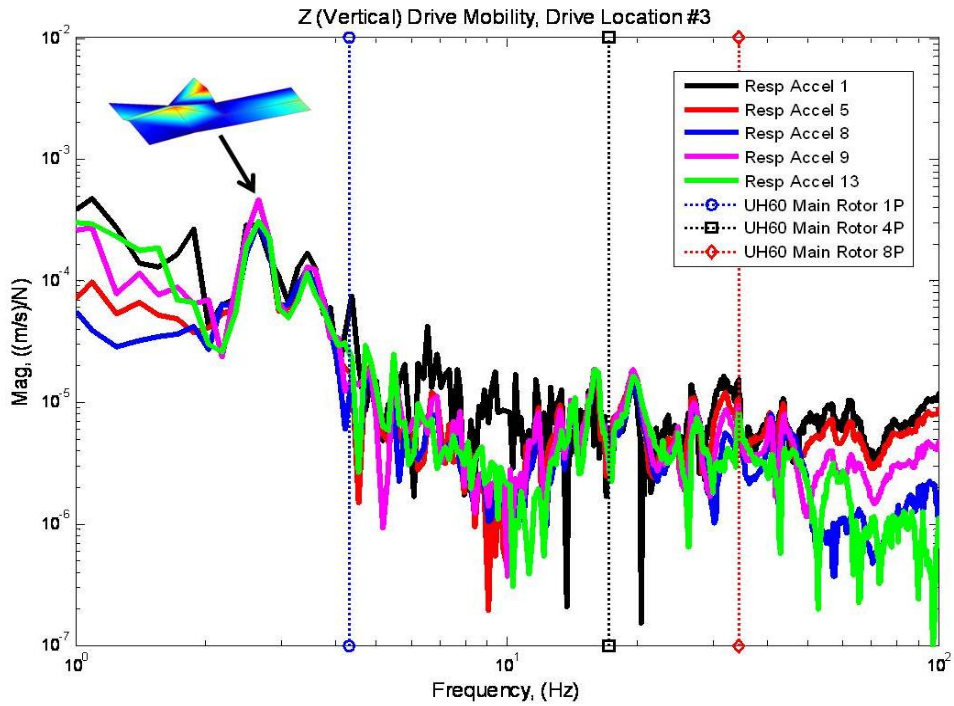

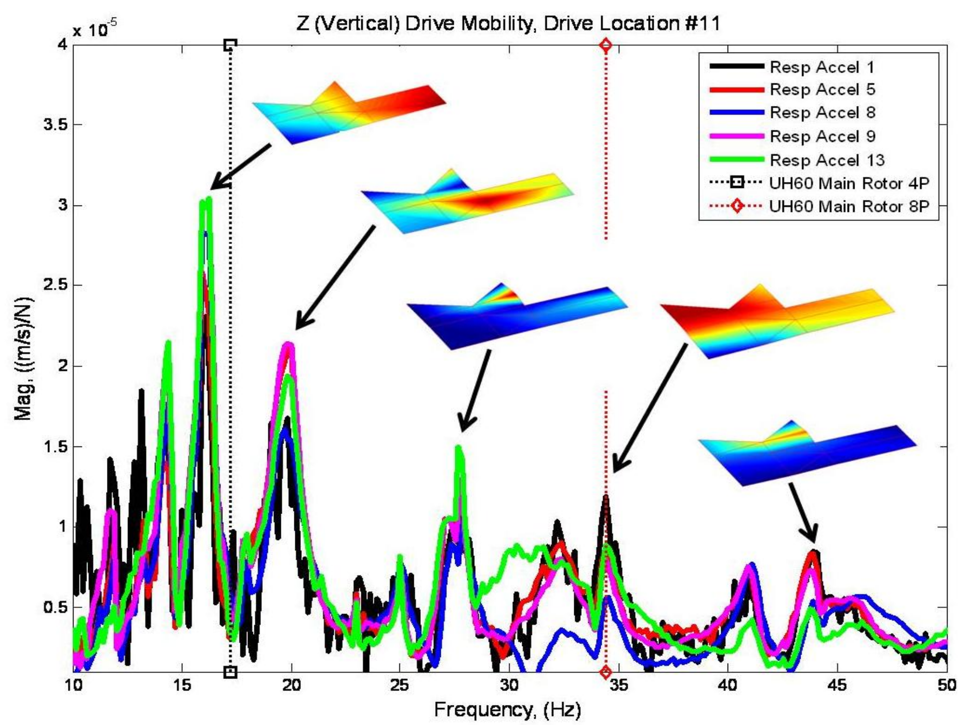

Figure 5.11. Mobility in z direction for a driving force at location 11 and associated mode shapes. BW 1-100Hz (top), BW 10-50Hz (bottom). The main rotor rotational frequencies (1/rev, 4/rev and 8/rev) are indicated for reference.

The structural parameters are those variables mainly related to the mechanical properties of the system. The damping levels and the flaw size were retained as the most meaningful structural parameters affecting the SI distribution. The damping levels were further classified in two categories:

- *Structural damping*, related to the material loss factor.
- *Viscous damping*, related to the dissipative power of the energy sink.

To evaluate the sensitivity of the SI technique to numerical/experimental parameters, the relationships between the power flow and the following parameters were analyzed:

- *Frequency resolution,* number of spectral lines retained for the FRF extraction.
- *Mesh size,* dimension of the FE grid used to discretize the test structure.
- *Contour mesh size,* dimension of the FE grid used to discretize the contour surface.

It will be demonstrated, in the following paragraph, how the damping has a strong effect on the SI distribution in a mechanical system. The experimental loss factors identified on the UH-60 transmission frame were used as reference damping values in the numerical simulations. This allowed for tailoring the sensitivity study on a more specific application for helicopter transmission frames. The loss factor in the FE simulations was then set to $\eta_{100\text{-}1000}$=0.075. This value corresponds to the maximum experimental loss factor measured in a frequency range 100-1000 Hz. This choice was driven by the observation that high damping values penalizes the total transmitted power (because the energy is dissipated into the structure before reaching the energy sink). This condition was therefore considered to produce conservative results.

5.4.1 Damping Levels

The first structural parameter investigated in the sensitivity study was the effect of the damping. Two different contributions to the overall damping level were considered:

- Structural Damping (i.e material loss factor)
- Viscous Damping

The structural or material damping is a property inherent to the material system. This type of damping is a distributed quantity with a low dissipative power in case of metallic structures. Generally, the effect of the structural damping is to spread the power flow over a larger area, which results in a reduced energy gradient. Viscous damping was applied to the test structure through the implementation of a concentrated viscous passive damper, which simulated the energy sink.

In a complex structure, the total damping is a combination of several factors including structural damping, losses at structural joints and the addition of damping mechanisms for structural vibration control. The equivalent loss factor for the structural assembly could be much higher than the expected value simply estimated on the basis of the material damping. Experimental loss factors estimated on a real helicopter transmission frame were used in these numerical analyses in order to make the results more relevant to the specific application.

In this study, particular attention was given to the combined effects of the structural and viscous damping on the total transmitted power. Using the FE model described above, various combinations of structural and viscous damping (which in these analyses was used only to simulate the energy sink) were analyzed. The results of this study are summarized in Figure 5.12. For all the damping conditions, the TTP is integrated over a 100-1000Hz frequency bandwidth.

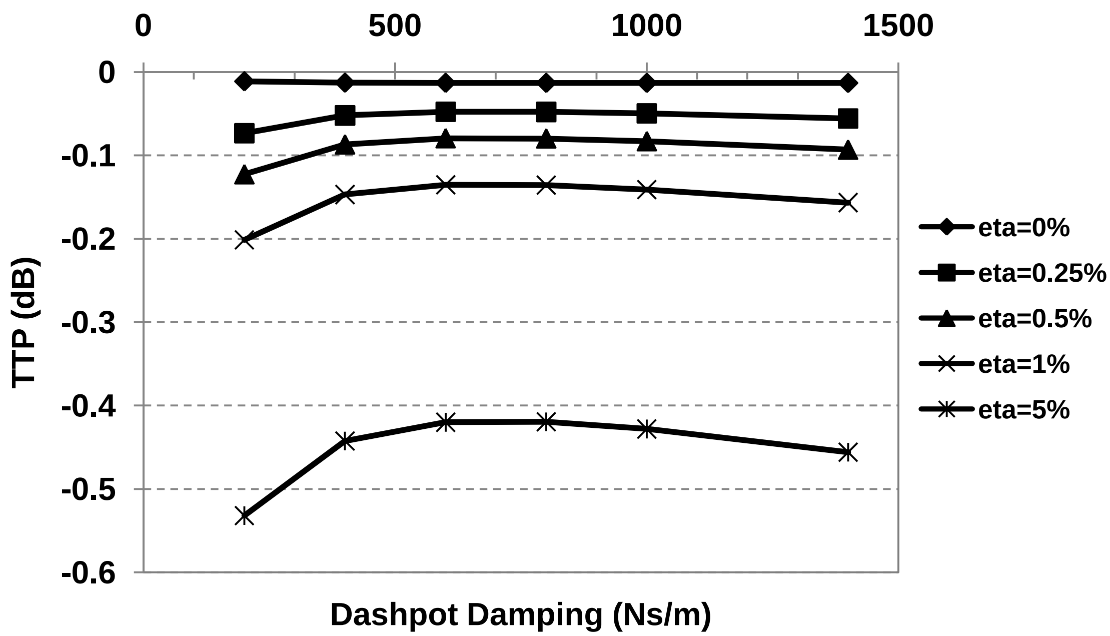

Figure 5.12. TTP versus viscous damping; the curves are parameterized in terms of structural damping. This plot shows the combined effect of the structural and viscous damping on the Total Transmitted Power.

It was observed that by increasing the material loss factor the TTP decreases. This effect was due to the higher energy dissipation occurring in the structure. If no material damping is selected, the increase in the viscous damping (i.e. the dashpot dissipative power) does not produce any increase in the TTP. This is an expected behavior because the only source of dissipation is represented by the dashpot which functions as a point source with local damping impact only. Independently of the equivalent localized viscous damper, the energy injected into the structure can only flow towards the energy sink.

When both the damping mechanisms coexist at the same time the TTP shows a different behavior. The curves in Figure 5.12 show a maximum TTP that corresponds to an optimal value of the viscous damper. The optimal value occurs when the mechanical impedance associated with the viscous damper matches the mechanical impedance of the structure in presence of the prescribed material loss factor. This mechanism results in an optimal condition for the mechanical energy transfer and coincides with the optimal point for damage detection purposes.

The same mechanism can be illustrated by Eqn. (5.10), where the mechanical impedance of a single degree of freedom system mass-spring-damper varies as a function of the viscous damping. The mechanical impedance Z of this system is analytically described by:

$$Z = \frac{(K - \omega^2 M) + i\omega C}{i\omega} \tag{5.10}$$

where $K=k(1+i\eta)$ is the spring complex stiffness, η is the loss factor, C is the viscous damping of the dashpot, M is the value of the mass, ω is the angular frequency and i is the complex unit. Figure 5.13 shows the behavior of the system described by Eqn. (5.10) in presence of different damping conditions and at a specified frequency.

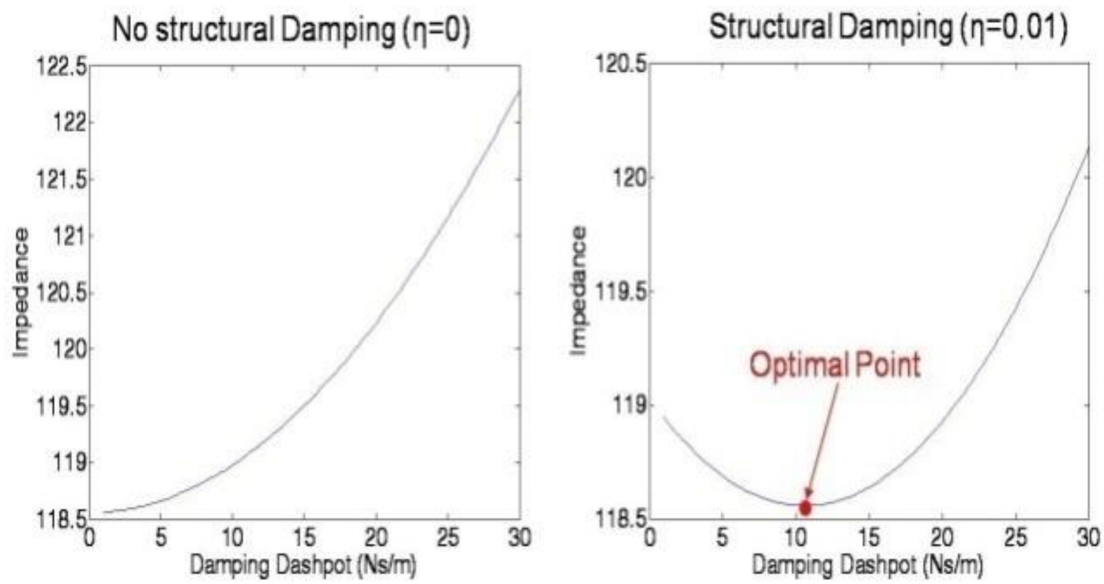

Figure 5.13. Mechanical impedance for a single dof system as a function of the structural and viscous damping.

Note that when the structural and viscous damping coexist the total mechanical impedance value has an absolute minimum. This point corresponds to the condition of maximum efficiency for the mechanical energy transfer (accordingly to the Maximum Power Theorem, Jacoby's Law).

It should be indicated from Figure 5.12 that the TTP estimated in the absence of material losses is slightly lower than 100%. This is due to numerical approximations in NASTRAN, which does not include the inertia forces at the grid points while estimating the nodal forces in a forced frequency response. Nevertheless, this numerical approximation does not produce any loss of generality on the presented results.

5.4.2 Damage Size

The second structural parameter analyzed in this study was the dependence on the damage size. An "open-crack" type defect was selected as a target fault for this study. The open crack was simulated in the FE model by coincident disconnected nodes. This model does not account for the nonlinear opening/closing behavior (i.e. contact). Several FE models were developed in order to assess the effects of the crack size on the total transmitted power. In particular, the relation between the crack size and the power flow through control surfaces was investigated in order to identify possible relationships between the crack size and the corresponding changes in the power flow.

The results from this sensitivity study are summarized in Figure 5.14 where TTP is plotted as a function of crack width for five different frequency bandwidths.

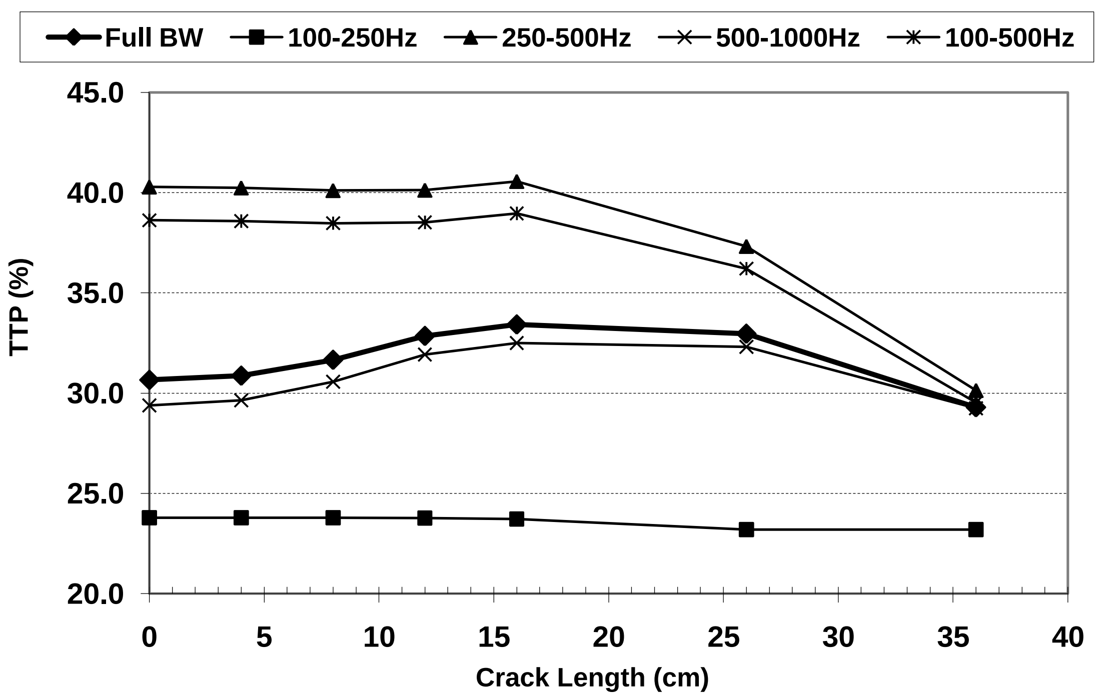

Figure 5.14. Dependence of the TTP from the crack size.

The increase in the crack size does not have a monotonic impact on the total transmitted power. This is due to a change in the mechanical impedance (related to a change in the stiffness matrix) which is no longer matching the impedance of the damper.

As discussed previously, the linear model used for the crack simulation does not introduce any additional source of energy dissipation. The power flow in presence of the crack is simply redistributed over new paths. This consideration also explains why for some damage size the TTP increases with respect to the healthy case.

These results suggest that the development of a nonlinear model of the damage, including dissipation and higher order harmonics generated at the crack interface, could considerably improve the performance of the SI based damage detection technique as well as provided sizing and localization capabilities. This approach will be further investigated in chapter 7.

5.4.3 Frequency Resolution

The frequency resolution was the first of the three numerical/experimental parameters considered in this study. As will be shown, this parameter had important implications to the numerical and the experimental analyses.

When the SI map is generated, either numerically or experimentally, the frequency step (or, equivalently, the number of spectral lines) must be fixed “a priori” in order to determine the frequencies at which the SI map will be calculated. This analysis will provide possible guidelines to choose the frequency resolution while performing numerical or experimental evaluations of the SI power distribution. It is evident that the optimal frequency step results from a tradeoff between the following conditions:

- *Small frequency step*: to correctly estimate the total power over the retained bandwidth.
- *Large frequency step*: to reduce the time for the numerical solution/data acquisition and to meet the maximum sampling frequency and the number of spectral lines allowed by the experimental equipments.

The frequency resolution study was performed using the FE model in Figure 5.2 assuming a loss factor η=0.075 (as indicated by the vibration tests on the UH-60) and a viscous damping coefficient C=600 Ns/m (value where the maximum TTP occurred for the plate test structure).

Five different frequency steps were used and compared. Figure 5.15 shows the results obtained from the process of integrating the mechanical power over three different frequency bandwidths. The retained frequency steps were: Δf_1=10Hz , Δf_2=5Hz , Δf_3=2Hz , Δf_4=1Hz , Δf_5=0.5Hz. The power percentage was calculated with respect to the finest frequency step Δf_5=0.5Hz.

The Δf_2 provided a relatively good estimate of the contour power (i.e. the power integrated over the contour surface C1 and C2). Depending on the frequency bandwidth used for the integration, the percentage power showed some fluctuations. Although the overall trend was maintained between the different bandwidths, the coarser frequency step tended to underestimate the power at the lower frequency resonant peaks while it overestimated the power at off-resonance frequencies. This behavior was particularly visible using the Δf_1 where the percentage error decreased while extending the frequency range.

A different way to look at the same concept is by using a running summation over the different frequencies. Figure 5.16 shows the running summation of the mechanical power for the contour C1 in the range 100-200Hz. Note that around 120Hz (where one of the low frequency modes is located), the Δf_1 overestimate the power. However, moving towards higher frequencies and including off-resonance components the trend is inverted and the coarser frequency steps underestimate the contour power.

It can be concluded that to estimate the contour power with a relatively good accuracy (on the order of 1% error) the frequency step must be lower than 5Hz at low frequencies but the coarser 10Hz frequency resolution could be used at higher frequencies.

These results are dependent on the damping levels considered for the analysis. They provide therefore useful general indications for the resolution bandwidth that could be used for measurements on the UH-60 transmission frame application. Numerical results show also that the choice of the frequency resolution follows the standard approach for the convergence of spectral quantities. The use of the standard approaches for the estimate of bias error [115] in spectral analyses can be envisioned as a useful tool to drive the selection of the resolution bandwidth.

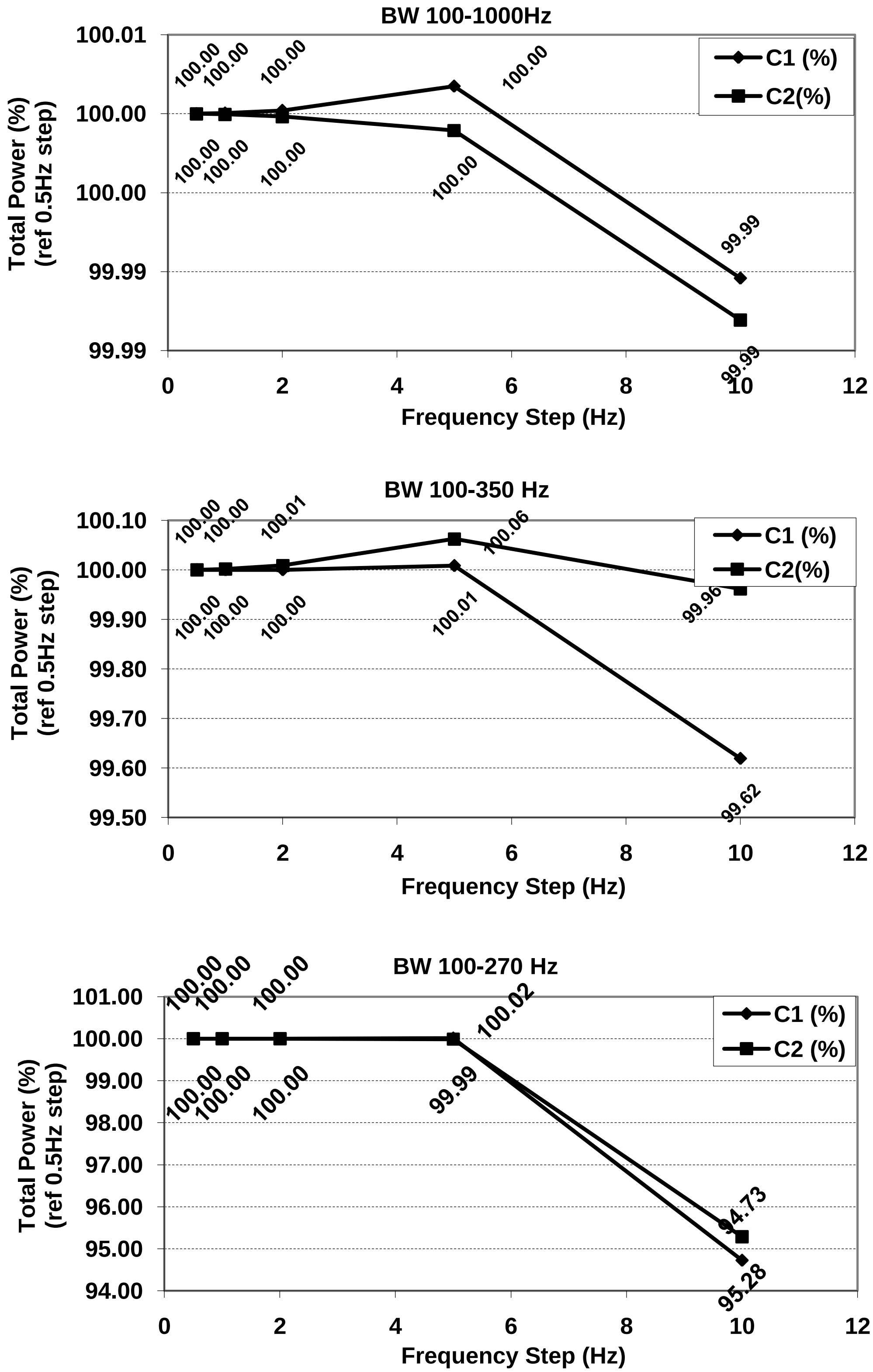

Figure 5.15. Dependence of the percentage contour power on the frequency step.

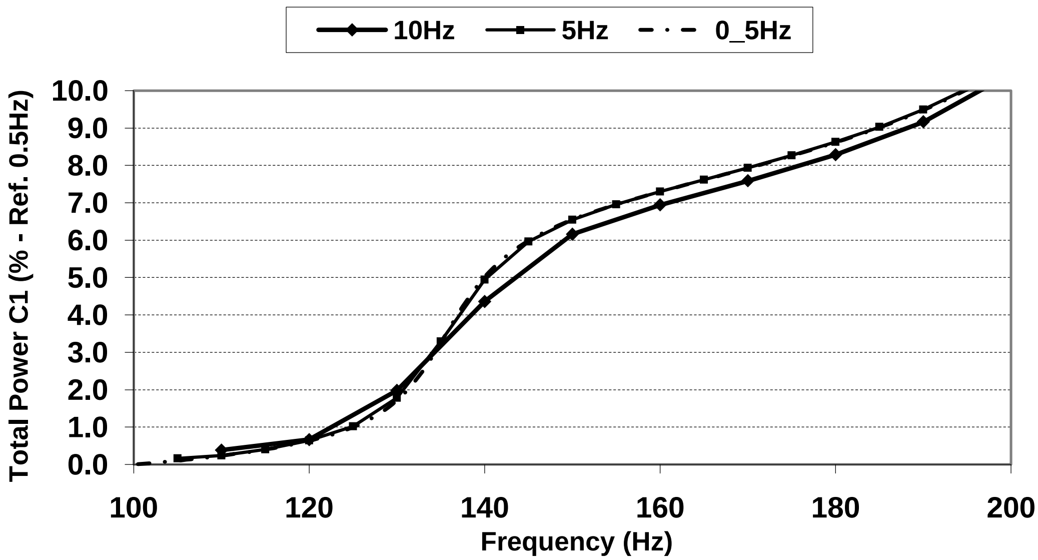

Figure 5.16. Running summation for the contour power C1.

As an example, the spectral resolution could be selected according to the following relation:

$$\varepsilon_b\left[\hat{G}_{xy}(f_r)\right] \approx \frac{-1}{3}\left(\frac{B_e}{B_r}\right)^2 \tag{5.11}$$

where ε_b is the bias error associated with the cross spectrum $\hat{G}_{xy}$ calculated at the resonance frequency f_r by using a resolution bandwidth B_e. B_r indicates the half power point bandwidth.

5.4.4 Mesh Size

The mesh size is a parameter that typically affects the FE numerical simulations. When a FE model is used to estimate the SI distribution on a specific structure under a certain loading condition, the size of the grid used to discretize a continuous structure plays an important role in determining the accuracy of the results.

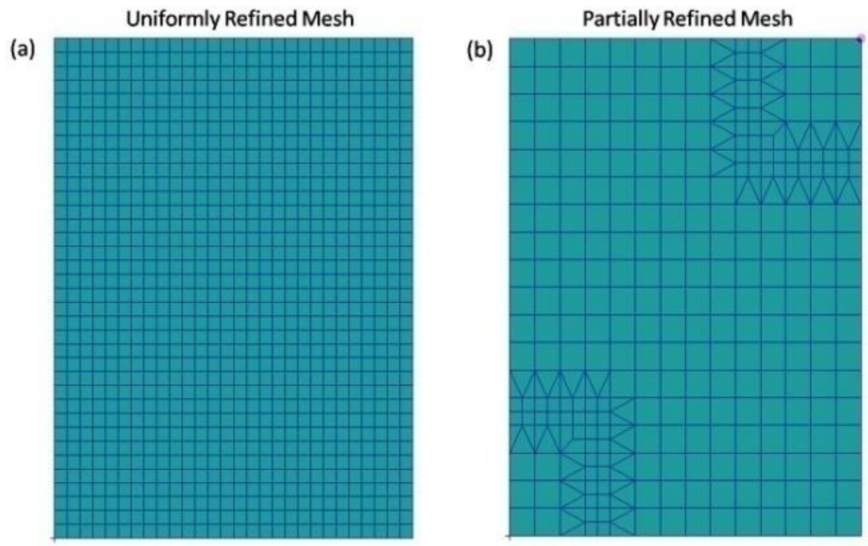

Figure 5.17. FE models used for the sensitivity study to the mesh size; (a) uniformly refined mesh with four time the number of elements of the coarse mesh, (b) partially refined mesh around the contour surface.

Three different mesh sizes were used to carry on this sensitivity study:

1. *Coarse mesh*: was the reference model used to perform the sensitivity study for the other parameters. (Figure 5.2)
2. *Uniformly refined mesh*: has four times the number of elements of the course mesh. (Figure 5.17a)
3. *Partially refined mesh*: was refined only in correspondence to the contour surfaces. (Figure 5.17b)

The SI results for the sensitivity study were calculated using a loss factor η=0.075, a viscous damping C=600Ns/m and a frequency step Δf=5Hz. The contour power integrated over the bandwidth 100-1000Hz is shown in Figure 5.18 for the different mesh sizes. A shift of the peaks occurs at higher frequencies (over 600Hz). This known characteristic behavior drives the standard practice of using a finer mesh to capture localized changes in the stress/strain and displacement fields in order to accurately represent the structural dynamic response at high frequencies.

The direct comparison of the total power integrated over the two contour surfaces is shown in Figure 5.19. The results indicated that the total contour power varies as a function of the mesh density. The data showed that the coarse mesh tended to under estimate the total contour power inducing an error of about 15%. When the mesh was refined only around the contour surfaces, the increased resolution of the stress/strain field at high frequency decreased the overall error to 5-8% with a negligible increase in the total number of elements and degrees of freedom. A lower error could probably be obtained by further increasing the mesh density on the contours.

These results demonstrated that, while performing numerical simulations of the SI field, a partial mesh refinement was sufficient to ensure relatively good accuracy of the estimated total contour power. From a general point of view, the application of the standard convergence criteria normally used for the calculation of stresses and resonance frequencies was sufficient to guarantee the convergence of the total contour power.

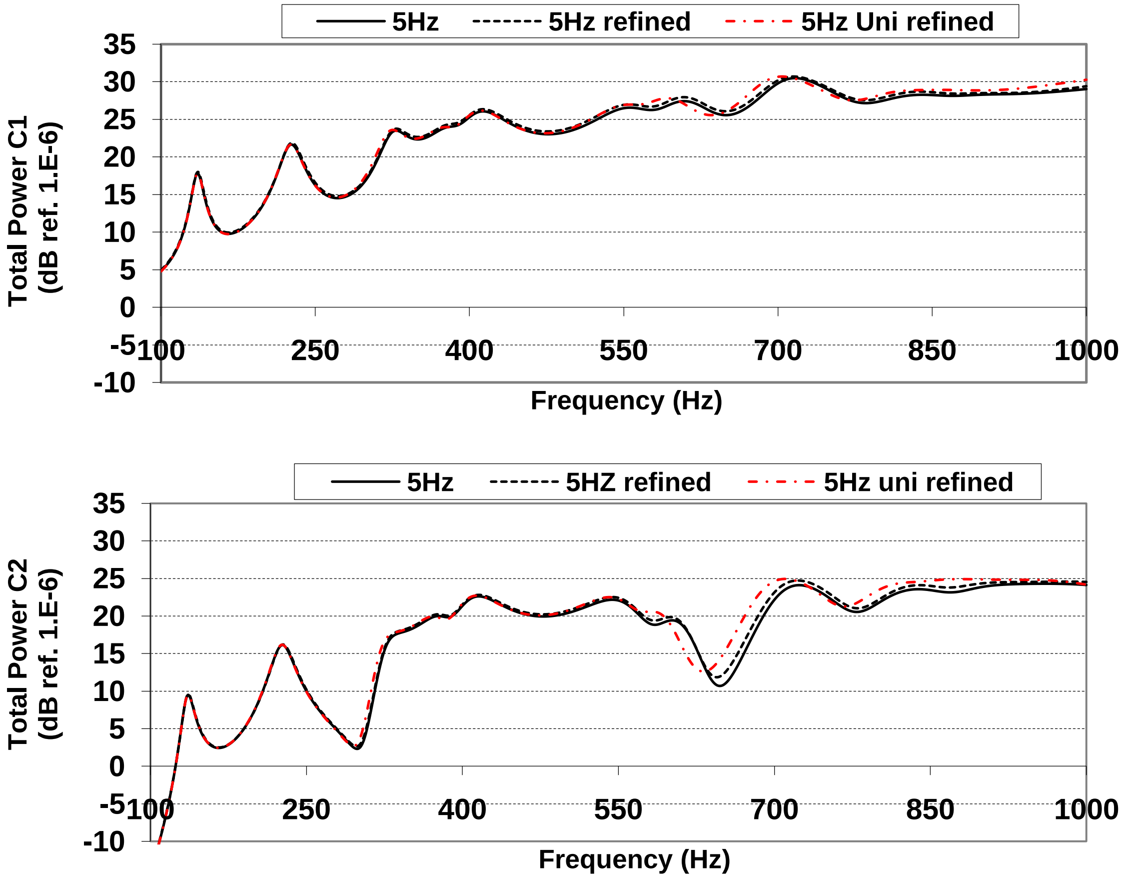

Figure 5.18. Contour Power in the BW 100-1000Hz for the different mesh size.

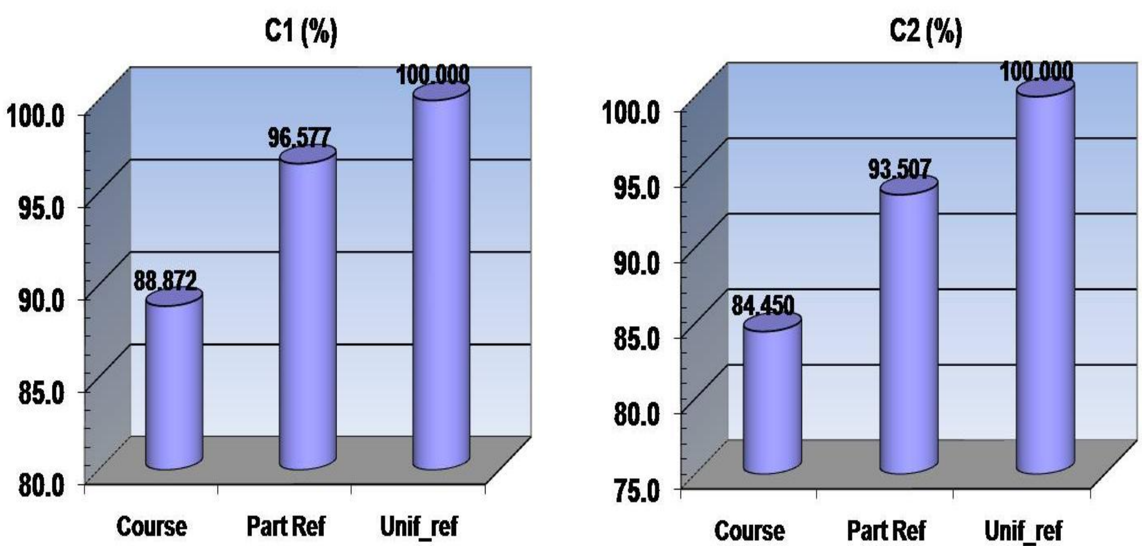

Figure 5.19. Dependence of the total contour power at the two contour surfaces on the mesh density.

5.4.5 Contour Mesh Size

The contour mesh size is a parameter that impacts the accuracy and the resolution of both the numerical and experimental SI data. This parameter refers to the dimensions and to the continuity of the elements constituting the boundary of the contour surface in a FE model or, alternatively, the size and the spacing of the strain sensors used to delimit the contour surfaces on a real structure.

Two different kinds of contour mesh (Figure 5.20) were investigated in this study:

- Fully closed contour
- Open contour

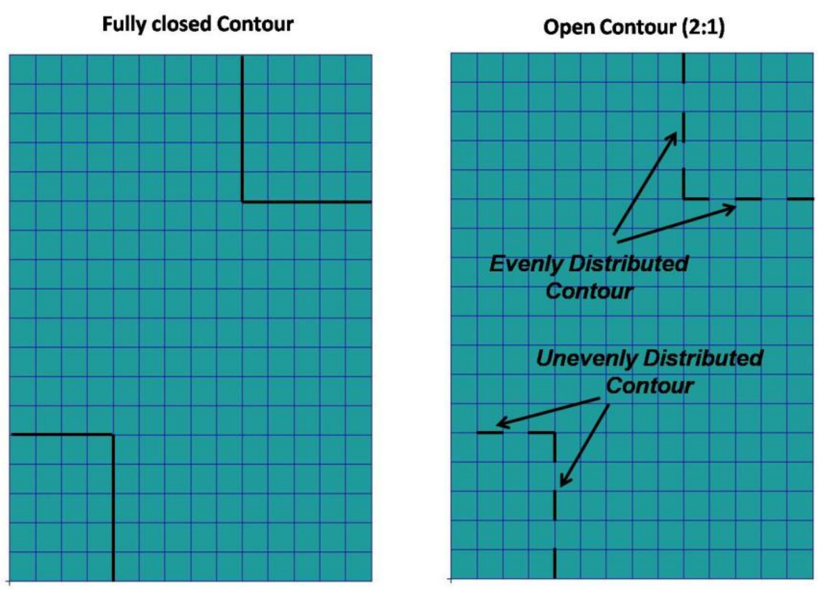

Figure 5.20. Definition of the contour mesh size; (left) continuous closed contour, (right) open contour.

In a closed contour, that is equivalent to the one used in the previous parametric studies, the edges of contiguous elements are retained to delimit the source and the sink areas. In an open contour, only one out of two edges of two consecutive elements is retained. In order to maintain a certain degree of generality, the two contour surfaces were chosen with different areas. This study was intended to provide guidelines about the spacing and placement of sensors for the SI experimental implementation. The results for this sensitivity study are summarized in Table 5.1.

Table 5.1. Effect of the contour mesh size on the total contour intensity. The total intensity is integrated over different frequency bandwidth.

Total Transmitted Intensity	**BW 100-1000 Hz**	**BW 100-500 Hz**	**BW 500-1000 Hz**
$C1_{2to1}/C1_{full}$	100.8	105.27	100.01
$C2_{2to1}/C2_{full}$	90.3	96.03	88.86

In order to compare the energy flowing through contours with a different total area, we must compare the structural intensity. The open contour gives a good estimate of the power at low frequencies (high wavelengths). It shows a lack of accuracy at higher frequencies where the shorter wavelengths produce localized changes in the contour intensity. This behavior is particularly visible on the power integrated over the control surface C2. Also, the running summation in Figure 5.21 confirms that the error associated with the open contour is mainly due to the high frequencies.

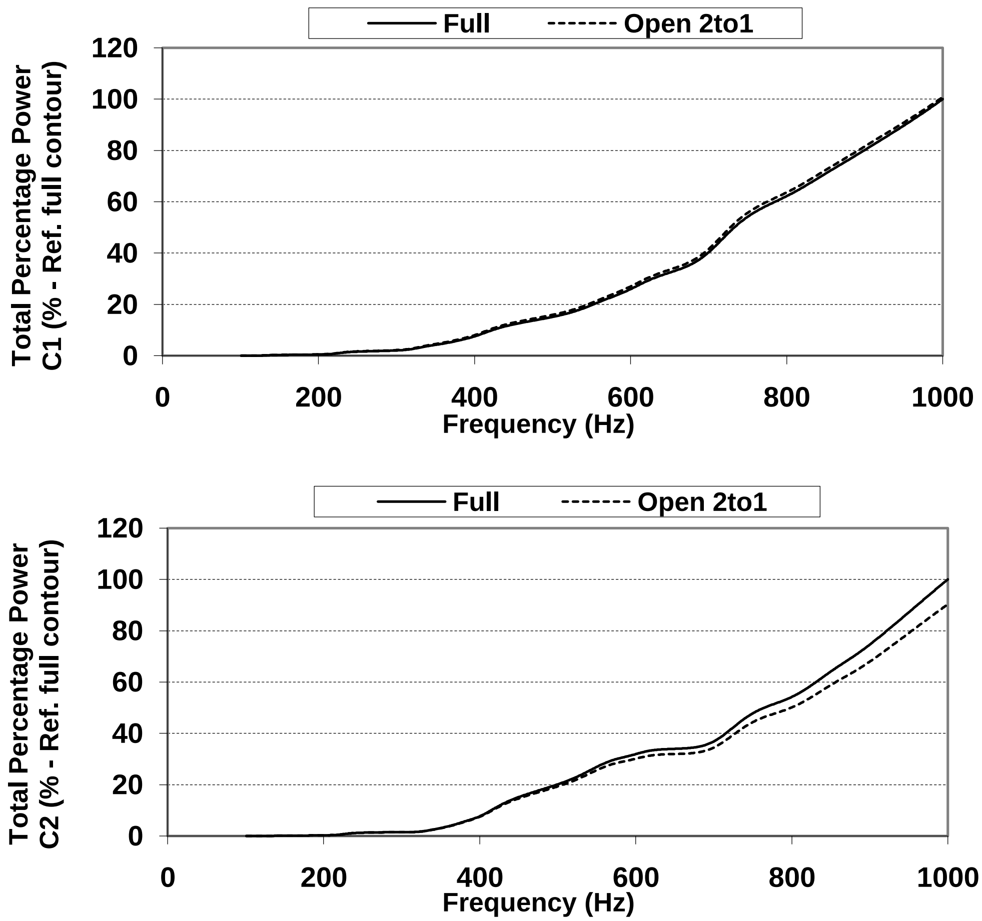

Figure 5.21. Running summation of the total contour power for different contour mesh.

Nevertheless, the definition of the contour mesh is driven also by a second parameter that is directly related to the presence of sudden changes in the output variables. In proximity of concentrated loads, boundary conditions or other sources of localized changes in the impedance of the structure, the power flow presents strong gradients. If the contour mesh is not fine enough to capture these sudden changes, it could result in a consistent error on the estimated power. This consideration explains why at the contour C1 the total intensity between 100-500Hz results greater than 100%. The combination of boundary condition and the energy source produces gradient that cannot be adequately represented by the mesh. This situation is even more accentuated by the use of an unevenly distributed mesh contour elements. Based on these results, it can be concluded that the selection of the sensor size and spacing should be done depending on the frequency range of interest and according to the criteria generally used to assure the convergence of the dynamic stress field. The sensors should also be evenly distributed in order to limit the effects of strong stress and velocity gradients.

5.5 Localization Technique for Linearly Behaving Structural Damage

The SI maps were used in this work as a mean to validate the numerical and experimental procedures developed to evaluate the structural intensity field on the test structure. The use of SI maps, however, is not a viable approach for the implementation of a damage detection technique on operating structures because the measured data will be available only at a prescribed and limited number of structural locations. Also, when the interrogation signal excites higher order modes the SI maps are typically too involved to give clear indications on the energy path. On the other hand, high frequencies (i.e. shorter wavelengths) are generally required to increase the sensitivity to the damage.

The approach based on the Total Transmitted Power introduced a possible approach for the interpretation of SI measurements collected at discrete locations. The numerical results from the sensitivity study to the damage size highlighted some limitations of the TTP in its original formulation. The comparison of the TTP of the damaged structure with the baseline signature allowed assessing the presence of the damage. The TTP, however, did not provide indications on the absolute size of the damage. In the following sections, the possibility of using the TTP to localize damage is explored.

5.5.1 Theoretical Approach

The present localization technique is intended to extend the performance of the SI based SHM by providing it with a localization capability for a class of damage exhibiting a linear dynamic response. This type of damage includes, as an example, open fatigue cracks, ballistic damage, open delaminations and all the defects that do not induce a nonlinear dynamic response.

The basic assumption for the implementation of this approach is the existence of a network of energy sources and sinks which can be properly selected either by the user or autonomous control logic. This network will allow selecting different structural locations for the energy source/sink pair. The use of a transducers network will enable focusing the vibrational energy in specific structural areas. The theoretical and practical aspects related to the experimental implementation of such a network will be treated in detail in Chapter 6. A second assumption consists in the availability of a baseline database previously acquired on the healthy structure. As a general remark, this is the only approach investigated in this work that does not meet the requirements set in Chapter 1 about the use of a baseline.

Consider the test structure and the sensors layout as in Figure 5.22. The test structure consisted in the same plate used for the numerical sensitivity. The active network is comprised of nine energy sources and four energy sinks. The damage was introduced in the form of an open crack (i.e. coincident disconnected nodes) with a total length l_c=8cm. Interrogation signals were applied in both the in-plane and out-of-plane direction. Although shell elements were used to model the plate, an offset between the plate surfaces and the neutral plane was defined in order to take into account the coupling between in-plane excitation and out-of-plane displacements (bending waves).

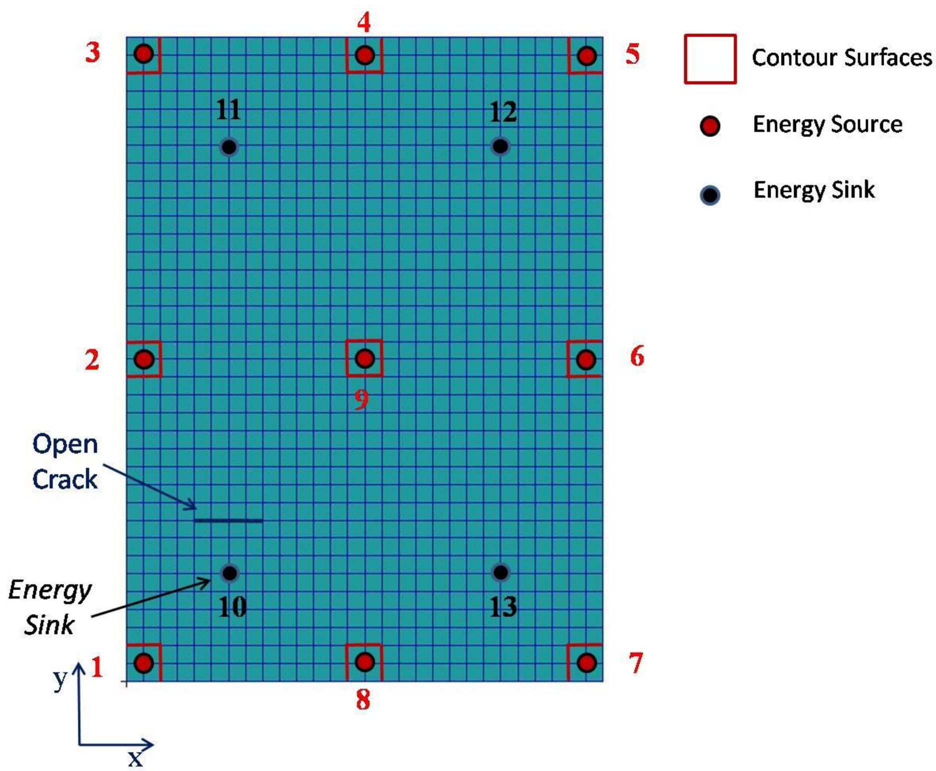

Figure 5.22. Test structure and sensors layout for the implementation of the linear localization algorithm.

Contour surfaces were defined around each transducer in order to allow the measurement of the total transmitted energy, according to the process described in §5.2.1. Due to the different total surface chosen for the sensors, the transmitted energy was evaluated in terms of *Total Transmitted Intensity* (TTI) which is independent of the integration area. In this study *m* independent energy sources and *n* independent energy sinks were defined, where *m*=9 and *n*=4.

The first step of the localization technique consisted in acquiring a reference baseline of the healthy structure in terms of TTI. Each one of the nine transducers was separately fired to simulate a periodic interrogation signal sweeping a prescribed frequency range. For each actuation signal (i.e. for each actuator) the TTI at the remaining eight sensors was collected. Using this approach a TTI baseline database was initially recorded and stored. The baseline consisted of (m×m-1×n) TTI profiles. The procedure to acquire the baselines is schematically described in Figure 5.23.

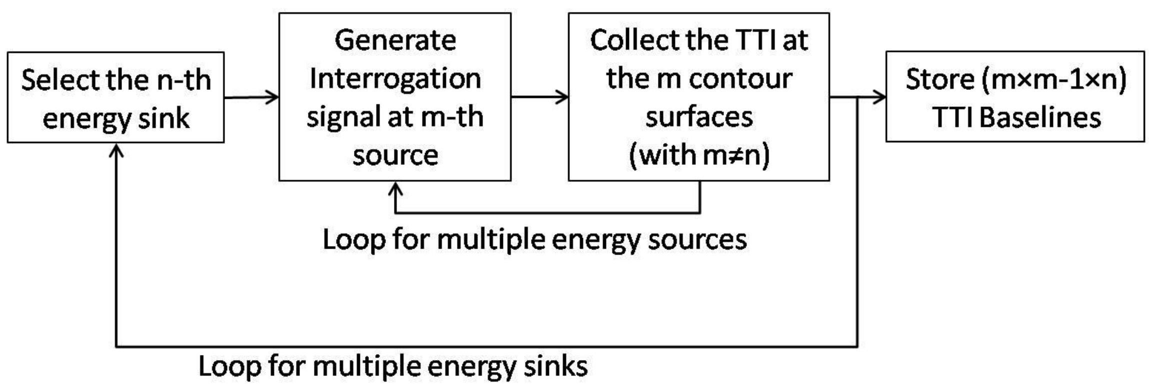

Figure 5.23. Flow diagram describing the sequence of operations to acquire the baseline signature on the healthy structure.

Once the baseline was acquired, the damage was introduced into the structure and data were acquired and processed according to the schematic in Figure 5.24.

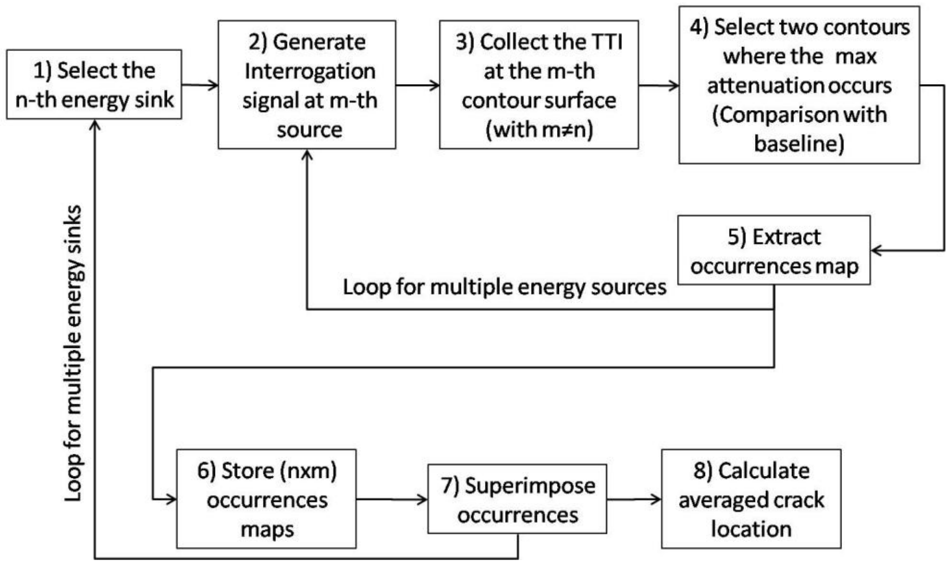

Figure 5.24. Flow diagram describing the implementation of the linear damage localization algorithm.

The starting point of the localization algorithm consisted in re-acquiring the TTI for all the combinations of energy sources and sinks (step 1-3), as was already done for the baseline signals. Once the total transmitted intensities were acquired, the two sensors recording the maximum attenuation in the TTI value (integrated over the considered bandwidth) were extracted (step 4). Using the location of the energy source and the two sensor's locations extracted at step 4, the structural area associated with the maximum TTI attenuation could be obtained by triangulating the points. Once this area was identified, all the structural grid points included in it were associated with an occurrence number (step 5-6) which ultimately describes how many times a point belongs to the maximum attenuation area. To clarify this concept, an example showing the selection of the maximum attenuation area is given in Figure 5.25.

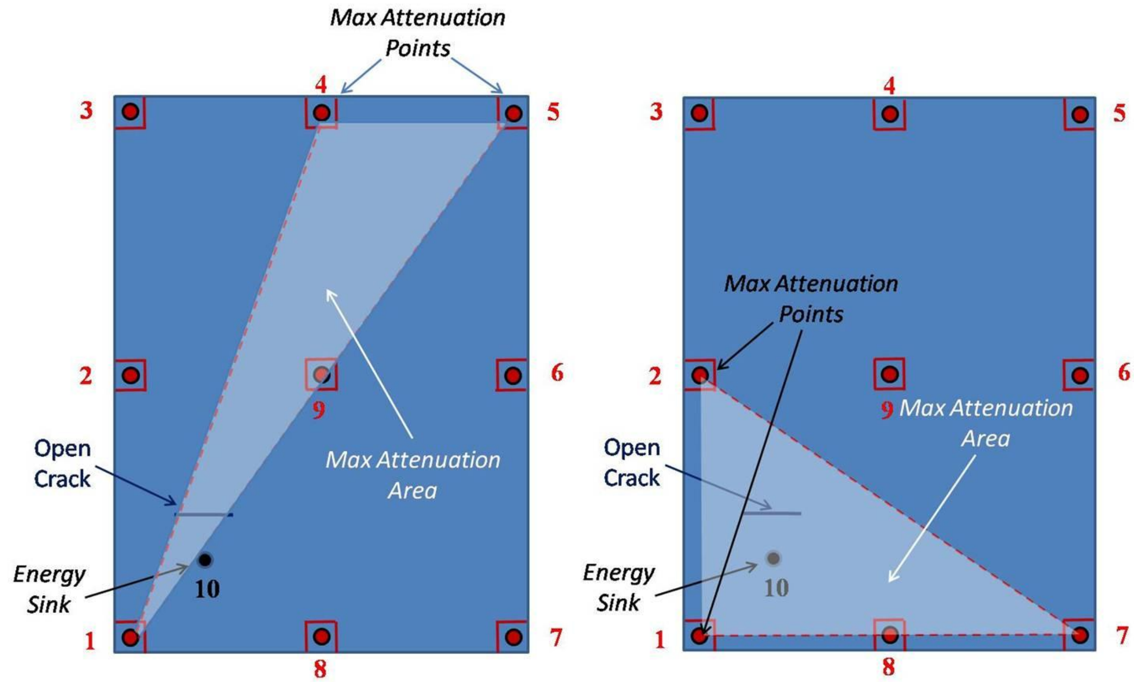

Figure 5.25. Schematic showing the selection of the maximum attenuation area for an actuation signal at (left) transducer 1 and (right) transducer 7.

In the proposed example, the procedure for the identification of the maximum attenuation areas for transducers #1 and #7 is shown. It was assumed that for the interrogation signal generated at the transducer #1 the maximum TTI attenuation was registered at sensors #4 and #5. The maximum attenuation area was then defined as the region having points #1, #4 and #5 as vertices. In a similar fashion, if sensors #1 and #2 registered the maximum attenuation for an excitation generated at transducer #7, the maximum attenuation area will have vertices at points #1, #2 and #7. The theoretical motivation for the selection of this structural area will be explained later in this chapter.

Once the (m×m-1) attenuation areas with their relative occurrences maps were estimated, they can be combined to give the total occurrences map for a specific excitation condition and energy sink location (step 7). The process can then be iterated considering multiple energy sink locations and excitation conditions. This approach will provide a database of occurrences maps whose data can be averaged (step 8) to improve the overall accuracy.

The theoretical foundation behind this damage localization algorithm comes from the relation between the transmitted energy and the presence and location of structural damage. When the damage is located on a main energy transmission path (as in Figure 5.25) the power flow is deflected and redistributed over new paths. The total transmitted energy is consistently reduced due to the presence of damage and depending on its size. High attenuation levels are generally associated with energy path striking damaged areas.

This concept can be better clarified through an analogy. Recall the concept of *view factors* in heat propagation problems based on an irradiative mechanism. Given an irradiating source, a receiving body and neglecting losses, the amount of thermal power which leaves the source and reaches the body depends on the percentage of the body's area exposed to the source. This percentage is generally taken into account through a parameter called "*view factor*". In a similar way, the presence of the damage reduces the contour surface area, at the sensor location, that can be seen by the contour surface around the source, i.e. reduces the *vibration energy view factor*.

By applying this concept, the main SI attenuation path (that more likely coincides with a damaged structural area) can be identified. Nevertheless, a main difference exists between the heat transfer and the vibration energy propagation problem. In vibrating structures the energy path is strongly dependent on the structural mode excited by the interrogation signal (§5.2.4). At higher order modes the energy follows convoluted paths which alter the assumptions this technique is based on. In order to increase the accuracy of the localization technique only the lower order modes, that are associated with clear and smooth energy path, should be retained. The mid-frequency range is associated with complex mode shapes that are too complex to provide meaningful information about the attenuation paths. The high frequency range, which is associated with highly directional waves, might have potential for this application but its use will not be addressed in this work and is left to future studies.

5.5.2 Numerical Results

In order to investigate the applicability and the performance of the proposed localization technique a numerical investigation was carried out using the test structure and the sensor layout described in Figure 5.22. The total occurrences maps were acquired for four different energy sink locations and for both in-plane and out-of-plane excitations.

Figure 5.26 provides an example of the sequence of the identified maximum attenuation areas (red area) for an out-of-plane excitation in the frequency range 100-500Hz and an energy sink at point #10. By superimposing the different attenuation areas the total occurrences map, (Figure 5.27) for a specific sink location and excitation condition, is obtained.

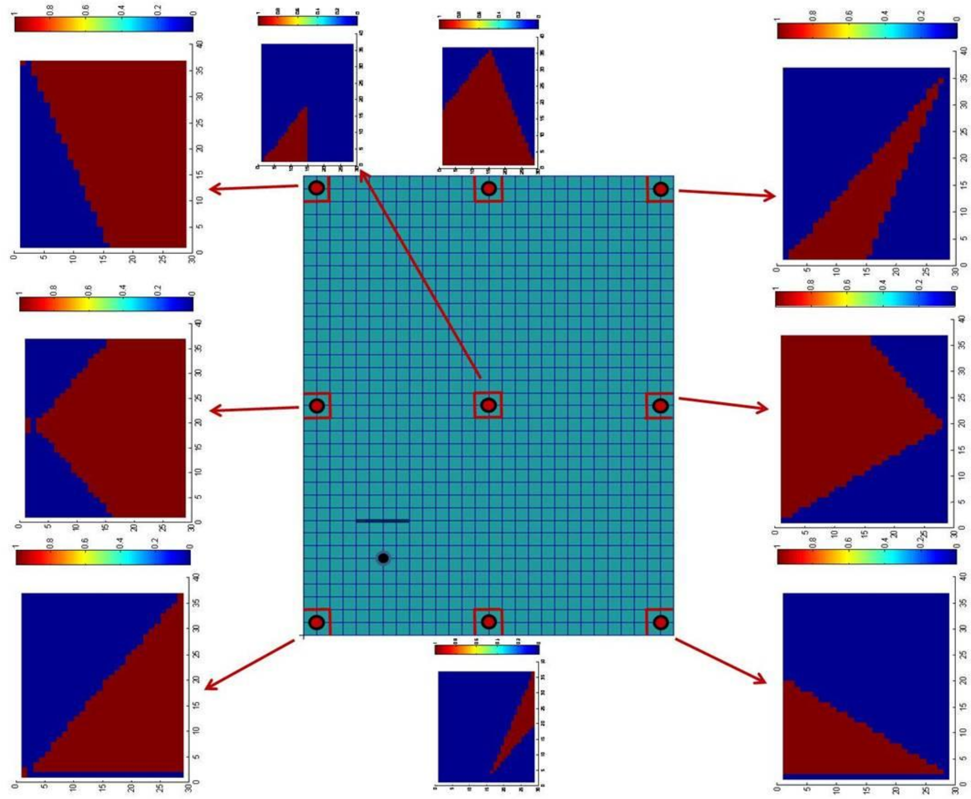

Figure 5.26. Numerical results showing the sequence of the identified attenuation areas. The red region indicates the selected attenuation area for a specific excitation condition. For each energy source the correspondent max attenuation area is plotted.

The dark red area in Figure 5.27 indicates the structural points associated with the highest number of occurrences. The points in this region have the highest probability of inducing energy attenuation and therefore of identifying the damage location.

Numerical simulations were carried on to evaluate the performance of the proposed damage localization technique by combining different excitation conditions and sink locations. In particular nine transducers, four energy sinks and two excitation conditions (in-plane and out-of-plane) were considered in this study according to the layout in Figure 5.22.

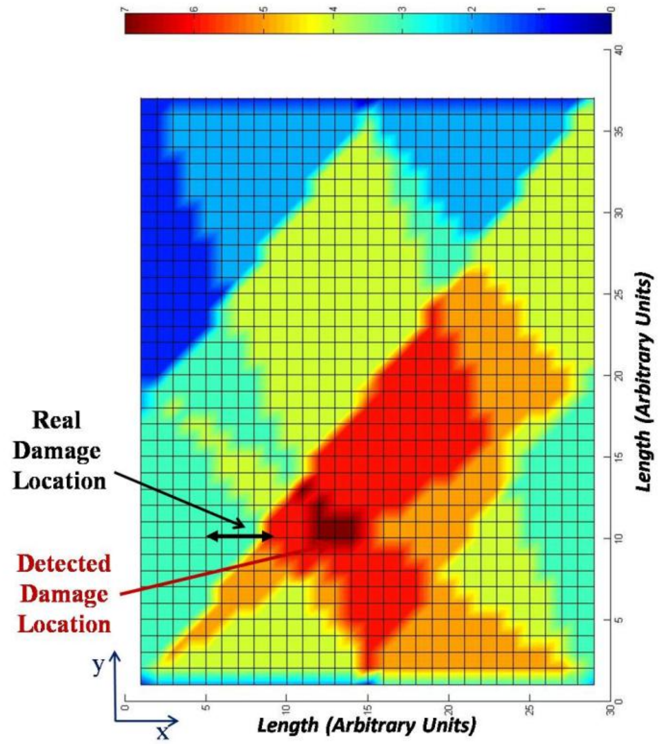

Figure 5.27. Total Occurrences map for an out-of-plane excitation in a frequency range 100-500Hz and for an energy sink at point #10. The colorbar shows the number of occurrences.

Three frequency ranges f_1=100-500Hz, f_2=500-1000Hz and f_3=1000-1500Hz were selected to test the damage localization algorithm. Selected examples for the resulting occurrences maps are presented in Figure 5.28 and Figure 5.29. As expected, the best estimates of the crack location were generally achieved in the low frequency range f_1. The mid range was associated with very involved mode shapes that prevent a meaningful interpretation of the attenuation paths. By increasing the frequency the wave fronts gain directionality which, as mentioned, could improve again the localization accuracy.

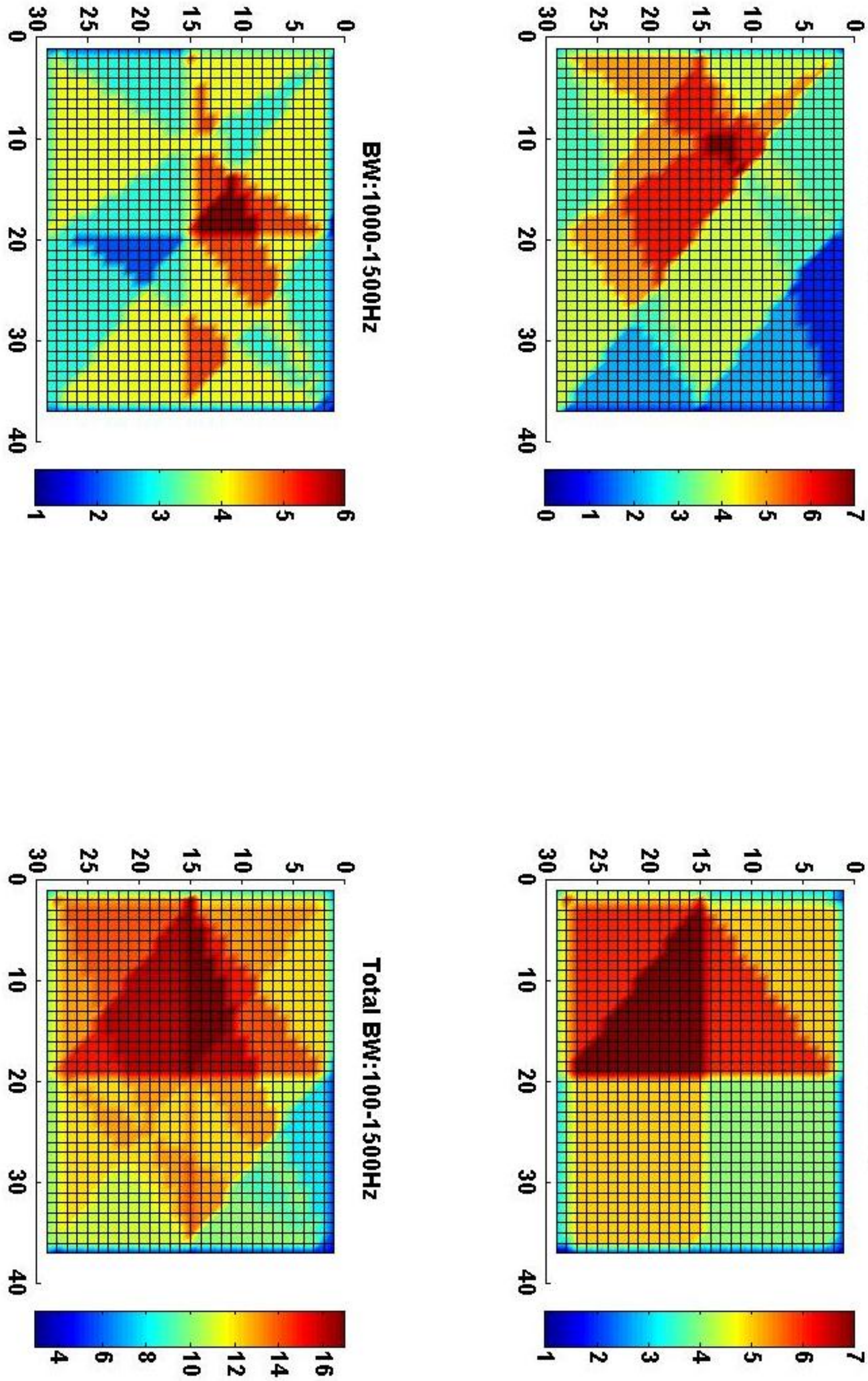

Figure 5.28. Occurrences maps for an out of plane excitation and an energy sink at point #10.

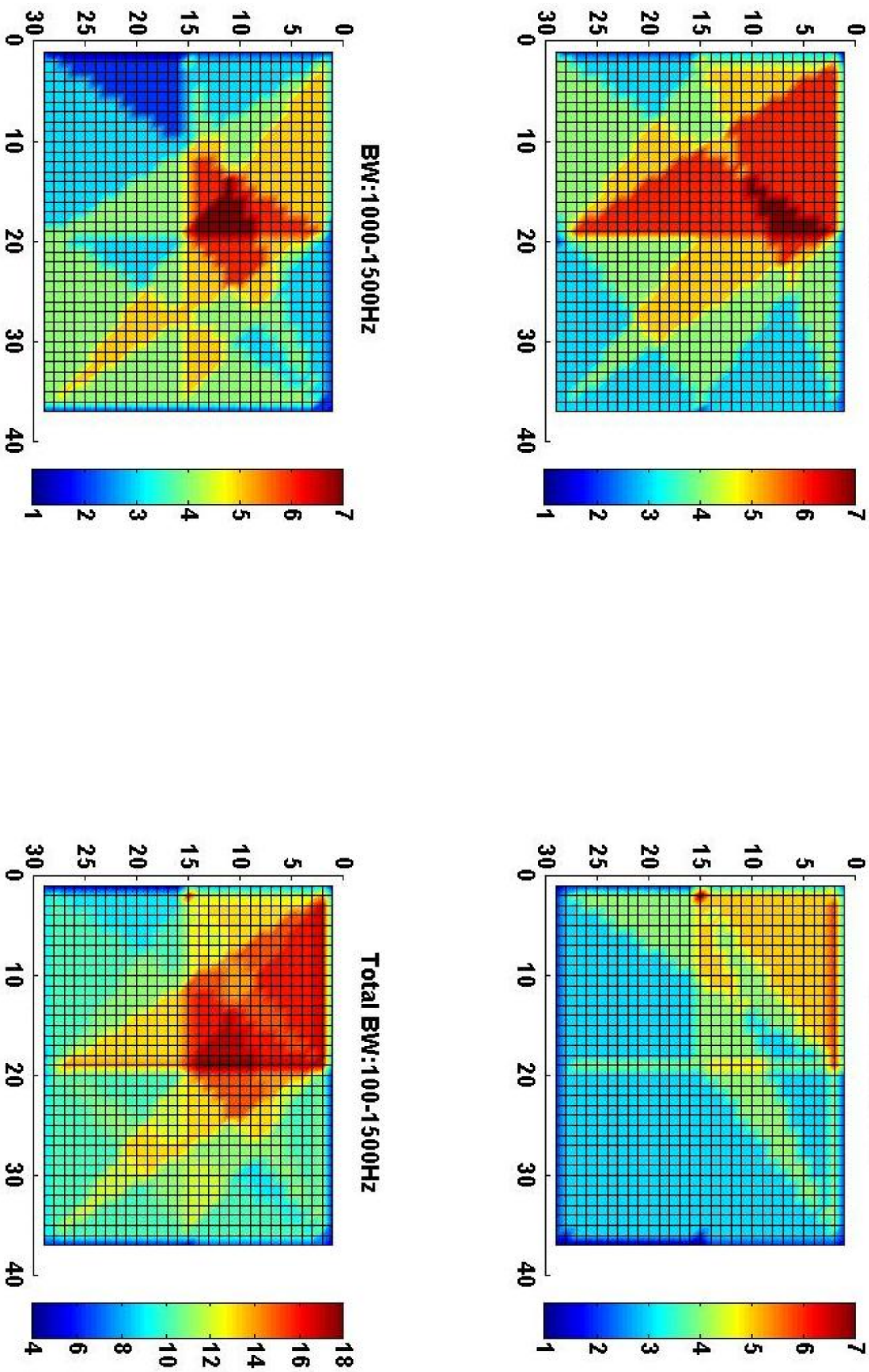

Figure 5.29. Occurrences maps for an out of plane excitation and an energy sink at point #12.

As already demonstrated in the sensitivity study, integrating the structural intensity over an extended frequency range generally deteriorates the quality of the information. This behavior is also confirmed by the occurrences map calculated over the total bandwidth (100-1500Hz). In this type of SI based approach integrating the power over large frequency ranges is generally not recommended.

The occurrences maps were calculated for both in-plane and out-of-plane excitations in the bandwidth 100-500Hz. In order to combine the information provided by the different data set it was decided to linearly average the coordinates of the points included in the maximum attenuation areas (i.e. points with the highest occurrence) for each map. This procedure resulted in the calculation of an average crack location for each combination of Out-of-Plane (OoP), In-Plane (InP) and energy sink (#), as shown in Figure 5.30.

The ensemble of the estimated locations was then averaged to give the final estimate of the crack position, represented by the blue circle in Figure 5.30. The resulting averaged position, indicated by the crack midpoint, is predicted with an absolute error on each coordinate axis of about 10cm (Table 5.2).

Although the error on the estimated location is not negligible, the proposed algorithm is able to provide general information on the damage position by using very low frequencies, i.e. high wavelengths.

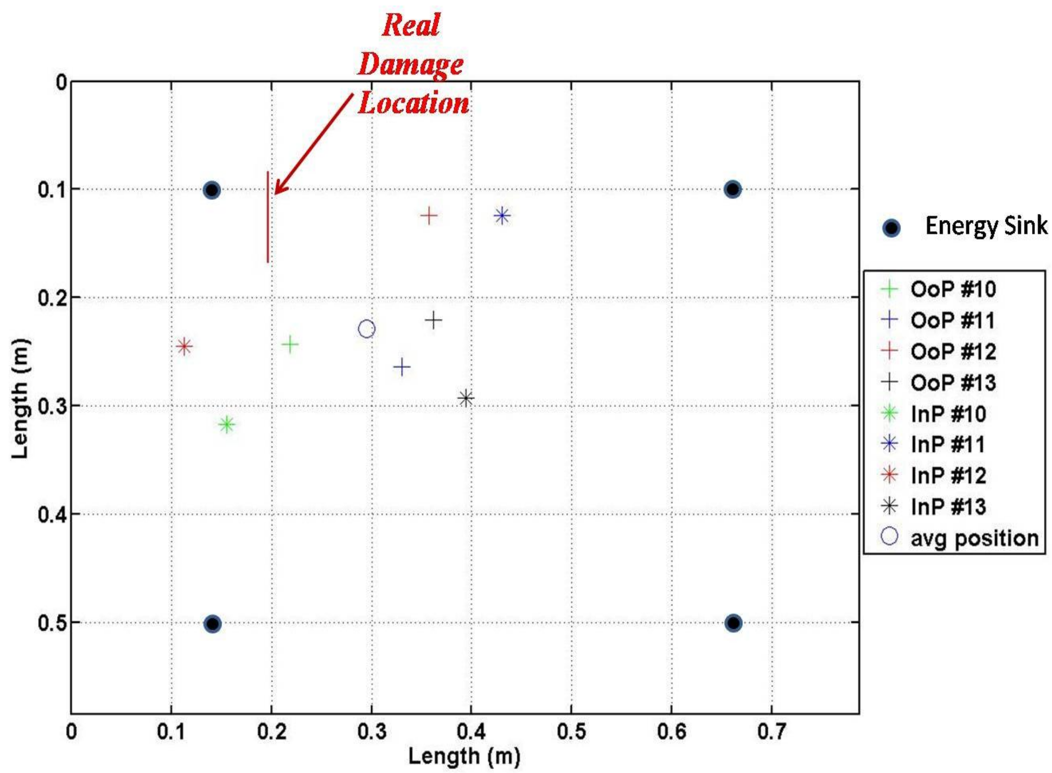

Figure 5.30. Estimated crack location versus real crack location. Each point indicates the estimated crack location when using a certain combination of Out-of-Plane (OoP), In-Plane (InP) and energy sink location (#).

Table 5.2. Comparison between the real and the estimated damage location.

	Real Location (m)	***Averaged Estimated Location (m)***	***Absolute Error (m)***
x	0.2284	0.1250	0.1034
y	0.2950	0.1968	0.0982

In particular, for the specific test structure the phase velocity and the corresponding wavelength for the first Anti symmetric (*A0)* and Symmetric (*S0)* modes are shown in Figure 5.31. As a reminder, the *A0* mode is associated with flexural waves, at different frequencies, producing an anti-symmetric displacement distribution through the plate thickness. The *S0* mode is, instead, associated with compressive waves producing a symmetric displacement distribution through the thickness.

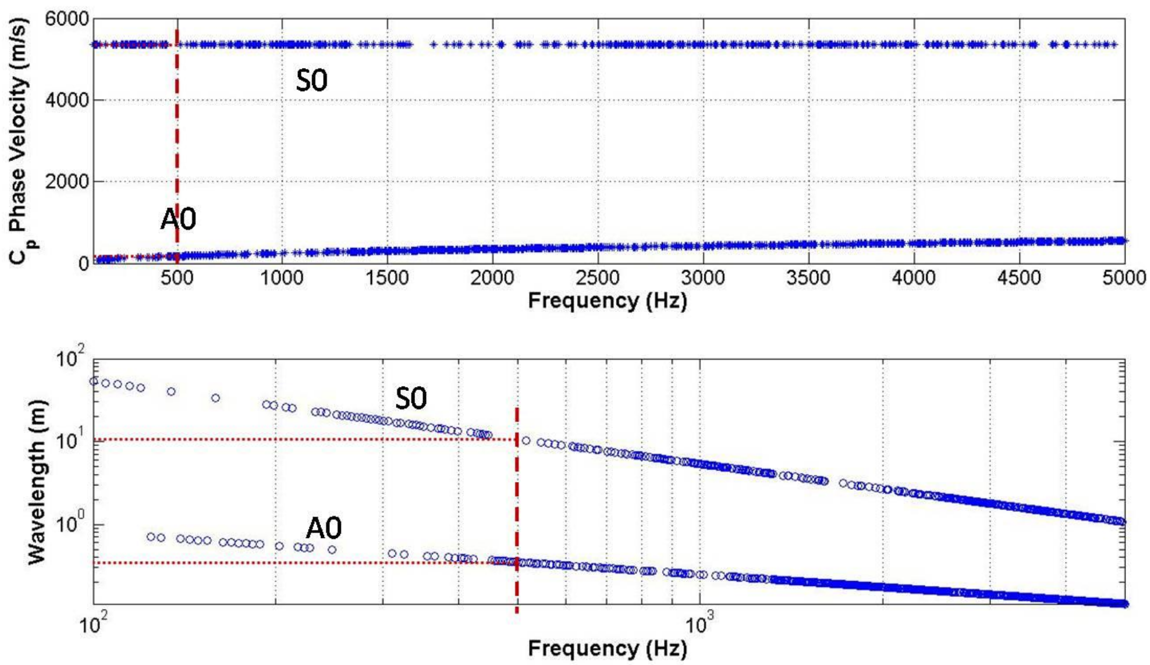

Figure 5.31. Phase velocity and wavelength for the A0 and S0 modes for the plate test structure.

The interrogation signal used in this investigation excites mainly the *A0* mode which is associated with bending waves and long wavelengths. It can be noted that at 500Hz, which is the upper bound of the retained frequency range, the wavelength of the *A0* mode is about 0.35m. By direct comparison between the damage size and the wavelength at 500Hz, it can be noted that the length of the detected damage is on the order of quarter wavelength. This is an encouraging result considering that, as a general rule of thumb, to assure a certain sensitivity to the damage, the half wavelength of the interrogation signal should be on the order of the damage size (or shorter). Results show that this technique has the capability of localizing the damage by exploiting low frequency ranges. Different benefits are associated with the use of low frequencies such as high Signal to Noise (S/N) ratios, lower mechanical impedance (i.e. easier injection of energy into the system), possibility to exploit operational loads (rotor loads, structural vibrations) actuating the damage detection system in passive mode (i.e. without active interrogation) etc.

These numerical analyses were intended to support a feasibility study proving the validity of the theoretical concept and of the numerical implementation for the proposed localization technique. A higher accuracy could be probably obtained by using pure compressive waves (S0 mode) that should provide larger changes in the Total Transmitted Intensity due to a higher interaction with the damage. Nevertheless, further analysis providing more rigorous information about the selection of the interrogation signal as well as its relation with the overall accuracy will be left to future studies.

5.6 Summary

This chapter introduced the concept of Structural Intensity (SI) as a possible tool for damage detection. In the past years, the SI technique was considered for several applications in the structural vibration and noise control fields. A very limited number of studies were carried out, however, to investigate the SI performance as a damage detection technique. After introducing the SI theoretical background, a possible metric to correlate the characteristic of the damage to changes in the SI field was presented. This metric was denominated Total Transmitted Power (TTP). A sensitivity study was then performed to evaluate the effects of structural, numerical and experimental parameters on the SI field. The correlation between these parameters and the SI were addressed in terms of the proposed TTP metric.

The sensitivity study highlighted the important role played by the characteristic structural loss factors and the nature of the damage on determining the SI field. In order to tailor these numerical results towards more specific applications on helicopter transmission frames, experimentally measured loss factors were acquired on a UH-60 helicopter and used for the numerical simulations. The parametric study provided also interesting directions for further enhancement of the SI based damage detection technique.

The chapter concluded with the formulation of a damage localization technique for detecting linear type of defects. The technique, based on the use of the TTP metric, assumed the existence of multiple energy sources which allowed for interrogating different part of the structure. The results from a numerical feasibility study showed that this technique was capable of localizing damage with discrete accuracy by using very low frequency interrogation signal (0-500Hz).

CHAPTER 6

Active Energy Sink: Design and Experimental Testing

The numerical results, presented in Chapter 5, highlighted the reasons and the benefits associated with the use of a tunable energy sink in order to optimize a SI based damage detection technique. Experimental investigations (Appendix) highlighted the difficulties of using a passive energy sink at the fundamental modes. The passive sink was not capable of introducing a sufficient amount of damping to control the energy flow at all frequencies of interest.

In this chapter a new concept of energy sink, specifically designed for structural intensity applications, is described. The new system is realized through a network of actively controlled transducers for energy dissipation and is referred to as an Active Energy Sink (AES). The concept of an active energy sink is first introduced analyzing the main technical requirements of the system. The AES concept is then proven through a simplified experimental configuration which relies on the use of electro-magnetic actuators. This approach was meant to test the validity of the concept and the potential to induce a dominant and stable energy sink. The theoretical approach and the experimental results will be presented in terms of induced active damping and SI maps.

The concept of AES is then extended to a possible implementation through a network of surface mounted piezoelectric transducers. Some parameters and the experimental procedure used to study the AES are based on the SI experimental measurement technique outlined in the Appendix. A preliminary reading of the Appendix could facilitate the understanding of the experimental analysis presented in this chapter.

6.1 Active Energy Sink Concept

In order to induce an energy flow following a precise path (i.e. from the source of the interrogation signal to the energy sink) the *energy sink* must be dominant with respect to the other sources of energy dissipation. When only a single energy source/sink pair is present in the system, even a weak energy sink is able to induce a clear energy flow. In this case, the energy injected at the source can exit the structure only at the energy sink. In real structures, however, the presence of structural joints, passive and active vibration control systems, non metallic materials, fluid-structure coupling etc., creates a situation where multiple (concentrated and distributed) energy sinks coexist at the same time.

A similar situation can occur for the energy source(s), particularly in an operational environment. For aeronautic structures the presence of external aerodynamic loads and of external/internal operating loads (rotor loads, propulsion system, etc.) creates a situation where the energy is injected into the structure at different locations due to both distributed and concentrated loads. This results in a situation where multiple energy sources and sinks, which are not necessarily related to the damage detection system, coexist at the same time.

In this scenario, the possibility to control both the amplitude and the location of the energy sources and sinks, assumes an important role in determining the overall performance of the SI-SHM system. The AES concept is based on the development of an energy dissipation system realized through a network of piezoelectric transducers (PZT), bonded onto the host structure, which can be controlled in real time through prescribed control logic.

Such a system will provide two major advantages over the passive energy sink:

1. User selectable sources and sinks locations.
2. Tunable dissipative power.

Through the AES network, each transducer can be effectively used either as actuator or sensor (or, equivalently, as energy source or sink). By activating prescribed pairs of transducers the user (or autonomous control logic) can decide how to place the energy source and sink for improving damage sensitivity and detectability. By controlling both the energy source/sink location and the frequency of the excitation signal the user can gain a considerable control on the energy path. This suggests that through the AES system the energy associated with the interrogation signal can be focused on specific areas, increasing the interaction between the interrogation signal and the structural damage.

Figure 6.1 shows a schematic of the possible paths that could be achieved by using transducer #1 as actuator and transducers #2, #3 and #4 as energy sinks, respectively. Along with the control of the location of the source-sink pair, the AES allows controlling the power dissipated at the energy sink or, in different terms, the amount of equivalent localized damping introduced into the system.

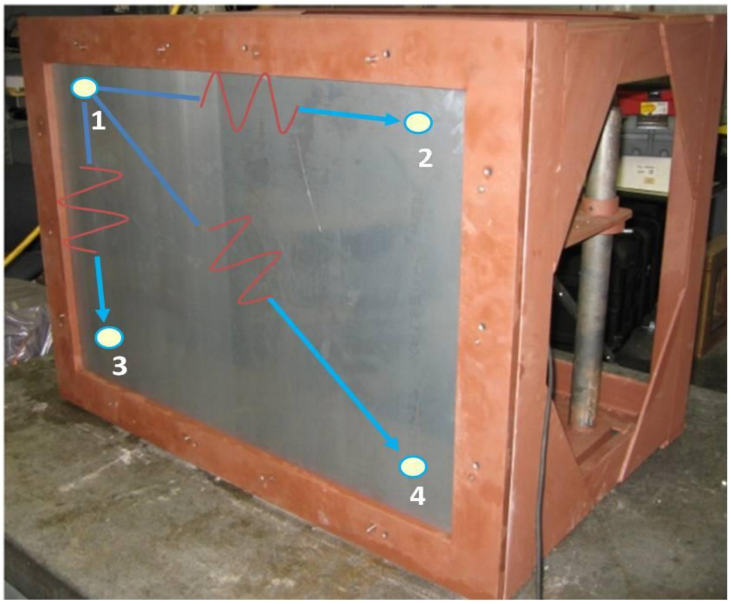

Figure 6.1. Schematic of the Active Energy Sink network.

The sensitivity study to the damping (Chapter 5) showed the existence of a working point which maximizes the TTP. This optimal point is defined by a specific value of the sink equivalent damping which allows matching the mechanical impedance of the system. The structural damping, as well as other external sources of damping, are inherent characteristics of the system and cannot be controlled. To optimize the power transmissibility therefore the only possibility is tuning the energy sink.

6.2 Active Control Development Strategy

The development of the AES concept was carried out in two different steps. The first step consisted of using an electro-magnetic shaker to control the out-of-plane dynamic response at a prescribed location. This initial step was meant to prove the conceptual design and the possible implementation of an active energy sink for structural intensity applications via feedback controlled actuators.

Once the first step was completed and the efficacy of the AES concept was demonstrated, the next step consisted of designing and developing the AES through a network of piezoelectric transducers located on the surface of the host structure. This second step becomes crucial for transferring the AES technology to complex system in operating conditions where the transducers must be surface mounted.

Although the AES works in principle as an active structural vibration control system, there is a main difference between the active energy sink and a vibration control device. In order to have a real energy sink the controller must be able to continuously extract energy from the system. In analytical terms this means that the power produced by the controller must always be negative. This condition is not necessarily true for an active vibration control system, especially if the control is non-collocated. In this last case, the controller might inject energy into the system in order to reduce the amplitude of the vibration at a different structural location by destructive interference.

6.3 Electro-Magnetic Shaker based Active Energy Sink

The validity of the AES concept was first demonstrated using an electro-magnetic (EM) shaker as a control device. The test structure consisted of the aluminum plate used in Appendix A for experimental SI measurements. The passive damper was replaced with an electro-magnetic shaker inserted in the control loop. The schematic of the experimental test bed is shown in Figure 6.2.

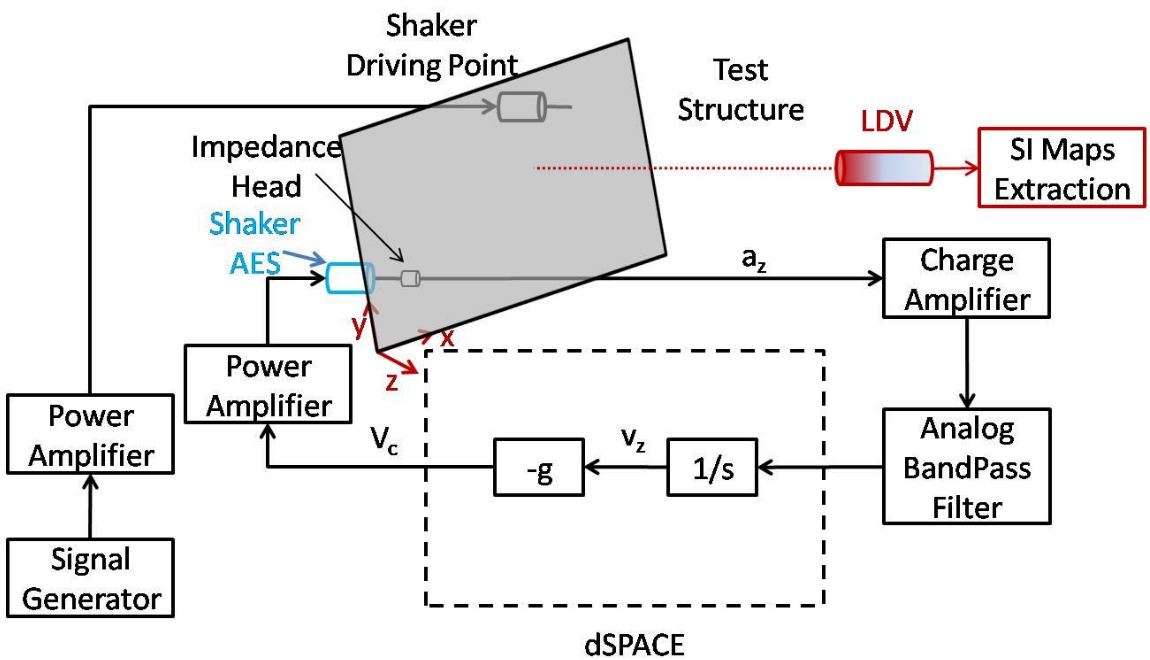

Figure 6.2. Schematic of the electro-magnetic shaker based AES closed loop.

The plate was excited in the out-of-plane direction through an EM shaker driven with a sinusoidal input signal at a prescribed frequency. The signal was produced by an external signal generator and then fed into a power amplifier.

The plate response was collected in terms of acceleration, a_z, at the AES location through an impedance head mounted on the shaker stinger. The acceleration signal, a_z, was amplified and bandpass filtered around the frequency to be controlled. The filtered signal was then fed into the real time control system to generate the control signal V_c which will drive the second actuator (AES shaker).

The closed loop control was developed with a dSPACE 1103 control system. The system ran in real time using a control model previously developed in SIMULINK®. The controller implements a direct velocity feedback control algorithm.

In order to test the design and the performance of the AES, it was decided to acquire SI maps in opened and closed loop configurations. In this way, a clear assessment of the AES performance can be produced by looking at the power flow path and at the divergence plots. The dynamic response of the test structure was measured through a Laser Doppler Vibrometer (LDV) system and the SI and divergence maps were calculated according to the procedure described in Appendix A.

6.3.1 Direct Velocity Feedback Control

The control algorithm selected for the shaker based AES relies on a Direct Velocity Feedback (DVF) control. The DVF is a well established algorithm which is particularly suitable for collocated control [116]. Besides being a simple controller, it has a very attractive characteristic for possible implementation in an AES system. Assuming ideal dynamics (linear and stationary) of the transducers this scheme guarantees continuous energy absorption at the control point [117]. If $v(t)$ is the velocity measured at the same location where the shaker is attached (collocated sensor/actuator configuration), the control force $F(t)$ produced by the shaker can be written as:

$$F(t) = KV(t) = -Kgv(t) \qquad\qquad g, K \epsilon R^{+} \qquad (6.1)$$

where *V(t)* is the input voltage to the active shaker, g is the closed loop gain and K is a parameter describing the dynamic of the shaker. The output force *F(t)* is proportional to the input voltage *V(t)* through a constant *K*. The voltage *V(t)* is chosen to be proportional to the velocity through a positive constant g which is the gain of the loop. The minus sign creates a 180 deg shift between the input and the output force. This kind of control logic implements a control force proportional to the velocity and, therefore, equivalent to a viscous damper. The power produced by the control system in the present configuration can be written as:

$$P(t) = F(t)v(t) = -Kgv^{2}(t) \leq 0 \qquad (6.2)$$

Eqn. (6.2) proves that the control system theoretically guarantees continuous energy absorption. As shown in Figure 6.2, the controller was implemented feeding the measured acceleration into a pure integrator in order to get the out-of-plane velocity profile $v_z(t)$. The velocity $v_z(t)$ was then multiplied by a negative gain and used to generate an analog output voltage that, once amplified, drove the AES shaker. This approach can be described, in the Laplace domain, by the following control law:

$$V(s) = \frac{-g}{s} a_z(s) \qquad (6.3)$$

where *V(s)* is the control voltage to the AES shaker, $a_z(s)$ is the acceleration input signal to the controller, g is the loop gain, and $\frac{1}{s}$ is an integrator in the Laplace domain..

6.3.2 AES Experimental Results

SI maps were acquired for both open and closed loop configurations using the experimental setup previously described. The specific plate that was used to test the AES had a 5” saw cut in the center. The presence of the crack does not create any loss of generality to the presented results.

Note that in the open loop configuration the shaker was still mechanically attached to the test structure. A small percentage of damping, due to friction of the shaker internal components, was still present in the system. In order to minimize the damping due to “shunt-like” effects (i.e. energy dissipation in internal resistors) the AES shaker was electrically disconnected from the control loop. An image of the experimental configuration showing the shakers layout is given in Figure 6.3.

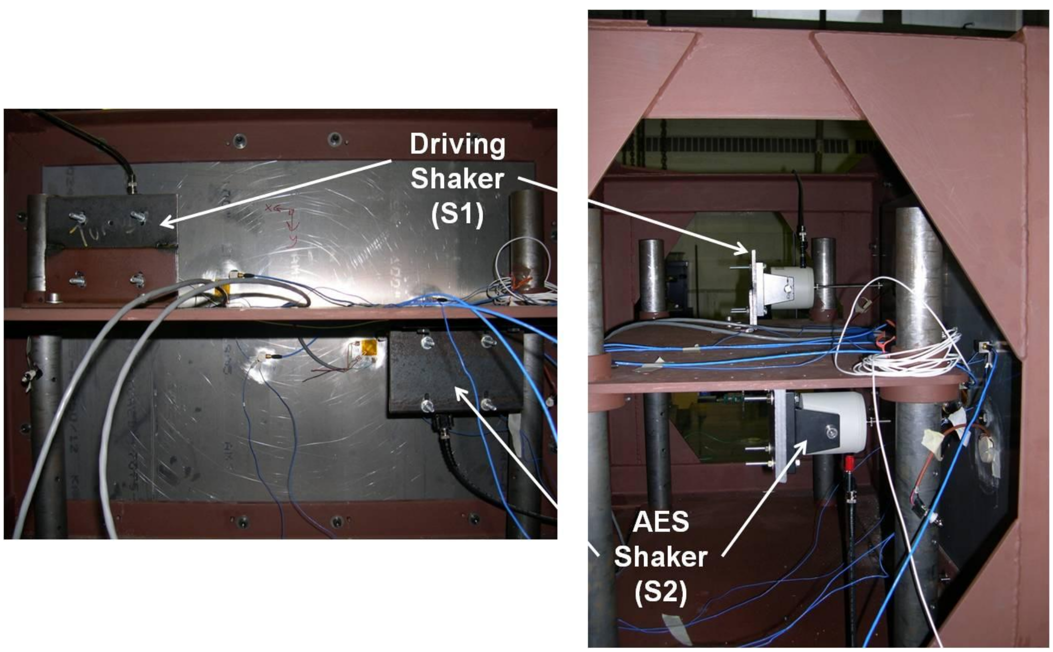

Figure 6.3. Experimental setup for the AES testing with shaker actuators. (left) rear view, (right) side view.

The experimental results were mainly collected at low frequencies where the passive damper was not able to provide a dominant energy sink. A comparison between open and closed loop response is presented in terms of SI maps, divergence plots and equivalent loss factors. Four resonant modes corresponding to frequencies of f_1=37.5Hz, f_2=50Hz, f_3=91Hz and f_4=141.6Hz were selected for the test.

Figure 6.4 shows a summary of the experimental results by providing the percentage increase in the loss factors between open and closed loop. For each frequency the Operating Deflection Shapes (ODS) are also reported in order to facilitate the understanding of the underlying dynamic response.

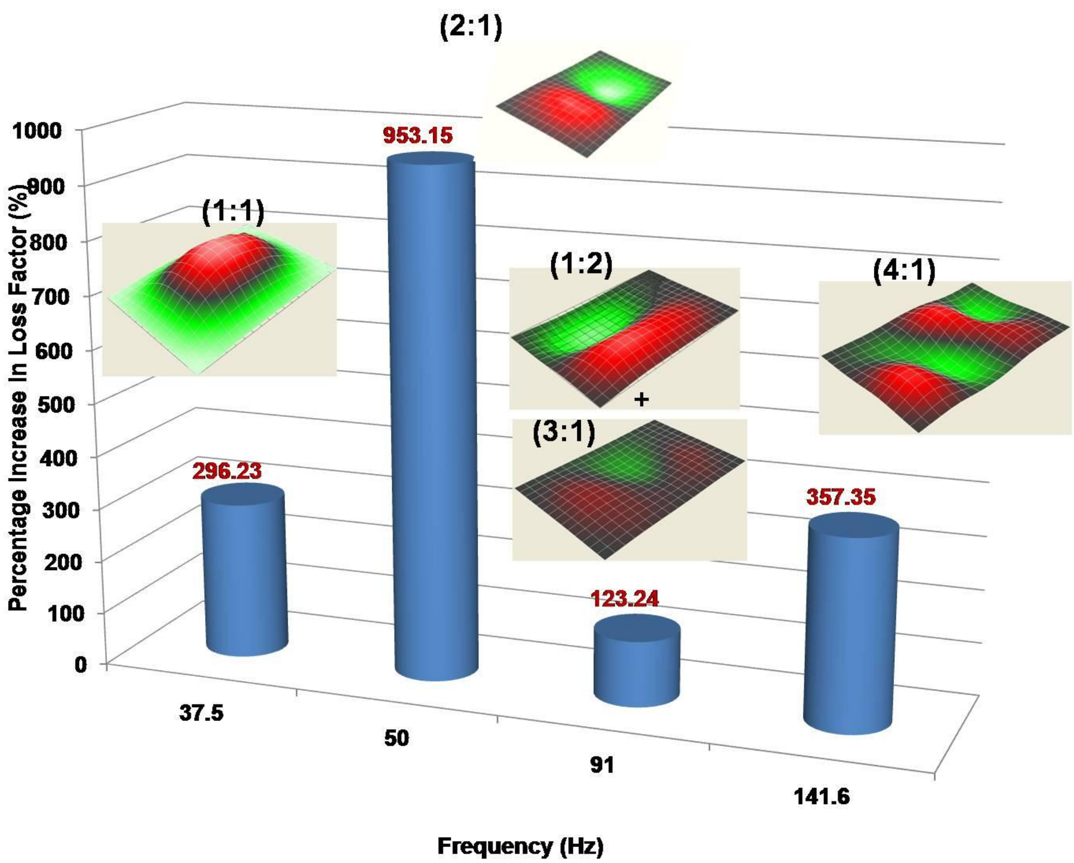

Figure 6.4. Percentage increase in the loss factor between open and closed loop. For each frequency the corresponding ODS is also shown.

The introduction of the active control produced a consistent increase of the loss factors at the four tested frequencies. In particular, the mode (2:1) was associated with the highest damping increase (~950%). This was due to the position of the active shaker relative to the peak of the ODS. For the mode (2:1) the maximum displacement of the second lobe occurred at the attachment point of the control device which conferred it large authority.

In this experimental investigation, transient measurements allowing for the estimate of the absolute value of the loss factors were not collected. In order to provide a general indication of the loss factor values, an estimate was done based on damping measurements available from data acquired on the healthy structure. From the frequency response functions collected on the healthy structure with and without the constrained layer damper, the loss factors can be estimated. As an example, the loss factor for the (2:1) mode at 50Hz is about η=0.03 either in the undamped or passive damped configuration. At this frequency the CLD passive damper was particularly ineffective (as shown by the SI maps [118]) therefore it is not surprising that the damping between the two configuration did not change. The configuration with the AES in open loop still applied a small amount of damping. Hence, it could be reasonably assumed that the loss factor will fall somewhere in between the undamped and damped (CLD) configurations. Assuming an open loop loss factor of η_{op}=0.03 and applying the previously estimated percentage increase, the loss factor in closed loop configuration for the mode (2:1) can be approximately estimated at η_{cl}=0.29.

The loss factors study highlighted that the active controller was particularly effective in increasing the damping of the system. The evaluation of the loss factor was a necessary but not sufficient condition to prove that the controller was working as an energy sink. The efficiency of the active controller was proven by acquiring SI maps and divergence plots in both open and closed loop. The results for the four selected modes are presented in Figure 6.5 to Figure 6.8. The red and blue circles show the location of the energy source and sink, respectively. It must be noted that the SI and divergence were not plotted in the same magnitude scale. This approach was chosen in order to improve the readability of the plots that span wide dB ranges.

The SI maps show that the increase in the localized damping resulted in establishing a clear energy flow. The divergence plots provide additional insight into the effect of the AES by indicating the location of the energy source and sink. As a reminder, the energy source is associated with a maximum in the divergence field, and the energy sink is associated with a minimum. The direct comparison of the SI maps clearly evidences the role of the AES. The considerable increase in the localized damping at the sink location, due to the feedback control, induces a well defined energy path (from the source to the sink). This is particularly visible in Figure 6.5 and Figure 6.6 where in the open loop the energy flow is clearly reverberant. The associated divergence plots also clearly show the location of the energy source and sink in the closed loop condition, while in the open loop this indication is absent. The same trend is also visible for the third and fourth mode in Figure 6.7 and Figure 6.8. In this case, the higher driving frequencies are associated with a higher equivalent viscous damping (which is proportional to the velocity) in the open loop. This justifies the presence of a defined energy path also in the open loop. The direct comparison of the divergence plots, however, shows the effectiveness of the AES through the clear indication of the source and sinks locations.

As a further remark, it should be observed that the SI localized maximum in the center of the plate, particularly visible at f_1 and f_2, is a clear signature of the damage. In the damaged area, the energy cannot flow through the cut and undergoes a sudden change in the direction (due to the structural discontinuity). The energy flow separates at the damage location and rejoins immediately after. This mechanism explains why the damage always appears in the divergence plot as a pair maximum/minimum.

For the sake of completeness, the SI maps and divergence plots obtained with the CLD passive damper (Appendix A) are also reported. A direct frequency match between the AES and the CLD data was not readily available. Nevertheless, in a few hertz bandwidth around the resonance the SI maps generally keep the same profile, even if the associated magnitude may undergo consistent changes. In order to compare the effectiveness of the AES in establishing a clear energy path this is a minor issue. Being aware of these discrepancies, a comparison between the AES and the CLD can still be done. The experimental results for a healthy plate with the CLD damper at 54Hz, 94Hz and 140Hz are shown in Figure 6.9 and Figure 6.10. The comparison between the CLD and the closed loop results confirm the improvement previously observed comparing open and closed loop. This was expected considering that the loss factor between CLD and AES in passive mode (i.e. open loop) were comparable. The SI distribution for the CLD and the open loop configurations (shaker in passive mode) must therefore be consistent.

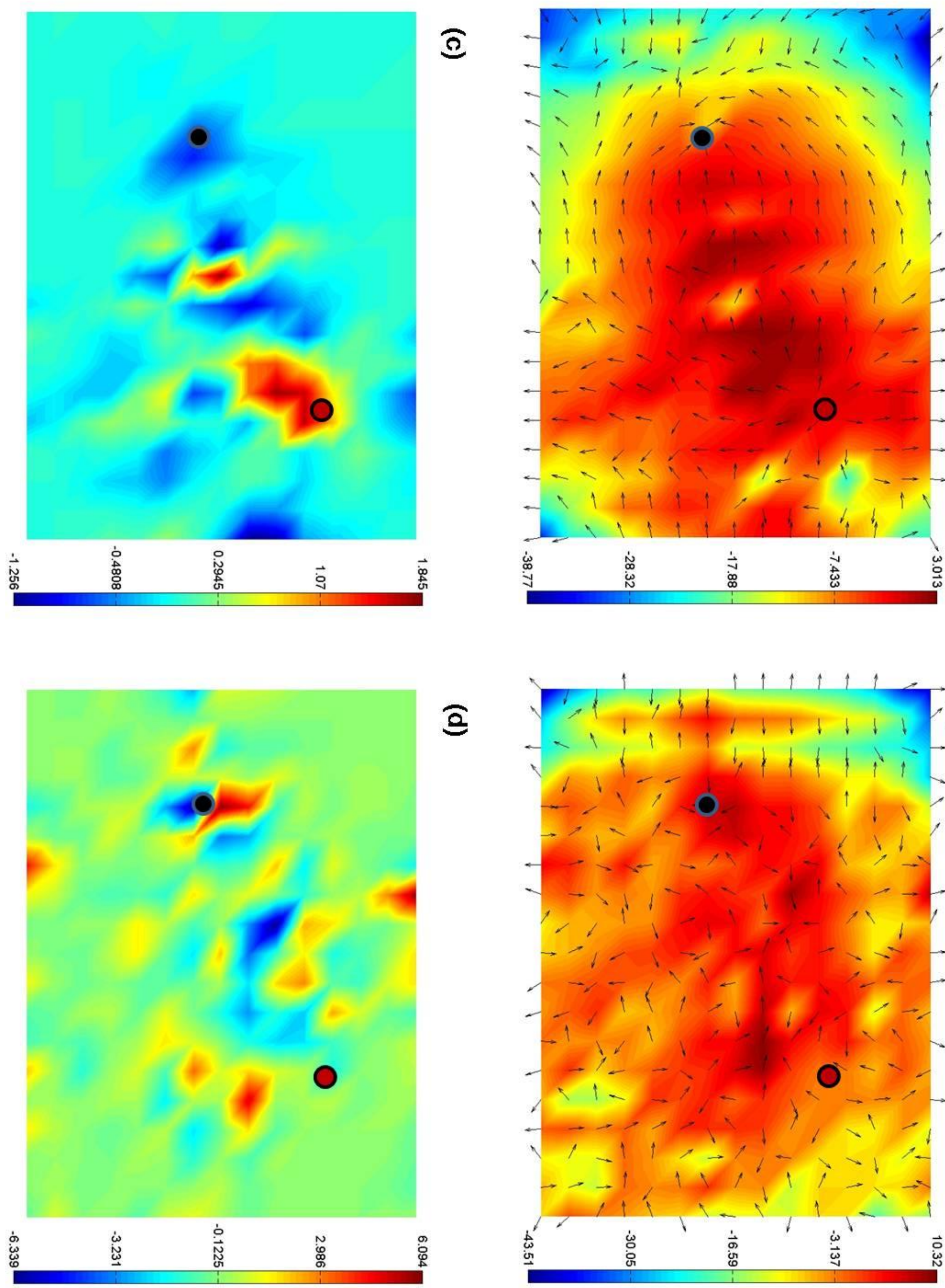

Figure 6.5. SI plot for the mode (1:1) at f=37.5Hz; (a) closed loop SI map and (c) divergence; (b) open loop SI map and (d) divergence. Red dot: Source; Black dot: Sink.

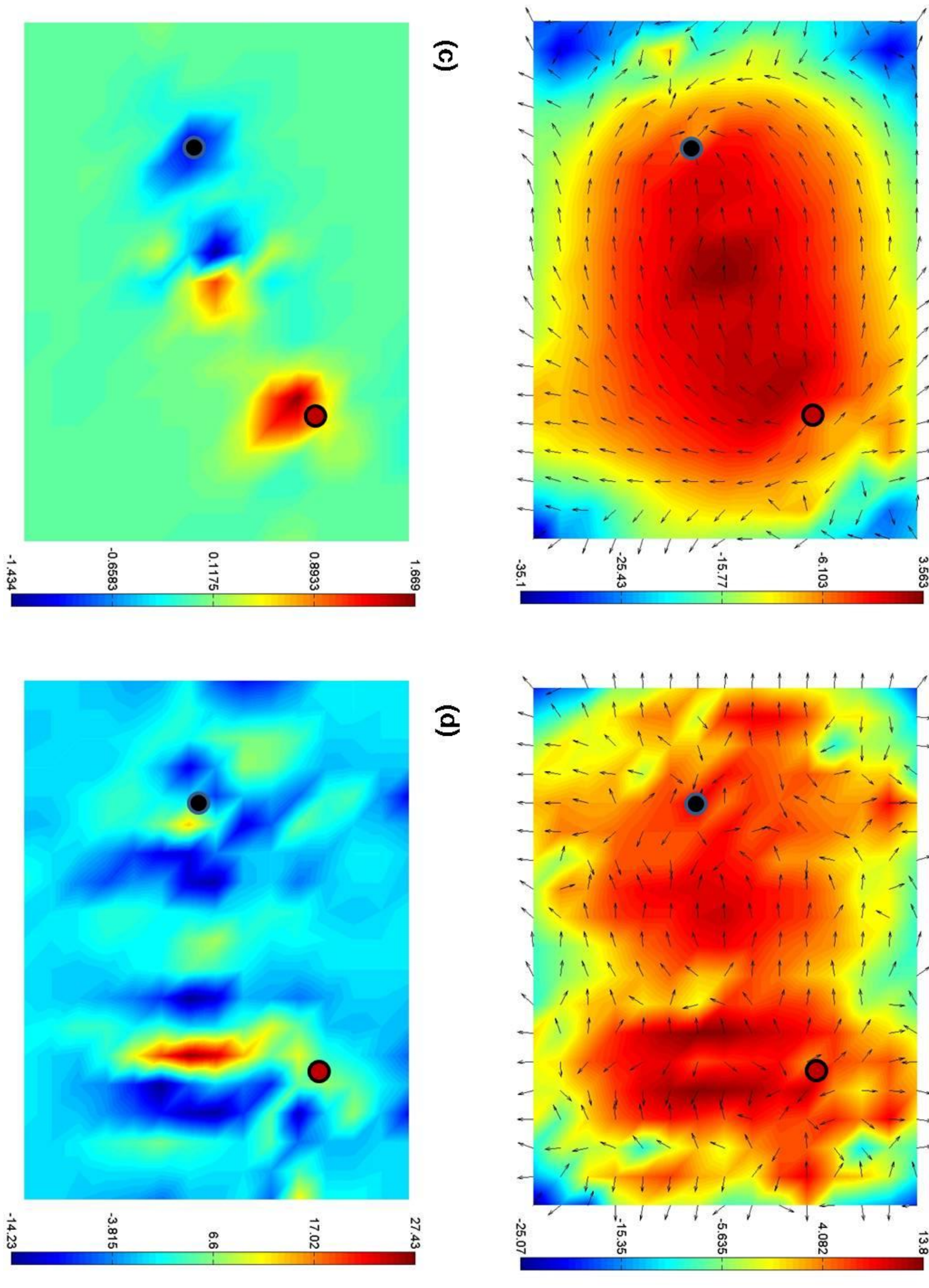

Figure 6.6. SI plot for the mode (1:1) at f=50Hz; (a) closed loop SI map and (c) divergence; (b) open loop SI map and (d) divergence. Red dot: Source; Black dot: Sink.

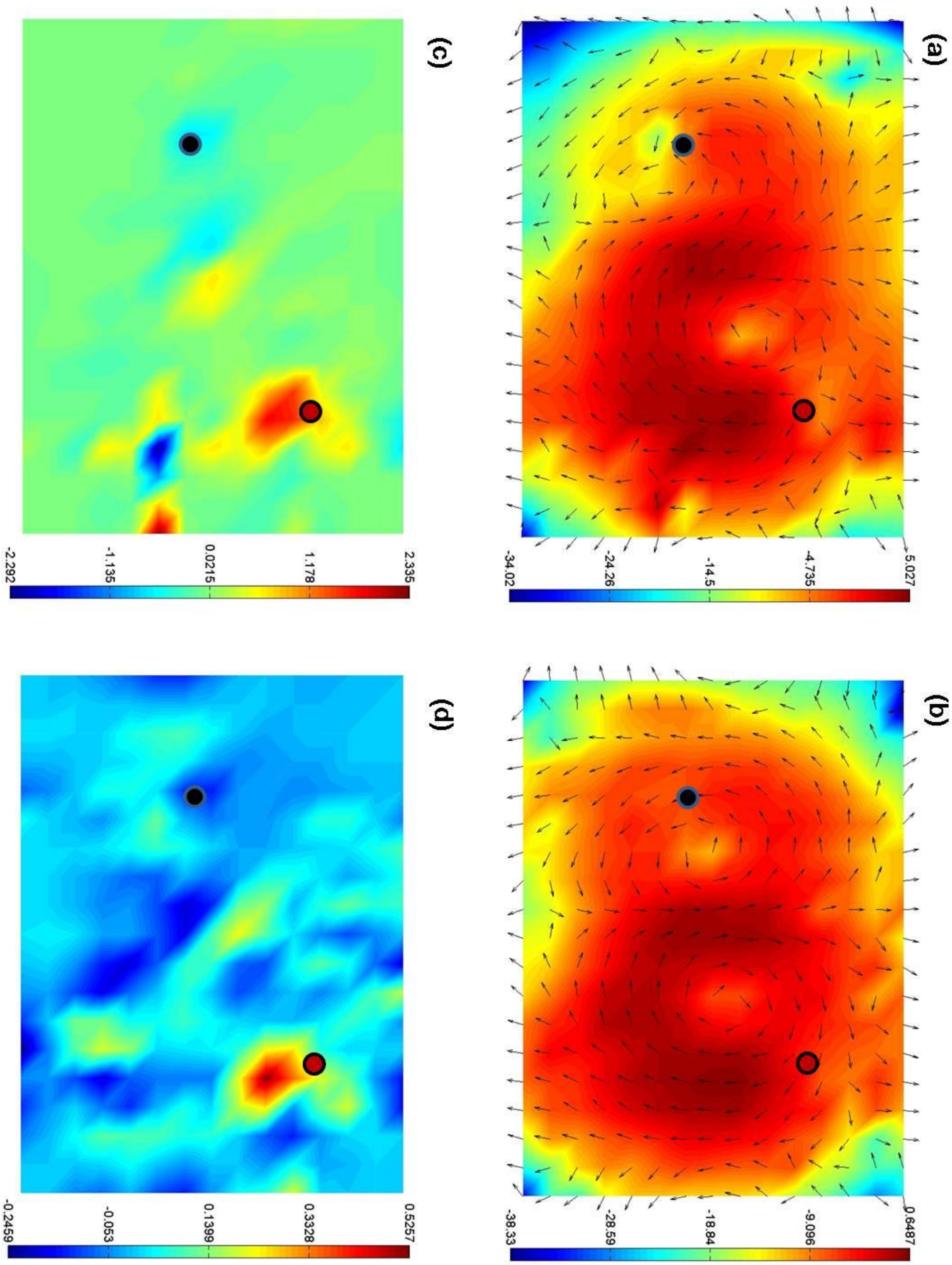

Figure 6.7. SI plot for the mode (1:1) at f=91Hz; (a) closed loop SI map and (c) divergence; (b) open loop SI map and (d) divergence. Red dot: Source; Black dot: Sink.

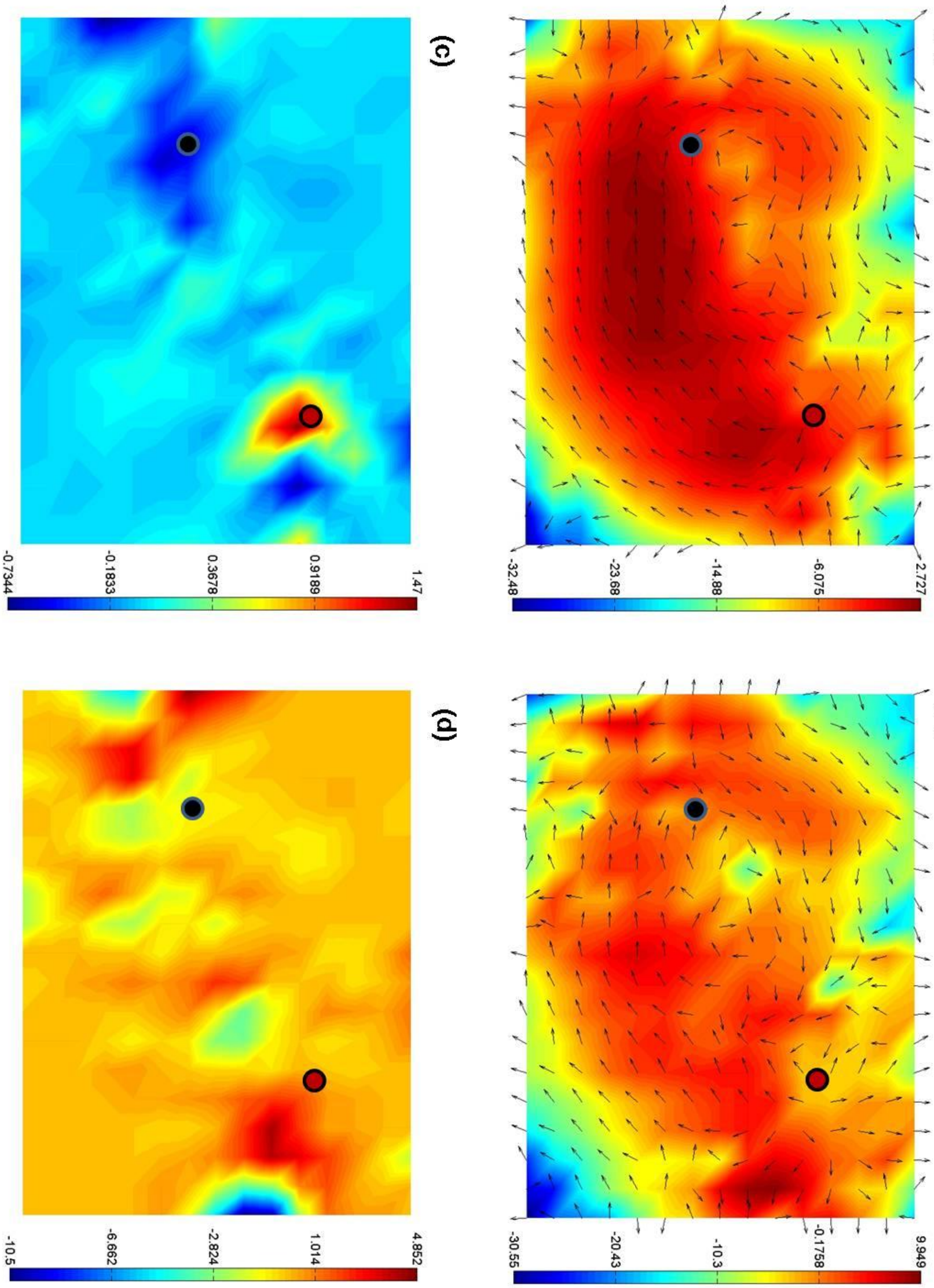

Figure 6.8. SI plot for the mode (1:1) at f=141.6Hz; (a) closed loop SI map and (c) divergence; (b) open loop SI map and (d) divergence. Red dot: Source; Black dot: Sink.

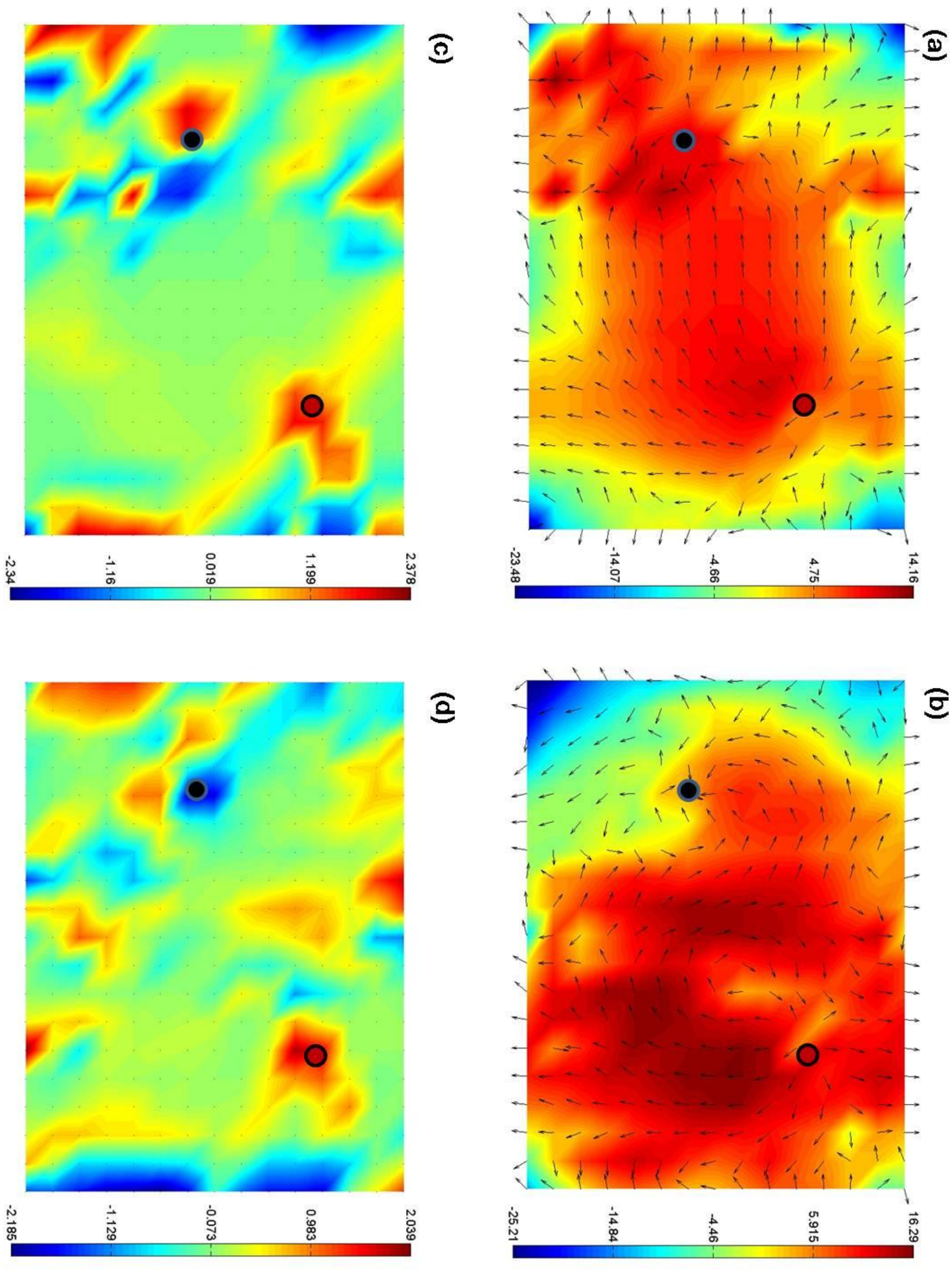

Figure 6.9. SI plot for the CLD configuration; (a) 54Hz SI map and (c) divergence; (b) 94Hz SI map and (d) divergence. Red dot: Source; Black dot: Sink.

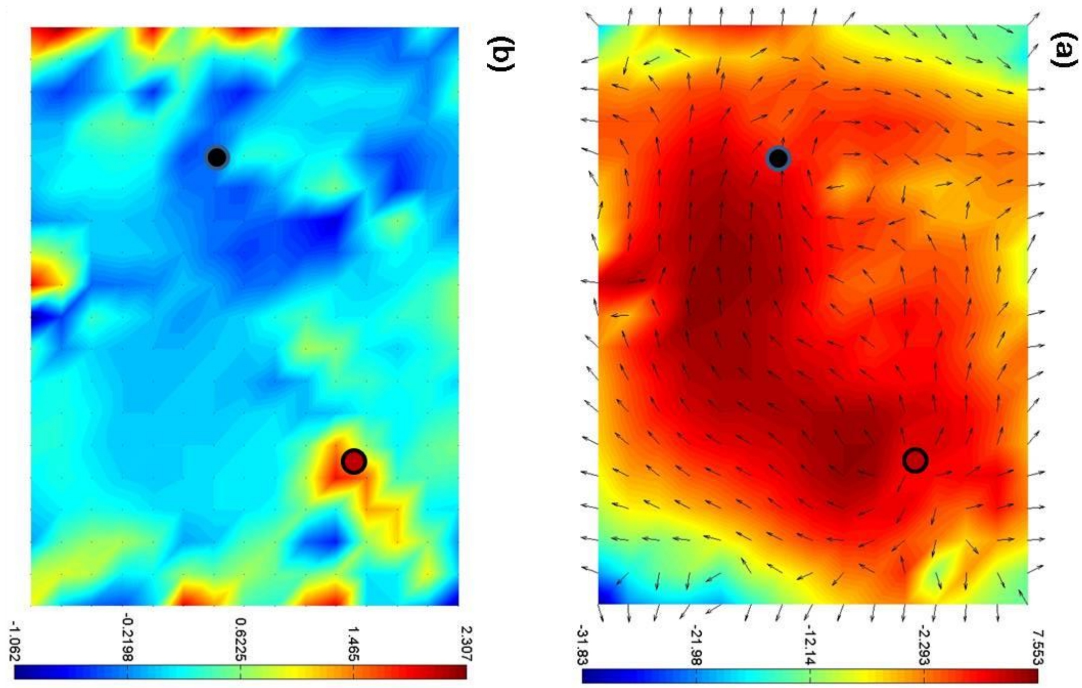

Figure 6.10. SI plot for the CLD configuration; (a) 140Hz SI map and (b) divergence.

The SI flow has many similarities with the results previously proposed for the AES in open loop. This is not surprising considering that the damping study revealed very similar loss factors between the CLD configuration and the AES in open loop.

The SI map for the (1:1) mode at 37.5 Hz in the CLD configuration was not available. The complete lack of effectiveness of the damper at this specific frequency made the flow completely reverberant. For this reason this frequency was never selected for damage detection purposes.

6.4 PZT based Active Energy Sink

In the previous paragraphs, it was experimentally demonstrated how the active energy sink concept for structural intensity applications can effectively be designed and implemented using a closed loop control. In order to move the AES concept forward towards a more realistic application on helicopter structures in operating conditions, the next step consisted in implementing the active system through surface mounted transducers.

In this study, the possibility of implementing an AES concept through piezoelectric sensors was investigated. Piezoelectric transducers (PZT) provide several advantages for a real time application. They can be easily mounted on the surface of the host structure and allow implementing a collocated control where the same device can be simultaneously used as a sensor and an actuator. The collocated transducer capability takes advantage of both the direct and indirect piezoelectric effect [119,120]. When a piezoelectric element is strained due to an applied external load it generates a surface charge and a difference of potential on the two electrodes. This phenomenon, called the direct piezoelectric effect, can be exploited to use the PZT element as a displacement sensor, strain gauge etc.. On the contrary, if a difference of potential is applied at the two electrodes the piezoelectric element will undergo a mechanical deformation. This last behavior is called the indirect effect and can be exploited to use the piezoelectric element as force transducers.

When a piezoelectric device is attached to a mechanical system, the direct and indirect effects can be simultaneously exploited in order to sense and actuate the structure at the same physical location. In this case, the transducer is called “collocated”. For a feedback control, the use of collocated transducers considerably increases the stability of the loop [121]. In order to use the PZT as a collocated transducer, a specific approach must be followed in order to decouple the voltage produced by the direct effect from that one associated with the indirect effect.

The possibility to exploit the self-sensing capability of a PZT transducer for collocated control purposes was originally proposed by Dosch [122] and Anderson [123]. In their studies, an *impedance bridge* was developed to extract the contribution of the active control and of the strain sensor from the overall difference of potential measured at the two electrodes.

The following section will deal with the conceptual design of a PZT based AES allowing for the implementation of an energy sink through a collocated strain rate feedback control.

6.4.1 Strain Rate Feedback Control

In order to use a PZT element as energy sink for SI applications a proper control logic must be applied. The control must be able to sense the dynamic response and to simultaneously apply a control voltage which results in mechanical power absorption. According to previous studies [122,123] investigating the active vibrations control of a cantilevered beam through collocated transducers, the strain rate feedback control was selected as an attractive option to implement the AES concept. The strain rate feedback control is relatively easy to implement, stable (under the assumption the impedance bridge is balanced) and generally more sensitive than strain feedback (another technique for pzt collocated control) for controlling high frequency modes.

The preliminary design of a PZT based AES followed the same guidelines applied to the electro-magnetic shaker based active control device. A single PZT element was bonded onto the host structure at the same location where the active shaker was originally attached (Figure 6.11). The active PZT element was then connected to the data acquisition system and to the controller following the schematic in Figure 6.12. The PZT based experimental setup was similar to what shown in Figure 6.2 for the EM shaker. The only exception of the circuitry (impedance bridge) needed to decouple the electric signal from the collocated transducer.

The impedance bridge allows the simultaneous measurements of the voltage V_1 and V_2. The voltage V_1 is composed by the sum of the actuation voltage and the voltage produced by the strain of the piezoelectric element. The voltage V_2 instead is due only to the control voltage.

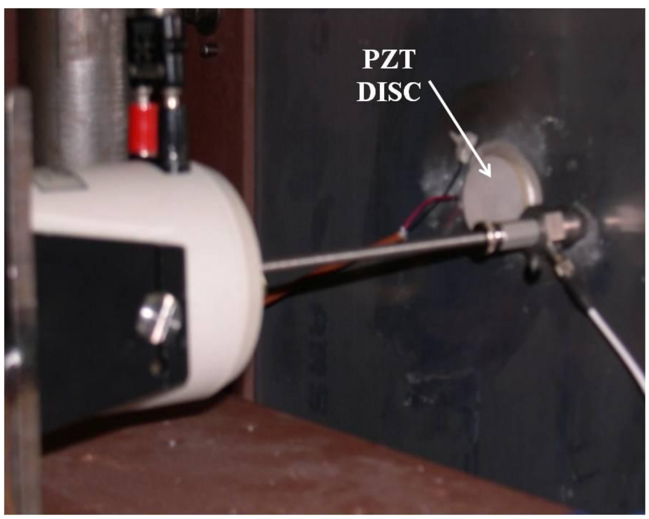

Figure 6.11. Piezoelectric transducer disc used for the AES implementation.

Subtracting V_2 from V_1 one can measure the portion of the voltage that is due to the strain on the PZT material induced by the dynamic response of the host structure.

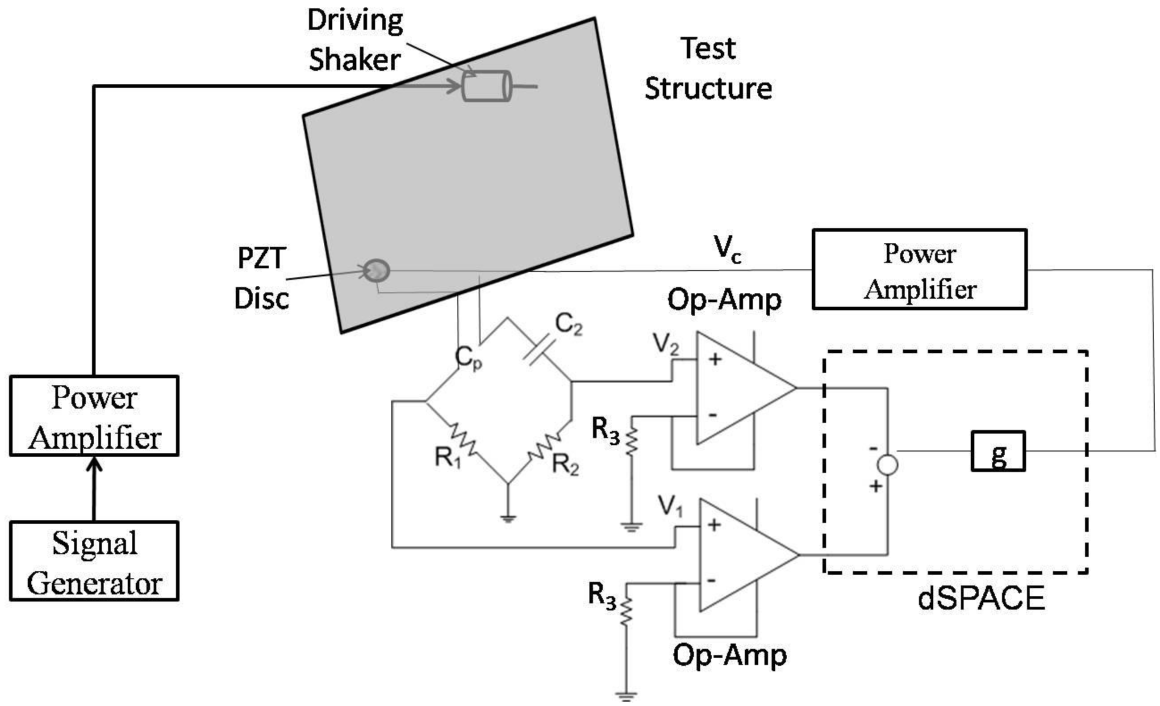

Figure 6.12. Schematic of the closed loop implementing the AES through PZT devices.

The impedance bridge is also needed to avoid short-circuiting the PZT element when connecting both the input and output channels of the control system. The output channel has almost null impedance which will result in short-circuiting the PZT element preventing the charge accumulation due to the mechanical strain.

According to [122], the circuit in Figure 6.12 can be described by the following equation in the Laplace domain:

$$V_s(s) = V_1(s) - V_2(s) = \frac{R_1 C_p s}{1 + R_1 C_p s} V_p(s) + \left(\frac{R_1 C_p s}{1 + R_1 C_p s} - \frac{R_2 C_2 s}{1 + R_2 C_2 s} \right) V_c(s) \qquad (6.4)$$

where $V_s(s)$ is the overall sensor voltage, $V_1(s)$ is the total voltage measured on the PZT (composed by the control voltage and the voltage produced by the vibrating PZT), $V_2(s)$ is the control voltage, $V_p(s)$ is the voltage due to the strained PZT, $V_c(s)$ is the control voltage, R_1 and R_2 are resistors, C_p is the capacitance of the PZT element, C_2 is the capacitance inserted in the impedance bridge to measure the control voltage ans s is the Laplace variable.

By choosing the time constants τ of the two branches to be equal:

$$\tau_1 = R_1 C_p = R_2 C_2 = \tau_2 \tag{6.5}$$

The voltage produced because of the strain of the PZT material is given by:

$$V_s(s) = \frac{R_1 C_p s}{1 + R_1 C_p s} V_p(s) \tag{6.6}$$

If the following condition is satisfied:

$$\omega \ll \frac{1}{R_1 C_p} \tag{6.7}$$

Then Eqn. (6.6) reduces to:

$$V_s = \dot{V}_p \tag{6.8}$$

where $\dot{V}_p$ represents the time derivative of the voltage component due to the strain. Under these assumptions the impedance bridge allows for measurement of a signal that is proportional to the strain rate.

Once the measured voltage V_s is available it is fed into a dSPACE control system in order to close the loop. The output from the dSPACE system is a control voltage which drives the PZT device in real time. Considering that the impedance bridge allows measuring a quantity that is already proportional to the strain rate, the vibration control signal was obtained multiplying V_s by a negative gain:

$$V_c = -g V_s \tag{6.9}$$

Eqn. (6.9) implements a feedback control logic for collocated PZT actuators that conceptually is similar to the DVF approach used for the shaker control.

6.4.2 Experimental Results

An experimental investigation was conducted in order to test the design and the performance of the active energy sink based on piezoelectric collocated transducers.

For the experimental investigation a piezoelectric disc element, whose properties are summarized in Table 6.1, was bonded onto the aluminum plate using silver conductive epoxy.

Table 6.1. Dimensions and properties of the pzt disc used for the AES implementation.

PZT Element	***Dia (in)***	***Thick. (in)***	***Capacitance (pF)***	***d_{33} ($x10^{-12}$ m/V)***
PZT-502	1.5	0.186	3844	490

The piezoelectric device was connected to the control system according to the scheme in Figure 6.12. The impedance bridge was designed on an electric prototype board using a capacitance C_2=C_p=3600pF, R_1=R_2=R=10kΩ and two National Semiconductor LM741 op-amps, as shown in Figure 6.13.

In order to test the design of the control loop the plate was driven through the EM shaker with a limited bandwidth white noise input signal between 0-1kHz and 0-2kHz, respectively.

Note that this driving condition penalized the performance of the AES because of the predominance of the out-of-plane versus the in-plane displacement components. The surface mounted PZT actuator has a low authority on the out-of-plane displacements in a plate. These components can be controlled only through the coupling with the in-plane forces. On the contrary, the PZT is particularly effective in controlling pure in-plane components. For these reasons, the PZT based AES is expected to be effective for the implementation of the active energy sink in Structural Surface Intensity (SSI) applications, which can be dominated by in-plane components. A detailed description of the theoretical aspects of the SSI will be provided in Chapter 7.

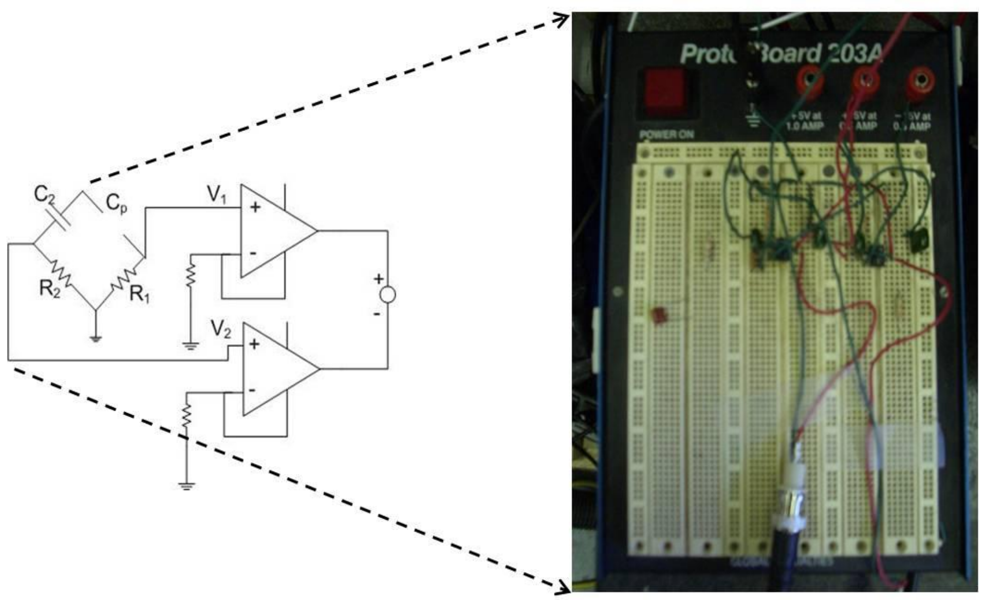

Figure 6.13. Implementation of the impedance bridge for collocated control.

The transfer function between the driving point and the energy sink location for the open and closed loop configurations are shown in Figure 6.14 and Figure 6.15. The input force signal was collected through the use of an impedance head mounted on the stinger of the driving shaker.

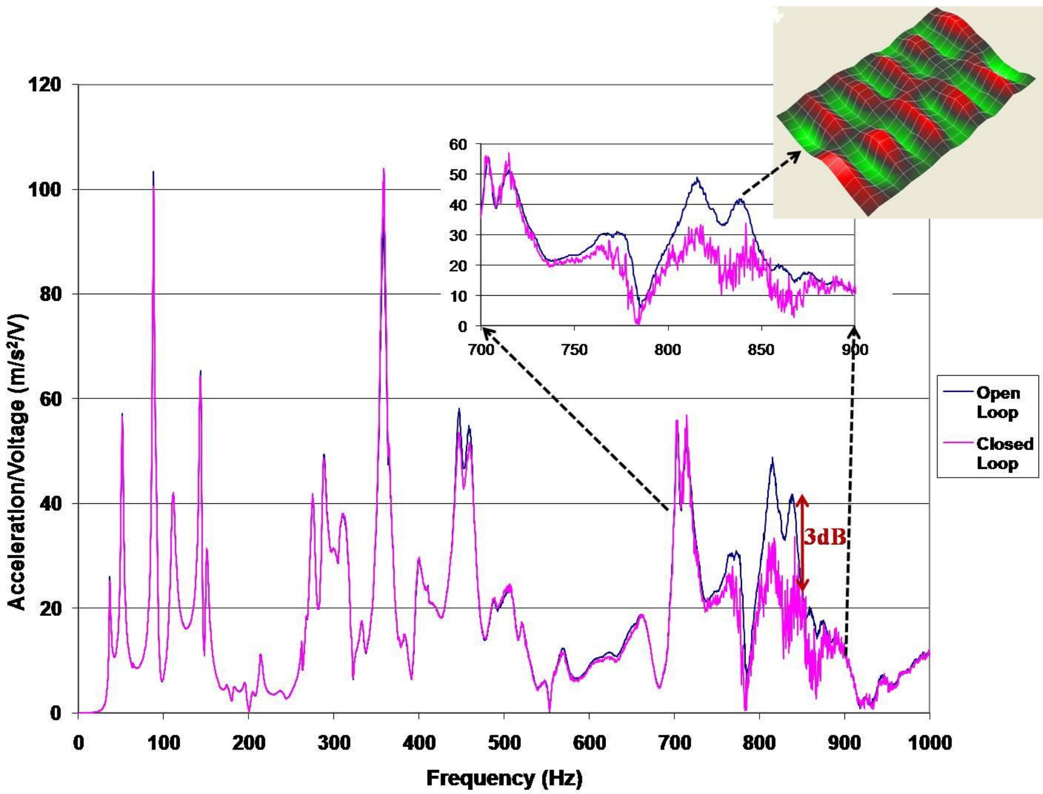

Figure 6.14. Transfer function in open and closed loop for the pzt based AES, frequency bandwidth 0-1kHz. A detailed view of the TF in the 700-900Hz BW and the ODS at 845Hz are also shown.

The response at a grid point close to the PZT energy sink was measured through the LDV. The input to the controller was lowpass filtered with a cutoff frequency f_c=2kHz to remove unwanted noise due to the high frequencies.

The results obtained through a band limited white noise driving signal in the range 0-1kHz are shown in Figure 6.14. A gain of g=-350 was chosen for the closed loop. This gain was selected by inspecting the point velocity at the PZT location measured through the LDV. This gain provided the maximum attenuation at the selected frequency. The PZT starts being effective (i.e. applying damping) in the high end of the frequency range. This behavior was expected because of the following reasons:

1. The PZT is designed to work in the KiloHertz/MegaHertz range depending on both material and geometric properties. As an example, the PZT element used in this experiment has the first radial resonance mode at 51kHz.
2. At low frequency the characteristic wavelengths are long compared with the footprint of the sensor.

The transfer function shows that the controller was able to apply 3dB attenuation at the two resonances occurring between 800Hz and 850Hz. Similar observations can be drawn for the results in the 1-2kHz frequency range (Figure 6.15).

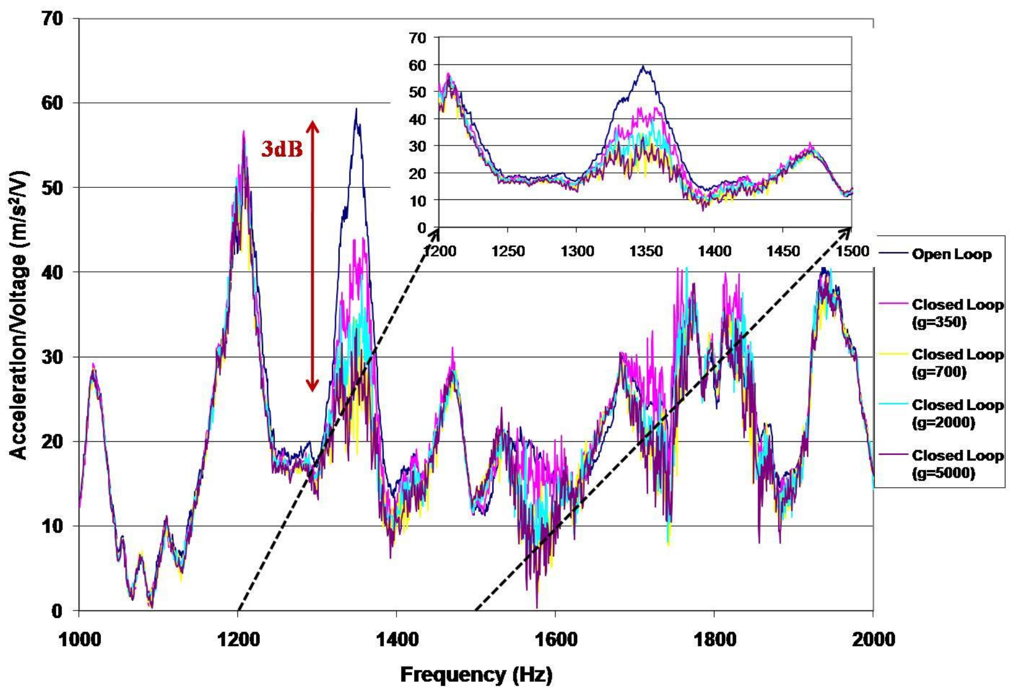

Figure 6.15. Transfer function in open and closed loop for the PZT based AES; frequency bandwidth 1-2kHz.

In this case a band limited white noise between 0-2kHz was applied and increasing gain values in closed loop were tested. The mode at 1348Hz showed a maximum attenuation equal to 3dB. The closed loop transfer function looked noisy especially in the range where the PZT was more effective. This background noise was related to the characteristics of the impedance bridge.

The impedance bridge is considered “balanced” when the capacitance C_2 matches the capacitance C_p of the piezoelectric element. This corresponds to the optimal working condition for the strain rate feedback control. An accurate estimate of the capacitance of the piezo-transducers is, however, complicated to obtain. The variability of the piezoelectric properties with the environmental and operating conditions makes this task even more challenging. In the experimental setup C_2 was initially matched with C_p. During the test there was no further control on the piezoelectric capacitance therefore a mismatch of the bridge parameters could have occurred.

The strain rate control algorithm is optimized for a frequency range satisfying Eqn. (6.7). The experimental bridge used in this experiment had $\frac{1}{\tau} = 27778\ 1/sec$. While increasing the frequency of the excitation the condition (6.7) approaches its limit and the resulting measured voltage is not necessarily equal to the strain rate.

6.5 Summary

A new concept of Active Energy Sink (AES) for specific applications in Structural Intensity based techniques was presented in this chapter. The AES is an energy absorption system which was implemented through active control logic. The design of this system was first presented using an electro-magnetic shaker actuated by velocity feedback control. Experimental results, collected on plate structures, proved the possibility of implementing an active energy sink for Structural Intensity applications. In particular, the AES system was validated through both loss factors measurements and Structural Intensity maps collected in open and closed loop. The results also showed the possibility of inducing a dominant energy flow at low frequencies where the CLD passive energy sink (based on a Constrained Layer Damper) was completely ineffective.

The concept of AES was then extended to be integrated in piezoelectric transducers (PZT) based system. The PZT transducers are more suitable for application on real systems because they can be bonded directly to the surface of the test structure. The PZT based AES system was implemented by using a strain rate feedback control for collocated actuators. The system was experimentally tested by using a single PZT disc bonded onto the structure and out-of-plane excitation. The transfer function between 0-2kHz was collected at the transducer location through the LDV. Results showed a limited control capability allowing up to 3dB attenuation on few high frequency modes (at high frequency the PZT becomes more effective). Note that the out-of-plane driving condition is particularly penalizing for the PZT which is particularly suitable to control in-plane waves.

CHAPTER 7

Nonlinear Structural Surface Intensity

In Chapter 5, the Structural Intensity (SI) concept was introduced as a possible tool for structural damage detection on complex mechanical systems. A preliminary investigation on this technique was performed by using plate structures and SI maps in order to understand the physical relations between the characteristics of structural damage and its impact on the SI properties. Although this approach was useful to build the necessary knowledge of the SI as damage detection tool, it might not be fully applicable to more realistic structures in the same form as it was formulated. Therefore, in this chapter the concept of Structural Surface Intensity (SSI) will be introduced as a more practical quantity extracted by surface measured data using discrete surface mounted sensors.

We must recall also that the sensitivity study to the damage size highlighted that the use of the Total Transmitted Power (TTP) in a linear domain was not able to provide information to evaluate the absolute damage size. To improve the performance of the TTP metric a nonlinear crack model will be introduced. The nonlinear model is more representative of the real behavior of the damage and, once combined with the SSI approach, will yield a novel concept called the Nonlinear Structural Surface Intensity (NSSI) technique.

This chapter will first present the theoretical background on linear Structural Surface Intensity introducing the numerical model for the calculation of the SSI in the time domain. Then, the nonlinear crack modeling and the HHRS concept, described in the first part of this thesis, will be combined with SSI in order to provide an approach for the calculation of the SSI in the nonlinear domain.

The NSSI is a new concept which combines the benefits associated with the HHRS and the SI/SSI techniques by obtaining a damage detection approach able to locate and size the defect without relying on a baseline signal.

In this chapter, a numerical approach for the calculation of the NSSI will be presented. This technique will allow the calculation of the SSI in cracked plate structure providing an approach to evaluate the SSI at nonlinear harmonic frequencies. Then, the results from a parametric study to the damage size will be presented. The main goal of this study is demonstrating that the NSSI is a physical quantity able to capture and keep track of the absolute change in size of the defect.

7.1 Linear Structural Surface Intensity

The evaluation of SI maps is not a practical approach when dealing with complex structures in operating conditions. To extract the SI maps one needs to collect the dynamic response on a number of structural points large enough to represent the geometry of the test structure. The structural mesh should also be carefully chosen to avoid spatial aliasing. This is not generally feasible when dealing with a real system where the dynamic response can be collected only at few structural points. In practice, the experimental data for the SI evaluation are measured through surface mounted sensors. The measurements are therefore representative of the quantities (strain and velocity fields) at the surface of the test structure. In plate structures, the assumption that these quantities are constant through the thickness allows for the calculation of the mechanical power by simply integrating the surface intensity over the cross sectional area. In structures that exhibit a strong tri-dimensional behavior this is not a viable approach. In this case, the measured quantities will be only representative of the structural intensity at the surface and does not allow for the reconstruction of the resulting power flow (through the cross section).

The Structural Intensity estimated from surface measured quantities is generally referred to as Structural Surface Intensity (SSI). The SSI concept was first introduced and numerically formulated by Pavic [124,125]. The main equations needed to estimate the SSI in the time domain on a 3D elastic body are summarized hereafter.

Consider a section of a 3D elastic body subjected to an external dynamic excitation. On the free surfaces the normal and tangential stresses must vanish. Defining a differential surface element and a coordinate reference system with the *z* axis normal to it and with the origin on the surface itself, as shown in Figure 7.1, it will results that:

$$\sigma_z = 0, \tau_{zx} = 0, \tau_{zy} = 0 \quad at \quad z = 0 \tag{7.1}$$

Therefore the component of the structural intensity in the *z* direction on a free surface is $I_z=0$ and the resulting intensity vector will lie in the plane of the surface.

The two components of this vector are:

$$I_x^S = -\overline{\sigma_x v_x} - \overline{\sigma_{xy} v_y}\ , I_y^S = -\overline{\sigma_y v_y} - \overline{\sigma_{yx} v_x} \tag{7.2}$$

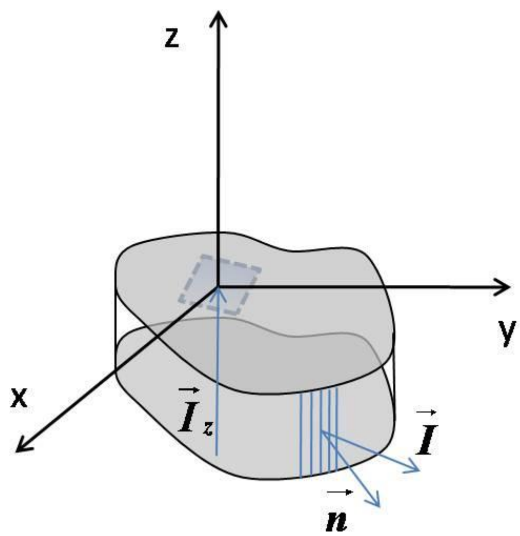

Figure 7.1. Schematic of the cross section of an elastic body.

The surface intensity is defined by three independent stresses (σ_x, σ_y and $\tau_{xy}= \tau_{yx}$) and two particle velocities (v_x and v_y) as shown by Eqns (7.2). These quantities are all time dependent.

As already observed for the SI calculation, the intensity cannot be directly estimated through these formulas because the stresses are not directly measurable. Observing that Eqns. (7.2) can be written in terms of strains by using the following constitutive equations:

$$\begin{aligned} \sigma_x &= \frac{E}{1-\upsilon^2}\left(\varepsilon_x + \upsilon\varepsilon_y\right) \\ \sigma_y &= \frac{E}{1-\upsilon^2}\left(\varepsilon_y + \upsilon\varepsilon_x\right) \\ \sigma_z &= 0 \end{aligned} \tag{7.3}$$

$$\tau_{xy} = \tau_{yx} = G\gamma_{xy} \qquad \tau_{xz} = \tau_{zx} = 0 \qquad \tau_{yz} = \tau_{zy} = 0$$

and the well known relation between the elastic moduli:

$$E = 2G(1 + \upsilon) \tag{7.4}$$

where *E*, *G* and υ represent the Young modulus, the shear modulus and the Poisson's ratio of the material, respectively.

By substituting Eqns. (7.3) and (7.4) in (7.2) we finally get the relations to calculate the surface intensity:

$$I_x^s = -G\left[\frac{2}{1-\upsilon}\overline{(\varepsilon_x + \upsilon\varepsilon_y)\upsilon_x} + \overline{\gamma_{xy}\upsilon_y}\right]$$

$$I_y^s = -G\left[\frac{2}{1-\upsilon}\overline{(\varepsilon_y + \upsilon\varepsilon_x)\upsilon_y} + \overline{\gamma_{xy}\upsilon_x}\right] \tag{7.5}$$

where the symbol $\overline{(\ldots)}$ indicates the time average of the quantity between brackets.

To estimate the structural surface intensity we must measure three independent strains at the surface of the body and the two in-plane components of the particle velocity, as shown by Eqns. (7.5)

The in-plane strain components can be simply measured by using strain gauges or other equivalent sensors providing strain measurements. Strain gauges are only sensitive to longitudinal strain therefore sensors in rosette configuration (Figure 7.2) are generally used to evaluate the shear strain component. In this study, strain gauges in a 0°/45°/90° rosette configuration were used.

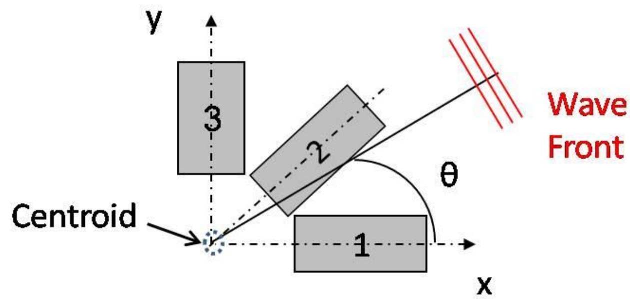

Figure 7.2. Strain gauges in 0°/45°/90° rosette configuration for the measurement of shear strain.

It was shown in Chapter 4 that, by measuring the longitudinal strains in the three sensors constituting the rosette, the axial and shear strains can be derived by the following relations:

$$\varepsilon_x = \varepsilon_1 \,, \quad \varepsilon_y = \varepsilon_3$$
$$\gamma_{xy} = 2\varepsilon_2 - \varepsilon_1 - \varepsilon_3 \tag{7.6}$$

Note that, for simplicity, the global reference system was considered aligned with sensor 1 and 3 therefore ε_1 and ε_3 directly provide the axial strain components without performing additional coordinate transformations.

Equations (7.6) can be also used to find the principal direction of the strain wave in the following way:

$$\theta = tan^{-1} \frac{\gamma_{xy}}{\varepsilon_x - \varepsilon_y} \tag{7.7}$$

The evaluation of the principal strain angle from the measured quantities will play a key role in the nonlinear structural surface intensity formulation, proposed later in this chapter.

Once the strain components are available, the remaining two quantities to be determined are the in-plane components of the particle velocities. These quantities are measured through bi-axial accelerometers located at the rosette centroid. The resulting quantity calculated through Eqns. (7.5) will provide surface intensity at the centroid location.

7.2 Nonlinear Structural Surface Intensity

The use of the Structural Surface Intensity allows extension the SI concept to 3D elastic bodies. Of course, it must be kept in mind the underlying assumption that the resulting SSI vector field is representative of the mechanical energy flow only in a thin layer on the body surface. This quantity, however, is more practical when dealing with experimental data on tri-dimensional structures because the intensity field measured through surface strain gauges will be only representative of the energy field at that surface and at a very specific point (that is assumed to be the centroid of the rosette configuration). Although being a more significant quantity for bodies exhibiting a 3D behavior, the SSI is prone to the same kind of limitations encountered with the SI approach. The SSI generally converges to the SI field when the thickness tends to zero (membrane structures). For finite thickness structures subjected to bending waves (I^b), however, the stress profile at the two surfaces can be considerably different. In this case, discrepancies between SI and SSI could still persist.

In particular, it is expected that the SSI exhibits a non monotonic behavior versus the crack size when considering a linear crack formulation, in accordance with what discussed in §5.6.2 for the SI field.

In order to overcome this limitation and to provide the SSI based damage detection technique with sizing and localization capabilities, the integration of a nonlinear crack model within the SSI formulation is proposed. The HHRS nonlinear technique, proposed in the first part of this thesis for the active monitoring of cracked structures, will be combined with the SSI formulation to yield what will be addressed from now on as Nonlinear Structural Surface Intensity (NSSI).

The HHRS technique will provide the SSI with localization capabilities while the Total Transmitted Surface Intensity will provide information about the size of the damage. The introduction of the higher order harmonic concept will also allow removing the dependence from a baseline of the healthy structure.

Note that the transducer network used for the crack localization in plate structure (Chapter 4) is fully consistent with the hardware needed to experimentally evaluate the SSI. Only bi-axial accelerometers need to be added in order to provide the in-plane velocity components at the rosette centroids. This means that the HHRS localization technique can be integrated in the damage detection scheme without requiring any modification to the sensing system.

On the other hand, if the higher order harmonic concept associated with the nonlinear behavior of the crack is introduced into the SSI formulation, the Structural Surface Intensity calculated at subharmonic/superharmonic frequencies could be used as an indicator of the crack size. From Chapter 2, the generation of higher order harmonics is associated with the impacts taking place at the crack interface. These impacts represent the physical mechanism which transfers vibration energy from the driving frequency to the higher order harmonics. The energy transferred in an impact is a function of the contact area between the colliding bodies [126,127]. It follows that the energy transferred across the crack is a function of the crack area or, equivalently, of the cross sectional area of the two impacting edges. It results that the energy transmitted at higher order harmonic frequencies is a function of the crack area and, therefore, a suitable metric to monitor the damage size.

The NSSI approach allows for calculating the Structural Surface Intensity at the higher order harmonic frequencies. This parameter presents some advantages over the standard vibration parameters (acceleration, velocity etc.) available in the HHRS technique. The NSSI provides a direct measurement of the energy transferred at specific frequency, therefore can be immediately related to the energy transferred at the impact location. It also combines the in plane quantities (stresses and velocities) in a single parameter which is easier to be interpreted. Finally, the NSSI provides a measure of the energy flowing through a prescribed location. This is more representative of the energy associated with the travelling wave generated at the crack interface.

7.2.1 NSSI Numerical Implementation

An approximate estimate of the linear SSI could be obtained by using the software McPow if the associated FE model was built to have layers of thin elements on the body surface where the SI will be calculated. McPow, however, does not integrate any nonlinear capability. In order to overcome this limitation a specific numerical technique similar, in principle, to the approach used for the HHRS technique was developed.

The analytical NSSI formulation can be derived from Eqns. (7.3) and (7.5). The in-plane stress components induced by the higher order harmonic are:

$$(\sigma_x)_k = \frac{E}{1-\upsilon^2}\left((\varepsilon_x)_k + \upsilon(\varepsilon_y)_k\right)$$
$$(\sigma_y)_k = \frac{E}{1-\upsilon^2}\left((\varepsilon_y)_k + \upsilon(\varepsilon_x)_k\right) \tag{7.8}$$

where $(\sigma_x)_k$, $(\sigma_y)_k$, $(\varepsilon_x)_k$, and $(\varepsilon_y)_k$ represent the stress and strain components at the specific nonlinear harmonic *k*. In particular, the strain components are calculated (or measured in laboratory experiments) by using the strain gauge rosettes based technique, similarly to what described in §4.3.

The Cartesian components of the nonlinear structural surface intensity for the generic nonlinear harmonic of order *k* are:

$$(I_x^s)_k = -G\left[\frac{2}{1-\upsilon}\overline{\left((\varepsilon_x)_k + \upsilon(\varepsilon_y)_k\right)(\upsilon_x)_k} + \overline{(\gamma_{xy})_k(\upsilon_y)_k}\right]$$

$$(I_y^s)_k = -G\left[\frac{2}{1-\upsilon}\overline{\left((\varepsilon_y)_k + \upsilon(\varepsilon_x)_k\right)(\upsilon_y)_k} + \overline{(\gamma_{xy})_k(\upsilon_x)_k}\right] \tag{7.9}$$

Finally, the total NSSI associated with the harmonic *k* is:

$$(I^s)_k = (I_x^s)_k\hat{\imath} + (I_x^s)_k\hat{\jmath} \tag{7.10}$$

where $\hat{\imath}$ and $\hat{\jmath}$ are unit vector indicating the components along the coordinate axes.

The NSSI formulation was validated using a nonlinear finite element model of a cracked plate structure, described in §7.2.2. The model was used to calculate the transient response up to the steady state. The time histories of the input variables (strains $\varepsilon_{ij}(t)$ and velocities $v_{ij}(t)$) needed for the SSI calculation were stored and processed through a dedicated Matlab code. The code combined a Hilbert transform based technique for features extraction at higher order harmonics and the SSI formulation (Eqns. (7.9)) for the solution in the time domain.

The Hilbert Transform was used in a similar fashion to what done in the HHRS approach. The time histories of the strains and velocities, for each single rosette, were first bandpass filtered around the higher order harmonics. This process allowed extracting the harmonic components ($\left(\varepsilon_{ij}\right)_k(t)$ and $\left(v_{ij}\right)_k(t)$) relative to the nonlinear response of the crack. Then, the filtered time signals were processed through the Hilbert transform to get the time envelope of the strains $\left(\widetilde{\varepsilon_{ij}}\right)_k(t)$ and velocities $\left(\widetilde{v_{ij}}\right)_k(t)$for each selected harmonic. The time envelopes were finally used to calculate the structural surface intensity $(I^s)_k$ for each higher order harmonic components.

The numerical procedure used for the NSSI calculation is summarized in the schematic of Figure 7.3.

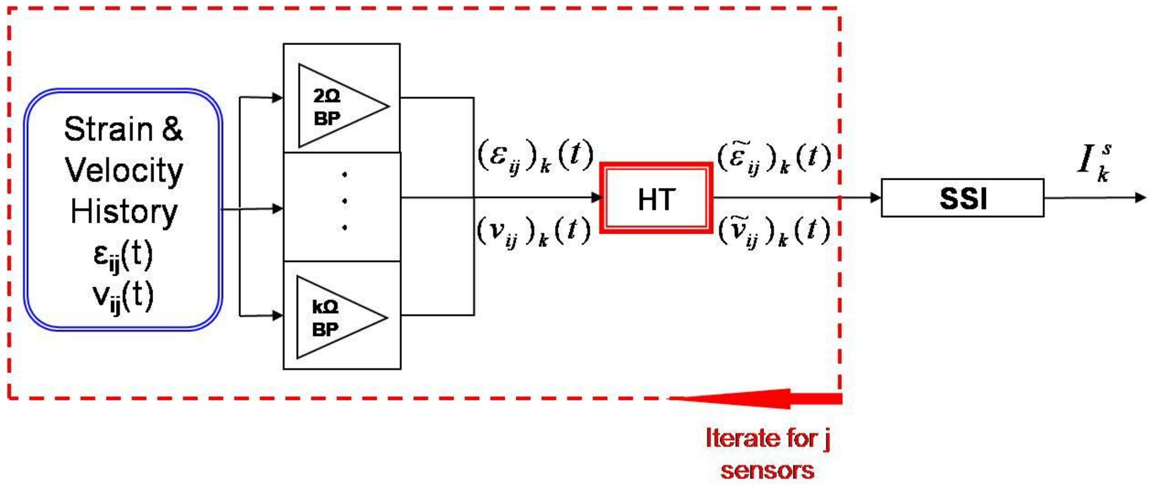

Figure 7.3. Schematic of the numerical procedure to calculate the NSSI. The time histories of strains and velocities are bandpass filtered around the superharmonic frequencies. The time envelope for each harmonic is obtained through the Hilbert Transform and then fed into the SSI equations.

7.2.2 Finite Element Model for NSSI Calculation

The numerical data necessary for the evaluation of the NSSI approach were generated by means of a specific finite element model. The test structure selected for carrying a numerical investigation on the NSSI was the same aluminum plate used in Chapter 4. Further details on the FE model can be found in §4.4. The nonlinear time response was obtained through the commercial software MSC-NASTRAN [128] using the same parameters previously indicated. The output was collected both in terms of strains and velocities at four different locations. The strains at the surface were calculated using plate elements (CQUAD4) which simulate the strain gauge sensors. The velocities were calculated at the rosette centroid (Figure 7.4). The time history of strains and velocities were then processed using the approach described in §7.2.1.

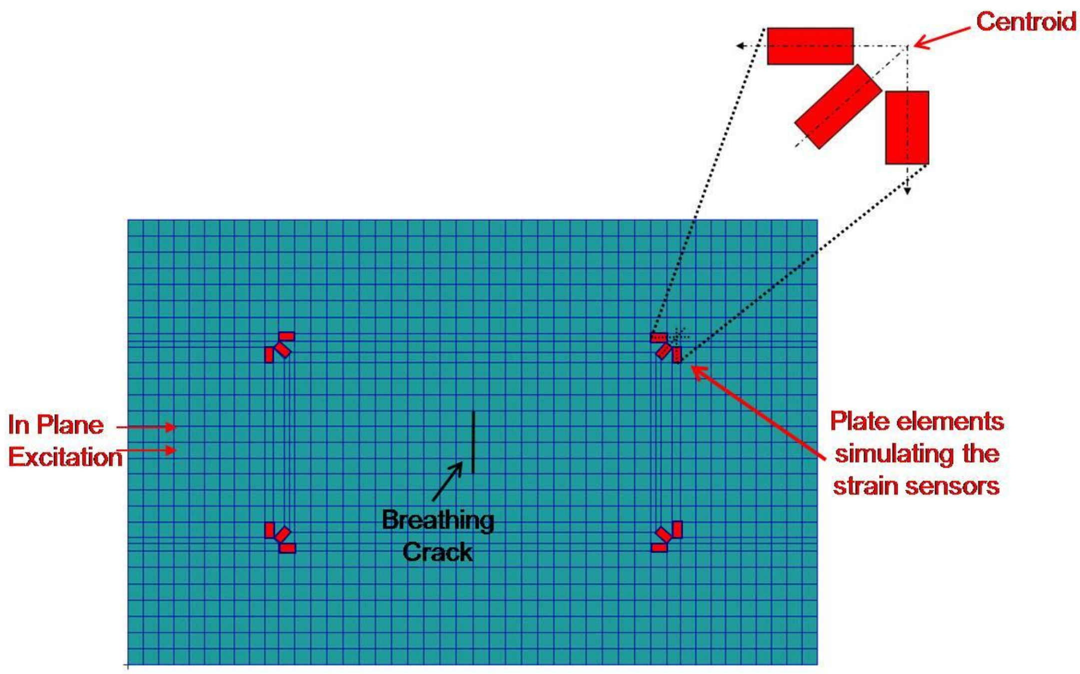

Figure 7.4. FE model used for the calculation of the NSSI. It shows the location of the nonlinear crack and of the four rosettes where the strains were measured.

7.2.3 Numerical Results

The results proposed in this section aim to demonstrate the main principle of the NSSI which is evaluating the change in the damage size by monitoring the energy transmitted at higher order harmonic frequencies.

A numerical sensitivity study to the damage size was carried out to prove the NSSI concept. Four different crack configurations were considered. In each configuration the damage size was incrementally increased while the damage location was kept constant. In particular, the considered type of damage was a through the thickness crack, located in the middle of the plate, with a total length varying from 0cm (healthy case) to 12cm, with a 4cm increment. The crack configurations are summarized in Table 7.1.

Table 7.1. Summary of the crack configuration used for the sensitivity study.

Configuration #	*Crack Length (cm)*	*Crack Length / Plate Thick.*	*Crack type*	*Location*
1	*0*	*0*	*Through crack*	*Plate center*
2	*4*	*26.6*	*Through crack*	*Plate center*
3	*8*	*53.3*	*Through crack*	*Plate center*
4	*12*	*80*	*Through crack*	*Plate center*

The structural surface intensity at the higher harmonic frequencies, previously defined as Nonlinear Structural Surface Intensity, was calculated at the four different sensor locations. The results are shown in Figure 7.5 where the NSSI is plotted versus the crack size for different higher order harmonic components. In the current analysis, the first three superharmonic frequencies were selected to extract the NSSI because they are associated with the lower β ratios.

The numerical results clearly showed that the NSSI had an increasing monotonic trend versus the crack size. This was a key result because it showed that the NSSI was a metric sensitive to the size of the damage and not only to its presence. These results also confirmed the validity of the physical mechanism relating the nonlinear response of the crack and the structural surface intensity values. The energy transferred through the crack at higher order harmonic frequencies is a monotonic function of the crack area. The analyses presented in this chapter were meant to validate the NSSI concept and its correlation with the damage size. Only one interrogation signal at a specific frequency was considered. Nevertheless, considerations drawn in Chapter 2 and 3 about the selection of the interrogation signal can be extended to the NSSI concept as well. From a theoretical point of view the use of superharmonics and subharmonics is absolutely equivalent. These components are all generated at the crack interface and therefore are suitable indicators of the damage properties. From an experimental point of view, however, the use of subharmonics could be advantageous in order to overcome any issues related to test apparatus Harmonic Distortion (HD).

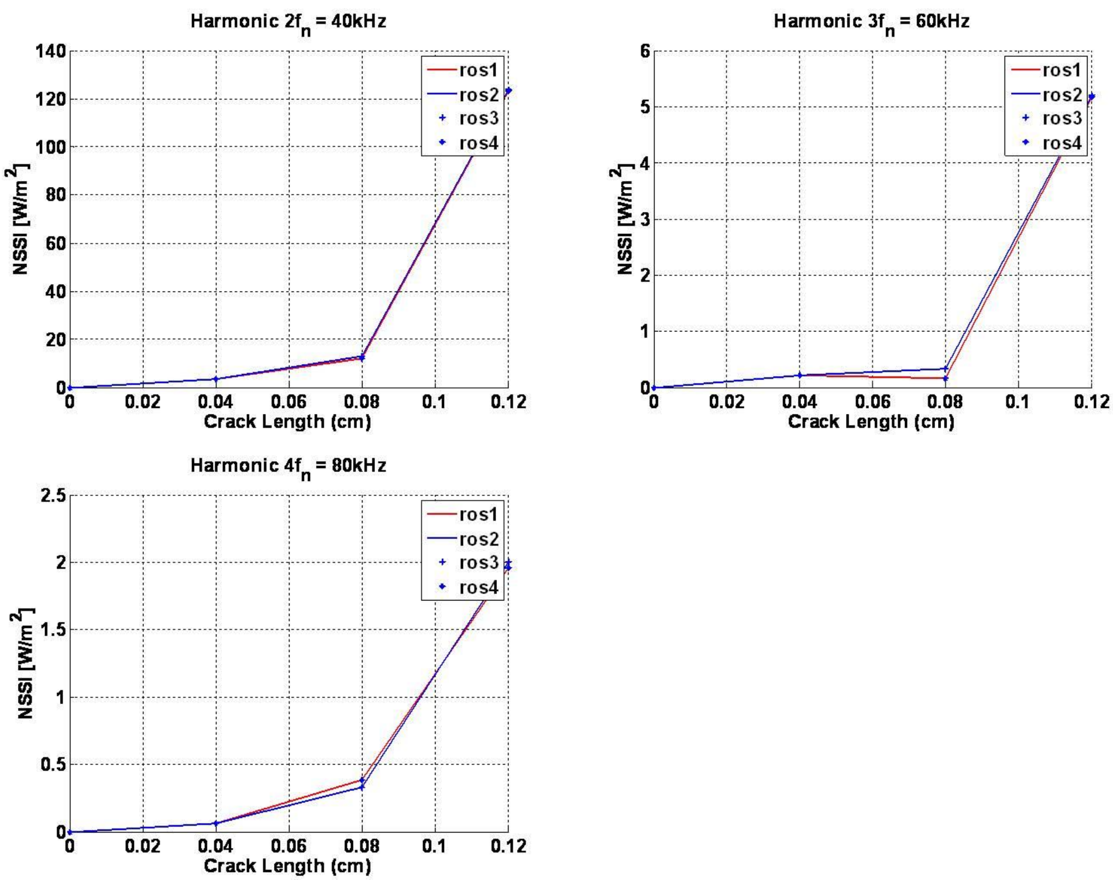

Figure 7.5. Numerical results showing the dependence of the NSSI from the crack size. Each plot provides the results at the four locations where the rosettes were located. The results for the first three superharmonics $2f_n$, $3f_n$ and $4f_n$ are provided.

As a reminder, the subharmonic components are not contaminated by HD effects, have larger S/N ratios and are generally associated with lower frequencies than the superharmonics (this allows to more easily fulfill the requirements associated with wavelength/sensor footprint).

As a minor remark, note that the transmitted energy exhibited almost the same trend and maximum value at the four different sensors. Considering that the crack configurations were symmetric with respect to the four sensors, this might provide additional information on the crack distance from the sensor.

7.3 Summary

In this chapter, a novel concept of Nonlinear Structural Surface Intensity (NSSI) was introduced. The NSSI derives from the combination of the two techniques presented in this research. The underlying idea combines the benefits of these techniques to yield a single methodology able to localize and size the defect. In particular, the resulting technique benefits the localization capability proper of the HHRS approach and the sizing capability proper of the SSI technique.

After a short review of the fundamental principles of the SSI, this chapter formulated the concept of Nonlinear SSI. A numerical technique for the calculation of the NSSI in cracked plates was presented. The technique is based on the calculation of the dynamic response of the cracked structure in terms of strain and velocity time histories. These quantities are then bandpass filtered around the nonlinear harmonic frequencies and processed through a Hilbert Transform based approach. The resulting data are used to evaluate the SSI at the higher order harmonics.

A sensitivity study to the damage size was conducted in order to validate the NSSI concept. Numerical results showed that the NSSI has a monotonic trend versus the crack size. The energy transmitted at higher order harmonic frequencies was shown to be a function of the crack area (the energy increases when the crack area increases). The NSSI is a quantity able to capture this physical mechanism and therefore is a suitable parameter for monitoring the crack size, as opposed to the Total Transmitted Power (TTP) in the linear domain.

CHAPTER 8

Conclusions and Recommendations

This chapter presents a summary of the research along with the main conclusions drawn on the basis of the numerical and experimental results presented in this dissertation. A summary of the concepts that are considered to be the most significant contributions of this research will be also presented. This chapter will conclude with an overview on possible topics that should be addressed, in future studies, to improve the readiness level of the proposed techniques paving the way towards applications on real helicopter platforms.

8.1 Summary of Research and Conclusions

This research presented a numerical and experimental investigation on two different damage detection techniques suitable for a possible implementation in a Health and Usage Monitoring Systems (HUMS) for application on helicopter primary structures.

The first technique presented in this study was based on the application of the Higher order Harmonic Response Signals (HHRS) characteristic of nonlinear cracked structures. This technique was initially conceived for damage detection applications on rotor blade structures. The main focus of this technique was the detection and localization of a breathing crack in slender isotropic structures by exploiting only experimental measurements. The HHRS represents one of the first attempts to identify and localize a fatigue crack without using either a baseline signal or a finite element model of the healthy structure. The HHRS technique relies on the characteristic response proper of cracked structures when subjected to an external dynamic excitation. The elastic wave fronts generated at the crack interface as result of the impacts of the two vibrating edges are reliable indicators of the damage. A specific technique, denoted Higher order Harmonic Response Signals, was theoretically formulated in order to extract from these elastic wave fronts information relevant to the damage. The main algorithm used for damage detection was theoretically demonstrated both through the wave propagation theory and the Harmonic Balance (HB) approach. This algorithm provided an approximate solution of the phase of the response signal at the steady state for nonlinear harmonic frequencies.

Then, a specific technique for simulating the nonlinear response of a cracked structure was proposed. The method used a finite element model of the test structure where the crack was represented through nonlinear gap elements. This model was able to capture the opening/closing behavior of the crack (generally referred to as “breathing”) along with the asymmetric restoring force associated to it. This technique was used to generate a database of simulated structural responses to numerically validate the HHRS algorithm.

The HHRS algorithm was implemented in a dedicated code able to extract and process the relevant information in the time response produced by the FE model.

Following a comparative study investigating different signal processing techniques, a Hilbert Transform based algorithm was selected an implemented in the HHRS code. This signal processing technique showed a significant ability in extracting accurate and repeatable phase values from nonlinear system. The HHRS technique was numerically validated by using the numerical database and the HT based technique. Numerical results also provided some general indications about the selection of key parameters for the experimental analysis as well as expected sensitivity and accuracy.

An experimental investigation was also performed in order to provide experimental evidence of the validity of the HHRS technique. First, a specific approach to fabricate a test specimen integrating a breathing crack was proposed. Then, a dedicated experimental setup was developed in order to measure the nonlinear structural response of cracked rods. General guidelines for the selection of a suitable sensory system for higher order harmonic measurements were also provided. The results of the experimental investigation proved that the HHRS technique is a valid approach for fatigue crack detection without using a baseline signature and a finite element model of the healthy structure. Experimental results also proved the possibility to practically implement the HHRS technique providing preliminary indications on the selection of the nonlinear harmonics to be used in the detection strategy.

In Chapter 4, the HHRS technique was extended to plate structures in an effort to develop a comprehensive technique able to be applied to a wide spectrum of structural components. The damage detection in plates exploited the same physical concept illustrated for the HHRS in rod but relies on a different post processing technique. The dispersive nature of the plate structure and the complex wave patterns generated after the reflection on the boundary conditions make the initial formulation of the HHRS algorithm, based on phase estimates, too involved for application on 2D structures. A different algorithm was presented to identify the crack location in plate-like structures. The algorithm was based on the evaluation of the principal angle associated to the propagating elastic strain waves generated at the crack interface. As for the cracked rod, these waves had a highly nonlinear spectral content due to the nonlinear response of the crack. The principal angle was evaluated at the superharmonic frequencies which are, therefore, indicators of the crack.

The principal angle was estimated, in the numerical simulations, through simulated strain sensors in rosette configurations. This approach was chosen to numerically demonstrate the possibility of experimentally implementing the presented technique. Following this approach, the direction of the travelling wave at multiple locations was evaluated. The crack location was then extracted by triangulating the information acquired at two or more locations. This technique was successfully tested through numerical simulations carried on by means of a nonlinear finite element model.

The second part of this research dealt with numerical and experimental investigations aiming to develop a Structural Intensity (SI) based damage detection technique. This research was focused, but not limited to, the development of a HUMS system for helicopter airframe structure.

Although the SI is a well known approach for applications on structural vibration and noise control its potentialities as a damage detection tool were not sufficiently investigated in the past. The proposed study was intended to build the necessary scientific background establishing the capabilities of a possible SI based Structural Health

Monitoring system. A numerical sensitivity study was initially carried out in order to investigate the correlation between the SI and key parameters for the numerical/experimental analyses. In the frame of this study a specific metric, denominated Total Transmitted Power (TTP), was introduced in order to extract information relevant to the damage from the SI field.

The sensitivity study highlighted the key role played by the loss factors (both material and viscous) and the type of damage (i.e. linear or nonlinear dynamic behavior) on the overall detection capabilities of the SI technique. The numerical results suggested some possible direction to enhance the SI based technique.

The first direction was the introduction of the Active Energy Sink (AES) concept. The AES is essentially an actively controlled energy absorption device (energy sink). The numerical results showed that the Total Transmitted Power was maximized for a specific value of the equivalent viscous damping associated to the energy sink. This damping value, however, is strongly dependent on the specific mechanical system (material loss factors, joints, vibration absorbers etc.). The possibility of having a tunable energy sink would allow setting the working point, maximizing the TTP, independently of the system characteristics. In some cases, passive damper devices do not have enough authority to make the energy sink dominant versus the other sources of energy dissipation. The AES allows tuning the dissipated power at the sink location in order to “tailor” the authority of the active control for the specific application.

In this research, the AES was designed and experimentally tested. Experimental results from a single transducer energy sink configuration demonstrated the applicability of this concept for generating a dominant energy sink. Results were presented in terms of both increased loss factors and SI maps.

The concept of AES opened the way to the use of a network of tunable and selectable energy sinks for SI applications. The use of an AES network would allow the damage localization according to a technique presented in this research. Assuming the availability of an AES network, a technique able to localize linear type of damage (open fatigue cracks, ballistic damage etc.) by exploiting the change into the TTP collected at discrete locations on the host structure was developed. A feasibility study based on numerical results is proposed to support and validate the new localization technique. This linear localization technique is effective for damage localization.

The last concept investigated in this research dealt with the possible development of a Nonlinear Structural Surface Intensity (NSSI) approach. This technique was based on a combination of the two damage detection techniques proposed in this work, the HHRS and the Structural Intensity. In particular, the Structural Surface Intensity was extended to applications for the nonlinear response of cracked plate structures. This goal was achieved by integrating the physical and theoretical concepts exploited by the HHRS technique into the formulation of the structural intensity.

The resulting NSSI is a physical quantity able to combine the advantages of the two methodologies in just one approach. In particular, the new technique benefits of the localization capability, deriving from the HHRS technique, and of the sizing capability deriving from the SI approach. In this research, the concept of NSSI for the detection of nonlinear fatigue cracks in plate structures was presented. A numerical procedure to evaluate the NSSI in cracked structure was formulated by integrating the Hilbert

Transform processing technique (from the HHRS algorithm) with the time formulation of the SSI. A parametric study to the damage size was performed and the numerical results showed that the NSSI varies monotonically with the crack area, therefore proving that the Nonlinear SSI is a physical quantity able to monitor the absolute size of the damage. These results overcome the limitation associated with the use of the TTP and indicate a possible way to size damage without using any baseline or FE model of the test.

8.2 Contributions

In this paragraph the concepts that are considered to be the main contributions of this research are briefly summarized. The different contributions are classified under the specific technique they refer to.

8.2.1 Higher order Harmonic Response Signal

1. A new damage detection concept for the localization of nonlinear fatigue cracks was presented. The technique, denominated Higher order Harmonic Response Signal (HHRS), integrates concepts of Contact Acoustic Nonlinearities (CAN) into a damage detection algorithm suitable for use in a Health and Usage Monitoring Systems. The HHRS technique allows detecting the crack location without relying on the use of a baseline signal or a finite element model of the healthy structure. Only the dynamic response of the test structure to a prescribed external excitation and an estimate of the phase velocity are needed to perform the localization. This approach

allows overcoming the problems related to the variability of the baseline signal with the environmental and operating conditions. It also eliminates the dependence on accurate FE models and cumbersome optimization techniques proper of the “Model Update” methodologies.

2. A specific numerical technique for the dynamic simulation of cracked structures was presented. The numerical approach was based on the combined used of commercial finite element software, which gives large flexibility in modeling complex mechanical system, and a dedicated numerical code for the implementation of the HHRS technique. A comparative study of different post-processing techniques was also carried out to select the most appropriate approach for features extraction. A Hilbert Transform (HT) based technique was presented and selected as the most effective signal processing technique for the HHRS algorithm.

3. An experimental technique to induce and measure the nonlinear dynamic response of a cracked structure was successfully developed. A High Cycles Fatigue approach was chosen to fabricate a test specimen including a breathing crack up to the desired size. The experimental test bed, needed to measure the nonlinear response of a cracked structure, was designed and built. Specific guidelines for the selection of the sensory system able to induce and capture nonlinear harmonics were provided.

4. The HHRS technique was successfully extended to perform damage localization in plate structures. The physical concept, being the basis of the HHRS technique, was

transferred to analyze cracked plate. A specific post-processing technique was developed to extract damage relevant features in 2D structures. The new algorithm was based on the evaluation of the principal angle of strain waves at superharmonic frequencies. A numerical technique for the simulation of cracked plate was presented and used to perform a parametric study to different damage locations. The post-processing technique was an extension to plate structures of the HT based algorithm previously developed. Numerical results proved that this was a viable approach to deal with dispersive systems and with the interaction of the wave with the geometric boundaries. This approach provides a baseline-free and model-free technique for fatigue crack localization in plate structures.

8.2.2 Structural Intensity

1. Structural Intensity (SI) was investigated as a suitable technique for the implementation in a Health and Usage Monitoring System for helicopter applications. An extensive numerical sensitivity study was proposed to identify the relation between structural, numerical and experimental parameters and the changes produced in the SI profile. General guidelines for conducting numerical SI analysis and setting up the experimental test bed were proposed supported by the numerical results.

2. A possible metric for the interpretation of SI data collected at discrete locations on the test structure was proposed. This metric was denominated Total Transmitted Power (TTP) and described, from a physical point of view, the efficiency of the energy

transfer mechanism between two structural points. This quantity allowed for extracting information relevant to the damage by the SI values calculated at discrete points therefore without requiring an extensive data acquisition on the full test structure.

3. An algorithm for the localization of linear behaving defects was proposed. The TTP was used, compared to a previously acquired healthy baseline, to identify the spatial location of the damage in plate structures. This approach was intended to be used in conjunction with an AES or, at least, a network of energy sources. The proposed approach is similar, in principle, to the use of "view factors" in heat transfer problems. The numerical results showed that the technique is able to capture, with discrete accuracy, the location of the crack by using interrogation signals at very low frequencies.

4. An Active Energy Sink (AES) concept based on actively controlled transducers was designed and experimentally tested in this research. The possibility of generating a dominant energy sink through an active control device was demonstrated and its dissipative power was compared with passive energy sink devices. The generation of a dominant energy sink is not always achievable when using passive devices. The AES concept overcomes this issue providing a way to adjust the damping level based on the mechanical impedance on the test structure. The AES also allows choosing the relative location of the energy source/sink pair which ultimately provides an enhanced control capability on the energy path. Finally, the AES provided also the

necessary foundation for the development of the linear localization techniques presented in Chapter 5.

5. A new concept of Nonlinear Structural Surface Intensity (NSSI) was formulated to detect, localize and size fatigue cracks exhibiting a nonlinear dynamic behavior. The NSSI derived from combining the two techniques investigated in this research to create a single approach able to combine the advantages proper of the HHRS and the SI techniques. Preliminary numerical investigations showed that the NSSI is a physical quantity able to capture changes in the crack area and therefore it lands itself as a suitable parameter to size the defect. Therefore the NSSI allows overcoming the limitation associated with the use of the TTP in a linear domain.

8.3 Recommendations for Future Work

This research presented two new approaches for possible future implementation in HUMS systems. The theoretical foundation and the experimental validation of these concepts were provided in this research. Nevertheless, further investigations should be performed to enhance the readiness level of these techniques and to facilitate the transition towards applications on helicopter platforms.

The main recommendations for future works are briefly summarized hereafter.

8.3.1 Higher order Harmonic Response Signal

The following subjects are recommended for further studies to improve the Higher order Response Harmonic Response Signal Technique.

8.3.1.1 Analytical Formulation of Subharmonic in Cracked Structures

Problem Statement:

Experimental results presented in Chapter 3 highlighted the difficulties in exploiting the nonlinear response at superharmonic frequencies because contaminated by the Harmonic Distortion (HD) of electronic equipment. The use of subharmonic response signal has been proven to be a viable way to overcome this issue. Subharmonic are not generated due to the HD and generally exhibit a larger response which make them more reliable indicators of the crack presence. Nevertheless, subharmonic are associated with a threshold behavior [85] which results in very specific requirements for the amplitude and frequency of the interrogation signals. A better understanding of the physical mechanism leading to the generation of higher order harmonics will provide a deterministic way to choose the interrogation signal to trigger a specific subharmonic response.

Objectives:

The subharmonic nonlinear components are characterized by a threshold behavior strictly related to the property of the excitation signal. An analytical model describing the subharmonic generation in cracked structures should be developed to identify a deterministic way of choosing the interrogation signal properties (amplitude and frequency).

Technical Approach:

Very few models able to simulate the generation of subharmonics by taking into account the real physics of a breathing crack are currently available in the literature [85,86]. An interesting model proposed by [85] and summarized in Chapter 3 is based on a combination of inter-atomic, inertia and excitation forces. By taking into account these forces into the dynamic response of the structure, the subharmonic can be modeled. This model could be used as a basis to develop an analytical model able to predict the characteristic of the excitation signal to trigger a specific subharmonic response. The definition of specific parameters in this crack model must be further addressed. As an example, possible guidelines to choose the inter-atomic force models and the parameters characterizing the crack planes should be defined.

The formulation of the subharmonic model in cracked structures could allow addressing also another key issue in structural health monitoring that is "Multiple Damage Identification". The current HHRS technique, so as the greatest part of the "Vibration based" technique, cannot separate the information associated to multiple damage. The higher order harmonic generated at the cracks interfaces will be analyzed by the HHRS algorithm as a single wave front. The resulting phase front is a combination of the phase associated to the wave fronts generated at the single interface. This situation will result in an estimated crack location that is a spatial average of the real cracks location. An analytical model, able to correlate the generation of subharmonic response with the parameters of the interrogation signal, will allow focusing the vibrational energy in specific structural areas. Based on this model, the interrogation signal could be tailored to excite specific damaged areas so to trigger, in a selective way, the response from a specific crack.

8.3.1.2 Extension of Formulation to General Boundary Conditions

Problem statement:

The boundary conditions have a major impact on the overall accuracy of the HHRS algorithm for rod. As illustrated in Chapter 2, the phase measurement collected at the steady state is influenced by incident and reflected waves (from the boundaries). When a wave impinges on a boundary it is reflected with an additional "phase jump" that is strictly related to the nature of the boundary itself.

Two main distinctions have to be done when considering boundary conditions (BCs):

1. *Ideal vs non-ideal BCs.*
2. *Symmetric vs Asymmetric BCs.*

The assumption of ideal boundaries assumes that the structural response at the boundary is perfectly consistent with the nature of the boundary itself. At an ideal clamped boundary the measured displacement vector is therefore equal to zero (i.e infinite stiffness) according to what specified by the boundary condition itself. In real structures, boundaries do not behave accordingly to their ideal conditions so that clamped boundaries may exhibit a finite stiffness.

The second distinction is based on the symmetry of the BCs. In particular, in the case of:

1. *Ideal Symmetric Boundaries:* the boundaries produce the same phase jump in the reflected waves. At the measurement point, the phase contribution from the reflected waves cancels out.
2. *Ideal Asymmetric Boundaries*: the boundaries produce the different phase jump in the reflected waves. At the measurement point, the phase contribution from the reflected waves does not cancel out. It is expected that this term could be neglected in long slender structures due to wave attenuation. The effect of these terms, however, becomes dominant when the crack is close to the boundaries. In this last case, a more rigorous theoretical approach to integrate the effect of the asymmetric boundaries in the HHRS algorithm is needed.

Objectives :

The HHRS algorithm in rod was tested with symmetric boundary conditions (free-free) both in the numerical and experimental phase. To extend the range of applicability to more realistic 1D structure the effect of non-ideal and asymmetric boundary conditions (e.g. clamped-free) must be tested.

Technical Approach:

The proposed approach to solve the problem of asymmetric boundaries relies on the use of passive or active control devices which might allow imposing *virtual boundary conditions* on a sub-domain of the test structure. These control devices will be used to impose a prescribed displacement field at specific locations in order to force the structure to respond as if it were effectively constrained.

The use of an active controlled device is preferred (over a passive device) because it is expected to provide a better controllability on different boundary conditions. It could be also implemented by using the same hardware already used by the HHRS based damage detection system. The considerable increase in the performance of the commercial real time controller based on FPGA (Field Programmable Gate Array) technology will allow controlling waves at higher order frequencies.

The proposed approach, based on the concept of "virtual boundary", is intended to mitigate the effect of the boundary conditions on the performance of the HHRS algorithm. Ideally, this approach will allow to completely isolate the dynamic response of the structure from the boundary conditions in specific frequency range (e.g. at the nonlinear harmonic frequencies).

8.3.1.3 Extension to Flexural Waves in Beam (dispersive systems)

Problem Statement:

Flexural waves are dispersive in nature and introduce a higher degree of complexity in the data post-processing and crack localization through the HHRS approach. Nevertheless, it is expected that they could provide a more effective way to excite the nonlinear response of a cracked structure requiring a lower amplitude interrogation signal. For a rotor blade application this is even more appealing because the damage detection system could take advantage of the flapping motion of the blade to reduce the actuation force required to make the crack breathing.

In some cases flexural waves could be the only waves that can actually be excited in the test structure, therefore this task will results in a consistent improvement of the HHRS algorithm which will be able to address almost the entire spectrum of the beam dynamics.

Objectives:

The HHRS technique has been conceived and tested, at this time, for non-dispersive system. In order to provide a greater versatility to the HHRS based damage detection method for future applications on complex mechanical system (where the dynamic response might be mainly dispersive) a further extension of the algorithm is proposed. In particular, a possible update of the main damage detection algorithm oriented to integrate the nonlinear response due to flexural waves in beams will be studied.

Technical Approach:

The HHRS algorithm will be updated in order to include the spatial nonlinear terms, often referred to as "ringing" term, which represents the spatially damped vibration produced by the interaction of the flexural waves with discontinuities. Depending on the frequency range of interest the use of a Bernoulli-Euler beam theory versus the higher order Timoshenko beam theory will be analyzed and compared in order to select the most suitable mathematical model.

Following the approach used to derive the HHRS algorithm for non dispersive structure, the updated algorithm will first be tested numerically through Finite Element simulation in order to estimate the validity and the accuracy of the algorithm. An experimental phase will then be conducted on simple beam specimen in order to provide experimental evidence of the proposed theoretical approach.

8.3.1.4 Multiple Interrogation Signals

Problem Statement:

The numerical and experimental results proposed in Chapter 2 and 3 were based only on the structural response to one interrogation signal. Multiple excitations could be used to interrogate the structure in different frequency ranges in order to create a *database* of nonlinear harmonic responses. The different harmonics provide, theoretically, the same information about the damage. Nevertheless, the use of averaging techniques on an extended set of data is expected to provide results more robust against different sources of error (β ratio, noise, boundary reflections etc.).

Several techniques ranging from the selection of the interrogation signal to the data post-processing techniques can be envisaged to improve the accuracy of the damage detection technique and its robustness versus different sources of error. However, these techniques will not be treated in this work and will be addressed in future studies.

Objectives:

The main objective is to perform a parametric study assessing the dependency of the accuracy of the estimated location on the number of excitation signals. This process will result in establishing guidelines to select “a priori” the number of interrogation signals to be used to achieve a prescribed accuracy.

Technical Approach:

The numerical procedure presented in §2.2.5 can be used to generate a database of dynamic responses to different excitation signals. Indications from recommendation §8.3.1.1 can be used to drive the selection of the interrogation amplitude and frequency to generate a high quality (low β ratio) subharmonic response. The analysis should be performed keeping the size and location of the defect constant while the response to different interrogation signals is collected. The resulting information on the damage location should be collected using a β ratio weighted average approach (§3.5).

8.3.1.5 HHRS for Closing Delamination and Loosened Fasteners

Problem Statement:

The HHRS technique relies on the nonlinear behavior associated to the contact between two bodies. Although in this research only the case of fatigue cracks was investigated, it can be proved that different kinds of damage produce a similar nonlinear response. As an example, closing delaminations [129] and loose riveted joints (§A.6) exhibit a dynamic response dominated by nonlinear harmonics. This behavior suggests that the HHRS technique could be extended to these types of damage by exploiting the same physical principle.

Objectives:

The main objective is to numerically demonstrate the validity of the HHRS approach for delamination in composites materials and loose riveted joints. Numerical simulations should demonstrate the possibility of locating the damage by exploiting the nonlinear harmonic components, in a similar fashion to what done in this research for fatigue crack type defect.

Technical Approach:

The numerical simulation technique presented in Chapter 2 and based on the use of gap elements (i.e. contact elements) can be easily extended to model these types of damage. It is recommended that the HHRS algorithm is tested on plate structures. Due to the nature of the damage, flexural wave (inducing dominant out-of-plane displacements) are most likely required to trigger the nonlinear harmonic response. The HHRS algorithm for plate was conceived for modeling dispersive systems. It is also more robust versus the effects of reflected waves. Nevertheless, this kind of damage can be tested on beam structures once the recommendation §8.3.1.3 is addressed.

8.3.2 Structural Intensity

The following subjects are recommended for further studies to improve the Structural Intensity based technique.

8.3.2.1 Experimental testing of the PZT based AES network

Problem Statement:

The concept of Active Energy Sink was experimentally demonstrated in Chapter 6. The lab tests, performed using a feedback controlled Electro-Magnatic shaker, proved the possibility of creating a dominant active energy sink for SI applications. Experimental results also provided an estimate of the increase in the loss factors between passive and active devices. The AES was then extended to integrate a PZT network of transducers in order to prove the applicability of the concept with surface mounted sensors. Although 3dB attenuation was visible at some frequencies, the out-of-plane drive was too penalizing to assess the overall performance of the system. By using this drive the out-of-plane components are predominant with respect to the in-plane where the PZT is much more effective. The performance of the collocated transducer depends also on the balancing of the impedance bridge. A better monitoring capability of the PZT capacitance is required to optimally tune the impedance bridge (i.e. C_p=C_2 in Eqn. 6.5).

Objectives:

The main objective is to test the performance of the AES PZT based system with in-plane driving condition in a high frequency range (e.g. 1-10kHz). The impedance bridge should also be updated to include tunable capacitance and PZT capacitance measurements capabilities to optimally tune the bridge.

Technical Approach:

The AES performance will be tested using the same test structure presented in Chapter 6. This will allow exploiting the existing software for experimentally evaluate the SI field. A high frequency in-plane drive will be provided by using a PZT transducer mounted on the surface of the plate. This driving condition will allow generating dominant in-plane displacement components. The offset between the plane of the applied force and the neutral plane will provide coupling with bending waves as well.

A suitable metric to evaluate the performance of the PZT based AES must be established. At high frequencies the SI maps are too involved to give a clear evidence of the presence of the energy sink. The attenuation of the resonance peaks in the transfer functions gives a necessary but not sufficient indication that the PZT is behaving as energy sink. A metric proving a continuous energy extraction (i.e. negative power) at the sink location must be applied.

A prototype of the impedance bridge should be developed including tunable capacitance to calibrate the system. A real time measurement of the PZT capacitance could provide the input for tuning the system in different frequency range and environmental conditions.

8.3.2.2 Parametric and experimental study for the TTI linear localization technique

<u>Problem Statement:</u>

In Chapter 5, a technique for the localization of linear defects was presented. The technique is based on changes in the Total Transmitted Intensity (TTI) calculated with respect to a baseline of the healthy structure. Numerical simulations show that the technique is able to localize the crack with discrete accuracy by using very low interrogation frequencies (100-500Hz). The selection of the frequency range to be retained for the analysis is one of the key parameters to guarantee the accuracy of the technique. A rigorous approach to select the driving frequency as well as its correlation with sensitivity and accuracy should be developed. The localization technique was demonstrated through numerical simulations. An experimental validation should also be addressed to confirm the validity of the proposed approach.

<u>Objectives:</u>

The main objective is to develop a theoretical approach to select the interrogation signal to be used in the linear localization technique. Numerical simulation must be carried out to address accuracy and sensitivity of the proposed technique. The localization approach will then be validated through experimental measurements.

<u>Technical Approach:</u>

The TTI linear localization technique is based on a concept similar to the use “view factors” in heat propagation. The energy flow path becomes a key parameter for the interpretation of the data. Either low frequencies (where the associated low order modes generates clear energy paths) or high frequencies (where the wave gains directionality) could be suitable ranges for damage localization. An equivalent “Energy View Factor” concept could be investigated to discriminate between the information provided at different frequencies.

An extensive numerical sensitivity must be performed by using the approach established in Chapter 5. The numerical study should provide data to support and validate the development of the theoretical approach for the selection of the interrogation signal. In particular, the dependency on the frequency range of accuracy and sensitivity must be clearly addressed. Location and number of energy sinks for optimal detectability must be addressed as well. This process should also provide indication of the minimum detectable size of damage.

The TTI localization technique was presented for damage detection in plate structures. The experimental validation should be performed on a test bed similar to what described in Appendix A. The insight already gained through numerical and experimental results on this structure will allow an easier interpretation of the results.

The experimental validation of this technique could be performed by integrating the concept of AES presented in Chapter 6 and Recommendation 8.3.2.1. Nevertheless, an electro-magnetic shaker drive provided in different structural location could be used as an alternative.

8.3.2.3 Formulating a Nonlinear SSI sizing algorithm

Problem Statement:

The Nonlinear SSI was proposed in Chapter 7 as a possible technique able to combine the benefits of the HHRS and SSI approach. In particular, the NSSI benefits of the localization capability provided by the HHRS technique and of the sizing capability provided by the SSI. Numerical results (§7.2.3) showed that the NSSI is a metric sensitive to the change in size of the damage. Even more important, the NSSI changes monotonically with the damage size being, therefore, a suitable candidate to estimate the absolute size of damage. A theoretical approach to convert the measured NSSI in the equivalent damage size is needed. The equivalent damage size could be the total surface of the crack, delamination etc.

Objectives:

The main objective is to develop a theoretical approach allowing the evaluation of the equivalent damage size from the NSSI measurements.

Technical Approach:

The NSSI measures the vibrational energy associated to nonlinear harmonics at prescribed structural locations. The nonlinear harmonics are associated to the impacts generated at the crack interface. The total energy transmitted at higher order harmonic frequency is a function of the energy generated through the impact and, therefore, a function of the crack area. By applying concepts of impact theory between elastic bodies, the impact surface can be related to the amplitude of the elastic waves propagating in the structure. This quantity can be finally related to the expected change in the NSSI.

Appendix

Experimental Procedure for Structural Intensity Measurements

The numerical results produced by the sensitivity study, presented in chapter 5, were used to direct a preliminary experimental investigation. This experimental phase was meant to validate the numerical tools and the experimental methods used throughout this research for the evaluation of the SI distribution on plate-like structures.

This Appendix provides a description of the experimental procedure used to evaluate the SI maps on plate-like structures. The Appendix is divided in three main sections. In the first part the SI experimental formulation as well as its application to the experimental data is reviewed. Next, the experimental test bed and setup used to acquire the data for SI maps is described. Finally, some selected examples of the experimental results are presented.

The results presented in this Appendix are not meant to provide a basis to evaluate the characteristics of the SI-SHM as a viable damage detection approach. Although the SI maps will be measured for both healthy and damaged structures and will show experimental evidence of the sensitivity of this technique to the structural damage, the main goal of the presented results is the validation of the experimental procedure.

A.1 Experimental SI Computational Technique

The experimental technique used in this research to evaluate the SI maps on plate-like structure is based on the methodology outlined by Arruda [130] and Daley [131,132]. From a general point of view, the computational approach is based on a combination of Multi-Input/Multi-Output (MIMO) system modeling techniques and a finite differencing scheme for the evaluation of the spatial derivatives in the SI formulation (Chapter 5 Eqs. 5.2). In order to apply this computational approach, the test structure is first discretized in a finite number of measurement grid points, as shown in Figure A.1.

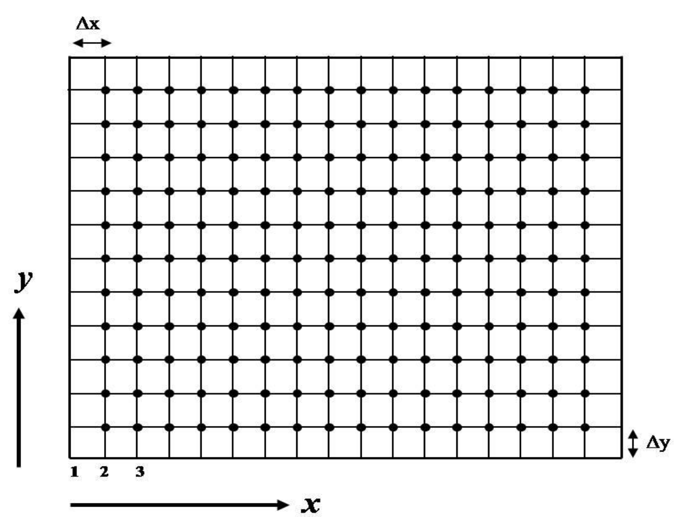

Figure A.1. Schematic of the experimental measurement grid used for the application of the finite differencing scheme approach.

Then, two different quantities are measured at each grid point:

1. The auto-spectrum G_{ff} of the input load at the driving point(s).
2. The transfer functions H_{fq} between the driving point(s) (f) and each one of the structural points (q) used to discretize the plate.

Once these two quantities are measured, the response cross-spectra G_{qq} between each pair of structural points can be obtained through a matrix multiplication. According to the MIMO system theory [133] the cross-spectra is:

$$G_{qq}(\omega) = H_{fq}^{*T}(\omega)G_{ff}(\omega)H_{fq}(\omega) \tag{A.1}$$

where the superscript $^{(*T)}$ indicates the complex conjugate transpose. The matrix H_{fq} includes the complete set of transfer functions between the driving points and the measured outputs. The matrix H_{fq} has the following form:

$$H_{fq}(\omega) = \begin{bmatrix} H_{fq_{1,1}} & \cdots & H_{fq_{1,n}} \\ \vdots & \ddots & \vdots \\ H_{fq_{m,1}} & \cdots & H_{fq_{m,n}} \end{bmatrix} \tag{A.2}$$

where the subscripts m and n indicate respectively the grid points number and the number of excitation points. The transfer function matrix given by Eqn. (A.2) is defined for a specific frequency. Therefore, it must be expected that the global transfer function matrix including the whole set of frequencies is represented by a tri-dimensional matrix.

In a similar way, the cross-spectrum matrix resulting from Eqn. (7.1) has the following form:

$$G_{qq}(\omega) = \begin{bmatrix} G_{q_1q_1} & \cdots & G_{q_1q_m} \\ \vdots & \ddots & \vdots \\ G_{q_mq_1} & \cdots & G_{q_mq_m} \end{bmatrix} \tag{A.3}$$

It can be noted that the terms on the main diagonal ($m=n$) represent the auto spectra at each structural point, while the other terms are the cross spectra between pair of grid points. G_{qq} is a tri-dimensional matrix whose third dimension is represented by frequency. Eqs. (7.1), (A.2) and (A.3) describe a general formulation which can be used to model a distributed external load (e.g. pressure load). In the present study, however, the plate was driven through a point force applied at a single grid point therefore both the matrices (A.2) and (A.3) reduce to a vector for each specific frequency.

A.1.1 13 Point Finite Differencing Scheme

Once the experimental cross-spectra are evaluated the data is fed into a finite differencing scheme used to calculate the spatial derivatives in Eqn. (5.2) and, ultimately, the SI components. Several schemes are available in the literature. In this research, a 13 point central finite differencing scheme (Figure A.2) was used because it was demonstrated to be more stable near structural and load discontinuities [131]. The 13 point scheme also allows the calculation of the spatial derivatives up to the third order.

According to Daley [131], in order to obtain the SI equations in terms of acceleration and spatial derivatives we can substitute Eqns. (5.4) and (5.5) in Eqn. (5.2). By assuming a time harmonic dependence, the derivatives are written in terms of acceleration. As an example, the x component including only the shear waves will result in:

$$I_x^S = \frac{D}{h}\langle\frac{+i}{\omega^3}(1+i\eta)\left(\frac{\partial^3\ddot{w}}{\partial x^3}+\frac{\partial^3\ddot{w}}{\partial x\partial y^2}\right)\ddot{w}\rangle_t \tag{A.4}$$

where D is the flexural rigidity, h is the plate thickness, ω is the circular frequency, η is the material loss factor, i is the imaginary unit, $\ddot{w}$ is the second order time derivative of w and $\langle ... \rangle_t$ is the time average.

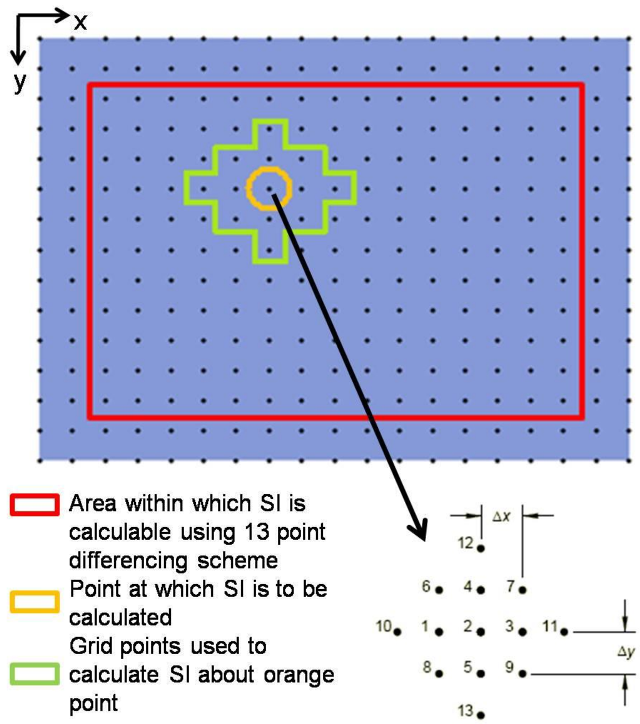

Figure A.2. 13 point finite differencing scheme for the SI experimental calculation.

By writing the spatial derivatives through a finite difference approximation with the 13 point scheme we obtain:

$$I_x^S = \frac{D}{2\omega^3 h \Delta x} \langle i(1+i\eta) \left[\frac{\ddot{w}_{11}\ddot{w}_2 - 2\ddot{w}_3\ddot{w}_2 + 2\ddot{w}_1\ddot{w}_2 - \ddot{w}_{10}\ddot{w}_2}{\Delta x^2} + \frac{\ddot{w}_9\ddot{w}_2 - \ddot{w}_8\ddot{w}_2 - 2\ddot{w}_3\ddot{\omega}_2 + 2\ddot{w}_1\ddot{w}_2 + \ddot{w}_7\ddot{w}_2 - \ddot{w}_6\ddot{w}_2}{\Delta y^2} \right] \rangle_t \tag{A.5}$$

where $\ddot{w}_n$ is the acceleration at the *n-th* point while Δx and Δy represents the distance between two consecutive grid points in the coordinate directions.

Remembering that the time average of two sinusoidal quantities can be calculated, in the frequency domain, as:

$$\langle x(t)y(t)\rangle_t = \frac{1}{2}\Re\{X^*(\omega)Y(\omega)\} \tag{A.6}$$

where *X(ω)* and *Y(ω)* are complex quantities obtained through the Fourier transform of *x(t)* and *y(t)* and where the $^{(*)}$ denotes the complex conjugate of that quantity.

Eqn. (A.5) can be transformed in the frequency domain:

$$I_x^S = \frac{D}{4\omega^3 h\Delta x}\Re\left\{i(1+i\eta)\left[\frac{\ddot{W}_{11}^*\ddot{W}_2 - 2\ddot{W}_3^*\ddot{W}_2 + 2\ddot{W}_1^*\ddot{W}_2 - \ddot{W}_{10}^*\ddot{W}_2}{\Delta x^2} + \frac{\ddot{W}_9^*\ddot{W}_2 - \ddot{W}_8^*\ddot{W}_2 - 2\ddot{W}_3^*\ddot{W}_2 + 2\ddot{W}_1^*\ddot{W}_2 + \ddot{W}_7^*\ddot{W}_2 - \ddot{W}_6^*\ddot{W}_2}{\Delta y^2}\right]\right\} \tag{A.7}$$

where $\ddot{W}$ is the complex amplitude of the acceleration in the out-of-plane direction and $\Re$ is the real part of the quantity between brackets.

The cross-spectrum between two sinusoidal signals can be calculated as:

$$G_{xy}(\omega) = \frac{1}{2}\{X^*(\omega)Y(\omega)\} \tag{A.8}$$

Therefore applying Eqn. (A.8) and removing the imaginary unit *i* from the braces we obtain:

$$I_x^S = -\frac{D}{4\omega^3 h\Delta x}\Im\left\{(1+i\eta)\left[\frac{G_{\ddot{w}_{11}\ddot{w}_2} - 2G_{\ddot{w}_3\ddot{w}_2} + 2G_{\ddot{w}_1\ddot{w}_2} - G_{\ddot{w}_{10}\ddot{w}_2}}{\Delta x^2} + \frac{G_{\ddot{w}_9\ddot{w}_2} - G_{\ddot{w}_8\ddot{w}_2} - 2G_{\ddot{w}_3\ddot{w}_2} + 2G_{\ddot{w}_1\ddot{w}_2} + G_{\ddot{w}_7\ddot{w}_2} - G_{\ddot{w}_6\ddot{w}_2}}{\Delta y^2}\right]\right\} \tag{A.9}$$

where $\Im$ is the imaginary part of the quantity between brackets and $G_{\ddot{w}_n\ddot{w}_m}$ represent the cross-spectrum between the accelerations of two generic points *n* and *m* on the plate. I_x^S represents the x-component of the structural intensity due to shear waves and expressed in terms of cross-spectra.

The remaining SI components as well as the contribution of bending waves can be obtained using a similar approach. The equations are reported here below for completeness:

$$I_y^S = -\frac{D}{4\omega^3 h\Delta x}\Im\left\{(1+i\eta)\left[\frac{G_{\ddot{w}_{13}\ddot{w}_2} - 2G_{\ddot{w}_5\ddot{w}_2} + 2G_{\ddot{w}_4\ddot{w}_2} - G_{\ddot{w}_{12}\ddot{w}_2}}{\Delta y^2} + \frac{G_{\ddot{w}_9\ddot{w}_2} - G_{\ddot{w}_7\ddot{w}_2} - 2G_{\ddot{w}_5\ddot{w}_2} + 2G_{\ddot{w}_4\ddot{w}_2} + G_{\ddot{w}_8\ddot{w}_2} - G_{\ddot{w}_6\ddot{w}_2}}{\Delta x^2}\right]\right\} \tag{A.10}$$

$$I_x^b = \frac{D}{4\omega^3 h\Delta x}\Im\left\{(1+i\eta)\left[\frac{\left(G_{\ddot{w}_3\ddot{w}_3} - 2G_{\ddot{w}_2\ddot{w}_3} + G_{\ddot{w}_1\ddot{w}_3}\right) - \left(G_{\ddot{w}_3\ddot{w}_1} - 2G_{\ddot{w}_2\ddot{w}_1} + G_{\ddot{w}_1\ddot{w}_1}\right)}{\Delta x_2} + \frac{\left(G_{\ddot{w}_5\ddot{w}_3} - 2G_{\ddot{w}_2\ddot{w}_3} + G_{\ddot{w}_4\ddot{w}_3}\right) - \left(G_{\ddot{w}_3\ddot{w}_1} - 2G_{\ddot{w}_2\ddot{w}_1} + G_{\ddot{w}_4\ddot{w}_1}\right)}{\Delta y^2/\upsilon}\right]\right\} \tag{A.11}$$

$$I_y^b = \frac{D}{4\omega^3 h\Delta x}\Im\left\{(1+i\eta)\left[\frac{\left(G_{\ddot{w}_5\ddot{w}_5} - 2G_{\ddot{w}_2\ddot{w}_5} + G_{\ddot{w}_4\ddot{w}_5}\right) - \left(G_{\ddot{w}_5\ddot{w}_4} - 2G_{\ddot{w}_2\ddot{w}_4} + G_{\ddot{w}_4\ddot{w}_4}\right)}{\Delta y_2} + \frac{\left(G_{\ddot{w}_3\ddot{w}_5} - 2G_{\ddot{w}_2\ddot{w}_5} + G_{\ddot{w}_1\ddot{w}_5}\right) - \left(G_{\ddot{w}_3\ddot{w}_4} - 2G_{\ddot{w}_2\ddot{w}_4} + G_{\ddot{w}_1\ddot{w}_4}\right)}{\Delta x^2/\upsilon}\right]\right\} \tag{A.12}$$

Using the 13 point scheme, the intensity at each one of the grid points of the test plate was calculated based on the data acquired at the other 12 points surrounding it. It is worth noting that due to the nature of the applied scheme, which relies on central finite differences, the intensity cannot be calculated at the two outer rows/columns of the grid (Figure A.2). This limitation, however, can be easily overcome using a forward/backward moving scheme to process the data on the grid boundary [134].

A.2 SI Experimental Test Bed

The SI experimental measurements were conducted on an aluminum plate structure (35”×23”×0.01”), having the same dimensions of the FE model used for the sensitivity study. The plate was supported by a massive steel frame which provided pinned boundary conditions on the four edges (Figure A.3). The frame was specifically designed in order to place the fundamental resonance frequency above 150Hz. This allowed reducing the dynamic coupling between the frame and test structure improving the confidence in the quality of the boundary conditions at low frequencies.

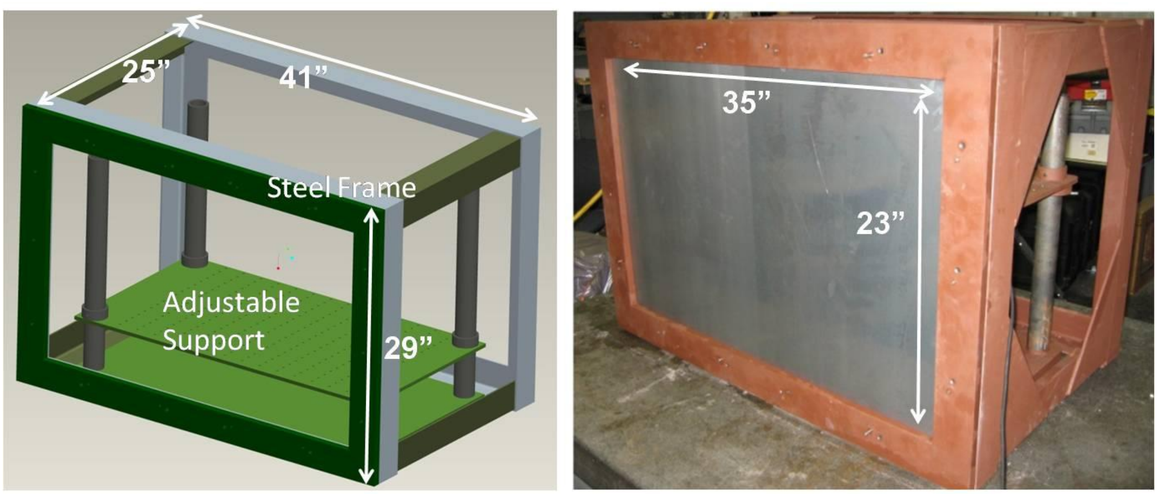

Figure A.3. Experimental test bed. (left) CAD model showing the fixture and the adjustable support to mount the shaker, (right) picture of the actual test bed showing the aluminum test plate.

The test bed had an adjustable mounting support placed in the area inside the frame in order to facilitate the installation of electro-magnetic shakers that provided the external driving conditions.

In order to ensure the correct extraction of the vibration features, the design of the test fixture was validated through numerical and experimental measurements. In particular, the experimentally acquired Operating Deflection Shapes (ODS), the corresponding mode shapes, and the resonance frequencies were compared with the results provided by the FE model of the test bed. The model included a detailed representation of the steel frame in order to accurately simulate the boundary conditions. The ODS were measured through a Laser Doppler Vibrometer while the plate was driven in the out-of-plane direction by an electromagnetic shaker. For the normal mode extraction the input signal to the shaker was a limited bandwidth noise between 0-1 kHz. The experimental vibration data were fed into DIAMOND [135], a freeware code, for vibration features extraction (resonance frequencies, damping loss factors, and mode shapes).

As an example, Figure A.4 shows a comparison between the predicted 2:1 mode and the experimental results. The mode shape was correctly predicted along with the numerical resonance frequency at 49.1Hz versus the corresponding experimental value at 50.5Hz.

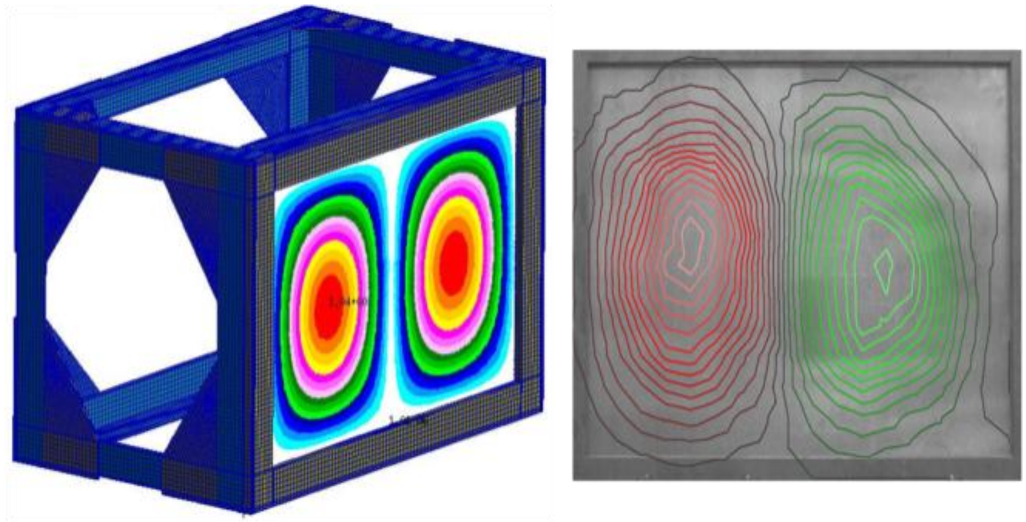

Figure A.4. Numerical and experimental results for normal modes analysis. (left) Numerical (1:2) mode, (right) experimental ODS.

A.3 SI Experimental Measurements

The experimental procedure followed to acquire the necessary input data for the SI maps extraction is briefly outlined hereafter. The external excitation was provided in the out-of-plane direction through an electromagnetic shaker (KCF ES020), mounted on the rear side of the plate on the adjustable support (Figure A.5). The driving force was measured at the plate interface through an impedance (PCB 288D01) head mounted on the connecting stinger. The energy sink was realized by means of a passive Constrained Layer Damper (CLD). The CLD is constituted by a composite beam (24” ×2”×0.125”) having an intermediate layer of viscoelastic material and two external constraining layers made out of brass. The three layers were assembled using epoxy glue.

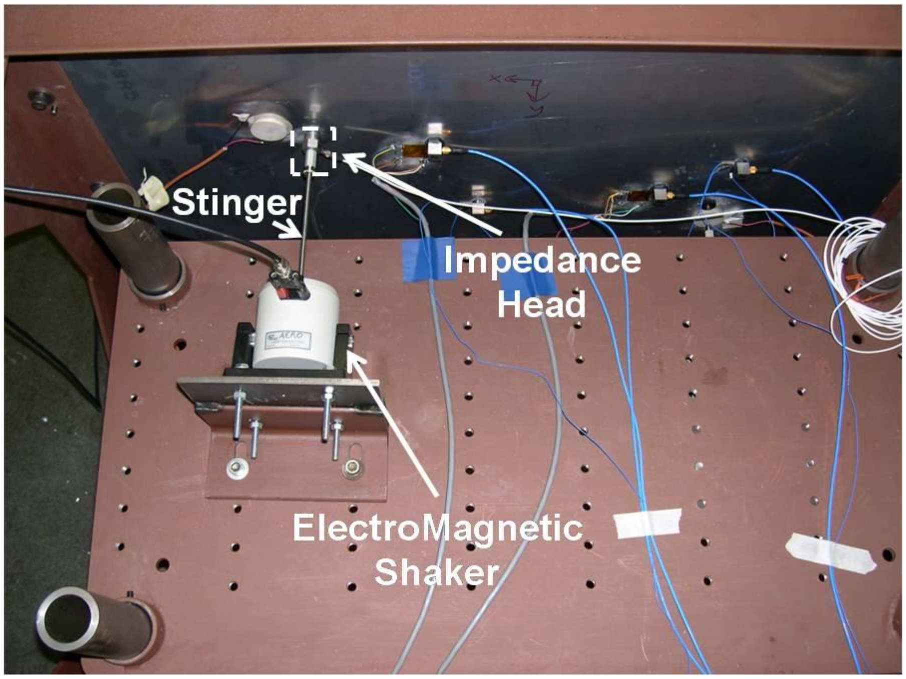

Figure A.5. Rear side of the test panel showing the electromagnetic shaker used to provide the external excitation.

The CLD was attached to the rear side of the test plate with an offset of about 1" between the neutral axis of the beam and the neutral plane of the plate. In this way, the propagating energy travelling through the plate is transmitted to the CLD and dissipated into the viscoelastic layer.

The dynamic response of the plate was measured with a scanning Polytec PSV400 Laser Doppler Vibrometer (LDV) (Figure A.6) which allowed measuring the out-of-plane point velocity.

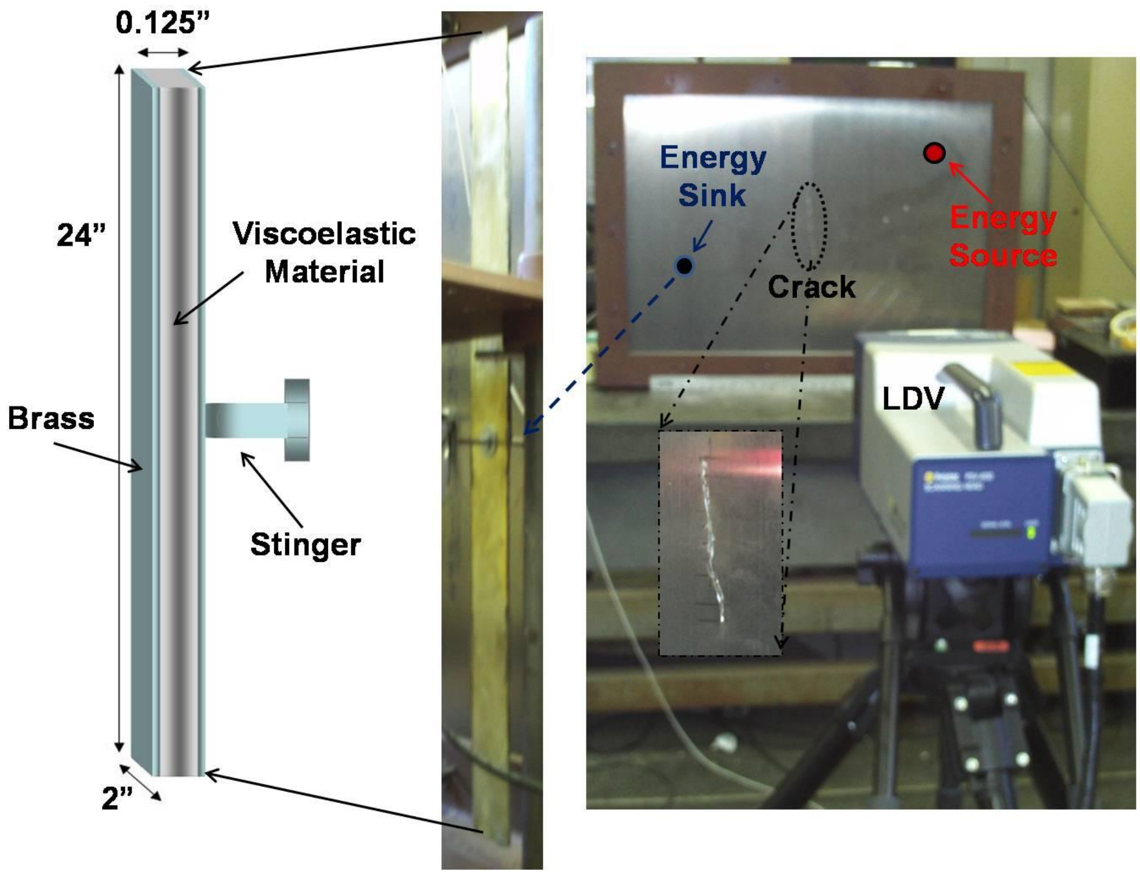

Figure A.6. (Right) Experimental test bed and LDV system. The location of the energy source, the energy sink and the crack are identified. (Left) Detailed view of the passive energy sink (CLD).

The driving force applied by the shaker was also acquired with the LDV controller and used as reference channel for phase measurements. The scanning was performed discretizing the structure into an array of 18 x 14 (width x height) elements and the experimental data was acquired at 285 points. The experimental grid size coincided with the coarse mesh used for the sensitivity study.

This procedure allowed measuring the transfer functions H_{fq} between the excitation point and the response grid points as well as the auto-spectrum G_{ff} at the driving point. The data were measured in a frequency range of 0-1kHz.

A.3.1 Drive Input Signal

Two different approaches could be followed to select the input signal to drive the electromagnetic shaker in order to acquire SI maps. The first approach consisted in using a band limited white noise in the range of interest (e.g. 0-1kHz). In this way, a full set of transfer functions could be collected performing a single scan. The results allowed for the calculation of the SI maps at any given frequency or, more specifically, at any spectral line. The drawback of this approach is that for some frequencies the input power is too low to efficiently excite the CLD (i.e. efficiently dissipating energy into the passive damper). If the CLD does not dissipate energy the flow is reverberant and a defined energy path is not clearly visible. The experimental results will show that this approach is still effective for the SI estimate for the higher order modes.

The second approach consisted in driving the plate using a sinusoidal signal at a specific frequency which was previously selected. This technique provided a higher input power at a single frequency and, therefore, higher vibrational energy flows at the prescribed frequency. This approach was particularly suitable for acquiring SI maps at the fundamental frequencies and to get a high Signal to Noise (S/N) ratio over the entire spectrum. The drawback is that each frequency must be scanned separately and this considerably increases the overall data acquisition time.

An effective strategy, that was the one retained in this experimental analysis, consisted in acquiring preliminary data/SI maps using a white input noise over a broad bandwidth. Then, these results were used to select the frequencies of interest for the experimental study. Once the resonance frequencies were identified, sine waves centered at the selected interrogation frequencies were used to excite the structure and measure the SI field.

A.3.2 On-resonance versus off-resonance driving conditions

The SI based damage detection approach belongs to the category of "vibration based" techniques. These techniques typically show a lack of sensitivity when the damage is located on a nodal line. In this case, in fact, the contribution of the damage to the modal response (in terms of modal displacements, modal strains etc.) is attenuated considerably producing, therefore, a negligible effect on the overall response. In a damage detection approach where the location of the damage is one of the unknowns it is not possible to choose "a priori" an excitation so that the damage location will not possibly coincide with a nodal line.

For these reasons, both on-resonance and off-resonance driving forces were considered in this experimental analysis two evaluate the characteristics of these two different driving conditions in terms of damage sensitivity.

When the driving signal is centered at a resonance frequency (on-resonance drive) the dynamic structural response will be dominated by the associated normal mode. In this case, the vibrational energy is concentrated in a very narrow bandwidth (ideally at a single frequency) and is amplified through the structural amplification factor. This driving condition produces larger displacements and a high SN ratio. As a drawback this driving condition is more prone to the so called "false negative" detection (the damage is present but is not detected by the SHM system) when the flaw is close or onto a nodal line.

When an off-resonance driving signal is used, instead, the input energy excites multiple modes at once. Under this condition, the energy is carried by several modes. In this case, the driving force at a single frequency is reduced but the structural response is dominated by multiple modes. With this driving condition, the flaw is less likely to be located on a pure nodal line of all the constituting nodes.

Both on and off resonance driving conditions were experimentally tested and the results will be presented in the following paragraphs.

A.4 SI Experimental Results

The experimental data acquired by the LDV were processed through a Matlab® code according to the procedure described in §A.1. This experimental study was meant to test the numerical tools and the experimental setup for SI measurements and not to assess the capability of the SI technique. Nevertheless, SI maps for both healthy and damaged configurations were acquired. The damage was introduced in the form of a saw cut (which is roughly equivalent to an “open crack” type of damage). The cut was introduced at the center of the plate and incrementally extended to 1”, 3” and 5” in length.

Several on and off resonance frequency spanning a bandwidth from 0 to 1 kHz were analyzed [134]. It must be observed that below 75Hz the passive energy sink (CLD) was not able to dissipate enough power to induce a clear energy flow. SI maps could not be measured for the first (35Hz) and second resonance mode (50Hz). The CLD dissipates energy through a layer of viscoelastic material which becomes more effective when the response is associated with higher velocity profiles and, therefore, at higher frequencies. The dynamic response and the SI data were acquired for the healthy structure in order to provide a baseline for the undamaged state.

The plot progressions in Figure A.8 and Figure A.10 show selected examples of experimental SI maps. The plots show the evolution of the SI field through the different damage states. Figure A.8 shows the results for an off-resonance response at 75 Hz where the Operating Deflection Shape shows a travelling wave component close to the mode 3:1 (Figure A.7). The coincidence of the maximum displacement area of the center lobe with the damaged region induces a considerable participation of the crack to the overall dynamic response.

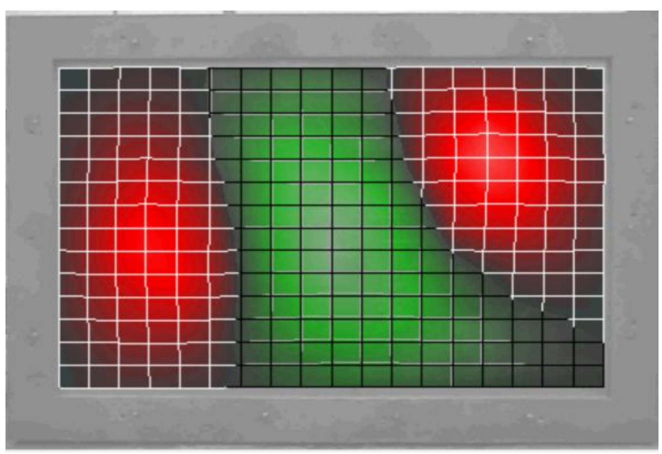

Figure A.7. Operating Deflection Shape (ODS) for the healthy plate at 75Hz.

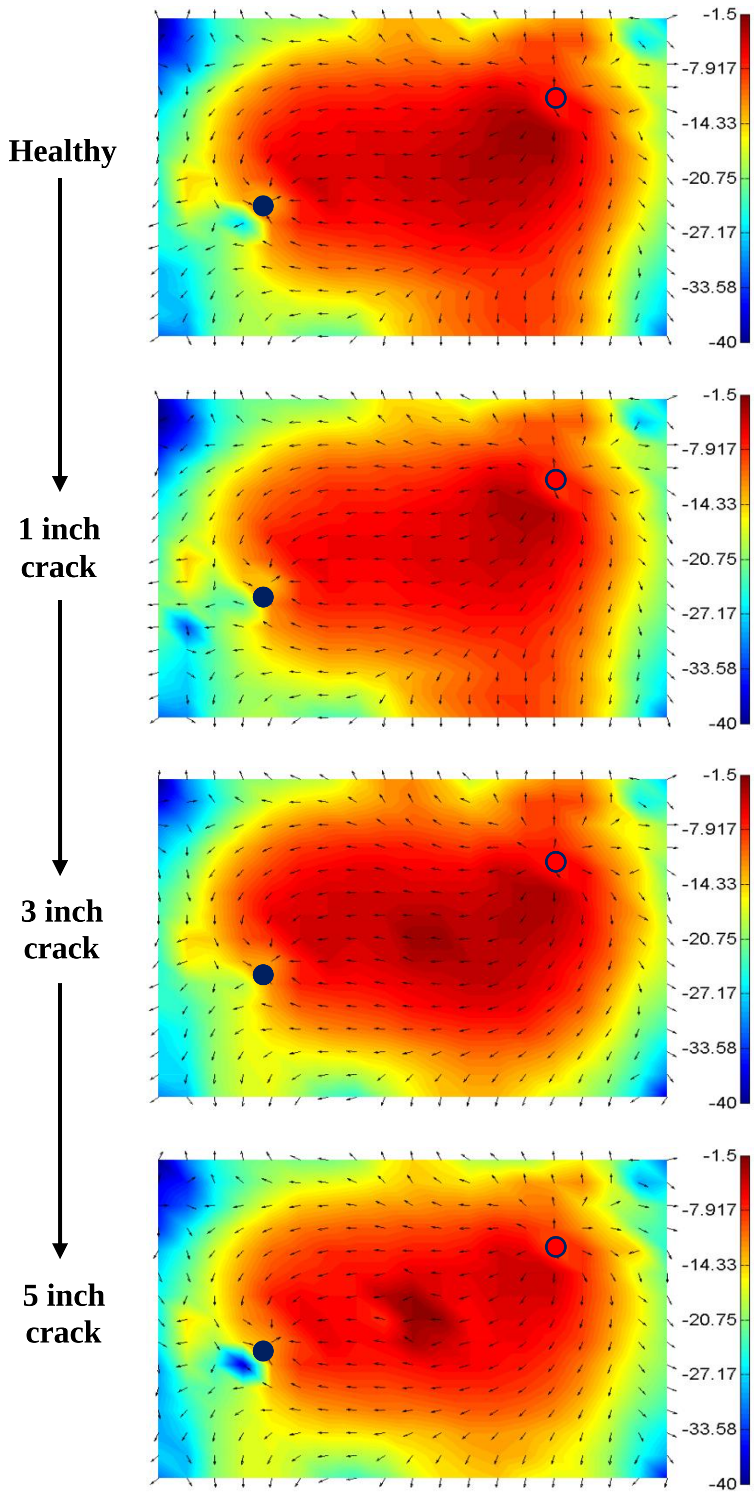

Figure A.8. Experimental SI maps for healthy and damaged plate measured at 75 Hz (off-resonance frequency). The locations of the energy source (red) and sink (blue) are indicated by a circle.

In the presented set of measurements, the 1” crack does not produce an appreciable change in the SI distribution. The 3” and 5” increment, however, show a clear SI peak localized around the cracked area with an increase in the overall intensity magnitude up to 10dB. For a better interpretation of the results, the SI maps for the different configurations are presented all in the same scale.

A second set of results is presented for an on-resonance frequency at 409 Hz which corresponds to the mode shape 7:1, as indicated by the ODS in Figure A.9. These results show a trend similar to the response at 75 Hz. The 1” increment does not show substantial evidence of the crack while in the 3” and 5” damage increment a localized SI maximum is clearly visible in the intensity distribution.

The results obtained for both frequencies show, as expected, the presence of an energy flow directed from the source to the sink where the specific path is tailored by the mode shape characteristic of the selected frequency.

A better insight into the spatial localization of the energy source and sink can be obtained by applying the divergence operator to the SI field (Eqn (A.13).

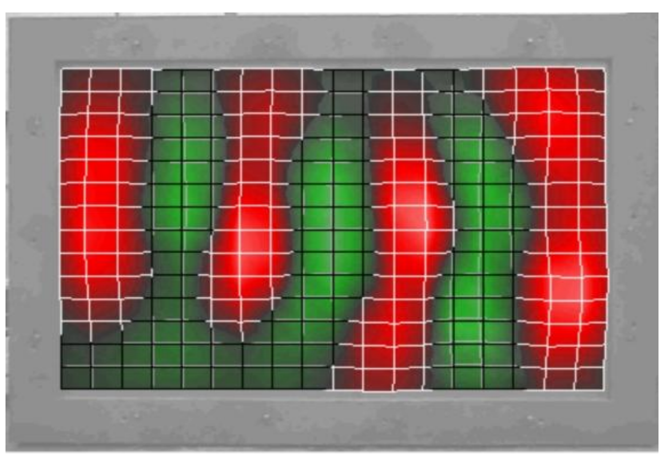

Figure A.9. Operating Deflection Shape (ODS) for the healthy plate at 409Hz.

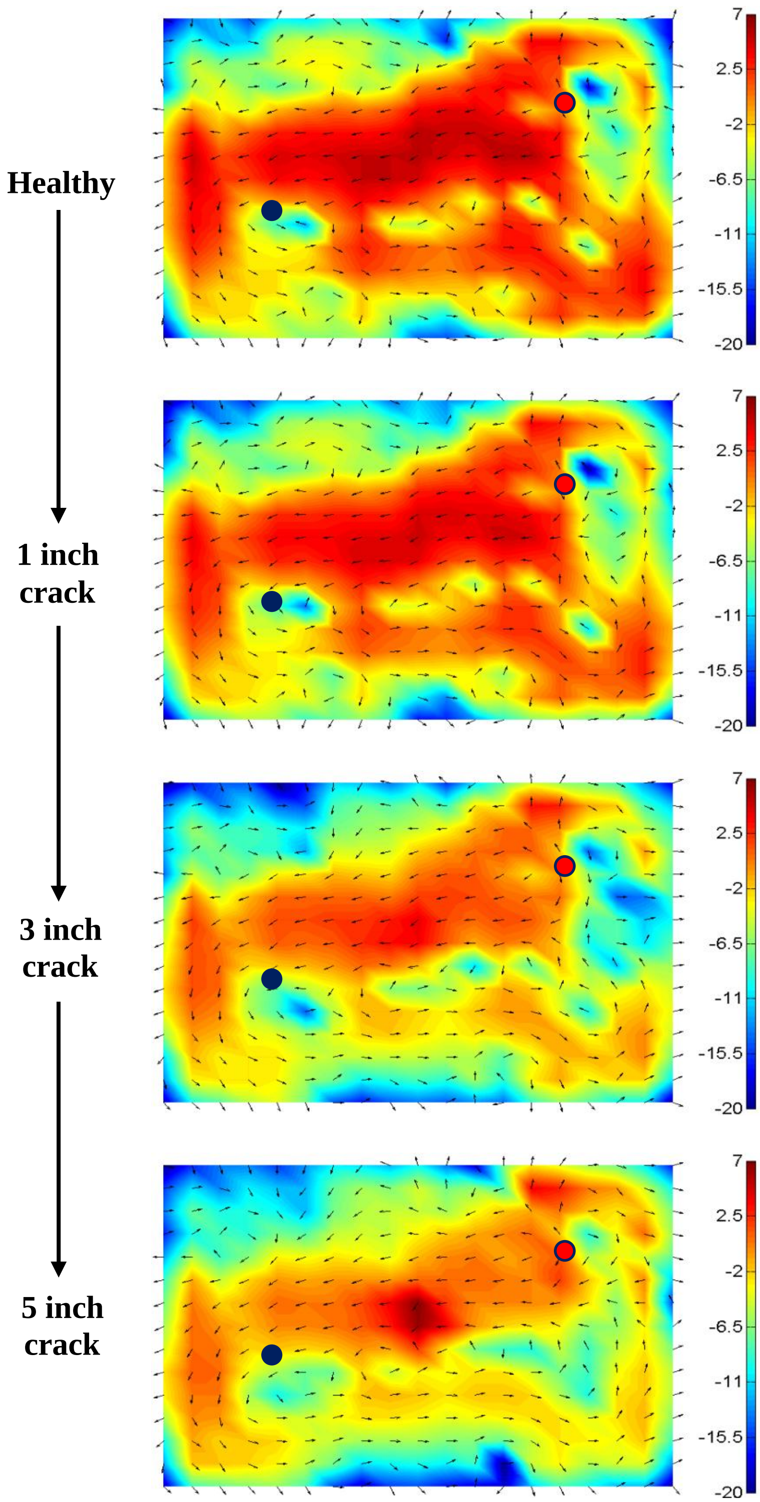

Figure A.10. Experimental SI maps for healthy and damaged plate measured at 409 Hz (off-resonance frequency). The locations of the energy source (red) and sink (blue) are indicated by a circle.

The divergence of a 3D vector field is a positive or negative scalar representing the rate of expansion/contraction per unit volume of the quantity on which the operator is applied.

When the divergence is applied to the SI field the results highlight the areas where the rate of change of the energy per unit volume is either the highest or the lowest. The divergence of the SI should provide useful information for the localization of the energy source(s) and sink(s) in the test structure.

The divergence for the SI is simply defined as:

$$div(SI) = \frac{\partial I_x}{\partial x} + \frac{\partial I_y}{\partial y} \tag{A.13}$$

where I_x and I_y are the total components of the SI in the coordinate directions.

Figure A.11 shows the divergence field for the response at 75 Hz. It can be seen how the maximum of the divergence is localized around the energy source, while the minimum is localized around the energy sink.

The presence of the damage is also indicated by a pair max/min in the divergence field. At the crack location the energy flow undergoes a sudden change in direction because energy cannot flow through the open crack. This change in direction is associated with a maximum where the flow separates and with a minimum where the flow rejoins.

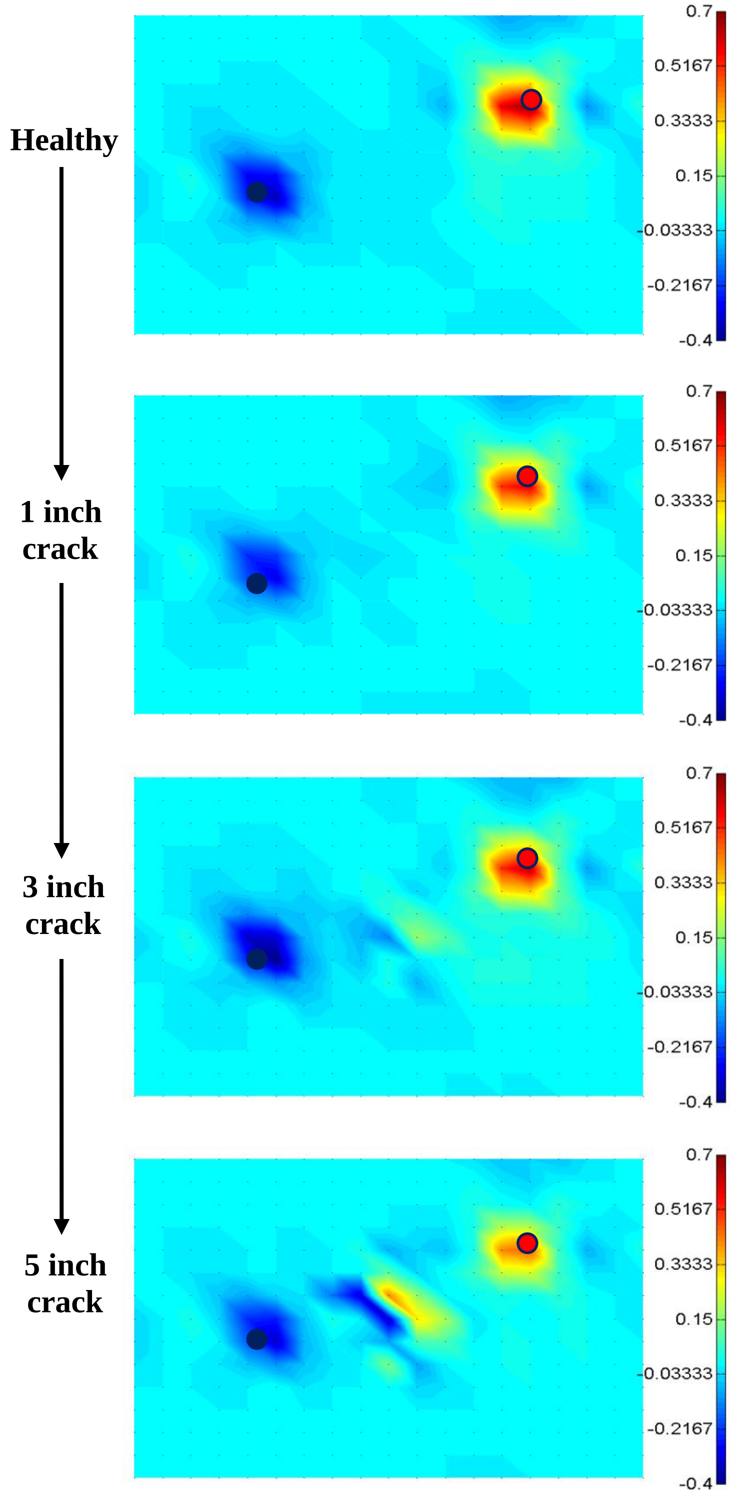

Figure A.11. Divergence plots for the 75 Hz. The locations of the energy source (red) and sink (blue) are indicated by a circle.

As a general remark on the proposed experimental results, the absence of a clear damage signature in the 1” crack SI map does not necessarily demonstrate a limitation in the sensitivity of the methodology. For this damage increment, spatial aliasing could occur due to the size of the cells (about 2”×2”) used to discretize the test structure. This phenomenon could mask localized changes in the SI. This observation is also supported by the numerical results from the sensitivity study for the mesh size which clearly showed the need for a refined mesh to capture localized phenomena.

The experimental results presented in this Appendix are intended to illustrate the experimental procedure used to acquire SI experimental measurements. Reference [134] provides an extensive analysis of the experimental SI data (2D SI maps). In [134] an assessment of the SI technique as a feature based damage detection approach is also presented and evaluated through a comparison with more standard damage indices.

A.5 SI measurements on Stiffened Panel

The test bed described in A.2 was used to evaluate the effect of a structural stiffener and loosen fasteners on the SI distribution. An I-section aluminum beam was mounted on the surface of the aluminum plate with equally spaced (2”) bolts (Figure A.12). The stiffener changes the dynamic properties of the plate shifting resonance frequencies and increasing the coupling between wave types (bending, shear and torsional). By using the experimental technique previously illustrated, the effect of the structural stiffener on the SI distribution was investigated.

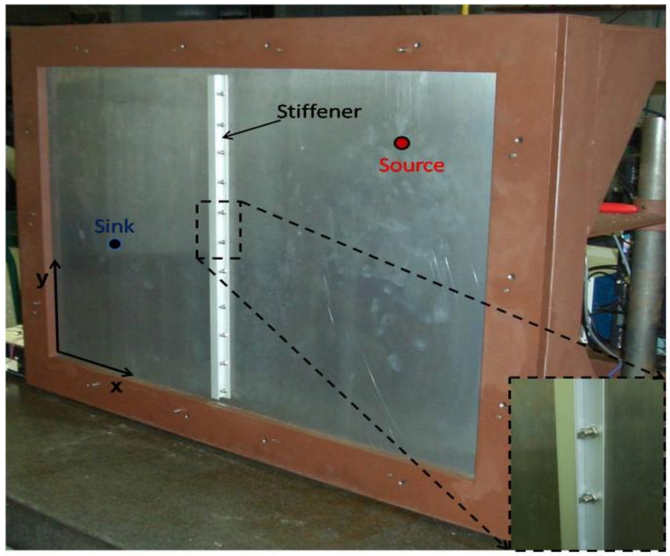

Figure A.12. Reinforced Aluminum panel for SI Experimental measurements.

The driving condition was still provided by the EM shaker and the energy sink was realized through the CLD damper, both attached in the same locations. The spatially averaged Frequency Response Function (FRF) obtained through a limited bandwidth noise input between 0-1kHz is shown in Figure A.13.

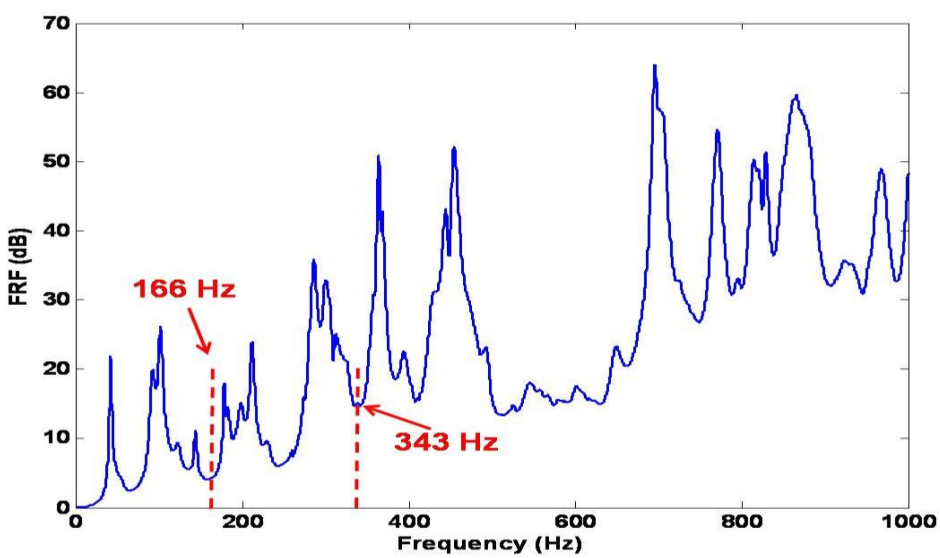

Figure A.13. Spatially averaged FRF of the stiffened panel.

An example of SI map and divergence plot at f_e=166Hz (off-resonance) for the stiffened panel is shown in Figure A.14. It can be noted how the effect of the stiffener was to confine the energy flow in the area where the energy source was located. This was a quite reasonable result considering that the shaker drove the plate in the out-of-plane direction generating essentially bending waves at low frequencies. The main effect of the stiffener was increasing the bending stiffness of the plate which explained the effect on the SI map.

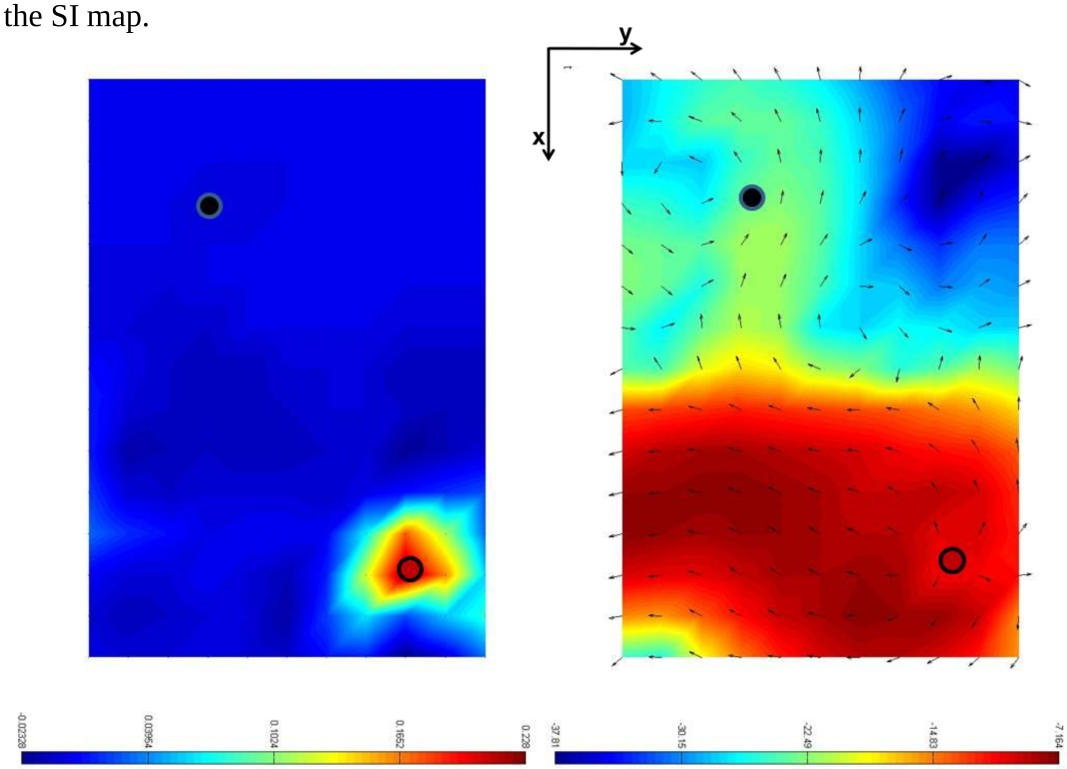

Figure A.14. (right) SI map and (left) divergence plot corresponding to the frequency f=166Hz for the healthy panel (no fasteners removed).

The clear signature of the energy source in the divergence plot versus the complete absence of the energy sink signature was also consistent with the effect of the stiffener. Under this condition, the energy going across the stiffener through the other side of the plate was a small percentage of the input energy. The percentage of energy getting to the sink was not high enough to generate a high vibration level on the CLD and, therefore, energy dissipation.

A second off-resonance frequency at f_e=343Hz was also considered. The dynamic response of a plate is generally dominated by bending waves at low frequencies and is coupled more and more with shear and torsional waves as the frequency increases. In this condition, a larger contribution of in-plane displacement components can be expected. These components are influenced less by the stiffener which mainly alters the out-of-plane dynamics. The in-plane components could allow part of the energy to pass by the stiffener. This behavior was confirmed by the SI results at f_e=343Hz (Figure A.15) where part of the vibration energy can flow through the stiffener to the other section of the plate.

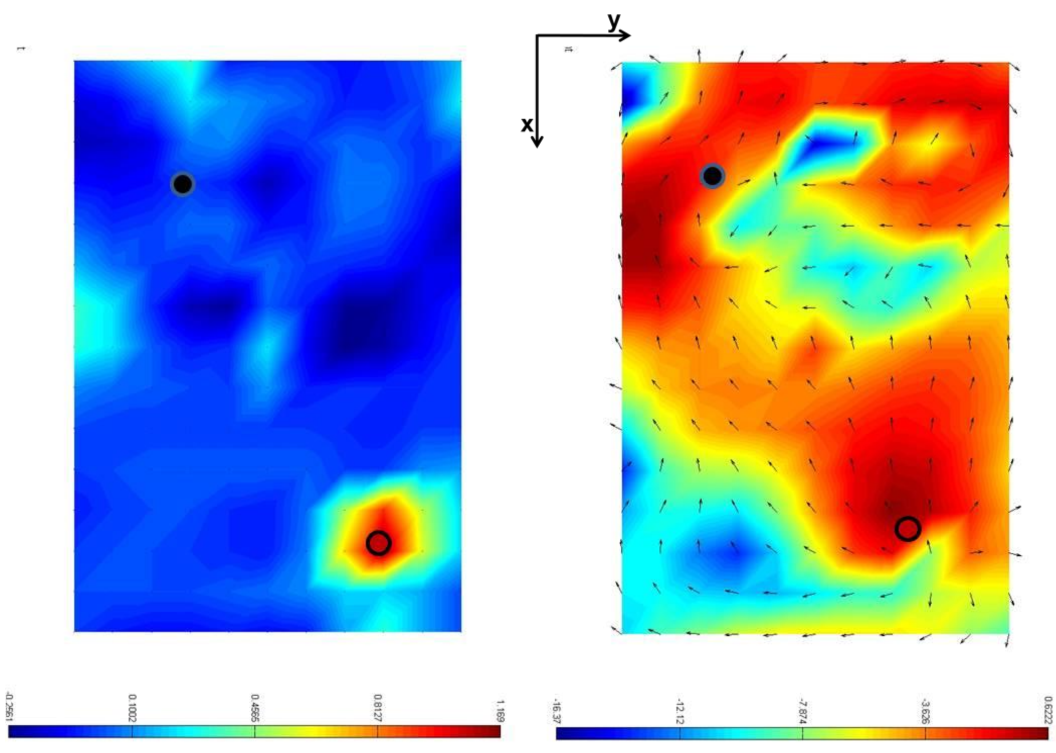

Figure A.15. (right) SI map and (left) divergence plot corresponding to the frequency f=343Hz for the healthy panel (no fasteners removed).

A.6 Nonlinear Structural Intensity

The experimental setup illustrated in §A.5 was also used to study the effect of a "loosened fastener" type defect on the SI field. In particular, the bolts connecting the stiffener to the plate were loosened to simulate the effect of broken fasteners. In this case, a mechanism similar to what illustrated in Chapter 2 and 3 for fatigue cracks takes place. In the area with loosen fasteners, a local nonlinear contact problem between the stiffener and the plate originates. When the plate vibrates, the stiffener can follow the plate motion only when the relative displacement of the structural points on the contact line is null. This results in the two conjugate points (one on the plate and one on the stiffener) being in contact and undergoing the same absolute displacement. When the relative displacement is positive, conjugate points move in opposite directions and the two structural components are no longer in contact. The periodic opening and closing of this structural interface originates a nonlinear contact problem which results in a series of impact between the stiffener and the plate. This mechanism is absolutely equivalent, in principle, to the nonlinear response characteristic of a fatigue crack under an external dynamic excitation. Consequently, the generation of nonlinear frequency components can be expected (similarly to what shown for a fatigue crack).

Under this assumption, the periodic impact of the stiffener with the plate will inject energy into the system at a very specific location and at higher order harmonic frequencies. If an SI map is acquired by driving the structure at a single frequency f_e (sine wave excitation), the nonlinear response of the coupled nonlinear system plate-stiffener could produce either superharmonic or subharmonic response. The SI map and the divergence plot should show evidence of this phenomenon by indicating the presence of an energy source located at the impact point. This source will be indicated later on as *secondary energy source*, as opposed to the primary source due to the driving excitation.

To validate this concept, SI measurement were acquired on the stiffened plate with increasing damage size. The damage was introduced in the form of loosened rows of bolts. The results in terms of SI maps and divergence plots for the first super-harmonic ($2f_e$) are shown in Figure A.16 and Figure A.17.

In particular, an excitation at f_e=706Hz was found to trigger the nonlinear response at the first superharmonic components $2f_e$. The results for the healthy structure at a frequency $2f_e$ are reported for reference in Figure A.16.

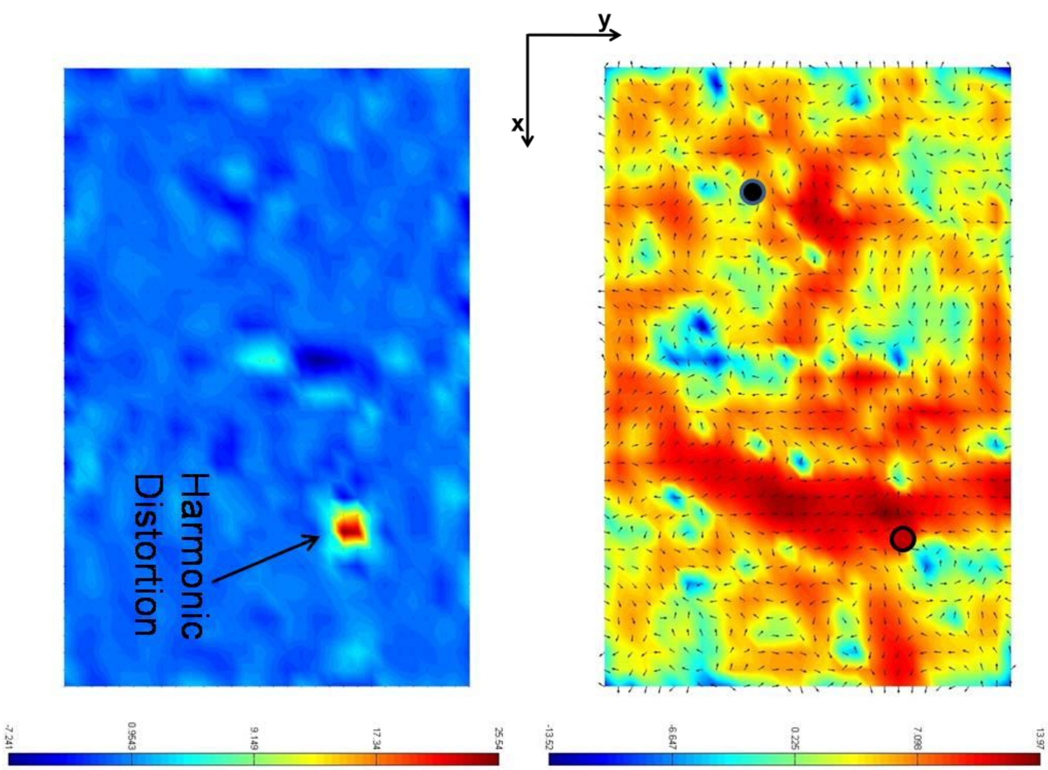

Figure A.16. (right) SI maps and (left) divergence plots at $2f_e$=1412Hz for the healthy plate (no loosened bolts).

In healthy condition the structure should not show any consistent energy signature associated with the higher order harmonic components. Although any real structure is intrinsically nonlinear, generally, this is not sufficient to spill off energy in higher order harmonic frequencies. The divergence plot, however, showed clear evidence of an energy source at the shaker location. This result was related to the Harmonic Distortion phenomenon (introduced and discussed in Chapter 3). Although the driving signal was set to be a pure sine, the HD generated by the electronic equipment in the experimental chain inevitably produced higher order harmonics. The shaker was, therefore, no longer driven only at the main frequency f_e but received also input signals at superharmonic frequencies. This behavior was what prevented the use of superharmonic components in the experimental analysis presented in Chapter 3.

The damage was introduced by removing 1 and 2 rows of bolts, respectively. The results (Figure A.17) show that the nonlinear contact generated at the damage location produced vibrational energy which was clearly identified by both the divergence plot and the SI map. In particular, for the “2-rows damage” the intensity of the secondary energy source is much higher than the primary which, in fact, does not appear in the plot. In the SI map this phenomenon is associated with energy clearly flowing into the plate from the damage location.

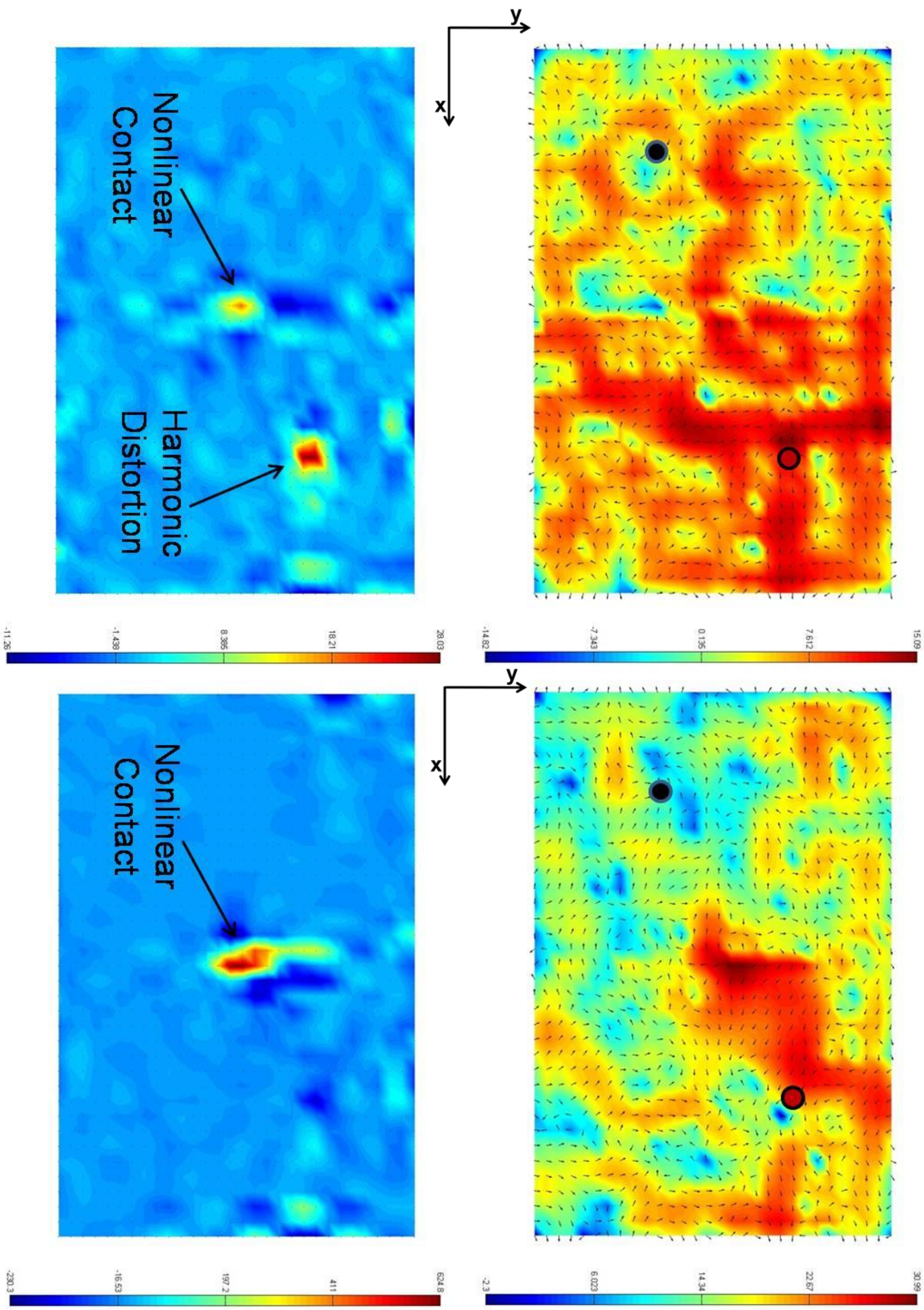

Figure A.17. (right) SI maps and (left) divergence plots at $2f_e$=1412Hz for the (top) 1-row and (bottom) 2-row damage condition. The divergence plots show that energy is injected into the plate due to the nonlinear contact with the stiffener. The HD effects are also clearly identified for the first damage increment (1-row removed).

This technique, which pertains to evaluating the SI distribution at higher order harmonic frequencies, is referred to as *Nonlinear Structural Intensity* (NSI). The main advantage of the NSI is the capability of visually showing the effect and the location of nonlinear defects under an external interrogation signal. This technique also allows discerning the different contributions generating the measured nonlinear signal. In particular, the effect of the harmonic distortion and of the structural nonlinearity at superharmonic frequencies can be clearly separated and quantified through the divergence maps.

BIBLIOGRAPHY

1. Farrar, C., R., Worden, K., 2006, “An Introduction to Structural Health Monitoring”, *Philosophical Transaction of the Royal Society*, Vol.365, pp.303-315.

2. Rytter, A, 1993, “Vibration Based Inspection of Civil Engineering Structures”, *PhD Thesis*, Aalborg University, Denmark.

3. Ji Y. Shen and Lonnie Sharpe, Jr., “An Overview of Vibrational-Based Nondestructive Evaluation Techniques”, *Proceedings of SPIE - The International Society for Optical Engineering*, v 3397, 1998, p 117-128.

4. Doebling, Scott W. (Los Alamos Natl Lab), Farrar, Charles R., Prime, Michael B., 1998, “A summary review of vibration-based damage identification methods”, *Shock and Vibration Digest*, v 30, n 2, pp. 91-105.

5. Doebling, S.W., Farrar, C.R., Prime, M.B., and Shevitz, D.W., 1996, “Damage Identification and Health Monitoring of Structural and Mechanical Systems from Changes in their Vibration Characteristics: a Literature Review,” *Los Alamos National Laboratory Report LA-13070-MS*, Los Alamos, NM.

6. Montalvao, D., Maia, N.M.M., Ribeiro, A.M.R., 2006, “A review of vibration-based structural health monitoring with special emphasis on composite materials”, *Shock and Vibration Digest*, v 38, n 4, pp 295-324.

7. Salawu, O.S., 1997, “Detection of Structural Damage Through Changes in Frequency: A Review,” *Engineering Structures*, Vol.19, (9), pp. 718-723.

8. Jiang, L.J., Tang, J., Wang, K.W., 2006, “Structural damage detection using sensitivity enhancing feedback control through eigenstructure assignment”, *Proceedings of SPIE*, v 6174, pp. 617428.

9. West, W. M., 1984, “Illustration of the use of modal assurance criterion to detect structural changes in an orbiter test specimen”, *Proceedings of the Air Force Conference on Aircraft Structural Integrity*, pp. 1-6.

10. Allemang, R. J. and Brown, D. L, 1982, "A Correlation Coefficient for Modal Vector Analysis", *Proceedings of the 1st International Modal Analysis Conference (IMAC I)*, Orlando, FL, pp. 110–116.

11. Fox, C.H.J., 1992, "The Location of Defects in Structures: A Comparison of the Use of Natural Frequency and Mode Shape Data," *Proc. of the 10th International Modal Analysis Conference*, 522–528.

12. Lieven, N. A. J. and Ewins, D. J, 1988, "Spatial Correlation of Mode Shapes: The Coordinate Modal Assurance Criterion (COMAC)", *Proceedings of the 6th International Modal Analysis Conference (IMAX VI)*, Kissimmee, FL, pp. 690–695.

13. Kim, J. H., Jeon, H. S. and Lee, C. W, 1992, "Application of the Modal Assurance Criteria for Detecting and Locating Structural Faults", *Proceedings of the 10th International Modal Analysis Conference (IMAC X)*, San Diego, CA, pp. 536–540.

14. Pandey, A. K., Biswas, M., and Samman, M. M., 1991, "Damage detection from changes in curvature mode shapes", *Journal of Sound and Vibrations*, Vol. 145(2), 321-332.

15. Stubbs, N., Kim, J. T., Topole, K., 1992, "An efficient and robust algorithm for damage localization in offshore platforms", *Proceedings of the ASCE Tenth Structures Congress*, pp. 543-546.

16. Stubbs, N., Kim, J. T. and Farrar, C. R, 1995, "Field Verification of a Nondestructive Damage Localization and Severity Estimation Algorithm", *Proceedings of the 13th International Modal Analysis Conference (IMAC XIII)*, Nashville, Tennessee, pp. 210–218.

17. Stubbs, N., Kim, J. T.,1996, "Damage localization in structures without baseline modal parameters", *AIAA J.*, 34(8), pp. 1644-1649.

18. Atkan, A. E., Lee, K. L., Chuntavan, C., Aksel, T., 1994, "Modal testing for structural identification and condition assessment of constructed facilities", *Proceedings of the 12th International Modal Analysis Conference*, pp. 462-468.

19. Pandey, A. K., Biswas, M., 1994, "Damage detection in structures using changes in flexibility", *Journal of Sound and Vibrations*, Vol. 169(1), pp. 3-17.

20. Lim, T. W., 1990, “A submatrix approach to stiffness using modal test data”, *AIAA J.*, Vol. 28(6), pp. 1123-1130.

21. Lim, T. W., 1991,” Structural damage detection using modal test data”, *AIAA J.*, Vol. 29(12), pp. 2271-2274.

22. He, J., Ewins, D. J., 1986, “Analytical stiffness matrix correction using measured vibration modes”, *Modal Analysis: The International Journal of Analytical and Experimental Modal Analysis*, Vol. 1(3), pp. 9-14.

23. Park, Y. S., Park, H. S., Lee, S. S., 1988, “Weighted-error-matrix application to detect stiffness damage – Characteristic measurements”, *Modal Analysis: The International Journal of Analytical and Experimental Modal Analysis*, Vol. 3(3), pp. 101-107.

24. Salawu, O. S., Williams, C., 1993, “Structural damage detection using experimental modal analysis – A comparison of some methods”, *Proceedings of the 11th International Modal Analysis Conference*, pp. 254-260.

25. Peterson, L. D., Alvin, K. F., Doebling, S. W., Park, K. C., 1993, “Damage detection using experimentally measured mass and stiffness matrices”, *Proceedings of the 34th AIAA/ASME/ASCE/AHS/ASC Structures, Structural Dynamics and Material Conference*, AIAA-93-1482-CP, pp. 1518-1528.

26. Ojalvo, I. U., Pilon, D., 1988, “Diagnostic for the geometrically locating structural math model errors from modal test data”, *Proceedings of the 29th AIAA/ASME/ASCE/AHS/ASC Structures, Structural Dynamics and Materials Conference*, pp. 1174-1186.

27. Zimmerman, D. C., Smith, S. W., 1992, “Model refinement and damage location for intelligent structures”, *Intelligent Structural Systems*, H. S. Tzou and G. L. Anderson, eds., Kluwer Academic, pp. 403-452.

28. Lim, T. W., Kashangaki, T. A-L., 1994, “Structural damage detection of Space truss structures using best achievable eigenvectors”, *AIAA Journal*, Vol. 32, N.5.

29. Inman, D. J., Minas, C., 1990, “Matching analytical models with experimental modal data in mechanical system”, *Control and dynamics Systems*, Academic Press Inc., Vol. 37.

30. Zimmerman, D. C., Widengren, W., 1990, “Model correction using a symmetric eigenstructure assignment technique”, *AIAA Journal*, Vol. 28, N.9.

31. Kim, H. M., Bartkowicz, T. J., 1993, "Damage detection and health monitoring of large space structures", *Journal of Sound and Vibrations*, Vol. 27(6), pp. 12-17.

32. Kim, H. M., Bartkowicz, T. J., 1997, "A two-step structural damage detection approach with limited instrumentation", *Journal of Vibrations and Acoustics – Transactions of the ASME*, Vol. 119(2), pp. 258-264.

33. Liang, C., Sun, F. P., Rogers, C. A., 1994, "Coupled Electromechanical analysis of adaptive material systems – Determination of the actuator power consumption and energy transfer", *Journal of Intelligent Material Systems and Structures*, Vol. 5, pp. 12-20.

34. Bhalla, S., Soh, C. K., 2004, "Structural Health Monitoring by Piezo-Impedance Transducers. I: Modeling", *Journal of Aerospace Engineering*, Vol. 17, N. 4, pp. 154-165.

35. Bhalla, S., Soh, C. K., 2004, "Structural Health Monitoring by Piezo-Impedance Transducers. II: Applications", *Journal of Aerospace Engineering*, Vol. 17, N. 4, pp. 166-175.

36. Bhalla, S., Soh, C. K., 2004, "Electromechanical Impedance Modeling for Adhesively Bonded Piezo-transducers", *Journal of Intelligent Material Systems and Structures*, Vol. 15, pp. 955-972.

37. Stokes, J. P., and Cloud, G. L., 1993, "The Application of Interferometric *Techniques to the Nondestructive Inspection of Fiber-Reinforced Materials," Experimental Mechanics*, Vol. 33, pp. 314–319.

38. Esteban, J., 1996, "Modeling of the Sensing Region of a Piezoelectric Actuator/Sensor," *Ph.D. Dissertation*, Virginia Polytechnic Institute and State University, Blacksburg, VA.

39. Raju, V., 1998, "Implementing Impedance-Based Health Monitoring Technique," *Master's thesis*, Virginia Polytechnic Institute and State University, Blacksburg, VA.

40. Castanien, K.E., and Liang, C., 1996, "Application of Active Structural Health Monitoring Technique to Aircraft Fuselage Structures," *Proceeding of SPIE Smart Structure Conference*, Vol. 2721, pp. 38–50.

41. Park, G., Sohn, H., Farrar, C. R., Inman, D., 2003, "Overiview of Piezoelectric Impedance-Based Health monitoring and Path Forward", *The shock and Vibration Digest*, Vol. 35, N. 6, pp. 451-463.

42. Park, G., Cudney, H. H., Inman, D. J., 2000, "Impedance-Based Health Monitoring of Civil Structural Components", *Journal of Infrastructure Systems*, Vol. 6, N. 4, pp. 153-160.

43. Lamb, H., 1917, "On waves in an elastic plate", *Proceedings of the Royal Society of London, Containing papers of a mathematical and physical character*, Vol. 93, pp. 293-312.

44. Rose, J. L., "Ulatrsonic waves in solid media", *Cambridge University Press* 1999.

45. Saravanos, D. A., Birman, V., Hopkins, D. A., 1994, "Detection of delaminations in composite beams using piezoelectric sensors", *Proceedings of the 31th AIAA/ASME/ASCE/AHS/ASC Structures, Structural Dynamics and Material Conference*, pp. 181-191.

46. Alleyne, D. N., Cawley, P., 1992, "The interaction of Lamb waves with defects", *IEEE Transactions on ultrasonics, Ferroelectrics and Frequency Control*, Vol. 39, pp. 381-397.

47. Monkhouse R. S. C, Wilcox P. D., Cawley P., 1997, "Flexible interdigital PVDF transducers for the generation of Lamb waves in structures", *Ultrasonics*, Vol. 35, pp. 489–98.

48. Monkhouse R S C, Wilcox P W, Lowe M J S, Dalton R P and Cawley P, 2000, "The rapid monitoring of structures using interdigital Lamb wave transducers", *Smart Materials and Structures*, Vol. 9, pp. 304–9.

49. Kessler, S. S., Spering, S. M., Soutis, C., 2002, "Damage detection in composite materials using Lamb wave methods", *Smart Materials and Structures*, Vol. 11, pp. 269-278.

50. Mobasher, B., Stang, H., Shah, S. P., 1990, "Micro-cracking in fiber reinforced concrete", *Cement and Concrete Research*, Vol. 20, pp. 665-676.

51. Bray, D., McBride, D., 1992, "Nondestructive testing techniques", *Wiley*, New York.

52. Ng, E. T., Qi, G., 2001, " Material fatigue behavior characterization using the wavelet-based AE technique – a case study of acrylic bone cement", *Engineering Fracture Mechanics*, Vol. 68, pp. 1477-1492.

53. Colla, C., Lausch, R., 2002 " Influence of source frequency on impact-echo data quality for testing concrete structures", *NDT&E International*, Vol. 36, pp. 203–213.

54. Kim, H., Mehlem, H., 2004, "Damage detection of structures by wavelet analysis", *Engineering Structures*, Vol. 26, pp. 347-362.

55. Yan, Y. J., Yam, L. H., 2002, "Online detection of crack damage in composite plates using embedded piezoelectric actuators/sensors and wavelet analysis", *Composite Structures*, Vol. 58, pp. 9-38.

56. Amaravadi, V., Rao, V., Koval, L. R., Derriso, M., 2001, "Structural Health Monitoring using Wavelet Transforms", Smart structures and integrated systems, *Proceeding of SPIE*, pp. 258-269.

57. Kitada, Y.,1998, "Identification of nonlinear structural dynamic systems using wavelets", *Journal of Engineering Mechanics*, Vol.124(10), pp. 1059-1066.

58. Hatem, T. M., Foutouh, M. N. A., Negm, H. M., 2004, "Application of genetic alghoritms and neural networks to Health Monitoring of composites structures", *Proceedings of the 2nd European Workshop on Structural Health Monitoring, Munich*, Germany, pp. 616-623.

59. Yam, L. H., Yan, Y. J., Cheng, L., Jiang, J. S., 2003, "Identification of complex crack damage for honeycomb sandwich plate using wavelet analysis and neural networks", *Smart Material and Structures*, Vol. 12, pp. 661-671.

60. Rosenberg, G., C., 2009, "Upgrade Fluid System Filter Element Monitoring to Increase Operational Reliability and Support Condition Based Maintenance Capability", *AHS CBM Specialist Meeting*, Huntsville, AL.

61. Messer, K., 2009, "The Platform Maintenance Environment", *AHS CBM Specialist Meeting*, Huntsville, AL.

62. Stevens, P. L., 2001, "Active interrogation of helicopter main rotor faults using trailing edge flap actuation", *Ph.D. dissertation*, Penn State University, University Park, PA.

63. Land, J., Weitzman, C., “How HUMS have the Potential of Significantly Reducing the Direct Operating Costs for Modern Helicopters through Monitoring”, *Proceedings of the American Helicopter Society 51st Annual Forum, Forth Worth*, TX, 1995, pp. 744-757.

64. Fraser, K., F., 1994, ”An Overview of Health and Usage Monitoring Systems (HUMS) for Military Helicopters”, *Department of Defense – Defense Science and Technology Organization, DSTO Aeronautical and Maritime Research Laboratory*.

65. Sohn, H., 2007, “Effects of Environmental and Operational Variability on Structural Health Monitoring,” *A Special Issue of Philosophical Transactions of the Royal Society on Structural Health Monitoring*, Vol. 365, pp. 539-560.

66. Ohara, Y., Mihara, T., Sasaki, R., Ogata, T., Yamamoto, S., Kishimoto, Y., Yamanaka, K., 2007, “Imaging of Closed Cracks using Nonlinear Response of Elastic Waves at Subharmonic Frequency”, *Applied Physics Letters*, Vol. 90, 011902.

67. Nayfeh A. H. and Mook D. T., “Nonlinear Oscillations”, *Wiley –Interscience*, 1993.

68. Manevitch, I. A., Manevitch, I. L., “The Mechanics of Nonlinear Systems with Internal Resonances”, *Imperial College Press*, 2005.

69. Minorsky, N., “Nonlinear Oscillations”, *D. Van Nostrand Company INC.,* 1962.

70. Dimaragonas, A., D., 1996, “Vibration of Cracked Structures: A State of the Art Review”, *Engineering Fracture Mechanics*, Vol. 55, pp. 831-857.

71. Shen M. H. and Chu Y. C., 1992 “Vibrations of Beams with a Fatigue Crack”, *Computers & Structures*, Vol. 45, No. 1,79-93.

72. Cheng, S. M., Wu, X., J., Wallace, W., Swamidas, A. S. J., 1999, “Vibrational Response of a Beam with a Breathing Crack”, *Journal of Sound and Vibration*, Vol. 225, pp. 201-208.

73. Solodov I., Wackerl J., Pfleiderer K., Busse G., 2004, “Nonlinear Self-Modulation and Subharmonic Acoustic Spectroscopy for damage Detection and Location”, *Applied Physics Letters*, Vol. 84 (26), 5386-5388.

74 . Doyle J. F., “Wave Propagation in Structures”, *Springer-Verlag*,1989.

75 . Doyle J. F., 1987, “An Experimental Method for Determining the Location and Time of Initiation of an Unknown Dispersing Pulse”, *Experimental Mechanics*, Vol. 27, 229-233.

76 . Bayly P.V., 1996, “On the Spectral Signature of Weakly Bilinear Oscillators”, *J. Vibr. Acoust.*, Vol. 118, 352-361.

77 . Sundermeyer J. N., Weaver R. L., 1995, “On Crack Identification and Characterization in a Beam by Nonlinear Vibration Analysis”, *Journal of Sound and Vibration*, Vol. 183(5), 857-871.

78 . Musil M., 2006, “Localization and quantification of a breathing crack”, *Transactions of the ASME,* Vol. 128, 458-462.

79 . Sinha J. K., Friswell M. I., 2002, “Simulation of the dynamic response of a cracked beam”, *Computers and Structures*, Vol.80, 1473-1476.

80. Luzzato E., 2003, “Approximate computation of non-linear effects in a vibrating cracked beam”, *J. of Sound and Vibration*, Vol.265, 745-763.

81 . Douka E., Hadjileontiadis L.J., 2005, “Time–frequency analysis of the free vibration response of a beam with a breathing crack”, *NDT&E International*, Vol. 38, 3–10.

82 . Mickens R. E., “An Introduction to Nonlinear Oscillations”, *Cambridge University Press*, 1981.

83 . J. S. Bendat and A. G. Piersol, “Random Data: Analysis and Measurements Procedures”, *John Wiley and Sons Inc.*, 2000.

84. Korshak, B. A., Solodov, I. Y., Ballad, E. M., 2002,” DC effects, Subharmonics, Stochasticity and “Memory” for Contact Acoustic Non-linearity”, *Ultrasonics*, Vol. 40, pp. 707-713.

85. Yamanaka, K., Mihara, T., Tsuji, T., 2004, “Evaluation of Closed Cracks by Model Analysis of Subharmonic ultrasound”, *Japanese Journal of Applied Physics*, Vol. 43, pp. 3082-3087.

86. Solodov, I., Wackerl, J., Pfleiderer, K., Busse, G., 2004, “Nonlinear Self-Modulation and Subharmonic Acoustic Spectroscopy for Damage Detection and Location”, *Applied Physics Letters*, Vol. 84, N. 26, pp. 5386-5388.

87. Bovsunovsky, A. P., Surace, C., 2005, "Considerations regarding Superharmonics Vibrations of a Cracked Beam and the Variation in Damping Caused by the Presence of the Crack", *J. of Sound and Vibration*, Vol. 288, pp. 865-886.

88. Sundermeyer J. N., Weaver R. L., 1995, "On Crack Identification and Characterization in a Beam by Nonlinear Vibration Analysis", *Journal of Sound and Vibration*, 183(5), 857-871.

89. Brandon, J. A., Sufraud, C., 1998, "An Experimental Investigation into the Topological Stability of a Cracked Cantilever Beam", *J. of Sound and Vibration*, Vol. 211, pp. 555-569.

90. Ohara, Y., Mihara, T., Sasaki, R., Ogata, T., Yamamoto, S., Kishimoto, Y., Yamanaka, K., 2007, "Imaging of Closed Cracks using Nonlinear Response of Elastic Waves at Subharmonic Frequency", Applied Physics Letters, Vol. 90, 011902.

91. Ohara, Y., Mihara, T., Yamanaka, K., 2006, "Effect of Adhesion Force Between Crack Planes on Subharmonic and DC Responses in Nonlinear Ultrasound", Ultrasonics, Vol. 44, pp. 194-199.

92 Bishop, S. R., Thompson, M. G., Foale, S., Roceeding of the Royal Society of London, Vol. 452, pp. 2579.

93 Pippard, A., B., 1978, "The Physics of Vibrations I", Cambridge University Press, Cambridge.

94. Carpinteri, A., Pugno, N., 2005, "Towards Chaos in Vibrating Damaged Structures – Part I: Theory and Period Doubling Cascade", *J. of Applied Mechanics*, Vol. 72, pp. 511-518.

95. Minorsky, N., "Nonlinear Oscillations", *Princeton*, 1962.

96. Solodov, I. Y., Krohn, N., Busse, G., 2002, "CAN: an Example of Nonclassical Acoustic Nonlinearity in Solids", *Ultrasonics*, Vol. 40, pp. 621-625.

97. Moussatov, A., Gusev, V., Castagnede, B., 2003, *Phys Rev. Lett*. 90.

98. Solodov, I., Wackerl, J., Pfleiderer, K., Busse, G., 2004, "Nonlinear Self-Modulation and Subharmonic Acoustic Spectroscopy for Damage Detection and Location", *Applied Physics Letters*, Vol. 84, N. 26, pp. 5386-5388.

---

99. Kawiecki, G., Jesse, S., 2002, “Rosette Piezotransducers for Damage Detection”, *Smart Material and Structures*, Vol. 11, pp.196-201.

100. Thursby, G., Sorazu, B., Betz, D., Culshaw, B., 2004, “Comparison of Point and Integrated Fiber Optic Sensing Techniques for Ultrasound Detection and Location of Damage”, *Proceedings of SPIE*, 5768, pp. 313-322.

101. Betz, D., Thursby, G., Culshaw, B., Staszewski, W., 2003, “ Lamb Wave Detection and Source Location using Fiber Bragg Grating Rosettes”, Smart Material and Structures, Vol. 5050, pp. 117-127.

102. Matt, H. M., Lanza di Scalea, F., 2007, “ Macro-Fiber Composite Piezoelectric Rosettes for Acoustic Source Location in Complex Structures”, *Smart Material and Structures*, Vol. 16, pp. 1489-1499.

103 . Sharpe W., 2008, “Handbook of Experimental Solid Mechanics”, *Springer*.

104. Pavic, G. "Measurement of Structure Borne Wave Intensity, Part I: Formulation of the Methods." *Journal of Sound and Vibration (1976): 221-230.*

105. Conlon, S., May, R., Hambric, S., Banks, J., Reichard, K., 2007, “Structural intensity measurement for damage detection”, *Inter-noise Conf, Instanbul*, Turkey.

106. Banks, Jeffrey C., 2000, "Characterization of Machinery Condition using Structural Surface Intensity" *Master Thesis,* The Pennsylvania State University.

107. Conlon, Banks, J., Reichard, K., Brannen, N., 2005, “Structural Health Monitoring and Assessment using Structural Intensity Sensing”, *Proc. 5th Int. Workshop on SHM,* Stanford University, Stanford, CA, pp. 977-984.

108. Noiseaux, D. U., 1970, “Measurements of Power Flow in Uniform Beams and Plates”, *J. Acoustic Society America,* Vol. 47, pp. 238-247.

109. Arruda , J. R. F., Mas, P., 1996, “Predicting and Measuring Flexural Power Flow in Plates”, *Proc.SPIE, 2868,* pp.149-163.

110. Pavic, C., 1976, “Measurement of Structure Borne Wave Intensity, Part I: Formulationof Methods”, *J. of Sound and Vibration,* Vol. 49(2), pp.221-230.

111. May, R., 2007, “An Investigation of Flexural Wave Energy Flow Sensitivity to Crack Damage in Thin Beams”, *Master Thesis*, Pennsylvania State University.

112. Schmidt, W., T., Conlon, S., C., 2009, “Structural intensity based damage detection assessments of aluminum panel structures”, *Proceedings of Internoise*, Ottawa, Canada.

113. Hambric, S., A., 1996, “McPow User Manual”.

114. Conlon, S. C., Semperlotti, F., Schmidt, W., 2008, “UH-60A Transmission Frame Vibration Measurement Test Report”, *US ARMY AATD Test Report*.

115. Bendat, J., S., Piersol, A., G., 1993, « Engineering Applications of Correlation and Spectral Analysis”, *Wiley-Interscience*.

116. Balas, M., J., 1979, “Direct Velocity Feedback Control of Large Space Strutcures”, Journal of Guidance and Control, Vol.2, pp. 252-253.

117. Achkire, Y, Preumont, A., 1996, “Active Tendon Control of Cable-Stayed Bridges”, Earthquake Engineering and Structural Dynamics, Vol. 25, pp.585-597.

118. “Intensity Based Structural Health Monitoring Mid-Project Review”, Technical Report to U.S. Army AATD, May 2009.

119. Ikeda, T., 1990, “Fundamental of Piezoelectricty”, Oxford University Press, Oxford,NY.

120. Moheimani, S. O. Reza, 2006, “Piezoelectric Transducers for Vibrating Control and Damping”, *Springer,* London.

121. Preumont, A., 1997, “ Vibration Control of Active Structures, An Introduction”, Kluwer Academic Publisher, Dordrecht, The Netherlands.

122. Dosch, J. J., Inman, D. J., Garcia, E., 1992, “A Self-Sensing Piezoelectric Actuator for Collocated Control”, J. of Intelligent Material System and Structures, Vol. 3, pp. 166-185.

123. Anderson, E. H., Hagood, N. W., Goodliffe, J. M., 1992, “Self-Sensing Piezoelectric Actuation: analysis and application to controlled structures”, Proceedings of the 33rd AIAA/ASME/ASCE/AHS/ASC Structures, Structural Dynamics, Materials Conference, Dallas, USA, April 13-15, 1992, pp.2141-2155.

124. Pavic, G., 1985, “Structural Surface Intensity: a new approach in vibration analysis and diagnostics”, *Proceedings of Congrès International sur la Mesure de l’Intensité Acoustique*, 23-26 September, Senslis, France, pp. 219-225.

125. Pavic, G., 1987, “Structural Surface Intensity: an alternative in vibration analysis and diagnostics”, *Journal of Sound and Vibration*, Vol. 115, 405-422.

126. Macaulay, M., A., 1987, “Introduction to Impact Engineering”, *Chapman and Hall*, London.

127. Goldsmith, W., 1960, “Impact: The Theory and Physical Behavior of Colliding Solids”, *Edward Arnold LTD*, London.

128. “MD Nastran R2.1 - Quick Reference Guide”, *MSCSoftware*.

129 . Zak, M. Krawczuk and W. Ostachowicz, 2001, ”Vibration of a Laminated Composite Plate with Closing Delamination”, *Journal of Intelligent Material Systems and Structures*, Vol. 12, 545.

130. Arruda , J. R. F., Mas, P., 1996, “Predicting and Measuring Flexural Power Flow in Plates”, *Proc.SPIE*, 2868, pp.149-163.

131. Daley, M. J., 2003, “Prediction and Measurements of Structural Intensity in Thin Plates Excited by Distributed Random Fluctuating Pressure Fields”, *Ph.D. Dissertation*, The Pennsylvania State University.

132. Daley, J. M., Hambric, S. A., 2005, “Simulating and Measuring Structural Intensity Fields in Plates Induced by Spatially and Temporally Random Excitation”, *J. of Vibration and Acoustics*, Vol. 127, pp. 451-457.

133. Bendat, J. S., Piersol, A. G., 1986, “Random Data Analysis and Measurement Procedures”, *John Wiley and Sons*, New York, NY.

134. Schmidt, W., T., Conlon, S., C., 2009, “Structural intensity based damage detection assessments of aluminum panel structures”, *Proceedings of Internoise*, Ottawa, Canada.

135. “Diamond - User’s Manual”, *Los Alamos National Laboratory*.

VITA

Fabio Semperlotti was born March 26, 1975 in Rome, Italy. He obtained a M.S. in Aerospace Engineering in 2000 and a M.S. in Astronautic Engineering in 2002 from the University of Rome "La Sapienza". In 2001 he was one of the recipients for the "Leonardo" Scholarship program funded by the European Community in order to promote international research activities. Under this program, he spent a six months period at the European Space Agency (ESA-ESTEC), in the Netherlands, working on the development of active vibration control algorithm for large space flexible structures. Since 2000 he has been serving as structural engineer in different European industries and agencies mainly involved with the design of space propulsion systems.

In 2006 he joined the Aerospace Ph.D. program at Penn State. During this period he carried on a research in the field of Structural Health Monitoring with specific application on rotorcraft structures.

He is a member of the American Helicopter Society and of the American Institute of Aeronautics and Astronautics.